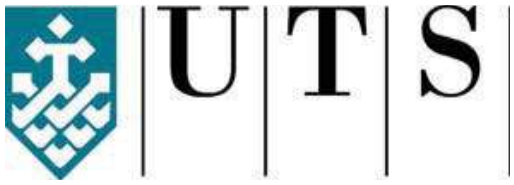

University of Technology, Sydney

Advanced Control in Smart Microgrids

Jiefeng HU

M.E. (Electrical Engineering), B.E. (Electrical Engineering)

School of Electrical, Mechanical and Mechatronic Systems
University of Technology, Sydney, Australia

A thesis submitted to the University of Technology, Sydney
for the Degree of Doctor of Philosophy

June 2013

CERTIFICATE OF AUTHORSHIP/ORIGINALITY

I certify that the work in this thesis has not previously been submitted for a degree nor has it been submitted as part of requirements for a degree except as fully acknowledged within the text.

I also certify that the thesis has been written by me. Any help that I have received in my research work and the preparation of the thesis itself has been acknowledged. In addition, I certify that all information sources and literature used are indicated in the thesis.

Signature of Candidate

Acknowledgements

First of all, I would like to express sincere gratitude and appreciation to my supervisor, Professor Jianguo Zhu, for his invaluable guidance, enthusiastic help, and consistent encouragement throughout the entire research project. I am also thankful to Associate Professor David G. Dorrell, the co-supervisor, for his fruitful discussions and useful suggestion.

Also, I would like to thank Dr. Glenn Platt, the external co-supervisor, from the Commonwealth Scientific and Industrial Research Organisation (CSIRO) for his kind support and encouragement. His rich industrial experience and advices broadened my mind of microgrids, which had a very positive impact on this work.

Thanks also go to my laboratory colleagues, in particular Dr. Greg Hunter and Dr. Gang Lei, of the Centre for Electrical Machines and Power Electronics, University of Technology, Sydney (UTS), for their helpful advices, technical support and friendship.

I appreciate the support provided by Professor Qishuang Ma from Beijing University of Aeronautics & Astronautics and Dr. Xiaoying Kong from UTS. I am also thankful to Professor Josep M. Guerrero from Aalborg University, Denmark, for his valuable discussions on smart microgrid technologies.

I would also like to express my deepest gratitude to my parents for their support and encouragement. Their inspiring suggestions and practical experience sharing are very important and helpful when I made my own decisions on various occasions.

Finally, I want to express my deepest love to Jenny Mok, for her encouragement and understanding throughout the thesis project.

TABLE OF CONTENTS

List of Symbols

C	Filter capacitance [μF]
D_i	Switching state of phase i ($i = a, b, c$) leg of the IGBT bridges
f_1, f_2, f_{11}, f_{22}	Slopes or derivatives
f_g	Grid frequency [Hz]
$\boldsymbol{i}_f$, $\boldsymbol{i}_L$, $\boldsymbol{i}_g$	Filter current, load current, and grid current [A]
$\boldsymbol{I}_\mathrm{d}$	Current through the diode [A]
$\boldsymbol{I}_\mathrm{PV}$	Photocurrent of the PV cell [A]
$\boldsymbol{I}_\mathrm{s}$, $\boldsymbol{I}_\mathrm{r}$	Stator and rotor phase current vectors [A]
K_p, K_i	Gain constant of the Proportional-Integral (PI) controller
L	Line inductance [mH]
L_m, R_m	Magnetizing inductance and resistance per phase [Ω]
$L_{\sigma\mathrm{s}}$, $L_{\sigma\mathrm{r}}$	Stator and rotor phase winding leakage inductance [Ω]
L_s, L_r	Stator and rotor phase winding self-inductance [Ω]
L_t	Tie-line inductance [mH]
m, n	Droop coefficients [rad/W, Wb/Var]
N	Coincidence point
P_1, P_2	Active power injected by DGs to microgrid [W]
P_L	Active load power [W]
P_g	Active power injected by utility to microgrid [W]
P_rated, Q_rated	Active and reactive power rating of the DGs [W]
P_s, Q_s	Stator active and reactive power [W]
p	Number of pole pairs
Q_1, Q_2	Reactive power injected by DGs to microgrid [Var]
Q_L	Reactive load power [Var]
Q_g	Reactive power injected by utility to microgrid [Var]
R	Line resistance [Ω]
R_L	Load resistance [Ω]
R_{PVs}, R_{PVsh}	Intrinsic series and shunt resistances of the PV cell [Ω]
R_s, R_r	Stator and rotor phase winding resistance [Ω]
R_t	Tie-line resistance [Ω]

Sk	Sector division
T_c	Computing time [μs]
T_e	Electromagnetic torque [Nm]
T_s	Sampling period [μs]
T_V	Virtual torque [Nm]
V_{dc1}, V_{dc2}	DC source voltage of the Distributed Generation [V]
$\boldsymbol{V}_i$, $\boldsymbol{V}_c$, $\boldsymbol{E}$	Inverter voltage, capacitor voltage, and load-side voltage [V]
V_g	Magnitude of the grid voltage [V]
$\boldsymbol{V}_s$, $\boldsymbol{V}_r$	Stator and rotor phase voltage vectors [V]
ω_1, ω_r, ω_s	Synchronous, rotor, and slip angular frequency [rad/s]
ω_c	Cut-off angular frequency [rad/s]
ω_g	Grid angular frequency [rad/s]
$\boldsymbol{\psi_s}$, $\boldsymbol{\psi_r}$	Stator and rotor flux vectors [Wb]
$\boldsymbol{\psi}_V$, $\boldsymbol{\psi}_E$	Inverter flux vector and load-side flux vector [Wb]
φ_{fV}, φ_{fE}	Phase angles of the inverter flux and load-side flux [rad]
φ_V, φ_E	Phase angles of the inverter voltage and load-side voltage [rad]
φ_Z	Phase angles of the line impedance [rad]
δ	Phase angle difference between inverter flux and load-side flux [rad]
λ	Leakage coefficient
λ_2, λ_3	Weighting factors

List of Abbreviations

ADC	Analog to Digital Conversion
ALS	Average Load Sharing
AMI	Advanced Metering Infrastructure
BDFTSIG	Brushless Doubly Fed Twin Stator Induction Generator
CHP	Combined Heat and Power Stations
3C	Circular Chain Control
CSCF	Constant Speed Constant Frequency
CSI	Current Source Inverter
CSIRO	Commonwealth Scientific and Industrial Research Organisation
DAC	Digital to Analog Conversion
DFC	Direct Flux Control
DFIG	Doubly-Fed Induction Generator
DG	Distributed Generation
DPC	Direct Power Control
DSP	Digital Signal Processor
DTC	Direct Torque Control
ESS	Energy Storage System
FACTS	Flexible Alternating Current Transmission Systems
FRT	Fault Ride Through
HVDC	High Voltage Direct Current Transmission Systems
ICT	Information Communication Technology
IEEE	Institute of Electrical and Electronics Engineers
IGBT	Insulated Gate Bipolar Transistor
IGCT	Insulated Gate Commutated Transistor
IPM	Intelligent Power Module
ISR	Interrupt Service Routine
LB	Load Bank
LPF	Low Pass Filter
MOMPC	Multi-Objective Model-Predictive Control
MPC	Model Predictive Control
MPDFC	Model Predictive Direct Flux Control
MPPT	Maximum Power Tracking Point

MS	Master-Slave
MT	Micro-turbine
NIST	National Institute of Standard and Technology
NPC	Neutral-point-clamped
PC	Personal Computer
PCC	Point of Common Coupling
PDPC	Predictive Direct Power Control
PDVTC	Predictive Direct Virtual Torque Control
PEMFC	Proton Exchange Membrane Fuel Cell
PI	Proportional-Integral
PMSG	Permanent Magnet Synchronous Generator
PV	Photovoltaic
PWM	Pulse Width Modulation
RTDX	Real Time Data Exchange
SCADA	Supervisory Control and Data Acquisition
SCIG	Squirrel Gage Induction Generator
SDFC	Switching Table Based Direct Flux Control
SDPC	Switching Table Based Direct Power Control
SGA	Smart Grid Australia
SOC	State of Charge
SPI	Serial Peripheral Interface
SPWM	Sinusoidal Pulse Width Modulation
STATCOM	Static Synchronous Compensator
STS	Static Transfer Switch
SVM	Space Vector Modulation
REIF	Renewable Energy Integration Facility
RF	Radio Frequency
THD	Total Harmonic Distortion
TSR	Tip Speed Ratio
UART	Universal Asynchronous Receiver Transmitter
UPS	Uninterruptible Power Supply
UTS	University of Technology, Sydney
VC	Vector Control
VOC	Voltage-Oriented Control

VSCF	Variable Speed Constant Frequency
VSI	Voltage Source Inverter
WFSG	Wound Field Synchronization Generator

LIST OF FIGURES

LIST OF TABLES

ABSTRACT

This thesis presents various advanced control strategies in smart microgrid applications.

In recent years, due to the rapid depletion of fossil fuels, increasing demand of electricity, and more strict compulsory government policies on reduction of greenhouse gas emissions, renewable energy technologies are attracting more and more attentions and various types of distributed generation (DG) sources, such as wind turbine generators and solar photovoltaic (PV) panels, are being connected to low-voltage distribution networks. Because of the intermittent nature of the renewable energy sources, it would be a good idea to connect these DG units together with energy storage units and loads to form a local micro power system, known as microgrid. This PhD thesis project aims to develop new and competitive control methods for microgrid applications.

Based on a review of the state of the art of the wind power techniques, a new predictive direct control strategy of doubly fed induction generator is proposed. This method can achieve fast and smooth grid synchronization, and after grid connection, the active and reactive power can be regulated flexibly, which enables the wind power systems contributing to the grid voltage support and power quality improvement. The proposed strategy is simple and reliable, and presents excellent steady-state and dynamic performance.

A new control approach using the model predictive scheme is developed for a PV system in microgrid applications. In the islanded operation, the inverter output voltage is controlled stably for the local loads. A simple synchronization scheme is introduced to achieve seamless transfer, and after being connected to the utility grid, the PV system can inject both active and reactive power into the grid flexibly within its capacity.

As the capacity of DGs getting larger, the power conversion efficiency becomes more important. In order to reduce the switching loss, a multi-objective model-predictive control strategy is proposed for the control of high power converters. By revising the cost function properly, the switching frequency can be reduced considerably without deteriorating the system performance. The control strategy is simplified using a graphical algorithm to reduce the computational burden, which is very useful in practical digital implementation where high sampling frequency is

required. The proposed method is very flexible and can be employed in both AC/DC and DC/AC energy conversions in microgrids.

For a microgrid consisting of several DG units, various system level control methods are studied. A novel flux droop control approach is developed for parallel-connected DGs by drooping the inverter flux instead of drooping the inverter output voltage. The proposed method can achieve autonomous active and reactive power sharing with much lower frequency deviation and better transient performance than the conventional voltage droop method. Besides, it includes a direct flux control (DFC) algorithm, which avoids the use of proportional-integral (PI) controllers and PWM modulators.

For a microgrid system consisting of a 20 kW PV array and a 30 kW gas microturbine, a coordinated control scheme is developed for both islanded and grid-connected operations. The experimental results from a renewable energy integration facility (REIF) laboratory confirmed the feasibility of the control strategy. The response of this microgrid under the condition of grid faults is investigated and the relevant protection mechanism is proposed.

Given the intermittent nature of the renewable energy sources, and the fluctuated load profile, an appropriate solution is to use energy storage systems (ESS) to absorb the surplus energy in the periods when the power production is higher than the consumption and deliver it back in the opposite situation. In order to optimize the power flow, a model predictive control (MPC) strategy for microgrids is proposed. This method can flexibly include different constraints in the cost function, so as to smooth the gap between the power generation and consumption, and provide voltage support by compensating reactive power during grid faults.

CHAPTER 1

INTRODUCTION

1.1 Distributed Generation

The rapid depletion (hence, increase of cost) of fossil fuels, rising demand of electricity, and ever tightening government policies on reduction of greenhouse gas emissions, together with the inability and inefficiency of the existing electricity grid, are driving major changes in electricity generation, distribution, and consumption patterns all around the world. In the last decade, serious concerns were raised about distributed generation units (DGs) including renewable and non-renewable sources, such as wind turbine generators, solar photovoltaic (PV) panels, gas microturbine generators, fuel cells, and gas/steam powered combined heat and power (CHP) stations. These DG sources offer competitive generation options and promise better economics with high reliability, high efficiency and reduced emissions [1.1].

DG is an electric power generation source that is connected to the distribution network or just to a local load like the uninterruptible power supply (UPS) system. The advantages of DG applications can be described as follows:

- High reliability of power supply, especially when interruption of service is unacceptable.
- More flexible to exploit the renewable energy sources
- High power quality
- Ideal power supply for remote area where utility grid is unavailable for customers.

Fig. 1.1(a) shows the configuration of a wind power system, which uses a doubly-fed induction generator (DFIG). The stator of the DFIG is directly connected to the grid, while a partial-scale power converter controls the rotor frequency and thus the rotor speed. The wind turbine captures the wind energy by means of turbine blades, converting the wind power into mechanical power. A gearbox is used to match the low turbine speed to the generator high speed. The generator converts the mechanical power into electrical power, which is then fed into a grid possibly through power electronic converters, and a transformer with circuit breakers and electricity meters.

Fig. 1.1(b) shows a typical configuration of a solar PV system, where numerous PV panels are connected in series and/or parallel to form an array to convert the solar energy into electricity and the electricity generated by the PV panels is fed to the untility grid via a centralized inverter, which converts the DC power to AC electricity for consumer use. The inverter monitors the terminal conditions of the PV module(s) and maintains the maximum power point tracking (MPPT) to maximize the energy capture.

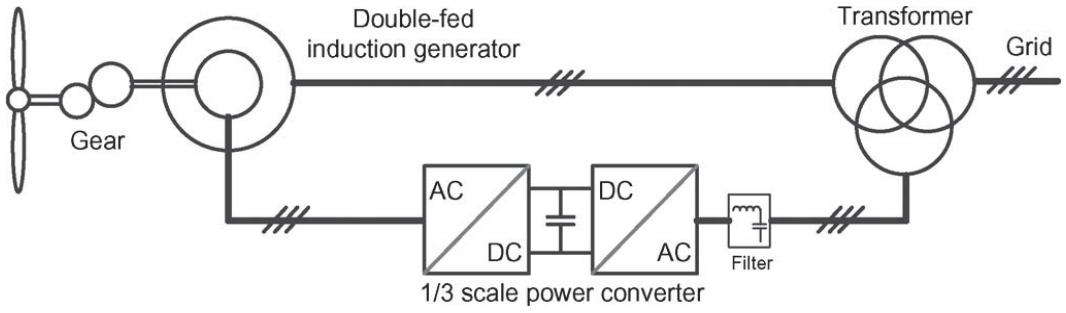

(a)

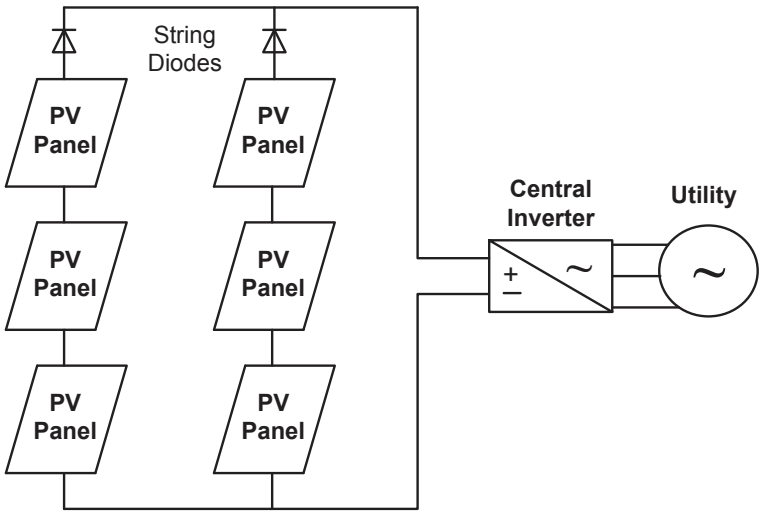

(b)

Fig. 1.1 Typical configurations of DG systems. (a) wind turbine system, and (b) PV system.

Despite the benefits provided by DGs mentioned above, there are technical limits in reality on the degree to which DGs can be connected. The main concerns of connecting DGs can be summarized as the following:

- The steady-state or transient over/under voltages at the point of connection due to sudden connecting or disconnecting a DG,

- The power output of the DG is fluctuated due to the intermittent nature of the renewable energy sources, which would cause negative impacts on the electric appliances,
- Connecting or disconnecting DGs will deteriorate the power quality and stability of the utility grid,
- Protection malfunctions such as breaker reclosing problem, over-current protection relaying interference, etc.,
- Possible power quality problems, such as voltage flickers and harmonics,
- Impact on power system dynamics, and
- Damage (to customers or DG itself) or safety (public or utility personnel) concerns of islanding operation of a single DG.

1.2 Control of Power Converters for Distributed Generation

1.2.1 Control strategies of a single converter

No matter how the DG sources are connected to the grid or to a local load, the essentials of this power conversion process are the power electronics, which provides the flexible interface between the energy sources and the power customers.

Fo DG applications, a large variety of pulse-width modulation (PWM) converters have been developed, and the control strategies have been the ongoing research subject over the last few decades. Recently, due to the sharp increase in the exploitation of renewable energy sources such as wind power, solar PV, and wave energy, more and more power converters have been used to interface the power sources with the AC and/or DC common buses in a DG system. As the penetration and capacities of DG units increase, the power converters are required to operate more efficiently and effectively to maintain high power quality and dynamic stability [1.2], [1.3]. To fulfill these requirements, advanced control techniques are desired.

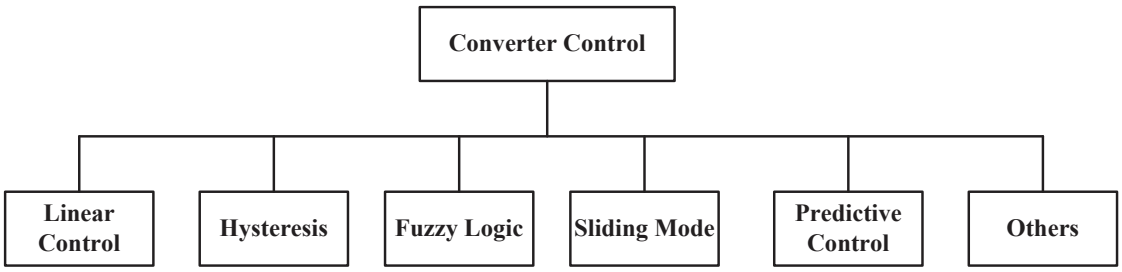

Fig. 1.2 Control methods of power converters

As illustrated in Fig.1.2, several control schemes have been proposed for the control of power converters. The classic linear controllers, together with modulation schemes and nonlinear controllers based on hysteresis comparators, have been the widely employed control strategies for power converters, and among them the voltage oriented control (VOC) and direct control are the most commonly used methods. Later on, more complex control techniques, such as the sliding mode control, fuzzy logic, and predictive control, were developed as rapid evolution of digital signal processing capacity. . Here, these control methods will be comprehensively investigated using a three-phase two-level rectifier based AC/DC conversion as an application example.

A. Voltage oriented control

This classic scheme is illustrated in Fig. 1.3. Since the line current vector, $\boldsymbol{i} = i_d + ji_q$, is aligned with the phase voltage vector, $\boldsymbol{v} = v_d + jv_q$, of the power line supplying the converter, a revolving reference frame aligned with $\boldsymbol{v}$ is used, and the active power of the converter output can be controlled by adjusting the reference value, i_d^*, of the quadrature component of $\boldsymbol{i}$, while the reactive power of the converter output can be regulated by adjusting the reference value, i_q^*, of the quadrature component of $\boldsymbol{i}$ [1.4], [1.5]. Generally, i_q^* is set to zero for unit power factor operation. The current references are compared with the actual values, and the errors are then delivered to the PI controllers to produce the voltage references. Finally, the switching signals for individual phases of the rectifier are generated by a classic space vector modulator (SVM).

VOC has various advantages including fixed switching frequency and insensitive to the line inductance variation. However, the requirement of coordinate transformation,

decoupling between active and reactive components, and proportional-integral (PI) regulators results in complex algorithm and compromised transient performance.

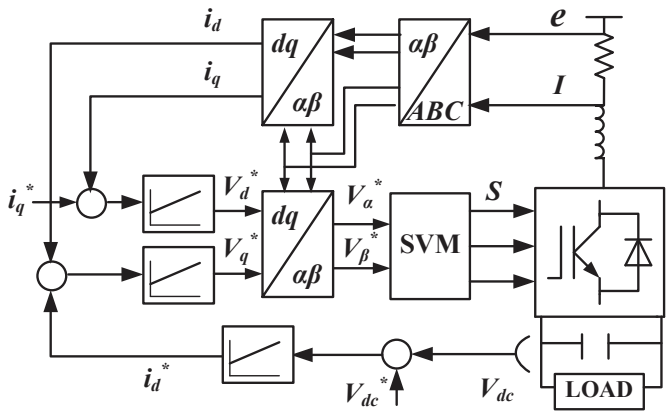

Fig. 1.3 Block diagram of VOC

B. Direct control

Over the past few years, an interesting emerging control technique has been the direct control strategy. Among the existing direct control methods for power converter control, the direct power control (DPC) is one of the most commonly used approaches. The conventional switching table-based direct power control (SDPC) is derived from the original direct torque control (DTC) for AC machine drives [1.6], [1.7], and has now become one of the most popular control strategies, because of its excellent transient performance, robustness, and simplicity. In the SDPC, the converter switching states are determined using a switching table, which is built up from the output signals of hysteresis active and reactive controllers as well as the position of grid voltage vector or virtual-flux vector [1.8]-[1.11]. Since then, several switching tables have been proposed, trying to improve system behavior [1.12]-[1.14].

Compared to VOC, SDPC does not need any internal current loop and modulator because the converter's switching states are selected via a switching table, and hence the coordinate transformation is also eliminated. However, large power ripples and variable switching frequency are two major significant challenges faced by these SDPC approaches.

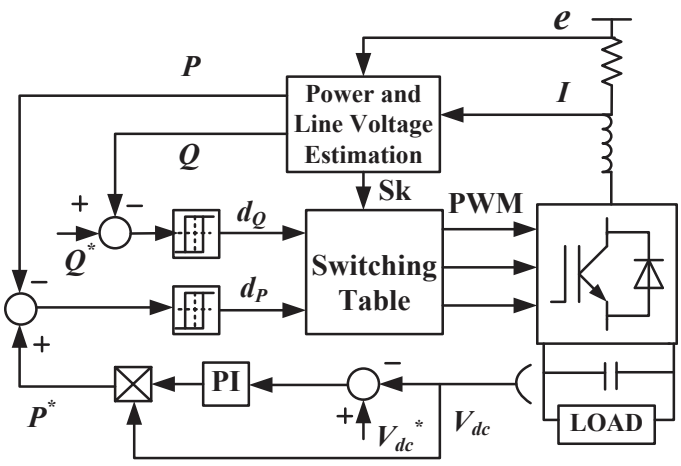

Fig. 1.4 Block diagram of DPC

Fig.1.4 illustrates the SDPC scheme applied on the AC/DC converter. It has had a great impact on the technology, and is often regarded as a benchmark to which new DPC strategies are compared. The referenced active power, P^*, is delivered from the PI DC voltage regulator while the referenced reactive power, Q^*, is usually set to zero for unity power factor control. The digitized signals, d_P and d_Q, are then generated by two fixed bandwidth hysteresis comparators using the tracking errors between the estimated and referenced values of active and reactive power. The converter switching states selected from a look-up switching table according to d_Q, d_P and the position of power-source voltage, which is located in an α-β plane of 12 sectors. This algorithm is implemented in the stationary reference frame without any involving modulation. The major drawbacks are the variable switching frequency and large power ripples, and a high sampling frequency is required to obtain a satisfactory performance.

C. Space vector modulation direct control

New approaches, e.g. the space vector modulation (SVM), have been incorporated into direct control to reduce the power ripples and achieve a constant switching frequency [1.15], [1.16]. The error obtained by comparing the commanded and estimated power values is sent to the PI regulators, and the average voltage vector is then delivered to the SVM to produce the switching signals. Whilst these approaches bring some benefits, complicated coordinate transformation and much tuning effort are required to ensure the system stability.

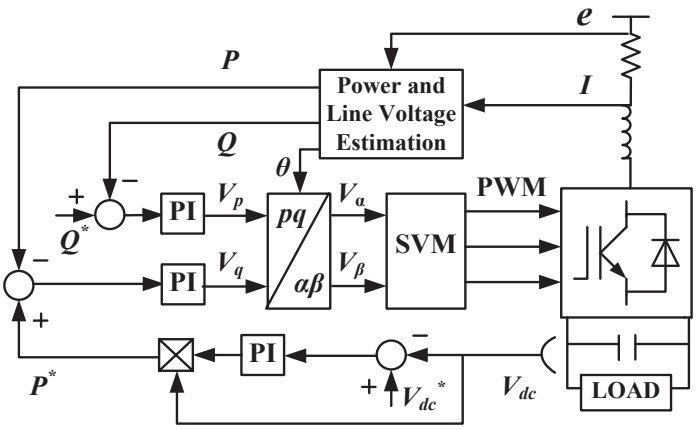

Fig. 1.5 Block diagram of SVM-DPC

By using SVM, the average voltage vector of the converter is produced by integrating linear voltage vectors in a fixed period, and thus constant switching frequency can be achieved. Various researchers have studied integration of SVM into DPC. The key of this approach is to select the referenced voltage vector for the modulator. Instead of using the hysteresis comparators and a switching table, the errors between the referenced and estimated active and reactive power values are fed directly to two PI regulators, as shown in Fig. 1.5. The output signals from the PI regulators are transformed into V_α and V_β in the stationary coordinate system before being sent to the SVM to generate the switching signals. Constant switching frequency and power ripple reduction can be achieved by integrating SVM into DPC. However, such an approach requires two additional PI regulators together with the coordinate transformation, which complicates the system and demands large computing power. The steady-state and transient performance is highly sensitive to the PI control parameters.

D. Fuzzy logic control

Fuzzy logic control has adaptive characteristics in nature, and can achieve robust response to a system with uncertainty, parameter variation, and load disturbance. It has been broadly used in the field of power electronics. Fig. 1.6 shows the schematic diagram of fuzzy logic control applied in AC/DC conversion system. Compared to the switching table based direct power control, this method selects the converter switching states by means of fuzzy logic rules using instantaneous errors of active and reactive power, εP and εQ, respectively. At each sampling instant, discrete values of power

errors, $\varepsilon P(k)$ and $\varepsilon Q(k)$, are converted to their corresponding fuzzy variables and used to select the optimum switching state [1.17].

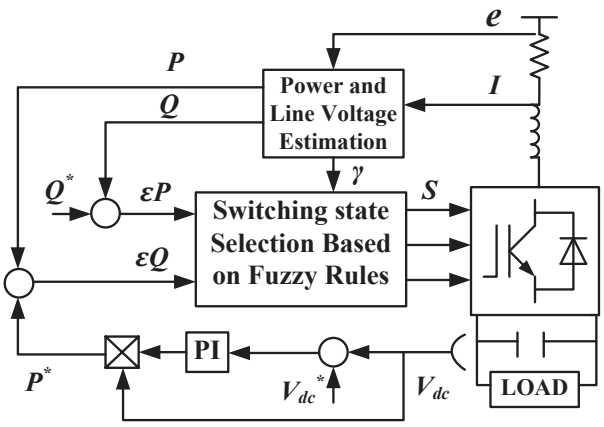

Fig. 1.6 Block diagram of fuzzy logic control

E. Sliding mode control

The sliding mode control (SMC) method utilises a relatively high frequency switching control signal to enforce the system trajectories onto a sliding surface (or hyperplane) after a finite time and remain within the vicinity of the sliding surface towards the equilibrium point thereafter. The sliding surface is designed to achieve desired specifications, depending on the applications and the control objectives. SMC is robust with respect to matched internal and external disturbances. However, undesired chattering produced by the high frequency switching may be considered as a problem for implementing the SMC approaches for practical applications.

The SMC strategy of AC/DC conversion is illustrated in Fig. 1.7. The error between commanded DC-bus voltage V_{dc}^* and measured DC-bus voltage V_{dc} is processed by SMC, which produces the reference active power, P^*, and reactive power, Q^*. They are then compared with the actual power values. The errors are sent to the hysteresis comparators, and the output is used to select an appropriate voltage vector. For the SMC controller, there are two components, namely the sliding surface and SMC law. The sliding surface is set to predefine the trajectories of the control objective. In order to maintain the enhanced transient response and minimize the steady-state error, the switching surfaces can be in the integral forms. Alternatively, they can also be designed via back-stepping and nonlinear damping techniques. On the other hand, for the design

of the SMC law, a Lyapunov approach is usually used for deriving conditions on the control law that will drive the state orbit to the equilibrium manifold. More details of this control method can be found in [1.18] and [1.19].

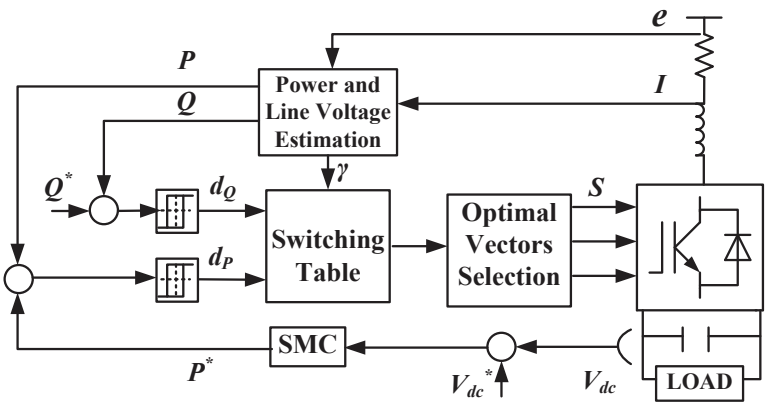

Fig. 1.7 Block diagram of sliding mode control

F. Predictive control

More recently, the concept of predictive control emerged as an attractive alternative for the control of electrical machines and power converters. Several kinds of control methods have been developed under the name of predictive control. The most important types are the deadbeat control, model predictive control (MPC) and vector-sequence-based predictive control (VPC). The deadbeat control uses a system model to predict the required reference voltage once every sampling period. This voltage is then generated using a modulator [1.20]-[1.28]. In the MPC, a system model is used to predict the behaviour of the variables over a certain time horizon, and a cost function as the criterion to select the optimal switching states [1.29]-[1.35]. The principle of the vector based predictive control is to force the system variables onto the pre-calculated trajectories, where several voltage vectors are typically used within each sampling period [1.36]-[1.42].

G. Deadbeat based predictive control

This type of predictive control approach uses the model of the system to calculate, once every sampling period, the required reference voltage to reach the reference value in the next sampling instant [1.20]-[1.28]. This average voltage vector is fed into the SVM to produce the switching signal. This approach has been applied for current

control in inverters, power control in rectifier, active filters, power factor correctors, DC/DC converters, uninterruptible power supplies, and torque control of electric drives.

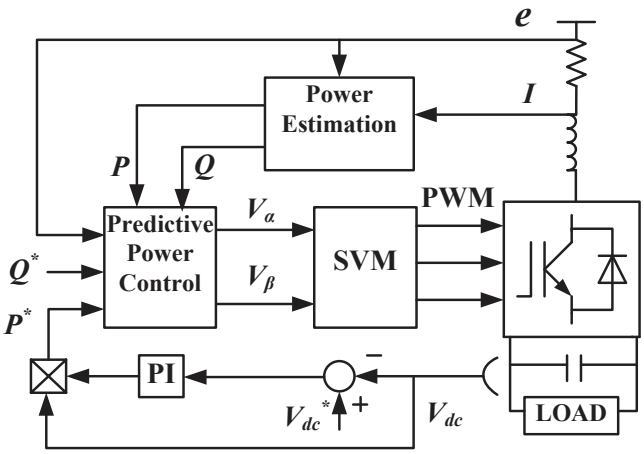

Fig. 1.8 Block diagram of deadbeat based predictive control

Fig. 1.8 depicts the implementation of the deadbeat based predictive control in AC/DC conversion. To eliminate the active and reactive power tracking errors at the end of a sampling period, the controller uses the model of the system to calculate, once every sampling period, the required reference voltage to reach the reference value in the next sampling instant. This average voltage vector is then fed into the SVM to produce the switching signal.

While this method has been used when a fast dynamic response is required, being deadbeat-based, it is often fragile. Indeed, errors in the parameter values of the model, un-modelled delays and other errors in the model often deteriorate the system performance and may give rise to instability. Another disadvantage of these deadbeat control schemes is that the non-linearities and constraints of system variables are difficult to incorporate.

H. Model predictive control

The MPC uses the system model to predict the behaviour of variables over an *N*-step time horizon, and a cost function subsequently as the criterion for selecting the appropriate switching states in the future [1.29]-[1.35]. Generally, the design of MPC controller can be divided into three steps: system predictive model, cost function and parameters selection. Firstly, the system model can be expressed as a discrete-time state-space model, the output of which is determined by the input, the current state of

the model, and the discrete interval. In this way, the future behaviour of the system can be predicted until a certain horizon of time. Secondly, the control problem can be defined as the determination of an appropriate control action that will force a generic system variable, $\boldsymbol{x}(t)$, as close as possible to a desired reference value, $\boldsymbol{x}^*$. A cost function over a finite horizon of length N is then utilized to evaluate each switching state, and the one minimizing the error between $\boldsymbol{x}(t)$ and $\boldsymbol{x}^*$ will be selected for the next sampling period. Finally, as the MPC allows the easy inclusion of system constraints and nonlinearities by revising the cost function, a trade-off between different control objectives should be taken into account in order to obtain the satisfied performance.

Fig. 1.9 depicts the block diagram of MPC system, where one step prediction is employed. The essential concept of this predictive DPC is to predict the power of the $(k+1)^{th}$ instant for different voltage vectors. By evaluating the effects of each voltage vector on the active and reactive powers according to a specific cost function, the voltage vector that produces the least power ripple can be determined. In the rectifier control, the control objectives are chosen as the DC-link voltage and the power factor of the AC input, which can be regulated by controlling the active power, P, and reactive power, Q, respectively.

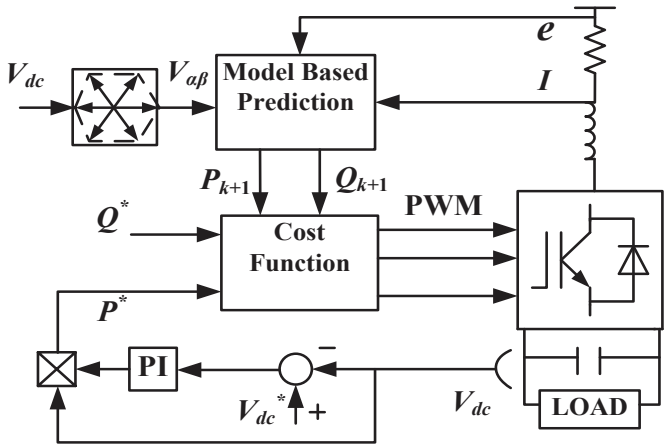

Fig. 1.9 Block diagram of model predictive control

I. Vector-sequence-based predictive control

This predictive approach selects an optimal set of concatenated voltage vectors in such a way that the controlled variables converge toward the reference values along a fixed predefined switching period [1.36]-[1.42]. The difference from deadbeat control is, for deadbeat control, the reference voltage, V^*, is calculated directly from the predictive

model and generated using modulators. For vector-sequence-based predictive control, voltage vectors are not determined by a reference voltage, but by a defined criteria, and thus no modulators are needed.

Fig. 1.10 illustrates the principle of the vector-sequence-based predictive control of rectifiers. The instantaneous active and reactive power slopes, f_p and f_q, for voltage vectors can be calculated. Under the condition that the line voltage is constant and the line current variations are small during each voltage vector application, the power slopes can be assumed constant for this period. Taking the symmetrical 3+3 vectors sequence as an example, the power increments can be predicted to force the power values at the end of a sampling period equal to the references. The key of this approach is to calculate the proper voltage vectors applied durations in order to minimize the power ripples.

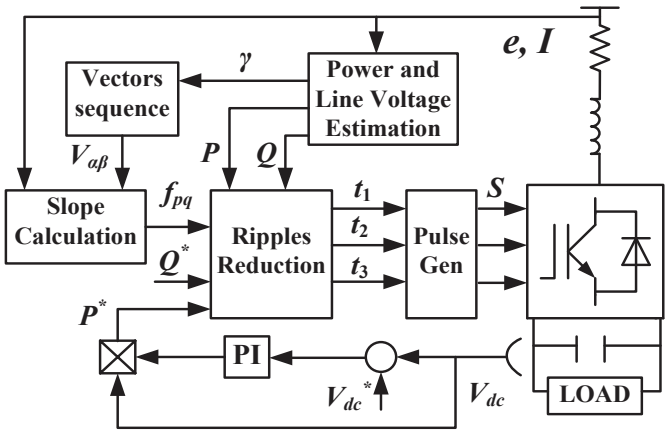

Fig. 1.10 Block diagram of vector-sequence-based predictive control

Because of the utilization of an optimal sequence of vectors in each period, the system objectives can be well controlled, and thus excellent steady state performance can be obtained. The drawbacks include complicated control structure and high sensitivity to the system parameter variation due to the complex calculation of "slopes".

1.2.2 Control strategies of parallel-connected converters

In a microgrid system, all the DGs are generally parallel connected to a common AC bus through inverters or AC/AC converters, the common bus is then connected to the utility grid via a static transfer switch. Proper operation of the microgrid in both the grid-connected and islanded modes requires the implementation of high performance power flow control and voltage regulation algorithms. For example, the DGs should be able to adjust their power outputs to taken up the changed power demand of the loads, which cannot be achieved by the control of a single DG. The parallel operation of converters is a challenging problem which is more complex than paralleling DC sources because every converter must properly participate in the load sharing. In this sense, appropriate control strategies for parallel connected DGs are required.

The control strategies for parallel-connected converters were initially developed for UPS applications [1.43], which can be generally categorized as following:

A. Centralized control

Fig.1.11 illustrates the centralized control, also known as concentrated control. Actually, it is an average current sharing scheme. The current reference of each module is set to the same value obtained by dividing the total load current by the number of modules N [1.44]. The current reference value is then subtracted by the current of each module in order to obtain the current error, which is delivered to a current control loop. The outputs of the current regulators are then sent to the PWM modulators to produce switching signals for each inverter.

On the other hand, an outer control loop in the centralized control adjusts the load voltage. Using this method, the measurement of the total load current is required, and thus it is impractical in a large distributed system. Alternatively a central control board is needed [1.45].

The overall implementation of this approach can be divided into three steps. The first step is to measure the total load current and calculate the reference value for each inverter. The second step is to obtain the current error and to decompose it into the direct component, Δi_p, and the quadrature component, Δi_q. Finally, Δi_p and Δi_p will be used to adjust the phase and amplitude of the output voltage for each inverter.

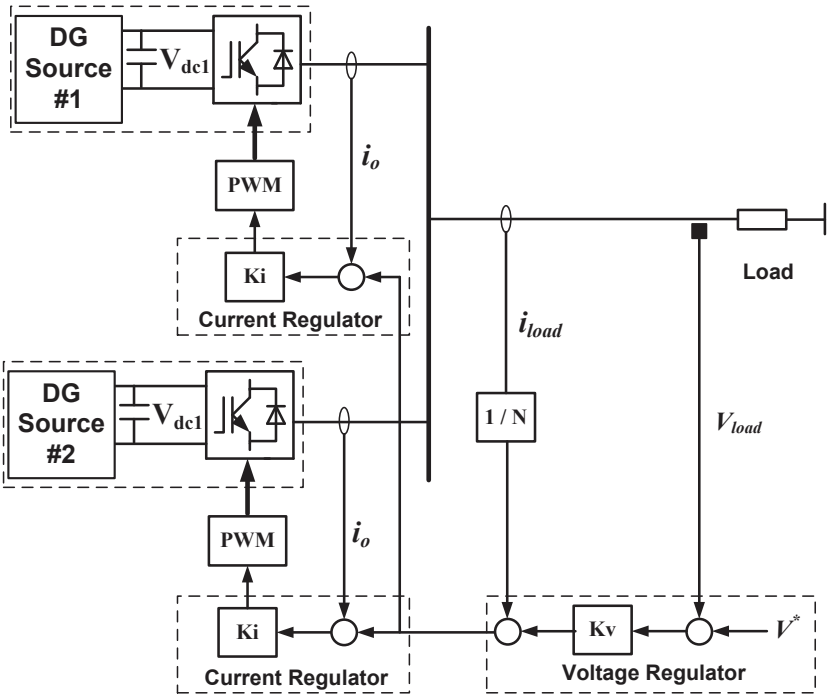

Fig. 1.11 Block diagram of the centralized control

B. Circular chain control (3C)

The control diagram of this method is illustrated in Fig. 1.12. Different to the centralized control mentioned previously, the 3C method takes the current reference of each unit from the aforementioned module to form a control ring, i.e. the current reference of the first unit is obtained from that of the last unit to form a circular chain connection. In other words, the current reference i_k^* from the k^{th} unit is taken from that of the $(k\text{-}1)^{th}$ unit $i_{k\text{-}1}$ [1.50], [1.51].

All the DG units have the same circuit configuration, and each unit includes an inner current control loop and an outer voltage control loop. A PI controller is normally adopted as the inner current loop controller to expedite the dynamic response. Since the successive unit tracks the current of its previous one to achieve an equal current distribution, a fast dynamic response can be obtained, and the proper current distribution among inverters can be achieved. Due to this specific structure, this approach can be quite suitable for distributed generation system based on power rings because of the distribution of the power lines.

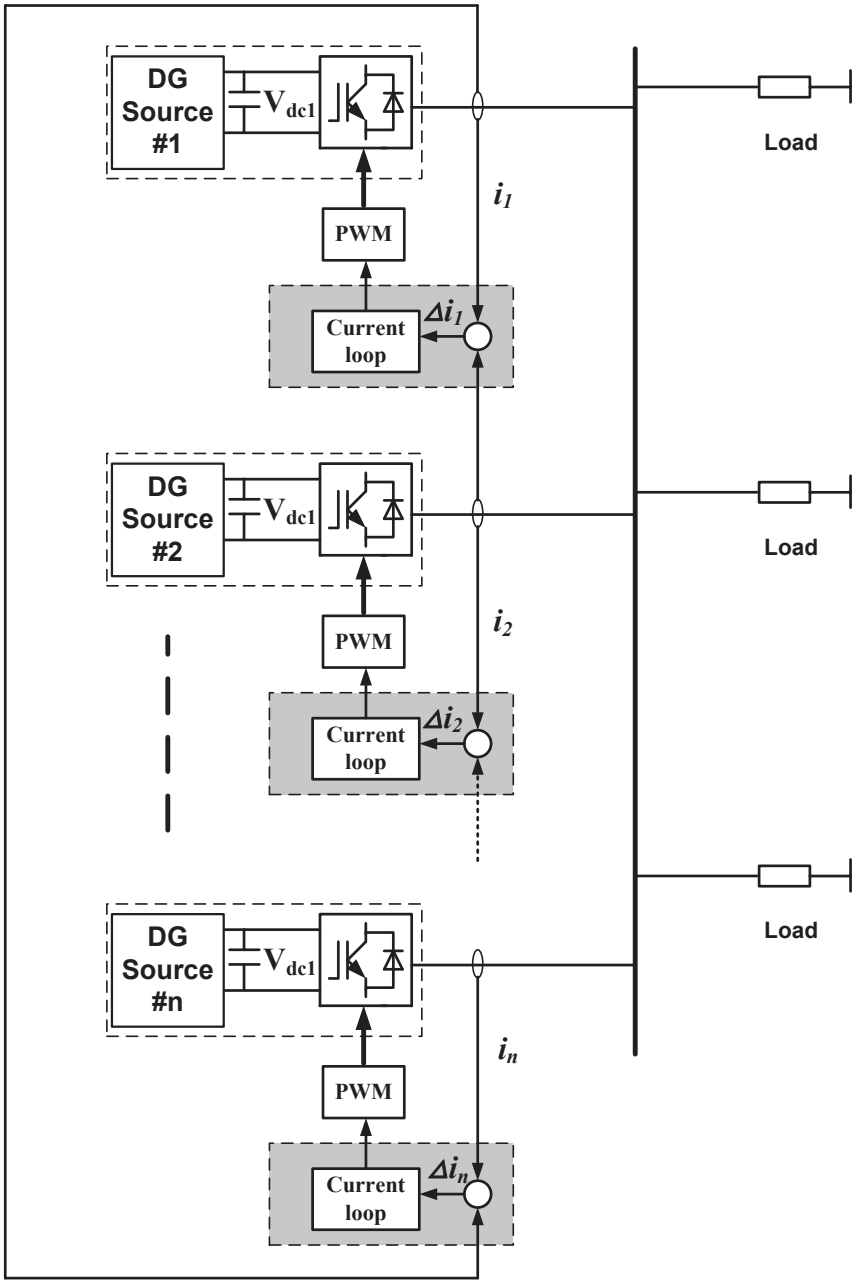

Fig. 1.12 Block diagram of the current chain control (3C)

C. Master-slave (MS) control

In this method, the master module regulates the load voltage, and the master current fixes the current references of the rest of the modules. Consequently, as shown in Fig. 1.13, the master acts as a voltage source inverter (VSI) while the slave works as a current source inverter (CSI).

The single VSI, as the master, is controlled to provide a constant sinusoidal wave output voltage. On the other hand, the *n* sets of CSIs, as the slaves, are controlled to

monitor the reference current which is distributed from the power distribution centre. The current control loop in the CSIs consists of the output voltage feed-forward to eliminate the voltage disturbance and the reference current feed-forward for fast current response. Therefore, the load current can track closely to the references from the power distribution centre [1.46], [1.47]. In this configuration, if the master unit fails, another module will take the role of master in order to avoid the overall failure of the system.

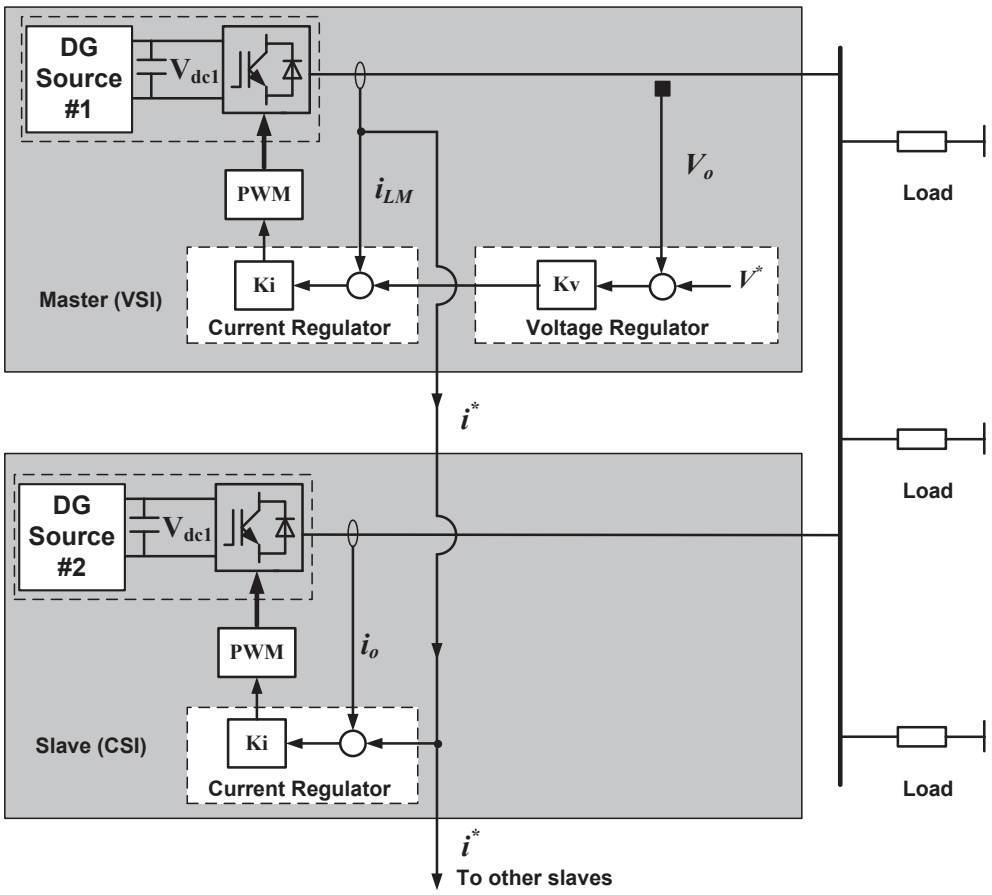

Fig. 1.13 Block diagram of MS control

D. Average load sharing (ALS)

The ALS approach can be implemented using average current and average power, as illustrated below:

Fig.1.14(a) depicts the ALS using average current scheme. The average current reference is firstly computed by a resistor connected to the current sensor of every single inverter. This current reference will be delivered by a single wire. By adjusting the resistor to a suitable value, the power rating of the parallel connected converters can

be set to a different value. It is noted that the average current of all the units is the reference for each individual one. Consequently, it is very reliable because every converter tracks the average current done by all the active converters [1.48]. In addition, this scheme is highly modular and robust, making it very useful for industrial applications.

This control strategy can be implemented by using an inner or an outer current loop. The problem of using the outer loop is that, the voltage loop has a narrow bandwidth and in order to avoid instabilities, the current loop needs a compensator. As a consequence of the bandwidth reduction of this loop, the current dynamics is very slow, provoking poor current sharing during transients.

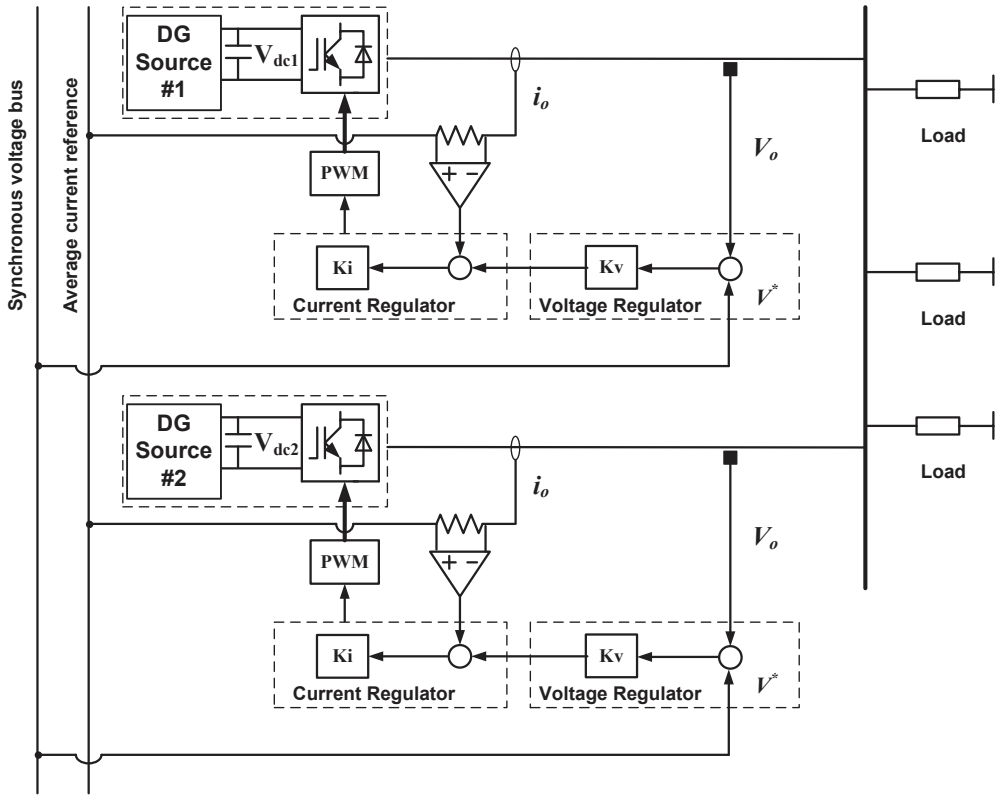

(a)

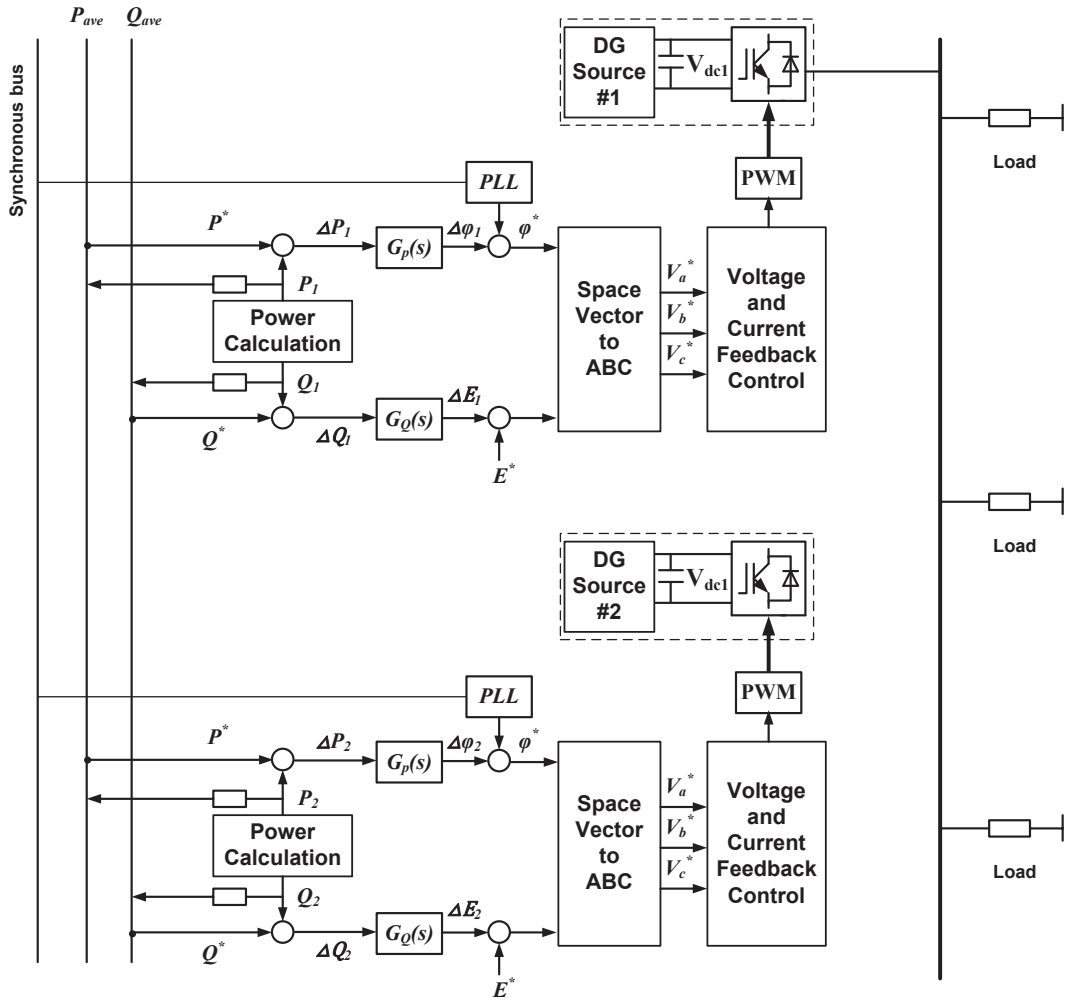

(b)

Fig. 1.14 Block diagram of ALS control, (a) average current sharing, (b) average power sharing

Another ALS technique is to use the active and reactive power information instead of the current to adjust the phase and magnitude of the output voltage of each module [1.49]. Fig. 1.14(b) presents the schematic diagram of the average power-sharing method. The active and reactive power are firstly obtained through the active and reactive component decomposition of the output current, and the average active and reactive power references are then computed by dividing the measured power by the number of converters, *N*. Similar to the average current scheme, these average active and reactive power references are taken as the power reference for each converter. Using this approach, each unit controls its output power to match the average active and reactive powers of the whole system, by adjusting the inverter output voltage. It is noticed that this technique does not require any master or slave unit, and only low-bandwidth digital communications are required to achieve good *P* and *Q* sharing.

However, it only acts correctly on the fundamental component of the output current, but incorrectly on the harmonic components. As a result, unbalances between the power stages and the power lines can produce large circulating harmonic current between the units.

So far, the control strategies for the parallel operation of converters mentioned above can be categorized as the active load-sharing techniques. Although these schemes can achieve both good output-voltage regulation and equal current sharing, they need critical intercommunication lines among modules that could reduce the system reliability and expandability.

E. Droop control

For operation of parallel converters, such as in a microgrid system, the implemented control algorithms should preferably have no communication links between the parallel DG units, which can be located far apart. Hence, only the feedback variables that can be measured locally should be used in the controller. Here, different to the active load sharing approaches mentioned before, another type of control technique for parallel-connected converters, namely droop control, is introduced. This concept stems from the power system theory, in which a synchronous generator connected to the utility mains drops its frequency when the power demand increases. By this technique, the active and reactive power sharing by the inverters is automatically achieved by adjusting the output voltage frequency and amplitude. It is able to avoid critical communication links, which can improve the reliability without restricting the physical location of the modules.

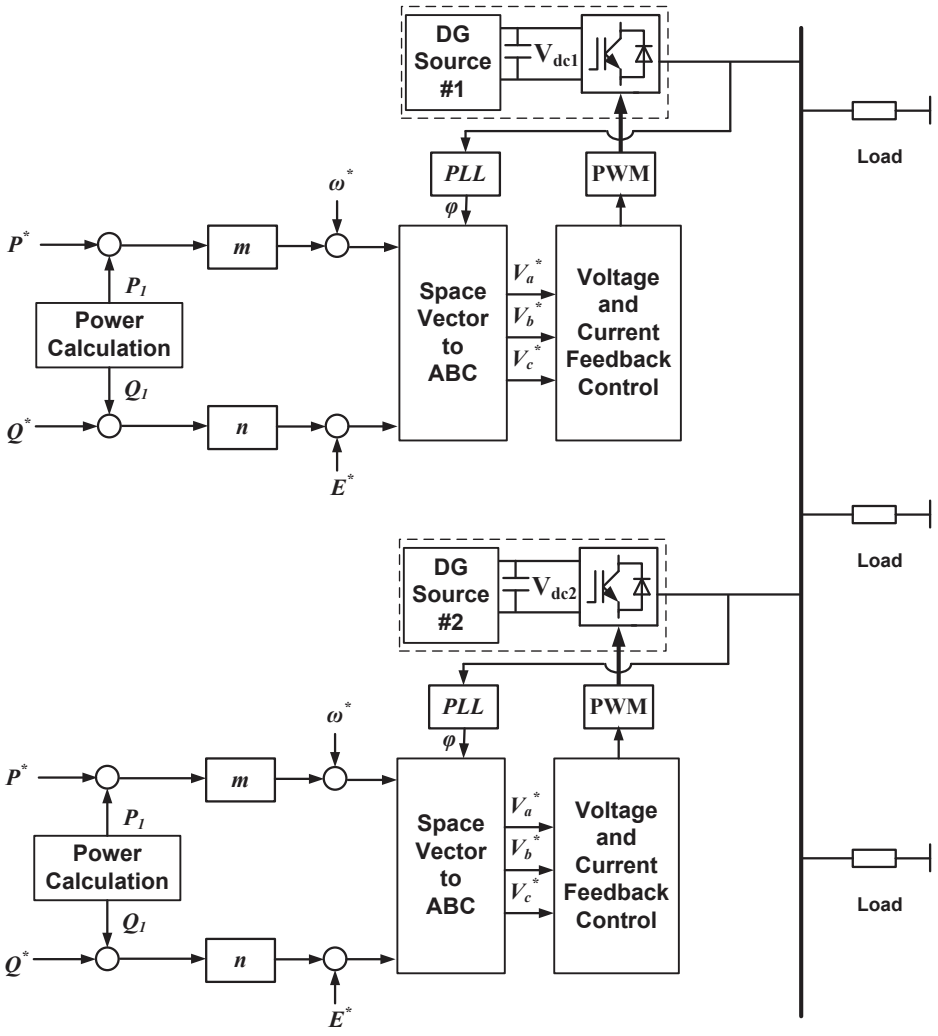

Fig. 1.15 Block diagram of the conventional droop control

Fig. 1.15 shows the block diagram of the droop control strategy, consisting of an inner voltage control loop and an outer power control loop. In the outer power control, the instantaneous P and Q are firstly calculated according to the inverter output voltages and output currents. These measured powers together with the power references, $P^*$and Q^*, are then sent to a pre-defined droop function, in order to obtain the desired voltage, E^*, which will be delivered to the inner voltage control loop. In the voltage control loop, a proportional compensator is used to force the inverter output voltage to track this specified E^*. The outputs of this voltage compensator together with the inner filter inductor currents are then fed to an inner current compensator to produce modulating signals for the sinusoidal PWM (SPWM). This permits each generator to take up changes in total load in a manner determined by its frequency droop characteristics and amplitude droop characteristics, and essentially utilizes the system frequency as a communication link between the generator control systems.

This type of control method is very suitable for microgrids where several DG units are parallel-connected to a common AC bus, which will be discussed further in Chapter 5.

1.3 The Concept of Microgrids

As mentioned previously, for various reasons, more and more distributed generation (DG) units are utilized to provide electric power, including both renewable and non-renewable sources such as wind turbines generators, photovoltaic arrays, fuel cells, micro gas turbine generators, and gas/steam powered combined heat and power (CHP) stations. Despite the benefits provided by DGs, there are technical limits in reality on the degree to which DG can be connected. To find a better way to realize the emerging potentials of DGs, more recently, a new paradigm known as microgrids is proposed, as shown in Fig. 1.16 [1.52].

A microgrid is a cluster of DGs and local loads that can offer many advantages to the current power grid in terms of power autonomy and the ability to incorporate renewable and non-renewable energy sources. In the grid-connected operation, the DGs together with the utility grid supply power to the local loads. If the power generation is greater than the load consumption, the excess can be either stored in the energy storage unit or injected into the grid if there is a need. On the other hand, if the power generation is smaller than the load demand, more power can be imported from the grid. In the islanded operation, the DGs should be able to provide a stable voltage at the point of common coupling (PCC) and pick up the loads automatically. In addition, the microgrid should be re-connected to the utility grid seamlessly when the grid is available.

Another promising function of microgrids is that each microgrid system at the distribution level can be served as a utility grid supporting ancillary. With increasing penetration of the DG systems in to the electrical power distribution network, the DG systems could be equipped with their own power converters with capability of supplying reactive power or VAr using power electronics primarily for power conversion. This design approach will help utilities to reduce investment into voltage regulation devices because the application of static synchronous compensator (STATCOM) at the distribution voltage level is not very common due to the high cost that the equipment adds to the system.

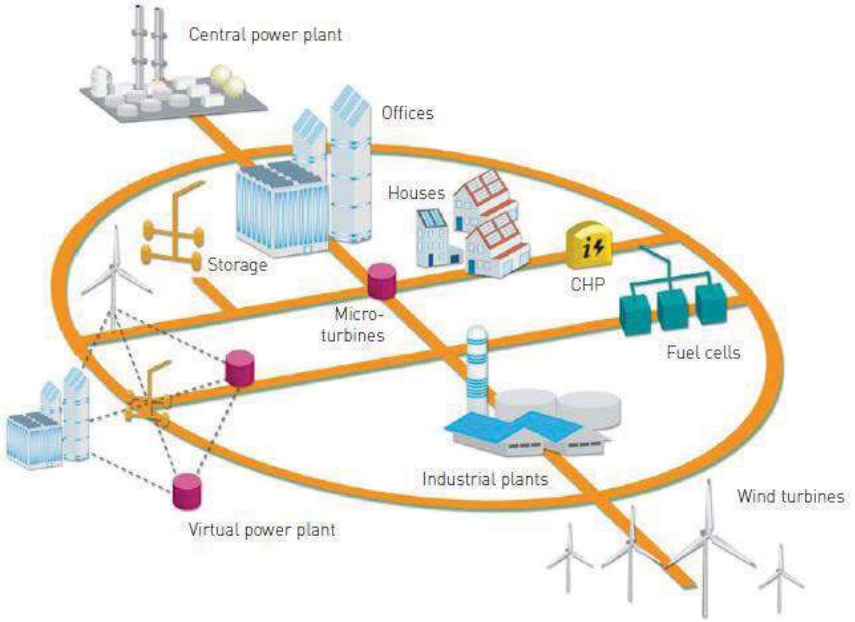

Fig. 1.16 Microgrid system

This new concept is becoming more and more attractive. Compared to a single DG unit, it offers many technical advantages in terms of power quality and reliability. Compared to the whole power system, it presents more control flexibilities. However, due to the discontinuous nature of these DG units, the output power is not stable and may cause negative influence to the quality of electricity or damage the electric appliances. For the spread of renewable energy in demand side, they must be installed with facilities which absorb the fluctuation. In addition, due to the complexity of such a small power system including several kinds of energy sources, energy storage systems, and loads, the coordinated control of these DGs to achieve optimal power flow and maintain high power quality becomes a big challenge. From the perspective of the energy sources, the power converters should be controlled to capture the maximum real power and inject the excess into the utility. On the other hand, from the utility/grid perspective, the power electronics interface should be also able to provide reactive power according to the requirement to improve power quality and enhance grid stability.

It is noted that the microgrids would and should coexist with the existing electricity grid, and it is required to be self-healing and resilient to system anomalies. Fig. 1.17 illustrates a smart city configuration in the future. Large-scale of renewable power distributed generation units such as wind turbine and PV arrays will supply electrical power to the grid together with the conventional power plants. The intelligent power transmission and distribution system will optimize the power flow and balance the

power generation and consumption effectively. At the power demand side, consumers not only can enjoy high-quality power, but also supply the surplus power back to the grid.

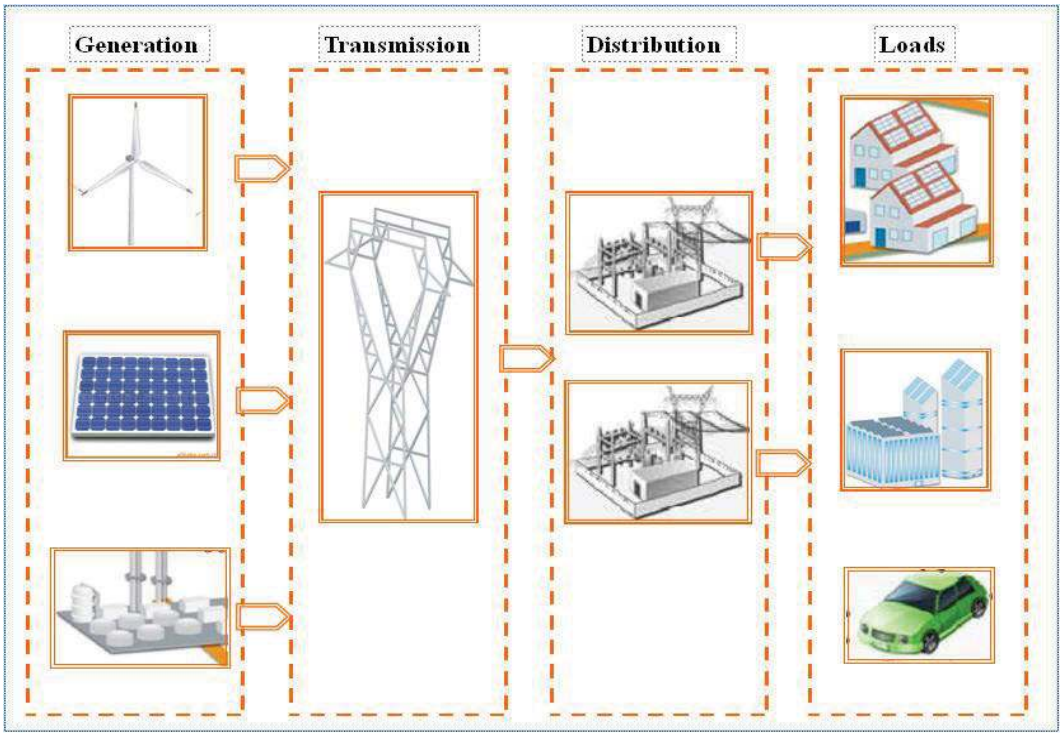

Fig. 1.17. Smart city

In microgrid development and standard establishment, North America and Europe are taking solid steps. The National Institute of Standard and Technology (NIST) Framework and Roadmap for microgrid standards and Euripean smartgrid technology platform have identified priority areas for standardization and application. In the Asian Pasific area, the Smart Grid Australia (SGA) research working group, consisting of experts from the Commonwealth Scientific and Industrial Research Orgonisation (CSIRO), Ausgrid, and various universities, is making efforts to contribute towards the microgrids. Some other countries, such as China, Singapore, and Japan also begin to budget much investment on microgrid research. Fig. 1.18 illustrates the current small microgrid installations around the world. It can be seen that nearly half of installation is located in North America (44%), followed by Europe (16%), Australia (12%), and Asia (8%).

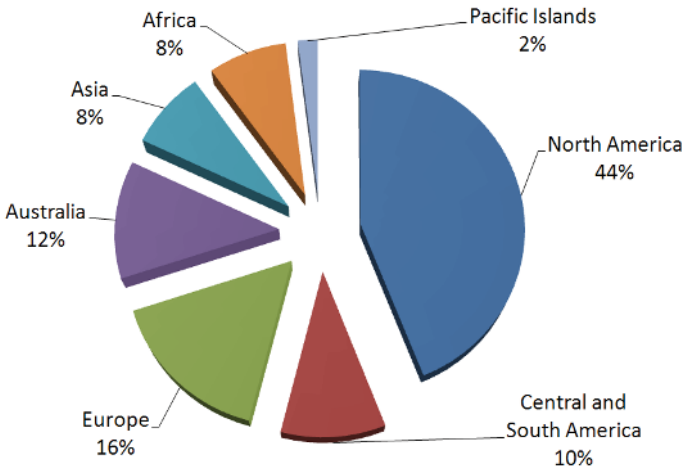

Fig. 1.18. Existing microgrid installations around the world

In general, the main issues of renewable power generation system that need to be addressed are power sharing, power quality and reliability, seamless transfer, system stability, and protection.

1.3.1 Power sharing

The converter interfaced DGs in a microgrid should pick up the load changes and smooth the voltage and frequency at the PCC. System regulations for quantities, such as frequency deviation and voltage drop, become very crucial during the decentralized power sharing through droop control. The most common strategy for load sharing in microgrid applications is the droop method, which was initially introduced in 1993 [1.53]. Since then, various improved schemes have been proposed. For example, better transient response was obtained by introducing the derivative-integral terms [1.54]-[1.57]. The power sharing accuracy was enhanced by employing a virtual power frame transformation or virtual impedance [1.58]-[1.60]. In [1.61], an angle controller was proposed to minimize frequency variation by drooping the inverter output voltage angle instead of the frequency. The voltage deviation caused by droop method is compensated by a multilayer control strategy in [1.62].

1.3.2 Power quality and reliability

Unstable output power from DGs, unbalanced and nonlinear loads, and disturbance of the grid could be a challenge for stabilization of the frequency and voltage, which can be evaluated in terms of voltage (magnitude and frequency) variation, flicker, and

harmonics, etc. In [1.63] and [1.64], compensators were designed for a microgrid with unbalanced and nonlinear loads with the purpose of improving power quality. On the other hand, much attention has been paid to enhance the microgrid power quality under grid voltage disturbance [1.65]-[1.67].

1.3.3 Seamless transfer

The isolation of microgrids should not cause any major influence on the local loads when a grid fault occurs. On the other hand, the re-synchronization of microgrids to the utility grid should be conducted smoothly and quickly [1.68]-[1.70]. Recently, a robust hierarchical controller was proposed for seamless transfer between the grid-connected and the islanded modes [1.71].

1.3.4 System stability

In an autonomous microgrid, all the DGs are responsible for maintaining the system voltage and frequency while sharing the real power and reactive power. Generally, the stability of microgrid is concerned as following: The system stability during load sharing; the transient stability of the power system with high penetration level of power electronics interfaced distributed generation; the low frequency stability problem with change in power demand; the robust stability of the control system. In addition, the influence of control parameters on system stability should be taken into account in terms of sensitivity analysis, using qualitative analysis and small-signal techniques [1.54], [1.60], [1.72]-[1.74].

1.3.5 Protection

Protection of devices in both utility and microgrid sides during any fault is always a major concern. In [1.75], a *RL* feedforward and a flux-charge-model feedback algorithm was proposed to limit the large line current surge during grid voltage sags, while the system transient of the microgrid under short circuit faults was studied in [1.76]. With strong penetration of distributed generation, an information and communication technology (ICT) method based on petri net (PN) modeling was introduced to identify failures in smart grids [1.77].

1.4 Research Objectives

In order to exploit the potential benefits that a microgrid could provide to the customer's as well as the utility grid's side, the focus of this thesis is development of controllers to solve technical problems related to the modelling, control, and power management of microgrid applications. The main objectives of this research project can be described as

- Development of advanced and flexible control techniques for DGs to achieve islanded operation, seamless transfer, and grid-connected operation.
- Power conversion efficiency improvement of microgrids.
- Autonomous power sharing, power quality improvement and grid support of microgrids.

1.5 Thesis Outline

The thesis is organized as follows:

In Chapter 1, the background and motivation of this thesis are introduced, defining the main focus in the development of distributed generation system. The control strategies of the power converters in distributed generation system are also reviewed comprehensively. After that, the objectives of the thesis are presented.

In Chapter 2, the state of art of the wind power techniques is studied, based on which the main concerns and tendency of the global wind market is illustrated. A new control strategy of doubly-fed induction generator using predictive direct control is proposed, this method can achieve fast and smooth grid synchronization and flexible power regulation. It is simple and reliable, and present excellent steady-state and dynamic performance.

In Chapter 3, the characteristics of photovoltaic is presented, the PV system structure is investigated. After that, an improved model predictive control strategy is developed for a three-phase two-level inverter based PV system. At islanded operation, the inverter output voltage is controlled stably. A simple synchronization scheme is introduced to

achieve seamless transfer. After connected to the main grid, the PV system can injects active and reactive power into the grid flexibly within its capacity.

In Chapter 4, in order to reduce the switching loss in distributed power generation, a multi-objective model-predictive control strategy is proposed for the control of power converters. By revising the cost function properly, the switching frequency is reduced considerably without significant system performance deterioration. The control strategy is also simplified using a graphical algorithm to reduce the computational burden. The proposed method is very flexible and can be employed in AC/DC and DC/AC applications in microgrids.

In Chapter 5, based on the study of distributed generation sources and the related control strategies in the last chapters, a microgrid consisting distributed generation units, local loads and energy storage system is presented, and the system level control of the whole microgrid is focused. Two parallel-connected inverters system is firstly investigated, and a novel flux droop approach combing direct flux control is proposed. After that, a microgrid with PVs and gas microturbine is studied, a coordinated control scheme is then developed for both islanded and grid-connected operation. Furthermore, a model predictive control strategy is proposed for a microgrid system, where the power generated by distributed energy sources, power consumed by the load, power stored by the energy storage system and the power injected to the utility grid are determined according to an optimized cost function, so as to smooth the gap between the generation and consumption and maximize the economic potentials.

In Chapter 6, the conclusions of the thesis are drawn accompanied by future work proposal.

References

[1.1] J. M. Guerrero, F. Blaabjerg, T. Zhelev, K. Hemmes, E. Monmasson, S. Jemei. M. P. Comech, R. Granadino, and J. I. Frau, "Distributed generation: Toward a new energy paradigm," *IEEE Magazine Ind. Electron.,* vol. 4, no. 1, pp. 52-64, March 2010.

[1.2] F. Blaabjerg, M. Liserre, and K. Ma, "Power electronics converters for wind turbine systems," *IEEE Trans. Ind. Apl.,* vol. 48, no. 2, pp. 708-719, March/April. 2012.

[1.3] J. Hu, J. Zhu, and D. G. Dorrell, "A Comparative Study of Direct Power Control of AC/DC Converters for Renewable Energy Generation," in *Proc. IEEE IECON Conf.,* pp. 3453–3458, 2011.

[1.4] J. Holz, "Pulsewidth modulation – a survey," *IEEE Trans. Ind. Electron*., vol. 39, pp 410-420, Oct. 1992.

[1.5] M. P. Kazmierkowski, R. Krishnan, and F. Blaabjerg, Control in Power Electronics. London, U.K.: Academic, 2002.

[1.6] I. Takahashi and T. Noguchi, "A new quick-response and high efficiency control strategy of an induction machine," *IEEE Trans. Ind. Appl*., vol. IA-22, pp 820-827, 1986.

[1.7] G. S. Buja and M. P. Kazmierkowski, "Direct torque control of PWM inverter-fed AC motor – a survey," *IEEE Trans. Ind. Electron.,* vol. 51, no. 4, pp. 744-757, August 2004.

[1.8] T. Ohnishi, "Three phase PWM converter/inverter by means of instantaneous active and reactive power control," *in Proc. IEEE IECON,* 1991, vol. 1, pp. 819-824.

[1.9] Noguchi, H. Tomiki, S. Kondo and I. Takahashi, "Direct power control of PWM converter without power-source voltage sensors," *IEEE Trans. Ind. Appl*., vol. 34, pp 473-479, 1998.

[1.10] M. Malinowski, M. P. Kazmierkowski S. Hansen, F. Blaabjerg and G. D. Marques, "Virtual-flux-based direct power control of three-phase PWM rectifiers," *IEEE Trans. Ind. Appl.,* vol. 37, no. 4, pp. 1019-1027, 2001.

[1.11] M. Malinowski, M. P. Kazmierkowski and A. M. Trzynadlowski, "A comparative study of control techniques for PWM rectifiers in AC adjustable

speed drives," *IEEE Trans. Power Electron.,* vol. 18, no. 6, pp. 1390-1396, November 2003.

[1.12] A. Bouafia, J. P. Gaubert and F. Krim, "Analysis and design of new switching table for direct power control of three-phase PWM rectifier," in *Proc. IEEE Int. Power Electronics and Motion Control Conf. EPE-PEMC*' 08, pp. 1-6, 2008.

[1.13] J. Alonso-Martinez, J. Eloy-Garcia, and S. Arnaltes, "Table-based direct power control: A critical review for microgrid applications," *IEEE Trans. Power Electron.,* vol. 25, no. 12, pp. 2949-2916, December 2010.

[1.14] A. Sato and Toshihiko Noguchi, "Voltage-source PWM rectifier – inverter based on direct power control and its operation characteristics," *IEEE Trans. Power Electron.,* vol. 26, no. 5, pp. 1559-1567, May 2011.

[1.15] M. Malinowski, M. Jasinski and M. P. Kazmierkowski, "Simple direct power control of three-phase PWM rectifier using space-vector modulation (DPC-SVM)," *IEEE Trans. Ind. Electron.,* vol. 51, no. 2, pp. 447-454, April 2004.

[1.16] D. Zhi, L. Xu, B. W. Williams, L. Yao, and M. Bazargan, "A new direct control strategy for grid connected voltage source converters," *Int. Conf. Electrical Machines and Systems, 2008 (ICEMS 2008),* pp. 1157-1162.

[1.17] A. Bouafia, F. Krim and J. P. Gaubert, "Fuzzy-logic-based switching state selection for direct power control of three-phase PWM rectifier," *IEEE Trans. Ind. Electron.,* vol. 56, no. 6, pp. 1984-1992, June 2009.

[1.18] V. S. C. Raviraj and P. C. Sen, "Comparative study of proportional-integral, sliding mode, and fuzzy logic controllers for power converters," *IEEE Trans. Ind. Appl*., vol. 33, no. 2, pp 518-524, 1997.

[1.19] J. Hu, L. Shang, Y. He, and Z. Zhu, "Direct active and reactive power regulation of grid-connected DC/AC converters using sliding mode control approach," *IEEE Trans. Power Electron*., vol. 26, no. 1, pp 210-222, 2011.

[1.20] P. Cortes, M. P. Kazmierkowski, R. M. Kennel, D. E. Quevedo and J. Rodriguez, "Predictive control in power electronics and dirves," *IEEE Trans. Ind. Electron*, vol. 55, no. 12, pp. 4312-4324, December 2008.

[1.21] D. Zhi, L. Xu, and B. W. Williams, "Model-based predictive direct power control of doubly fed induction generators," *IEEE Trans. Power Electron.,* vol. 25, no. 2, pp. 341-351, Feb. 2010.

[1.22] A. Bouafia, J. P. Gaubert and F. Krim, "Predictive direct power control of three-phase pulsewidth modulation (PWM) rectifier using space-vector modulation (SVM)," *IEEE Trans. Power Electron.,* vol. 25, no. 1, pp. 228-236, January 2010.

[1.23] J. M. Espí, J. Castelló, R. García-Gil, G. Garcerá, and E. Figueres, "An adaptive robust predictive current control for three-phase grid-connected inverters," *IEEE Trans. Ind. Electron*, vol. 58, no. 8, pp. 3537-3546, August 2011.

[1.24] Q. Zeng and L. Chang, "An advanced SVPWM-based predictive current controller for three-phase inverters in distributed generation systems," *IEEE Trans. Ind. Electron*, vol. 55, no. 3, pp. 1235-1246, Mar. 2008.

[1.25] O. Kukrer, "Discrete-time control of voltage-fed three-phase PWM inverters," *IEEE Trans. Ind. Electron*, vol. 11, no. 2, pp. 260-269, Mar. 1996.

[1.26] R. E. Betz, B. J. Cook, and S. J. Henriksen, "A digital current controller for three phase voltage source inverters," in Conf. Rec. IEEE IAS Annu. Meeting, New Orleans, LA, Oct. 2003, pp. 722-729.

[1.27] Y. Nishida, O. Miyashita, T. Haneyoshi, H. Tomita, and A. Maeda, "A predictive instantaneous-current PWM controlled rectifier with AC-side harmonic current reduction," *IEEE Trans. Ind. Electron*, vol. 44, no. 3, pp. 337-343, Jun. 1997.

[1.28] S.-M. Yang and C.-H. Lee, "A deadbeat current controller for field oriented induction motor drives," *IEEE Trans. Power Electron.,* vol. 17, no. 5, pp. 772-778, Sep. 2002.

[1.29] P. Cortes, J. Rodriguez, P. Antoniewicz, and M. Kazmierkowski, "Direct power control of an AFE using predictive control," *IEEE Trans. Power Electron.,* vol. 23, no. 5, pp. 2516-2523, September 2008.

[1.30] P. Cortés, G. Ortiz, J. I. Yuz, J. Rodríguez, S. Vazquez, and L. G. Franquelo, "Model predictive control of an inverter with output LC filter for UPS applications," *IEEE Trans. Ind. Electron.,* vol. 56, no. 6, pp. 1875-1883, February 2009.

[1.31] S. Kouro, P. Cortes, R. Vargas, U. Ammann and J. Rodriguez, "Model predictive control─A simple and powerful method to control power converters," *IEEE Trans. Ind. Electron.,* vol. 56, no. 6, pp. 1826-1838, June 2009.

[1.32] T. Geyer, G. Papafotiou, and M. Morari, "Model predictive direct torque control – Part I: concept, algorithm, and analysis," *IEEE Trans. Ind. Electron.,* vol. 56, no. 6, pp. 1894-1905, June 2009.

[1.33] P. Cortes, J. Rodriguez, D. E. Quevedo, and C. Silva, "Predictive current control strategy with imposed load current spectrum," *IEEE Trans. Power Electron.,* vol. 23, no. 2, pp. 612-618, March 2008.

[1.34] M. Preindl, E. Schaltz, and P. Thogersen, "Switching frequency reduction using model predictive direct current control for high-power voltage sources inverters," *IEEE Trans. Ind. Electron.,* vol. 58, no. 7, pp. 2826-2835, July 2011.

[1.35] M. A. Perez, J. Rodriguez, E. J. Fuentes, and F. Kammerer, "Predictive control of AC – AC modular converters," *IEEE Trans. Ind. Electron.,* vol. 59, no. 7, pp. 2832-2839, July 2012.

[1.36] S. A. Larrinaga, M. A. Rodriguez, E. Oyarbide and J. R. T. Apraiz, "Predictive control strategy for DC/AC converters based on direct power control," *IEEE Trans. Ind. Electron.,* vol. 54, pp. 1261-1271, June 2007.

[1.37] P. Antoniewicz, and M. P. Kazmierkowski, "Virtual-Flux-Based predictive direct power control of AC/DC converters with online inductance estimation," *IEEE Trans. Ind. Electron.,* vol. 55, no. 12, pp. 4281-4390, December 2008.

[1.38] J. Hu and Z. Zhu, "Investigation on switching patterns of direct power control strategies for grid-connected DC – AC converters based on power variation rates," *IEEE Trans. Power Electron.,* vol. 26, no. 12, pp. 3582-3598, December 2011.

[1.39] R. Morales-Caporal, and M. Pacas, "Encoderless predictive direct torque control for synchronous reluctance machines at very low and zero speed," *IEEE Trans. Ind. Electron.,* vol. 55, no. 12, pp. 4408-4416, December 2008.

[1.40] G. Abad, M. A. Rodriguez, and J. Poza, "Two-level VSC based predictive direct power control of the doubly fed induction machine with reduced power ripple at low constant switching frequency," *IEEE Trans. Energy. Convers.,* vol. 23, no. 2, pp. 570-580, Jun. 2008.

[1.41] G. Abad, M. A. Rodriguez, and J. Poza, "Two-level VSC based predictive direct torque control of the doubly fed induction machine with reduced torque and flux ripples at low constant switching frequency," *IEEE Trans. Power Electron.,* vol. 23, no. 3, pp. 1050-1061, May. 2008.

[1.42] G. Abad, M. A. Rodriguez, and J. Poza, "Three-level NPC converter-based predictive direct power control of the doubly fed induction machine at low constant switching frequency," *IEEE Trans. Ind. Electron.,* vol. 55, no. 12, pp. 4417-4429, 2008.

[1.43] J. M. Guerrero, L. Hang, and J. Uceda, "Control of distributed uninterruptible power supply systems," *IEEE Trans. Ind. Electron.,* vol. 55, no. 8, pp. 2845-2859, 2008.

[1.44] A. P. Martins, A. S. Carvalho, and A. S. Araujo, "Design and implementation of a current controller for the parallel operation of standard UPSs," in *Proc. IEEE IECON,* 1995, pp. 584-589.

[1.45] T. Iwade, S. Komiyama, and Y. Tanimura, "A novel small-scale UPS using a parallel redundant operation system," in *Proc. IEICE/IEEE INTELEC,* 2003*,* pp. 480-483.

[1.46] J. F. Chen and C.-L. Chu, "Combination voltage-controlled and current-controlled PWM inverters for UPS parallel operation," *IEEE Trans. Power Electron.,* vol. 10, no. 5, pp. 547-558, 1995.

[1.47] J. Holtz and K. H. Werner, "Multi-inverter UPS system with redundant load sharing control," *IEEE Trans. Ind. Electron.,* vol. 37, no. 6, pp. 506-513, 1990.

[1.48] X. Sun, Y.-S. Lee, and D. Xu, "Modeling, analysis, and implementation of parallel multi-inverter system with instantaneous average-current-sharing scheme," *IEEE Trans. Power Electron.,* vol. 18, no. 3, pp. 844-856, 2003.

[1.49] J. Tao, H. Lin, J. Zhang, and J. Ying, "A novel load sharing control technique for parallel inverters," in *Proc. IEEE PESC Conf.,* 2003, pp. 1432-1437.

[1.50] T. F. Wu, Y.-K. Chen, and Y.-H. Huang, "3C strategy for inverters in parallel operation achieving an equal current distribution," *IEEE Trans. Ind. Electron.,* vol. 47, no. 2, pp. 273-281, 2000.

[1.51] S. J. Chiang, C. H. Lin, and C. Y. Yen, "Current limitation control technique for parallel operation for UPS inverters," in *Proc. IEEE PESC,* 2004, pp. 1922-1926.

[1.52] J. Potocnik, European SmartGrids Technology Platform: Vision and Strategy for Europe's Electricity Networks of the Future, *European Commission,* 2006.

[1.53] M. C. Chandorkar, D. M. Divan, and R. Adapa, "Control of parallel connected inverters in standalone ac supply systems," *IEEE Trans. Ind. Appl.,* vol. 29, no. 1, pp. 136-143, 1993.

[1.54] J. M. Guerrero, L. G. Vicuna, J. Matas, M. Castilla, and J. Miret, "A wireless controller to enhance dynamic performance of parallel inverters in distributed generation systems," *IEEE Trans. Power. Electron.,* vol. 19, no. 5, pp. 1205-1213, 2004.

[1.55] J. M. Guerrero, J. Matas, L. G. de Vicuna, M. Castilla, and J. Miret, "Wireless-control strategy for parallel operation of distributed-generation inverters," *IEEE Trans. Ind. Electron.,* vol. 53, no. 5, pp. 1461-1470, 2006.

[1.56] A. M. Salamah, S. J. Finney, and B. W. Williams, "Autonomous controller for improved dynamic performance of AC grid, parallel-connected, single-phase inverters," *IET Gener. Trnasm. Distrib.,* vol. 2, no. 2, pp. 209-218, 2008.

[1.57] K. D. Brabandere, B. Bolsens, J. V. Keybus, A. Woyte, J. Driesen, and R. Belmans, "A voltage and frequency droop control method for parallel inverters," *IEEE Trans. Power. Electron.,* vol. 22, no. 4, pp. 1107-1115, 2007.

[1.58] J. C. Vásquez, J. M. Guerrero, A. Luna, P. Rodríguez, and R. Teodorescu, "Adaptive droop control applied to voltage-source inverter operating in grid-connected and islanded modes" *IEEE Trans. Ind. Electron.,* vol. 56, no. 10, pp. 4088-4096, 2009.

[1.59] Y. Li and C. N. Kao, "An accurate power control strategy for power-electronics-interfaced distributed generation units operating in a low-voltage multibus microgrid," *IEEE Trans. Power. Electron.,* vol. 24, no. 12, pp. 2977-2988, 2009.

[1.60] J. M. Guerrero, L. Hang, and J. Uceda, "Control of distributed uninterruptible power supply systems," *IEEE Trans. Ind. Electron.,* vol. 55, no. 8, pp. 2845-2859, August 2008.

[1.61] R. Majumder, B. Chaudhuri, A. Ghosh, R. Majumder, G. Ledwich, and F. Zare, "Improvement of stability and load sharing in an autonomous microgrid using supplementary droop control loop," *IEEE Trans. Power System.,* vol. 25, no. 2, pp. 796-808, 2010.

[1.62] M. Hua, H. Hu, Y. Xing, and J. M. Guerrero, "Multilayer control for inverters in parallel operation without intercommunications," *IEEE Trans. Power. Electron.,* vol. 27, no. 8, pp. 3651-3663, August 2012.

[1.63] G. Escobar, P. Mattavelli, A. M. Stankovic, A. A. Valdez, and J. Leyva-Ramos, "An adaptive control for UPS to compensate unbalance and harmonic distortion using a combined capacitor/load current sensing" *IEEE Trans. Ind. Electron.,* vol. 54, no. 3, pp. 839-847, April 2007.

[1.64] R. Majumder, A. Ghosh, G. Ledwich and F. Zare, "Load sharing and power quality enhanced operation of a distributed microgrid," *IET Renew. Power Gener.,* vol. 3, iss. 2, pp. 109-119, 2009.

[1.65] Y. Li, D. M. Vilathgamuwa, and P. C. Loh, "Microgrid power quality enhancement using a three-phase four-wire grid-interfacing compensator," *IEEE Trans. Ind. App.,* vol. 41, no. 6, pp. 1707-1719, Nov./Dec. 2005.

[1.66] S. Engelhardt, I. Erlich, C. Feltes, J. Kretschmann, and F. Shewarega, "Reactive power capability of wind turbines based on doubly fed induction generators," *IEEE Trans. Energy. Convers.,* vol. 26, no. 1, pp. 364-372, March 2011.

[1.67] A. Camacho, M. Castilla, J. Miret, J. Vasquez, and E. Alarcon-Gallo, "Flexible voltage support control for three phase distributed generation inverters under grid fault" *IEEE Trans. Ind. Electron.,* in press.

[1.68] R. Tirumala, N. Mohan, and C. Henze, "Seamless transfer of grid-connected PWM inverters between utility-interactive and stand-alone modes," in *Proc. IEEE APEC Conf.,* pp. 1081-1086, 2002.

[1.69] Y. Li, D. M. Vilathgamuwa, and P. C. Loh, "Design, analysis, and real-time testing of a controller for multibus microgrid system," *IEEE Trans. Power. Electron.,* vol. 19, no. 5, pp. 1195-1204, 2004.

[1.70] Z. Yao, L. Xiao, and Y. Yan, "Seamless transfer of single-phase grid-interactive inverters between grid connected and stand-alone modes," *IEEE Trans. Power. Electron.,* vol. 25, no. 6, pp. 1597-1603, 2010.

[1.71] Y. A. I. Mohamed and A. A. Radwan, "Hierarchical control system for robust microgrid operation and seamless mode transfer in active distribution systems," *IEEE Trans. Smart Grid.,* vol. 2, no. 2, pp. 352-362, 2011.

[1.72] N. Pogaku, M. Prodanovic and T. C. Green, "Modeling, analysis and testing of autonomous operation of an inverter-based microgrid," *IEEE Trans. Power. Electron.,* vol. 22, no. 2, pp. 613-625, 2007.

[1.73] E. Barklund, N. Pogaku, M. Prodanovic, C. H-Aramburo, and T. C. Green, "Energy management in automonous microgrid using stability-constrained droop control of inverters," *IEEE Trans. Power. Electron.,* vol. 23, no. 5, pp. 2346-2352, 2008.

[1.74] J. M. Guerrero, J. C. Vásquez, J. Matas, M. Castilla, and L. G. Vicuña, "Control Strategy for flexible microgrid based on parallel line-interactive UPS systems" *IEEE Trans. Ind. Electron.,* vol. 56, no. 3, pp. 726-736, 2009.

[1.75] D. M. Vilathgamuwa, P. C. Loh, and Y. Li , "Protection of microgrids during utility voltage sags," *IEEE Trans. Ind. Electron.,* vol. 53, no. 5, pp. 1427-1436, 2006.

[1.76] D. J. Cornforth, S. Sayeef, and T. Moore, "Beyond overcurrent protection: distributed generation in the future grid," in *Proc. IEEE PES Innovative Smart Grid Technologies Conf.,* 2011, pp. 1- 8.

[1.77] V. Calderaro, C. N. Hadjicostis, A. Piccolo and P. Siano, "Failure identification in smart grids based on petri net modeling," *IEEE Trans. Ind. Electron.,* vol. 58, no. 10, pp. 4613-4623, 2011.

CHAPTER 2

WIND POWER GENERATION

2.1 Introduction

2.1.1 Wind power generation system

Wind energy is relatively clean and sustainable, and it has become one of the most promising and fastest growing energy resources in the world. Due to the ever-growing electronic technology and the policy of governments and associations, the cost of electricity from wind energy has been reduced steadily. On the other hand, the global wind power installed capacity has increased from about 40,000MW in 2003 to 59,091MW in 2006. By the end of 2020, it is expected that this figure will increase to well over 1,260,000MW, which will be sufficient for 12% of the world's electricity consumption [2.1]. A typical wind power electronic system, consisting of renewable energy source, wind turbine, gearbox, generator, power converter, transformer, network and control unit, is shown in Fig. 2.1 while a typical cost share for the main components of a single wind generation system is shown in Fig. 2.2.

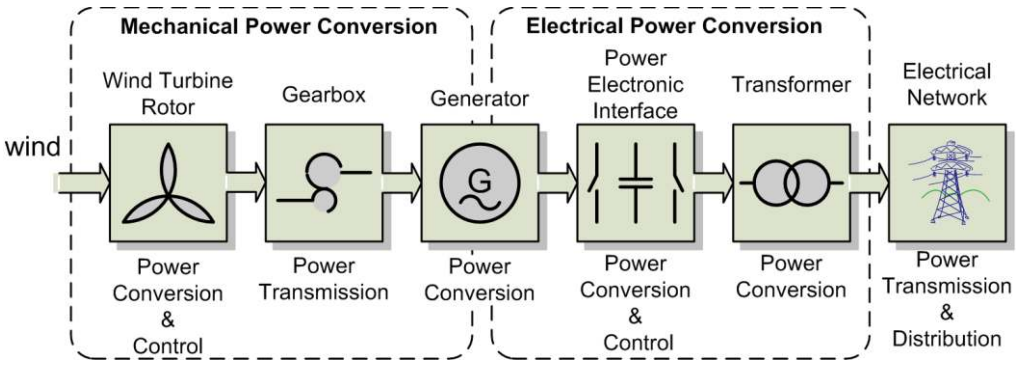

Fig. 2.1 Wind power generation system

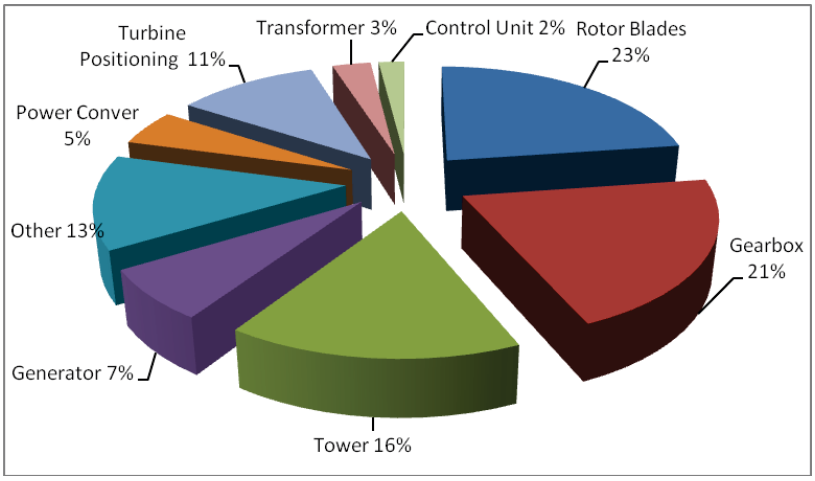

Fig. 2.2 Cost share of a variable speed wind system

As the growing presence of distributed generation and in particular the introduction of renewable sources as well as new grid code requirements, it is significant to improve the power quality generated from wind farms. The concept of smart grid has been proposed to better manage the available resources by integrating advanced sensing technologies, control methods and communication into the current grid [2.2]. Therefore, three important issues are of concern in wind energy generation system namely the reliability, the efficiency and last but not the least the cost and power quality improvement, and automated fault ride-through have become the main research topic of wind system nowadays.

A. Wind turbine characteristics

For a horizontal axis wind turbine, the amount of power that is capable of producing is given by:

$$P = 0.5\rho A C_p v^3 \tag{2.1}$$

where ρ is the air mass density, A the cross-sectional area of the turbine, C_p the power coefficient (which is a function of the tip speed ratio λ and the blade pitch angle β), and v the wind speed. The tip speed ratio λ is defined is the ratio of the turbine speed at the tip of a blade to wind velocity as

$$\lambda = R\frac{\omega}{v} \tag{2.2}$$

where ω is the turbine rotational speed and R the turbine radius. Fig. 2.3 shows an example of the relationship between P and ω. For different wind speed, there is only one specific λ at which C_p is maximized, i.e., where the turbine is most efficient [2.3]. This is why the rotational speed should be regulated to achieve maximum power point tracking (MPPT). In reality, turbines will come on-line at a wind speed of about 3 to 5 m/s. The generated power will then ramp up with respect to the wind speed in a linear fashion to the peak power point at a wind speed of about 12 to 15 m/s. The system then enters a constant-power profile up to the pull-out wind speed of around 25 m/s.

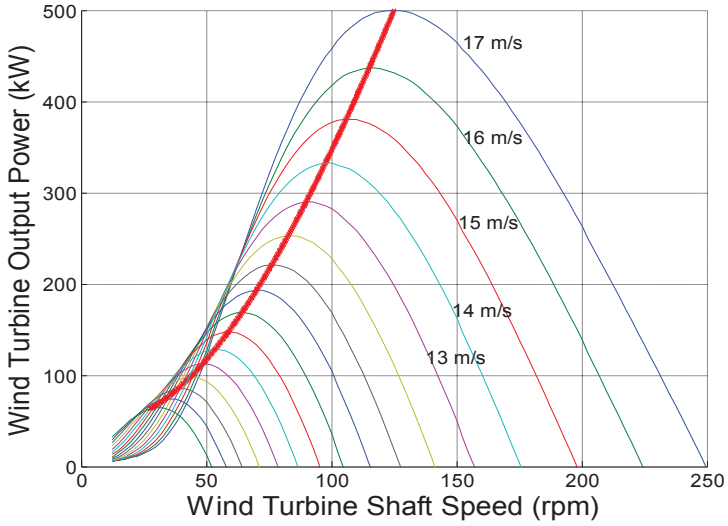

Fig. 2.3 Turbine output power characteristics for different wind speeds.

B. Constant speed constant frequency system

Wind turbines can be divided into two types, namely constant speed constant frequency (CSCF) system and variable speed constant frequency (VSCF) system. In CSCF system, originally the "Danish concept", regardless of the wind speed, the wind turbine rotor speed is fixed and determined by the grid frequency. CSCF systems are typically equipped with squirrel-cage induction generator (SCIG), soft-starter and capacitor bank and they are connected directly to the grid, as depicted in Fig. 2.4. The lagging reactive power is compensated by the addition of the capacitor bank [2.4].

The CSCF system has the advantage of being simple, robust and reliable. However, the maximum conversion efficiency can be achieved only at a given wind speed and will degrade at any other operating points. With the varying wind speed, the fixed speed

turbine generates highly fluctuating output power, causing disturbances to the power systems. This type of turbines also requires a sturdy mechanical design to absorb mechanical stresses.

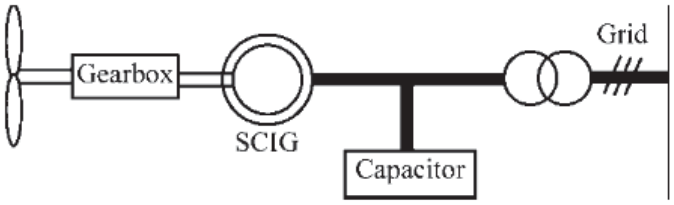

Fig. 2.4 CSCF system with squirrel-cage induction generator

An evolution of the SCIG-based CSCF system is the limited variable-speed system [2.5]. They are equipped with a wound-rotor induction generator (WRIG) with variable external rotor resistance controlled by power electronics. Thus, the total rotor resistance is adjustable, further controlling the slip of the generator and therefore the slope of the mechanical characteristic. Usually the control range is up to 10% over the synchronous speed. Another approach to broaden the dynamic speed is to use a generator with switchable poles or use two generators of different sizes. The operating speeds are determined by choosing the number of generator poles and/or the gear ratio. The smaller generator is used in low winds and the larger in high winds [2.6].

C. VSCF system

Since 2005, variable-speed wind system has become the main focus in wind generation market. The VSCF system can achieve maximum aerodynamic efficiency over a wide range of wind speeds. The turbine can continuously adapt its rotational speed to the wind speed. In doing so, the tip speed ratio can be kept at an optimal value for maximum power output by using the MPPT technique. To make the turbine speed adjustable, the generator is normally connected to the utility grid through a power converter system. Compared with the fixed speed wind turbine systems, VSCF wind systems have several advantages [2.7]:

- Mechanical stress of all parts of the turbine can be reduced because wind gusts can be absorbed by the turbine.

- Power fluctuations in the grid are reduced because the impacts of the wind are buffered in mechanical energy and are not passed onto the grid. Even the back pressure of the tower can be compensated.
- The system efficiency is improved by the adjustment of the rotational speed as a function of the wind speed. The maximum output power can be achieved over a wide wind speed range.
- The pitch control can be simpler because the time constant can be longer with variable speed and the noise emission is reduced in weak wind conditions because the turbine is rotating with lower speed.

In the following sections, the VSCF systems with different electrical generators are discussed and compared.

(1) Wound field synchronous generator (WFSG)

Fig.2.5 illustrates a VSCF system with wound field synchronous generator. The stator winding is connected to network through a four-quadrant power converter comprised of two back-to-back PWM-VSIs. The stator side converter regulates the electromagnetic torque, while the supply side converter regulates the real and reactive power. Synchronous generators of 500 kW to 2MW are significantly more expensive than induction generators with a similar size. One should know that the use of a multi-pole synchronous generator (large diameter synchronous ring generator) avoids the installation of a gearbox as an advantage but a significant increase in weight will be accepted in counterpart [2.6].

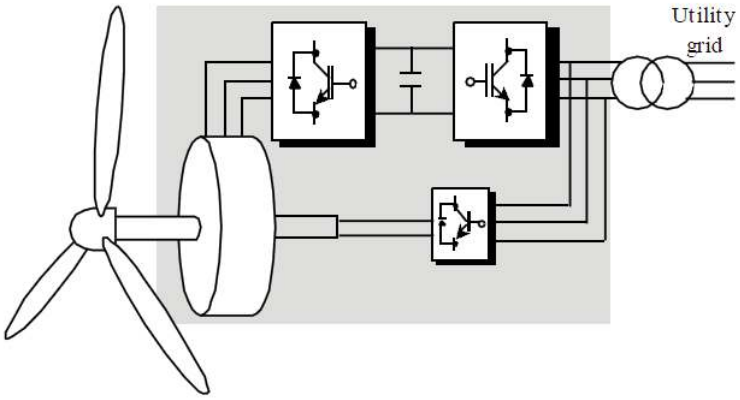

Fig. 2.5 Wound field synchronous generator system

(2) Permanent-magnet synchronous generator (PMSG)

Fig. 2.6 shows a VSCF system where a PMSG is connected to a three-phase rectifier which controls the electromagnet torque, and the supply side converter regulates the DC-bus voltage as well as controlling the output power factor. The PMSG seems attractive as a wind turbine generator. Advantages include self-excitation, high power factor, and high efficiency. It is a solution that is appreciated in small wind turbines. However, permanent magnet materials are still expensive at present, and are difficult to handle in manufacture. In design and operation, it is also important to maintain a low operating temperature as permanent magnets are sensitive to temperature, and they would lose magnetism at a temperature, known as the Curie Point [2.7]

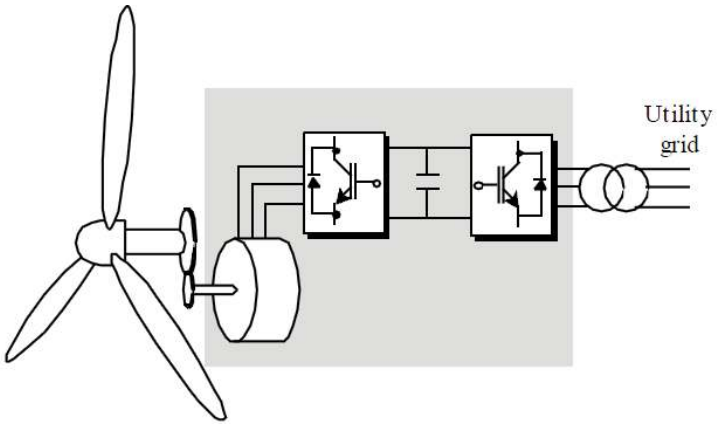

Fig. 2.6 Permanent magnet synchronous generator system

(3) Doubly fed induction generator (DFIG)

As illustrated in Fig. 2.7, this system consists of a DFIG, where the stator winding is directly connected to the network and the rotor winding is connected to the network through a four-quadrant power converter. Usually, the controller of the rotor side converter regulates the electromagnetic torque and supplies part of the reactive power to maintain the magnetization of the machine. On the other hand, the controller of the supply side converter regulates the power factor and maintains the DC link voltage.

The rotor circuit is capable of bidirectional power flow allowing sub-synchronous and super-synchronous modes of operation. During sub-synchronous generation, the rotor absorbs a fraction of the power generated by the stator, whereas under a super-

synchronous condition, both the stator and rotor feed in power to the grid. The converter rating can be kept fairly low, approximately 20% of the total machine power [2.8].

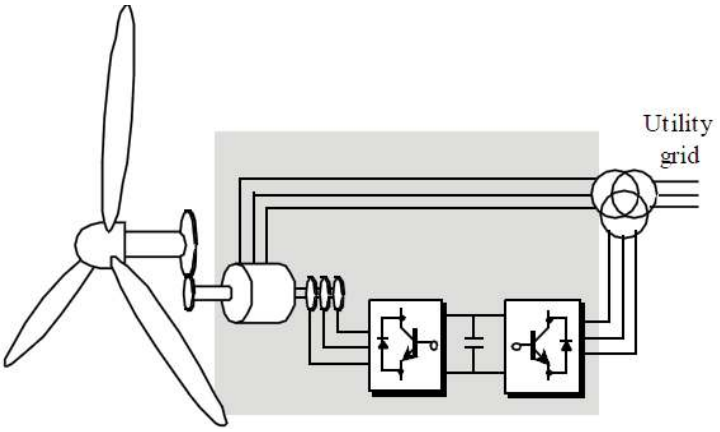

Fig. 2.7 Doubly fed wound induction generator system

Fig. 2.8 Prototype of a 30 kW CBDFIG at UTS

Fig.2.8 illustrates a brushless doubly fed twin stator induction generator (BDFTSIG) developed at the University of Technology, Sydney (UTS). It consists of two induction machines connected in cascade with their rotors interconnected in a way which makes the combined generator act as a DFIG but with the advantage of not requiring brushes [2.8], [2.9].

(4) Squirrel cage induction generator (SCIG)

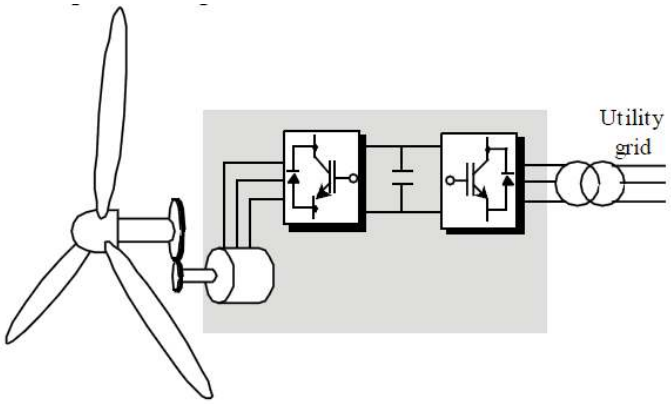

Fig. 2.9 Squirrel cage induction generator system

The stator winding is connected to network through an AC/DC/AC converter, as depicted in Fig. 2.9. The control system of the stator side converter regulates the electromagnetic torque and supplies the reactive power to maintain the machine magnetized. The supply side converter regulates the real and reactive power. SCIG is a very popular machine due to its mechanical simplicity and robust construction. A major problem is the necessity of obtaining the excitation current from the stator terminals. Besides, when connected to a weak grid with an unbalanced, three-phase load, overheating and torque pulsations may occur [2.7].

Overall, there are different features in these four kinds of generators and they can be commonly used in different systems. Table 2.1 lists the advantages and drawbacks between different generator systems.

TABLE 2.1 Advantages and Disadvantages of VSCF Wind Power Systems using Different Generators

Type	Pros	Cons
WFSG	✓ Full speed range ✓ Possible to avoid gear ✓ Complete control of reactive and active power	❖ Small converter for field ❖ Full scale power converter

PMSG	✓ Full speed range ✓ Possible to avoid gear ✓ Complete control of reactive and active power ✓ Brushless (low maintenance) ✓ No power converter for field	❖ Full scale power converter ❖ Multipole generator (big and heavy) ❖ Permanent magnets needed
DFIG	✓ Limited speed range -30% to 30% ✓ Inexpensive small capacity converter ✓ Complete control of reactive and active power	❖ Need for gear
SCIG	✓ Full speed range ✓ Complete control of reactive and active power ✓ Proven technology	❖ Full scale power converter ❖ Need for gear

2.1.2 State of Art of Wind Power Generation Techniques

A. Maximum power point tracking control

For optimum energy extraction in a VSCF system, the speed of the turbine should vary with the wind speed so that an appropriate tip-speed ratio is maintained. A control algorithm which uses wind speed measurements is shown in Fig. 2.10(a). In this algorithm, for the target tip speed ratio (TSR), the wind speed is measured and the required rotor speed for maximum power generation is computed. The rotor speed is also measured and compared to the calculated rotor speed reference. A novel algorithm for wind speed estimation using support-vector regression was proposed in [2.10]. Neither anemometers nor external memory for power-mapping look-up tables are required. Other methods which could be construed as sensorless systems were presented in [2.11]. However, all of these methods still require the use of the detected wind speed,

which means that there will be a degree of the power fluctuation under unstable wind conditions.

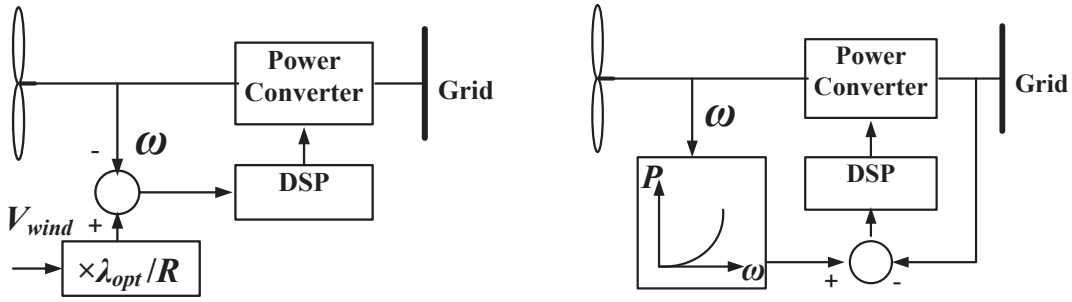

Fig. 2.10 MPPT strategies: (a) Wind speed measurement, (b) Power versus rotor speed characteristic.

Another commonly used control algorithm is shown in Fig. 2.10(b). The output power is measured and the target rotor speed for the required power generation is derived from the designed power versus rotor-speed characteristic. This algorithm is also called power signal feedback. Based on this principle, several evolved strategies have been proposed. Hill-climb searching is widely used because it needs no parameters and is extremely robust. A further development from this is the step-changed hill-climb searching technique, which also works well for large inertia wind turbines [2.12]. An advanced method, which uses a rotor position phase lock loop, and thus does not require a tachometer, position encoder or anemometer, was put forward in [2.13].

Since the MPPT techniques have been well developed, it is not the concern in this chapter.

B. Control strategies of DFIG

In the global wind market, the DFIG has become one of the most popular configurations in wind turbines. Its advantages include low capital cost due to the use of a partially rated converter, maximum power capture over a wider speed range, and decoupled active and reactive power control. As the penetration level of DGs increasing, concerns about power quality and system ability are raised. Wind-driven generators should meet the grid connection regulations, and should not deteriorate the power quality when they are connected to the grid. With advance control strategies, they

should also be able to help stabilize the grid voltage and frequency in order to improve the power quality and enhance the fault ride through (FRT) capability [2.14]-[2.20].

There are various existing control strategies for the DFIG. The most popular one is the field oriented control, also known as the vector control (VC), which regulates the active and reactive power by separately controlling the *d*- and *q*-axis components of the rotor current [2.21]-[2.24]. Unfortunately, this method requires a large amount of computing power to run the complex algorithm in real time. A significant amount of work is also required to tune the proportional-integral (PI) regulators, and it is sensitive to the machine parameter variation. To overcome these drawbacks, direct torque control (DTC) [2.25], [2.26], and later on direct power control (DPC) [2.27], [2.28], were developed for DFIGs. The DTC and DPC algorithms are much simpler and more robust than the VC algorithms. However, the conventional algorithms, which utilize switching tables, produce flux, torque and active/reactive power ripples and also result in a variable switching frequency. To address these issues, several modified strategies have been recently proposed and investigated [2.29]-[2.34].

Most DFIG control methods do not address the grid synchronization, which is an important and heavily regulated issue, and runs concurrently with protection [2.35]. The established method for grid synchronization using VC [2.36]-[2.40] utilizes an outer voltage loop and an inner rotor current loop to achieve the synchronization of frequency, phase and magnitude between the DFIG and the grid. These methods all inherit the drawbacks of VC and require measurements of the grid and stator voltages, rotor currents and position, resulting in complex control algorithms. A direct voltage control scheme using integral variable structure control without a current control loop was presented in [2.41]. However, it still requires the measurement of the grid and stator voltages. In addition, because of its complexity, the transient response is compromised.

Grid synchronization using DTC was proposed in 2002 [2.42]. In comparison with the VC, a better transient performance was achieved. This method used three PI regulators and required the measurement of the rotor position and currents, and the stator and grid voltages. In 2009, fast grid synchronization was achieved without the need for PI regulators and stator voltage measurement by introducing a virtual torque concept [2.43]. Unfortunately, the stator voltage waveform was distorted because of large torque and flux ripples. This is a major obstacle to smooth grid connection. Still, the switching frequency is variable.

Another important issue is the need for fast and flexible active and reactive power regulation after grid connection, which would enable DG units to contribute to energy management and power quality improvement of the system. A grid synchronization strategy based on DPC was proposed in 2009, which could achieve smooth transition between synchronization and normal operation with active and reactive power regulation without changing the control configurations [2.44]. This control strategy is almost identical to that proposed in [2.43] except that it uses the virtual power rather than the virtual torque. In terms of grid synchronization, DPC is not superior to DTC for the following two reasons. Firstly, the effects of power ripples of DPC are larger than that of the torque and flux ripples in a DTC scheme for the same system parameters, resulting in more distorted stator voltage waveforms. Secondly, in DTC, the stator and grid voltage magnitudes are matched during synchronization by directly controlling the rotor flux amplitude whereas in DPC, this condition is fulfilled by imposing zero reactive power, resulting in an algorithm that is more complex and sensitive to parameters variations.

Very recently, a new control strategy, known as the predictive control, was introduced in electrical drives [2.31]-[2.33], [2.45]-[2.51]. It has many merits, such as reduced torque, flux and active/reactive power ripples, constant switching frequency, and excellent steady-state and transient responses. Taking advantage of these merits of the predictive control, a grid synchronization strategy by combining predictive direct virtual toque control (PDVTC) and predictive direct power control (PDPC) was proposed in [2.52].

2.2 Grid Synchronization and Flexible Power Regulation

2.2.1 DFIG modeling

The mathematical equations for a DFIG can be expressed in the rotor frame using complex vectors as the following:

$$\boldsymbol{V}_s = R_s \boldsymbol{I}_s + \frac{d\boldsymbol{\psi}_s}{dt} + j\omega_r \boldsymbol{\psi}_s \tag{2.3}$$

$$\boldsymbol{V}_r = R_r \boldsymbol{I}_r + \frac{d\boldsymbol{\psi}_r}{dt} \tag{2.4}$$

$$\boldsymbol{\psi}_s = L_s \boldsymbol{I}_s + L_m \boldsymbol{I}_r \tag{2.5}$$

$$\boldsymbol{\psi}_r = L_m \boldsymbol{I}_s + L_r \boldsymbol{I}_r \tag{2.6}$$

$$T_e = \frac{3}{2} p\lambda L_m \operatorname{Im}\{\boldsymbol{\psi}_r^* \boldsymbol{\psi}_s\} \tag{2.7}$$

$$P_s = \frac{3}{2} \omega_1 \lambda L_m \operatorname{Im}\{\boldsymbol{\psi}_r^* \boldsymbol{\psi}_s\} \tag{2.8}$$

$$Q_s = \frac{3}{2} \omega_1 \lambda [L_r |\boldsymbol{\psi}_s|^2 - L_m \operatorname{Re}\{\boldsymbol{\psi}_r^* \boldsymbol{\psi}_s\}] \tag{2.9}$$

where the phasors and variables are defined as:

$\boldsymbol{V}_s$, $\boldsymbol{V}_r$	Stator and rotor voltage vectors
$\boldsymbol{I}_s$, $\boldsymbol{I}_r$	Stator and rotor current vectors
L_m, R_m	Magnetizing inductance and resistance
$L_{\sigma s}$, $L_{\sigma r}$	Stator and rotor phase winding leakage inductance
L_s, L_r	Stator and rotor phase winding self-inductance
R_s, R_r	Stator and rotor phase winding resistance
$\boldsymbol{\psi_s}$, $\boldsymbol{\psi_r}$	Stator and rotor flux vectors
T_e	Electromagnetic torque
P_s, Q_s	Stator active and reactive power
ω_1, ω_r, ω_s	Synchronous, rotor, and slip angular frequency
p	Number of pole pairs
λ	Leakage coefficient, $\lambda = 1/(L_s L_r - L_m^2)$

If the iron losses of the machine are considered, a resistance R_c can be introduced in parallel to the magnetizing inductance per phase. Consequently, two more expressions can be deduced [2.53], [2.54]:

$$\boldsymbol{I}_s + \boldsymbol{I}_r = \boldsymbol{I}_c + \boldsymbol{I}_m \tag{2.10}$$

$$\boldsymbol{I}_c R_c = L_m \frac{d\boldsymbol{I}_m}{dt} \tag{2.11}$$

where $\boldsymbol{I}_c$ and $\boldsymbol{I}_m$ are the currents flow through R_c and L_m, respectively. The power and electromagnetic torque expressions can then be derived accordingly. While in some

specific applications, e.g. small power applications, the iron losses cannot be ignored in comparison to the total machine power capacity [2.55], in the work presented below, the effects of iron losses of the DFIG are not included.

Since before being connected to the grid, the stator currents are zero, the DFIG model can be simplified as

$$\boldsymbol{V}_s = \frac{d\boldsymbol{\psi}_s}{dt} + j\omega_r \boldsymbol{\psi}_s \tag{2.12}$$

$$\boldsymbol{V}_r = R_r \boldsymbol{I}_r + \frac{d\boldsymbol{\psi}_r}{dt} \tag{2.13}$$

$$\boldsymbol{\psi}_s = L_m \boldsymbol{I}_r \tag{2.14}$$

$$\boldsymbol{\psi}_r = L_r \boldsymbol{I}_r \tag{2.15}$$

$$T_e = \frac{3}{2} p\lambda L_m \operatorname{Im}\{\boldsymbol{\psi}_r^* \boldsymbol{\psi}_s\} = \frac{3}{2} p L_m \operatorname{Im}\{\boldsymbol{I}_r^* \boldsymbol{I}_s\} = 0 \tag{2.16}$$

2.2.2 The Virtual torque method

For grid synchronization, the induced stator terminal voltage must match the grid voltage, i.e. the magnitude and frequency must be equal and they must be in phase.

The virtual torque concept was proposed in [2.43]. The purpose is to meet a set of fundamental requirements, which can be defined as

$$\boldsymbol{\psi}_g = \int \boldsymbol{V}_g dt \tag{2.17}$$

$$T_v = \frac{3}{2} p\lambda L_m \operatorname{Im}\{\boldsymbol{\psi}_r^* \boldsymbol{\psi}_g\} \tag{2.18}$$

where $\boldsymbol{\psi}_g$ is the virtual grid flux vector, $\boldsymbol{V}_g$ the grid voltage, and T_v the virtual torque.

According to (2.17), the stator voltage vector can be expressed in terms of the stator flux vector in the stationary reference frame as

$$\boldsymbol{V}_s = \frac{d\boldsymbol{\psi}_s}{dt} \tag{2.19}$$

To meet the synchronization requirements, from (2.17) and (2.19), it can be seen that $\boldsymbol{V}_s = \boldsymbol{V}_g$ is equivalent to $\boldsymbol{\psi}_s = \boldsymbol{\psi}_g$. Since there is no torque during synchronization, or $T_e =$

0, when the stator terminal is open circuit, and the angle between the stator flux and rotor flux vectors is zero, i.e. $\boldsymbol{\psi}_s$ and $\boldsymbol{\psi}_r$ are in-phase. It can be seen that controlling $\boldsymbol{\psi}_r$ to be in-phase with $\boldsymbol{\psi}_g$ will force $\boldsymbol{\psi}_s$ to be in-phase with $\boldsymbol{\psi}_g$, i.e., $\boldsymbol{V}_s$ will be in-phase with $\boldsymbol{V}_g$. Therefore, the frequency and phase angle can be made equal by making (2.18) equal to zero, or

$$T_v = \frac{3}{2} p\lambda L_m \left|\boldsymbol{\psi}_r\right|\left|\boldsymbol{\psi}_g\right| \sin\delta = 0 \tag{2.20}$$

For $\boldsymbol{\psi}_s = \boldsymbol{\psi}_g$, the relationship between the rotor and grid fluxes can be obtained from (2.14) and (2.15) as

$$\boldsymbol{\psi}_r = \frac{L_r}{L_m}\boldsymbol{\psi}_s = \frac{L_r}{L_m}\boldsymbol{\psi}_g \tag{2.21}$$

However, from (2.17), the relationship between the grid flux and grid voltage can be rewritten as

$$\boldsymbol{\psi}_g = \frac{\boldsymbol{V}_g}{j\omega_1} \tag{2.22}$$

Thus, the relationship between rotor flux and grid voltage for grid synchronization can be derived by substituting (2.22) into (2.21), which gives

$$\boldsymbol{\psi}_r = \frac{L_r}{L_m} \cdot \frac{\boldsymbol{V}_g}{j\omega_1} \tag{2.23}$$

Therefore, grid voltage synchronization can be achieved by setting the rotor flux amplitude to

$$\left|\boldsymbol{\psi}_r\right|_{ref} = \frac{L_r \left|\boldsymbol{V}_g\right|}{L_m \omega_1} \tag{2.24}$$

where ω_1 is the grid angular frequency in rad/s.

2.2.3 An improved predictive direct control strategy

A. Voltage vectors effect on torque/flux and active/reactive power

According to (2.7), the torque derivative can be expressed as

$$\frac{dT_e}{dt} = \frac{3}{2} p\lambda L_m \,\mathrm{Im}\left\{\frac{d\boldsymbol{\psi}_r^*}{dt}\boldsymbol{\psi}_s + \boldsymbol{\psi}_r^* \frac{d\boldsymbol{\psi}_s}{dt}\right\} \tag{2.25}$$

Substituting (2.4), (2.5) and (2.6) into (2.25) and considering $d\boldsymbol{\psi}_s/dt = j(\omega_1-\omega_r)\boldsymbol{\psi}_s$ [2.28], [2.33], the derivative becomes

$$\frac{dT_e}{dt} = k_1\left[\mathrm{Im}\{\boldsymbol{V}_r^*\boldsymbol{\psi}_s\} - k_2\,\mathrm{Im}\{\boldsymbol{\psi}_r^*\boldsymbol{\psi}_s\} + \omega_s\,\mathrm{Re}\{\boldsymbol{\psi}_r^*\boldsymbol{\psi}_s\}\right] \tag{2.26}$$

and the flux slope can be derived in a similar manner as

$$\frac{d|\boldsymbol{\psi}_r|}{dt} = \frac{1}{|\boldsymbol{\psi}_r|}\left[\mathrm{Re}\{\boldsymbol{V}_r^*\boldsymbol{\psi}_r\} - k_3 + k_4\,\mathrm{Re}\{\boldsymbol{\psi}_r^*\boldsymbol{\psi}_s\}\right] \tag{2.27}$$

In (2.26) and (2.27), $k_1 = 3p\lambda L_m/2$, $k_2 = \lambda R_r L_s$, $k_3 = \lambda R_r L_s|\boldsymbol{\psi}_r|^2$, $k_4 = \lambda R_r L_m$, and $\omega_s = \omega_1 - \omega_r$. Similarly, the derivatives of the active and reactive powers can be obtained as

$$\frac{dP_s}{dt} = \frac{3}{2}\omega_1\lambda L_m\left[\mathrm{Im}\{\boldsymbol{V}_r^*\boldsymbol{\psi}_s\} + \omega_s\,\mathrm{Re}\{\boldsymbol{\psi}_r^*\boldsymbol{\psi}_s\} - \lambda R_r L_s\,\mathrm{Im}\{\boldsymbol{\psi}_r^*\boldsymbol{\psi}_s\}\right] \tag{2.28}$$

$$\frac{dQ_s}{dt} = -\frac{3}{2}\omega_1\lambda L_m\left[\mathrm{Re}\{\boldsymbol{V}_r^*\boldsymbol{\psi}_s\} - \omega_s\,\mathrm{Im}\{\boldsymbol{\psi}_r^*\boldsymbol{\psi}_s\} - \lambda R_r L_s\,\mathrm{Re}\{\boldsymbol{\psi}_r^*\boldsymbol{\psi}_s\} + \lambda R_r L_m|\boldsymbol{\psi}_s|^2\right] \tag{2.29}$$

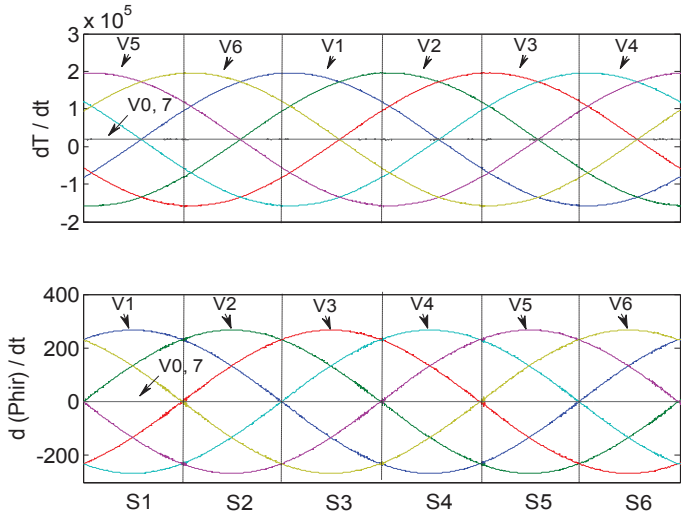

(a)

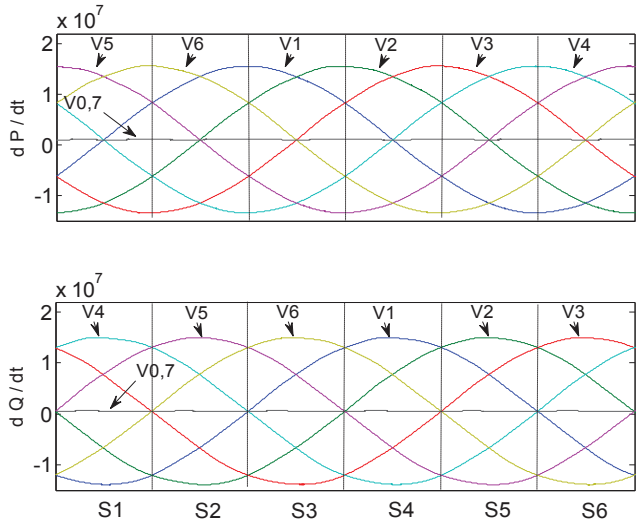

(b)

Fig. 2.11 Torque, rotor flux, active power, and reactive power derivatives against rotor flux position at sub-synchronism. (a) torque and flux derivatives, (b) active and reactive power derivatives

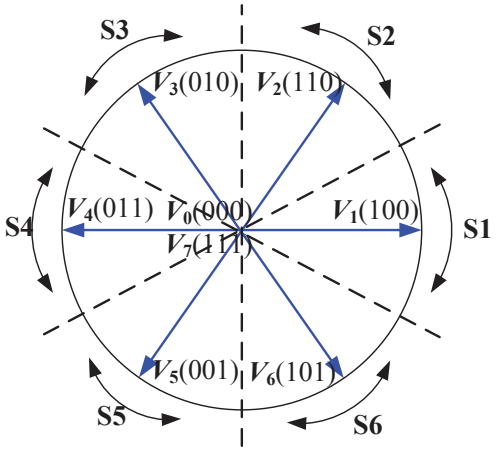

Fig. 2.12 Possible voltage vectors generated by the inverter and sector division

B. Vector selection strategy

To obtain an intuitive view of the torque, flux and active and reactive power derivatives, Fig. 2.11 illustrates graphically the derivatives against the rotor flux position in steady-state for a 20 kW DFIG, the parameters of which are listed in Section 2.3.1. There are eight possible voltage vectors generated by the inverter (six active vectors and two null vectors), and the $\alpha\beta$ plane is divided into six sectors, as shown in Fig. 2.12. In this vector selection strategy, two active vectors followed by one null

vector are applied during every control period. A new vector selection method is shown in Table 2.2. This is almost identical to the one proposed in [2.50] for a permanent magnet synchronous motor drive. The first active vector is chosen using the error between the command and estimated torque (or active power). The second active vector should have a torque derivative that has the same polarity as the first vector (whether positive or negative) but has an opposite flux derivative polarity (or reactive power). This is illustrated in Fig. 2.13 by f_1 and f_2 for torque derivatives, or "slopes", and f_{11} and f_{22} for flux "slopes". For example, consider the third Sector $S3$ in Fig. 2.13. If the rotor flux is within this sector is sub-synchronized (i.e. it is behind where it should be) and $\Delta T = T_e^* - T_e(k) < 0$ (i.e. the torque at point k is too high compared to the reference), V_4 and V_5 produce negative torque derivatives. These should be selected to correct the error. The null vector is used in the third step in the sequence to minimize the torque ripple. This is because it produces very small variation and creates a damping effect. This is in addition to flux ripple damping generated by the use of vectors V_4 and V_5, which produces opposite flux derivatives (positive for V_4 and negative for V_5).

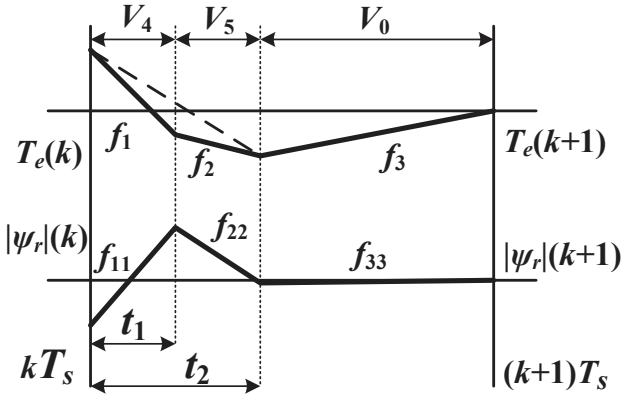

Fig. 2.13 Waveforms for three vectors based predictive direct control

TABLE 2.2 Vector Selection Strategy of Predictive Control

$\Delta T(\Delta P)$	VECTOR SEQUENCE
> 0	V_{k-1} V_{k-2} $V_{0,7}$
< 0	V_{k+1} V_{k+2} $V_{0,7}$

With further study of Fig. 2.11 it can be seen that $\Delta P = P_s^* - P_s(k) < 0$ under the same operating conditions, so that V_4 and V_5 also produce negative active power derivatives

and opposite reactive derivatives (negative for V_4 and positive for V_5). Therefore, Table 2.2 can be utilized for both predictive direct torque control and predictive direct power control, which makes the control structure very simple in mode transition. This will be further discussed in Section V. This vector selection strategy is more straightforward than that in [2.31] because there is no need to switch between two tables regardless of whether sub-synchronous or super-synchronous, steady-state or transient state, or motor mode or generator mode.

After the three vectors are selected, the duty ratio or the vector durations are calculated in a deadbeat fashion in order to achieve torque and flux ripple (or active/reactive power ripple) reduction at constant switching frequency by

$$t_1 = \frac{(x_2^* - x_2(k))(f_2 - f_3) - (x_1^* - x_1(k))f_{22} + T_s f_{22} f_3}{f_{11}(f_2 - f_3) + f_{22}(f_3 - f_1)} \tag{2.30}$$

$$t_2 = \frac{(x_2^* - x_2(k))(f_2 - f_1) + (x_1^* - x_1(k))(f_{11} - f_{22}) + T_s(f_{22} - f_{11}) f_3}{f_{11}(f_2 - f_3) + f_{22}(f_3 - f_1)} \tag{2.31}$$

where $\boldsymbol{x}_1$ is either the torque or active power, $\boldsymbol{x}_2$ either flux or reactive power, T_s the system control period, and f donates the torque or rotor flux derivatives.

C. System simplification

It can be seen that the derivative calculations in (2.26)-(2.29) are very complex and rely heavily on the machine parameters. It is necessary to simplify the calculations. Neglecting the rotor copper loss in (2.4) and substituting $\boldsymbol{V}_r = d\boldsymbol{\psi}_r/dt$ into (2.27), the flux derivative can be approximated to

$$\frac{d|\boldsymbol{\psi}_r|}{dt} = \frac{1}{|\boldsymbol{\psi}_r|} \mathrm{Re}\{\boldsymbol{V}_r^* \boldsymbol{\psi}_r\} \tag{2.32}$$

Similarly, it is not difficult to deduce the approximate torque, active and reactive derivatives as

$$\frac{dT_e}{dt} = k_1 \left[\mathrm{Im}\{\boldsymbol{V}_r^* \boldsymbol{\psi}_s + \omega_s \, \mathrm{Re}\{\boldsymbol{\psi}_r^* \boldsymbol{\psi}_s\} \right] \tag{2.33}$$

$$\frac{dP_s}{dt} = \frac{3}{2} \omega_1 \lambda L_m [\mathrm{Im}\{\boldsymbol{V}_r^* \boldsymbol{\psi}_s\} + \omega_s \, \mathrm{Re}\{\boldsymbol{\psi}_s \boldsymbol{\psi}_r^*\}] \tag{2.34}$$

$$\frac{dQ_s}{dt} = -\frac{3}{2}\omega_1 \lambda L_m [\mathrm{Re}\{\boldsymbol{V}_r^* \boldsymbol{\psi}_s\} - \omega_s \,\mathrm{Im}\{\boldsymbol{\psi}_r^* \boldsymbol{\psi}_s\}] \tag{2.35}$$

Numerical simulation and experimental results show that this simplification is sufficiently accurate with no detectable performance degradation.

2.2.4 A new strategy for grid synchronization and flexible power regulation strategy

Fast and smooth synchronization with minimal impact is essential in grid connection, not only for single DGs but also for local networks or microgrids, which are comprised of DGs, loads, and energy storage units, e.g. battery banks. Once a DG or microgrid is connected to the main grid, flexible active and reactive power regulation must be achieved to help improve system stability and power quality [2.56]-[2.58]. This section presents a novel grid synchronization strategy for DFIG-based wind turbines, which takes advantage of the predictive direct control algorithm proposed in Section 2.2.3 in terms of excellent dynamic response and ripple reduction. For simplicity, we denote the period before generating power as Mode 1 and the period when the generator generates power as Mode 2. Fig. 2.14 illustrates the control diagram.

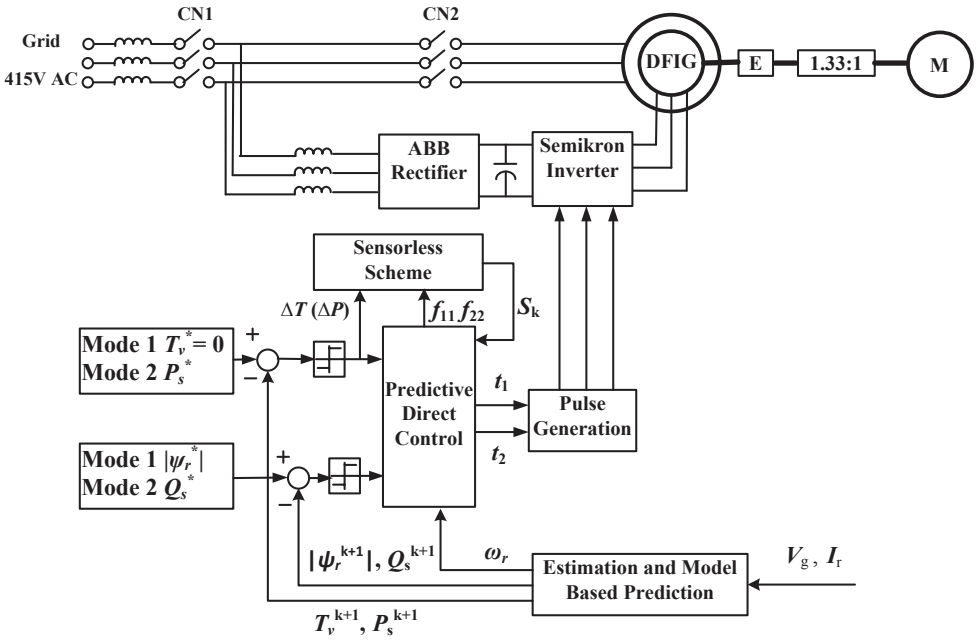

Fig. 2.14 Control diagram of DFIG

A. PDVTC in Mode 1

In Mode 1, the predictive direct torque and flux control loop is switched on, while the predictive direct power control loop is off. The referenced virtual torque value is set to zero and the referenced rotor flux is set using (2.24). The main aim before grid connection is to control the stator terminal voltage so that it is the same as the grid voltage. After the stator winding is connected to the grid, the generator is ready to supply power to the grid depending on the wind speed and load power requirement.

It should be noted that the derivative of the virtual torque can be expressed as

$$\frac{dT_v}{dt} = \frac{3}{2} p\lambda L_m \operatorname{Im}\left\{ \frac{d\boldsymbol{\psi}_r^*}{dt} \boldsymbol{\psi}_g + \boldsymbol{\psi}_r^* \frac{d\boldsymbol{\psi}_g}{dt} \right\} \tag{2.36}$$

Substituting (2.4) and (2.17) into (2.36) yields

$$\frac{dT_v}{dt} = \frac{3}{2} p\lambda L_m \operatorname{Im}\left\{ \boldsymbol{V}_r^* \boldsymbol{\psi}_g - \frac{R_r}{L_r} \boldsymbol{\psi}_r^* \boldsymbol{\psi}_g + \boldsymbol{\psi}_r^* \boldsymbol{V}_g \right\} \tag{2.37}$$

B. PDPC in Mode 2

After the stator is connected to the grid, flexible active and reactive power regulation is essential. This is especially true when considering reactive power compensation for voltage support and power quality improvement. Using the analysis in Section 2.2.3, it is found that the control effects on torque/flux and active power/reactive power are essentially the same. Therefore, flexible power regulation can be achieved without changing the switching table once the stator is connected to the grid. In simple terms, when the conditions of generating power are met, the system transits from Mode 1 to Mode 2 by switching on the predictive direct power control loop without changing the switching table. In Mode 2, the wind turbine can supply active and reactive power according to the grid conditions within the rated capacity of the DFIG.

C. Rotor position sensorless scheme

To increase the reliability of the grid synchronization process, it is important to implement the sensorless rotor position control. Supposing that the rotor flux is as in Sector $S3$ with $\Delta T > 0$, then the voltage vectors V_2, V_1 and V_7 can be used in that order to minimize the power ripple (Table 2.2). Fig. 2.11 illustrates that V_2 increases $|\psi_r|$ while V_1 decreases $|\psi_r|$. When the rotor flux steps forwards to $S4$, the effect of V_2 (1st vector) on $|\psi_r|$ will reverse. When the rotor flux rotates backwards to $S2$, the effect of V_1 (2nd vector) on $|\psi_r|$ will reverse. However, if $\Delta T < 0$, voltage vectors V_4, V_5 andV_0 are used; V_4 increases $|\psi_r|$ while V_5 reduces $|\psi_r|$. When the rotor flux steps forwards to Sector $S4$, the effect of V_5 (2nd vector) on $|\psi_r|$ will reverse whereas when the rotor flux rotates backwards to Sector $S2$, the effect of V_4 (1st vector) on $|\psi_r|$ will reverse.

TABLE 2.3 Direction of Change of Sector

$\Delta T(\Delta P)$	f_{11}	f_{22}
> 0	+	–
< 0	–	+

From this information, sector changing can be estimated as tabulated in Table 2.3. An in-depth analysis shows that this principle is also valid for PDPC in Mode 2, regardless of whether it is sub-synchronous or super-synchronous. In this method, the sector number can be updated by the polarity of ΔT or ΔP_s and the derivatives of $|\psi_r|$ or Q_s by applying the first two active vectors. This is the case even if the exact flux position and rotational direction are unknown. It is very simple and easy to implement.

D. One step delay compensation with Model based prediction

The influence of the one-step delay in practical digital implementation is clearly illustrated in Fig. 2.15, where x is the system variable set, x^k is the x sampled at the k^{th} instant, and T_c the time that the digital signal processor takes to do the calculation. In power converter control, x may be the voltages, line currents, or power, etc. In electrical machine control, x may be the stator voltages, rotor currents, or electromagnetic torque, etc. After the desired voltage vector V_r^k is determined, it will not be applied until the

$(k+1)^{th}$ instant. The problem is that the system variable set $\boldsymbol{x}^k$ has evolved into $\boldsymbol{x}^{k+1}$ at the $(k+1)^{th}$ instant. As a result, the vector applied at the $(k+1)^{th}$ instant which was decided during the sampling instants of k and $k+1$ is not necessarily the best one, which leads to the undesired torque/flux or active/reactive power ripples.

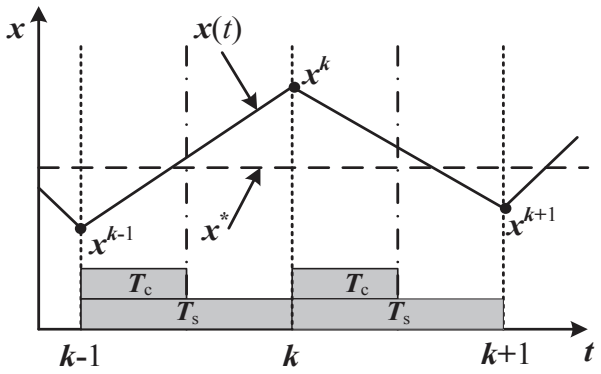

Fig. 2.15 One step delay in digital implementation

It is therefore worth compensating for the one-step delay for the predictive control. Otherwise, the effect on the performance in comparison to the basic direct control will be worse, especially when the sampling frequency is low [2.59]. Here, a model-based prediction is proposed to eliminate the influence of one-step delay. Using (2.3) and (2.4), at the k^{th} sampling instant, $\boldsymbol{\psi}_s^{k+1}$ and $\boldsymbol{\psi}_r^{k+1}$ can be estimated from $\boldsymbol{\psi}_s^k$, $\boldsymbol{I}_s^k$, $\boldsymbol{\psi}_r^k$ and $\boldsymbol{I}_r^k$, using

$$\boldsymbol{\psi}_s^{k+1} = \boldsymbol{\psi}_s^k + (\boldsymbol{V}_s^k - R_s \boldsymbol{I}_s^k - j\omega_r \boldsymbol{\psi}_s^{k+1})T_s \tag{2.38}$$

$$\boldsymbol{\psi}_r^{k+1} = \boldsymbol{\psi}_r^k + (\boldsymbol{V}_r^k - R_r \boldsymbol{I}_r^k)T_s \tag{2.39}$$

In the conventional direct torque and direct power control, $\boldsymbol{V}_r$ is the applied active vector within the period between the k^{th} and $(k+1)^{th}$ instants. However, in the proposed predictive direct control, $\boldsymbol{V}_r$ should be the resultant vector of the two active vectors and zero vector. In order to estimate the rotor flux more accurately, $\boldsymbol{V}_r$ can be expressed as

$$\boldsymbol{V}_r^k = \frac{t_1 \boldsymbol{V}_1^k + t_2 \boldsymbol{V}_2^k}{T_s} \tag{2.40}$$

Substituting (2.39) into (2.18), the virtual torque at the $(k+1)^{th}$ instant can be obtained, T_v^{k+1} and $|\boldsymbol{\psi}_r^{k+1}|$ are then used to determine $\boldsymbol{V}_r^{k+1}$, which will be applied at the $(k+1)^{th}$ sampling instant rather than $\boldsymbol{V}_r^k$. After the power control loop is switched on in Mode 2,

the active and reactive power at $(k+1)^{th}$ sampling instant can also be predicted in a similar manner by substituting (2.38) and (2.39) into (2.8) and (2.9).

2.3 Numerical Simulation and Experimental Verification

2.3.1 Numerical simulation

To check the feasibility of the proposed strategy, numerical simulations were carried out by using Matlab/Simulink. The system parameters are listed in Table 2.4. The nominal DC-link voltage is 400 V and the rotor speed is 1200 rpm unless explicitly indicated. The sampling frequencies of the conventional direct virtual torque control (CDVTC) and PDVTC were chosen to be 10 kHz and 4 kHz, respectively. The system was started at 0.05 s, the stator was connected to the grid at 0.2 s and the generator started producing power from 0.3 s.

TABLE 2.4 Parameters of Wind Power System

Symbol	Quantity	Value
P_N	Rated power	20 kW
$V_{N,S}$	Rated stator voltage	415 V (delta)
$V_{N,r}$	Rated rotor voltage	380 V (star)
$I_{N,S}$	Rated stator current	38 A
$I_{N,r}$	Rated rotor current	53 A
V_{dc}	DC link voltage	400 V
L_{m}	Magnetizing inductance	85.003 mH
$L_{\sigma \mathrm{s}}$	Stator leakage inductance	2.426 mH
$L_{\sigma \mathrm{r}}$	Rotor leakage inductance (referred to stator)	2.426 mH
R_{s}	Stator winding resistance	0.207 Ω
R_{r}	Rotor winding resistance (referred to stator)	0.218 Ω
p	Poles pairs	2
f_N	Operating frequency	50 Hz

A. System performance in Mode 1

To evaluate the performance of the proposed method, a comprehensive comparison between CDVTC and PDVTC was conducted. The average switching frequencies were 2.36 kHz and 2.01 kHz for CDVTC and PDVTC, respectively.

Fig. 2.16 shows the dynamic responses of the virtual torque and rotor flux. It can be seen that the torque and flux ripples of PDVTC are smaller than those of CDVTC. There is some obvious torque surge at the beginning of system startup in PDVTC. Both the rotor flux of CDVTC and PDVTC can reach the commanding values in less than 10 ms.

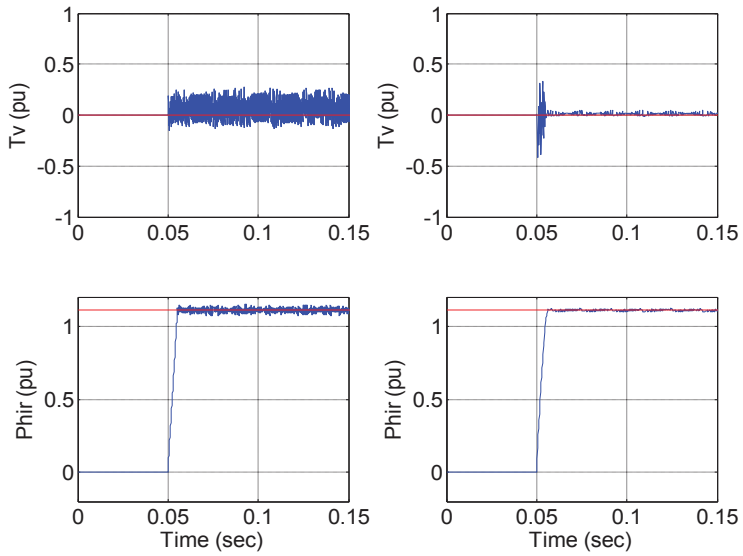

Fig. 2.16 Responses of virtual torque and rotor flux when system starts to operate in Mode 1. (a) CDVTC, (b) PDVTC.

Fig. 2.17 shows the stator voltage and rotor currents. It can be seen that the induced stator voltage of both cases can track the grid voltage to within 10 ms. However, the stator voltage of PDVTC is closer to the grid voltage than CDVTC. This demonstrates the smoother grid synchronization of PDVTC. Also, the rotor current of PDVTC is more sinusoidal.

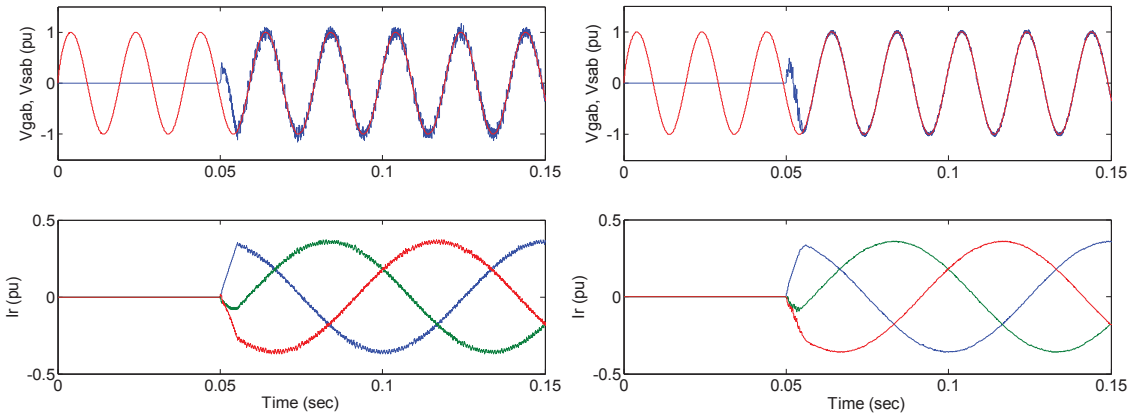

Fig. 2.17 Responses of stator induced voltage and rotor currents when system starts to operate in Mode 1. (a) CDVTC, (b) PDVTC.

Fig. 2.18 presents the harmonic spectrum analysis of the stator voltage and rotor current. It can be seen that the stator voltage THD of PDVTC is only 2.06 % with the higher order harmonics appearing at 4 kHz and its multiples, much lower than 6.22 % of CDVTC with a broad harmonic spectrum. On the other hand, it can be observed that the spectrum of the rotor currents presents very similar characteristics to that of stator voltage, both for CDVTC and PDVTC, and again, the rotor current THD of PDVTC is only 0.69 %, much lower than 2.54 % of CDVTC.

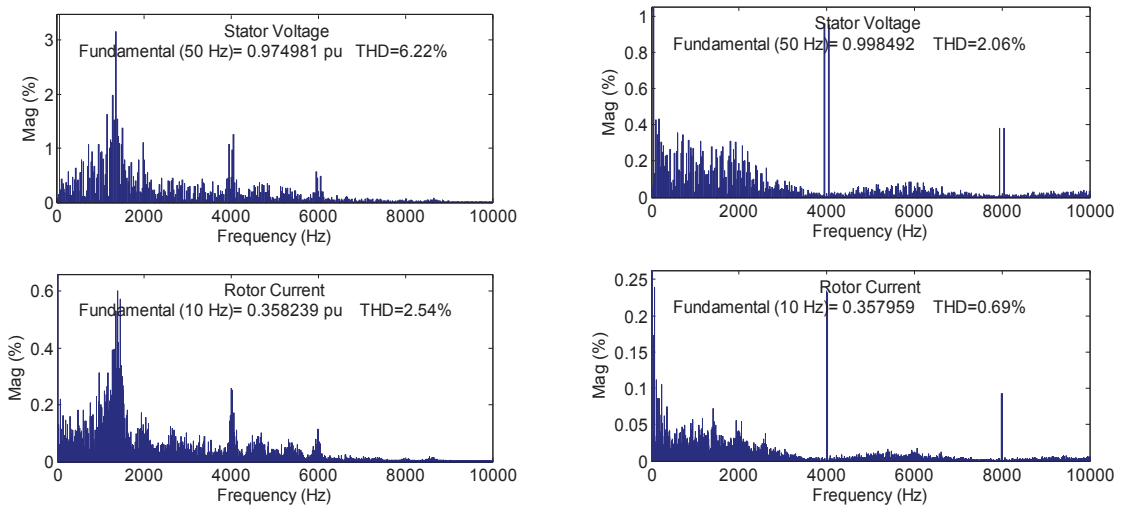

Fig. 2.18 Stator voltage and rotor current spectrum analysis. (a) CDVTC (stator voltage THD = 6.22%, rotor current THD = 2.54%), (b) PDVTC (stator voltage THD = 2.06%, rotor current THD = 0.69%).

B. Transient of grid connection in Mode 1

After synchronization, the grid connection can be carried out. The system performance of grid connection is shown in Fig. 2.19. From top to bottom, the curves are virtual torque, rotor flux, rotor current and stator current. It can be seen that there is no overshoot during the transient moment of grid connection. However, a slight surge of virtual torque in CDVTC can be observed.

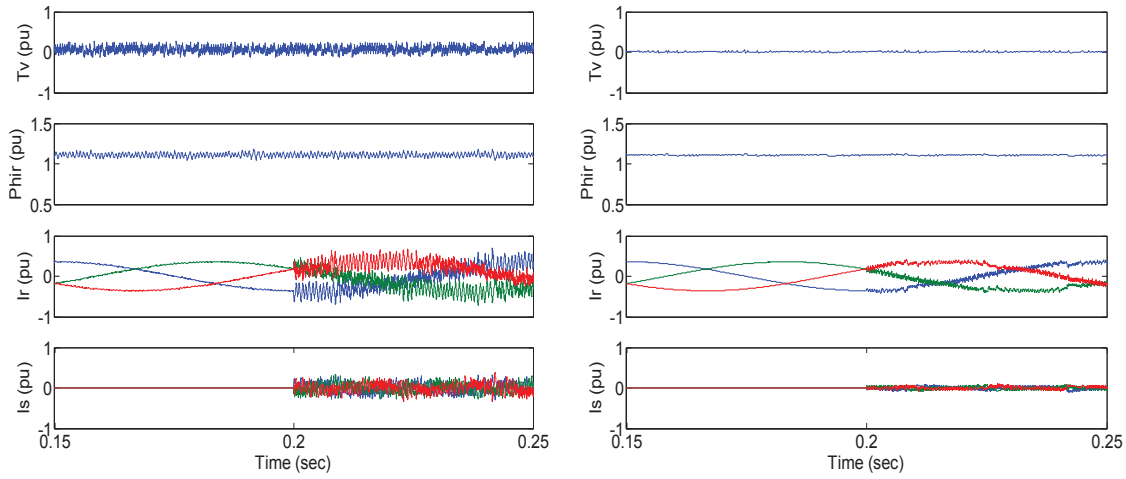

Fig. 2.19 Responses of virtual torque, rotor flux, rotor currents and stator currents at grid connection instant. (a) CDVTC, (b) PDVTC.

C. System Performance in Mode 2

After successful grid connection, the system can switch to Mode 2, i.e. supplying power to the grid. The predictive direct control algorithm allows for smooth transition from PDVTC in Mode 1 to PDPC in Mode 2. This achieves fast and accurate active and reactive power regulation.

The mode transition occurs at 0.3 s where the referenced active power is set to -15 kW (-0.75 pu) and the reactive power is maintained at 0 pu. At 0.4 s the active power reference was stepping from -0.75 pu to 0.5 pu and the reactive power reference stepping from 0 pu to 0.5 pu. The new active and reactive power references are obtained in about 2.5 ms. There is a reverse in both rotor and stator currents. All these phenomena can also be found in Fig. 2.20.

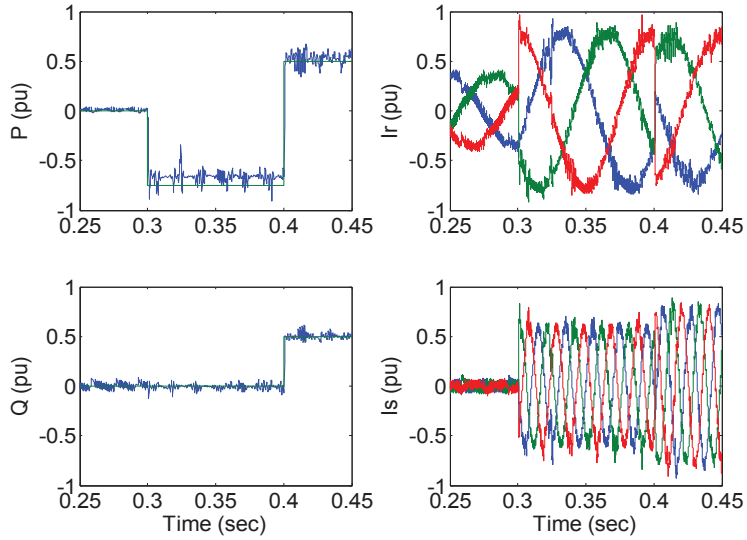

Fig. 2.20 Responses of transition from Mode 1 to Mode 2 and power regulation in Mode 2.

2.3.2 Experimental verification

The proposed control strategy is further validated experimentally. Fig. 2.21 shows the experimental setup, where (a) shows the DFIG and its control units and (b) the control panel of the dSPACE system. The wind turbine is emulated by a 20 kW DC motor driven by a 4 quadrant thyristor DC converter. This is controlled by a dSpace system using a DS1104 controller board. The DC motor is connected to a 20 kW DFIG via a 1.33:1 gear box for increased torque at lower speed. For DFIG control, a three-phase Semikron intelligent IGBT power module is used as the inverter while an ABB rectifier is used to converter the three-phase AC grid to constant 400 DC voltage. Another dSPACE DS1104 PPC/DSP control board was employed to implement the real-time algorithm coding using the C language for generator control. The grid voltage, stator voltage, rotor current and rotor position are sampled using the ControlDesk. This is interfaced with the DS1104 and PC at a rate of 10 kHz and 4 kHz for CDVTC and PDVTC (or PDPC), respectively. All the parameters and variables in the hardware are the same as those used in the simulations. The DFIG is driven by the DC motor at 1200 rpm, unless explicitly indicated.

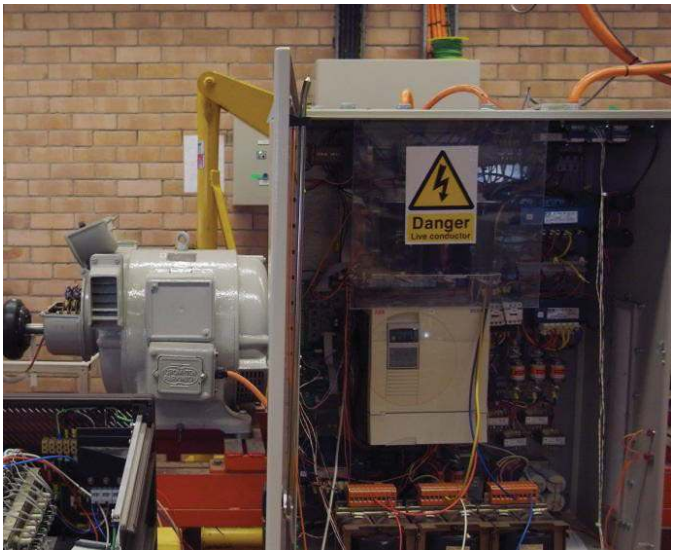

(a)

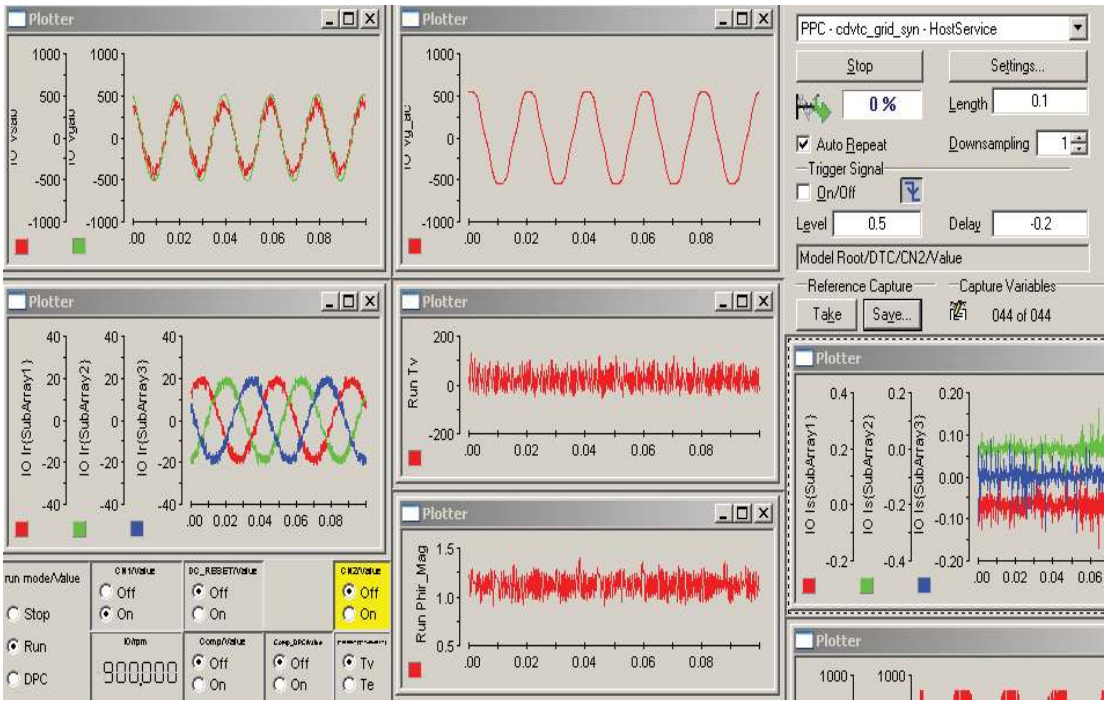

(b)

Fig. 2.21 Laboratory setup. (a) DFIG and its control centre, (b) part of the control panel of ControlDesk from dSPACE.

A. System performance in Mode 1

Fig. 2.22 presents the dynamic response of the induced stator voltage and rotor currents when the control algorithm starts. Again, PDVTC presents better performance than CDVTC not only in terms of the rotor currents, but more importantly, in induced stator voltage, which guarantees smoother grid synchronization. It is noted that the proposed control strategy also can achieve fast and smooth grid synchronization at lower rotor speed (i.e. lower wind speed), which is essential in practical wind power generation applications.

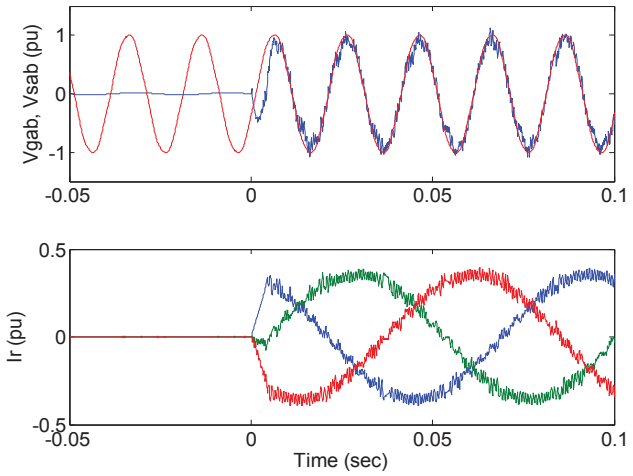

(a)

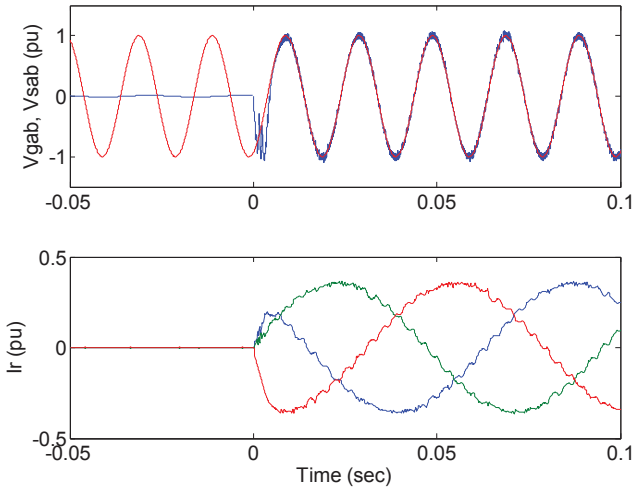

(b)

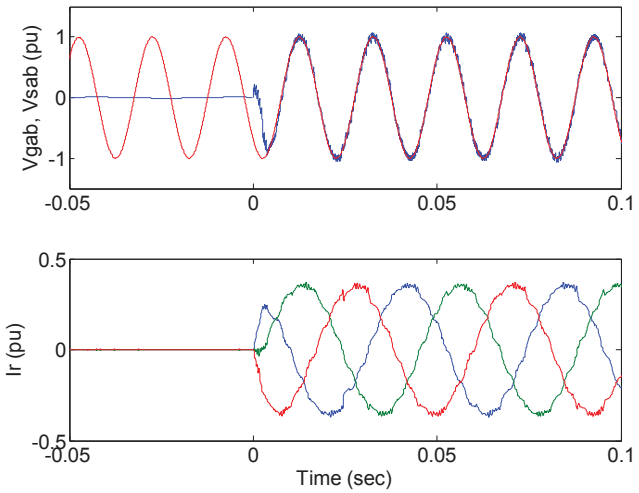

(c)

Fig. 2.22 Experimental results of stator induced voltage and rotor currents when system starts to operate in Mode 1. (a) CDVTC, (b) PDVTC, (c) PDVTC at 800 rpm

B. Model based prediction for one-step delay compensation

The one-step delay effect was reduced in the simulation results in Section VI using the method described in Section V. In order to show this effect a comprehensive set of tests were carried out. Fig. 2.23 shows the measured virtual torque and rotor flux with and without the use of the model-based prediction scheme (Section V). In Fig. 2.23(a) it can be seen that the torque and flux performance is slightly improved with the one-step compensation in CDVTC. However, the torque and flux ripples for PDVTC with compensation are reduced significantly, as shown in Fig. 2.23(b). These results illustrate that one-step delay compensation is very necessary in digital implementation, especially when the system control period is relatively low. One-step delay compensation has been implemented in all the experimental results in the remainder of this section.

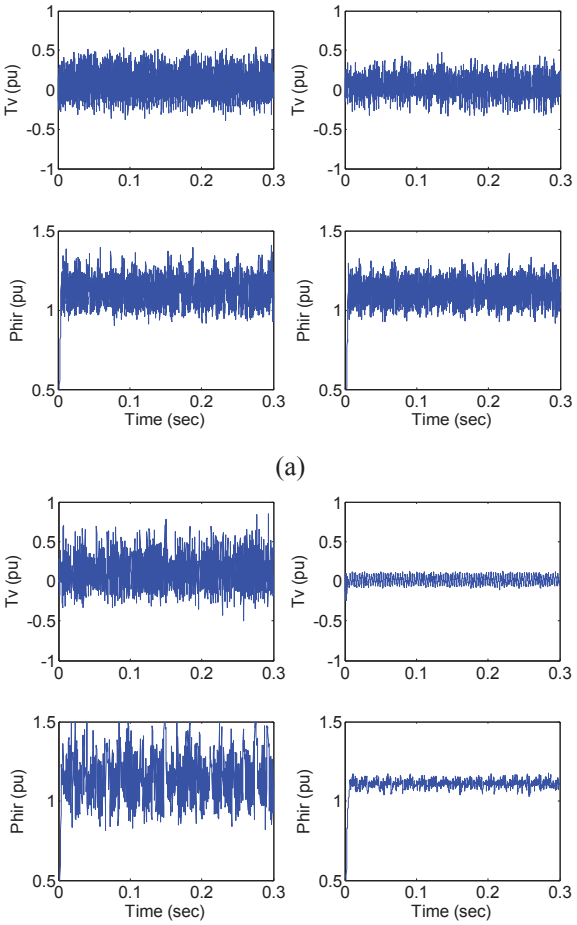

Fig. 2.23 Experimental results of one-step delay compensation using model based prediction. (a) CDVTC with and without compensation, left: without compensation, right: with compensation, (b) PDVTC with and without compensation, left: without compensation, right: with compensation.

In order to obtain a better comparison, the quantitative index of sampling frequency, average switching frequency, torque ripple, rotor flux ripple, stator voltage THD, and rotor current THD are listed in Table 2.5. The torque and rotor flux ripples are calculated using standard deviations. In Table 2.5, the asterisk * denotes the control strategy with one step delay compensation. It can be seen that the PDVTC with one step delay compensation presents the best performance in terms of torque and rotor flux ripples, stator voltage THD and rotor current THD, while its sampling frequency is only 4 kHz and the average switching frequency f_{sw} is only 1846.69 Hz. Another conclusion that can be drawn is that the performance is improved after using one step delay compensation in conjunction with model based prediction, especially for the PDVTC strategy, which can be explained in Section 2.2.3.

TABLE 2.5 Quantitative Comparison of Steady State at 1200 rpm before Grid Connection

Strategy	f_s (kHz)	f_{sw} (Hz)	T_{rip} (Nm)	ψ_{rip} (Wb)	THD of *V*s	THD of *I*r
CDVTC	10	1485.62	30.2023	0.0935	13.54%	5.13%
CDVTC*	10	2023.50	22.6800	0.0792	10.20%	4.22%
PDVTC	4	1592.34	41.0269	0.1163	15.42%	5.80%
PDVTC*	4	1846.69	9.2910	0.0215	3.97%	1.76%

C. Grid connection

Once the induced stator voltage matches the grid voltage in terms of frequency, magnitude, and phase angle, grid connection can be carried out. Fig. 2.24 presents the dynamic response of grid connection. No overshoot is observed in the currents in both control methods. However, compared to PDVTC, obvious harmonic components are present in the rotor and stator currents for CDVTC after grid connection. While the rotor flux does not change, there is distorted rotor current and non-zero stator current. This can be explained by (4), i.e. it is the non-zero component of the stator current $L_m I_s$ that compensates for the distorted rotor current $L_r I_r$, resulting in unchanged rotor flux. Hence in the three vectors based predictive direct control, the torque and flux ripples are reduced considerately, which leads to better performance.

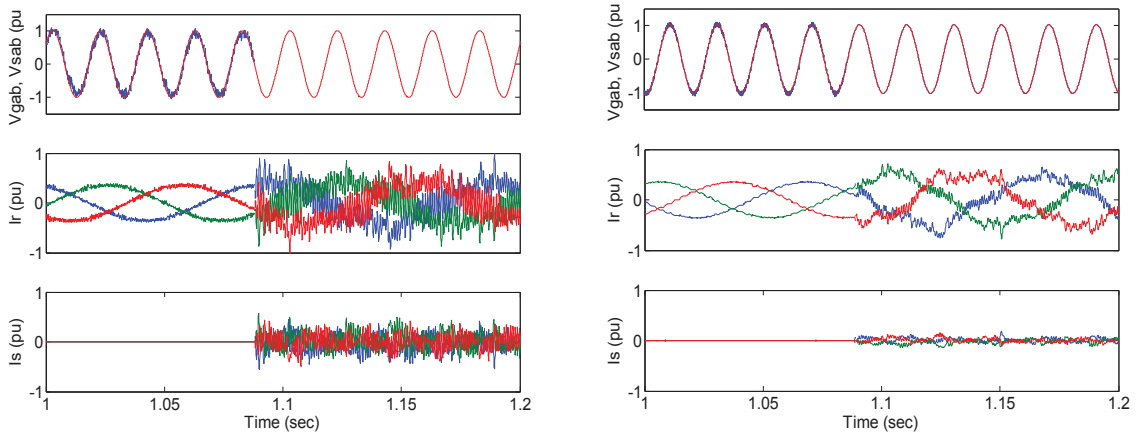

Fig. 2.24 Experimental results of grid connection. (a) CDVTC, (b) PDVTC.

D. Flexible power regulation

After grid connection, Mode 1 can be changed to Mode 2 for flexible power regulation by replacement of the virtual torque and rotor flux loop with the active power and reactive power loop. This is without changing the vector selection table. Therefore, the wind power generator can supply active power very quickly after grid connection. It can also participate in power quality improvement such as grid voltage support by providing reactive power flexibly. Fig. 2.25(a) shows the system performance with constant reactive power and step changing active power. Fig. 2.25(b) presents the results with constant active power and step changing reactive power.

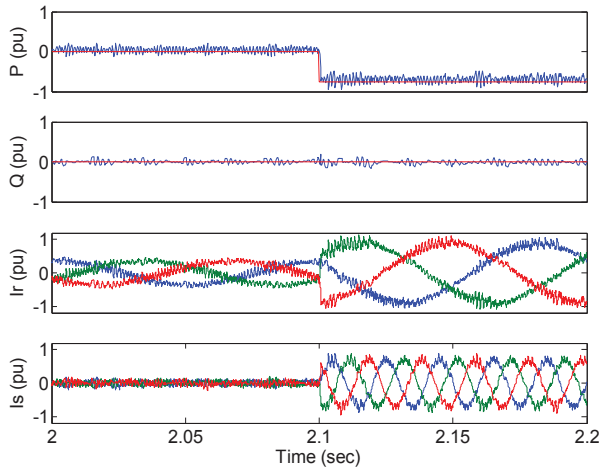

(a)

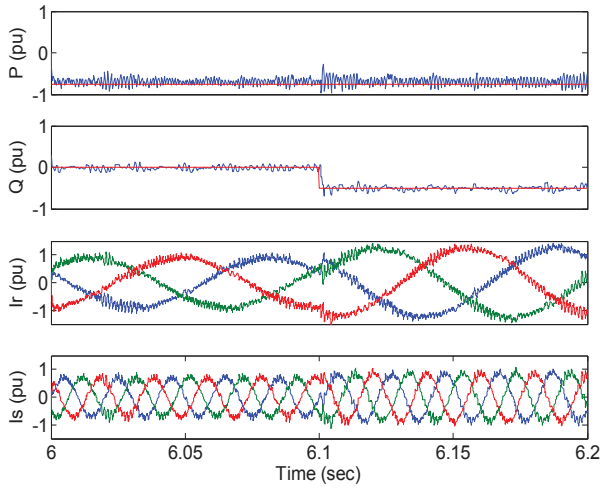

(b)

Fig. 2.25 Experimental results of power regulation. (a) constant reactive power, (b) constant active power.

E. Performance of rotor position sensorless algorithm

Before the results of rotor position sensorless scheme are presented, it is useful to review Table 2.3. This provides "The Direction of Change of Sector" using ΔT (ΔP) and the rotor flux derivatives (or reactive power derivatives) f_{11} and f_{22}. For instance, at the k^{th} sampling instant, the rotor flux is located at sector S_m and $\Delta P > 0$. If $f_{11}(k+1)$ changes its polarity with $f_{11}(k)$, this means that the rotor flux just steps forward (+) into sector S_{m+1}; if $f_{22}(k+1)$ changes its polarity with $f_{22}(k)$, this means that the rotor flux just steps backward (–) into sector S_{m-1}. If neither $f_{11}(k+1)$ nor $f_{22}(k+1)$ change polarity from the previous sampling instant, this means that the rotor flux is still within sector S_m. The system control diagram, with the rotor position sensorless algorithm incorporated within it, can be found in Fig. 2.14.

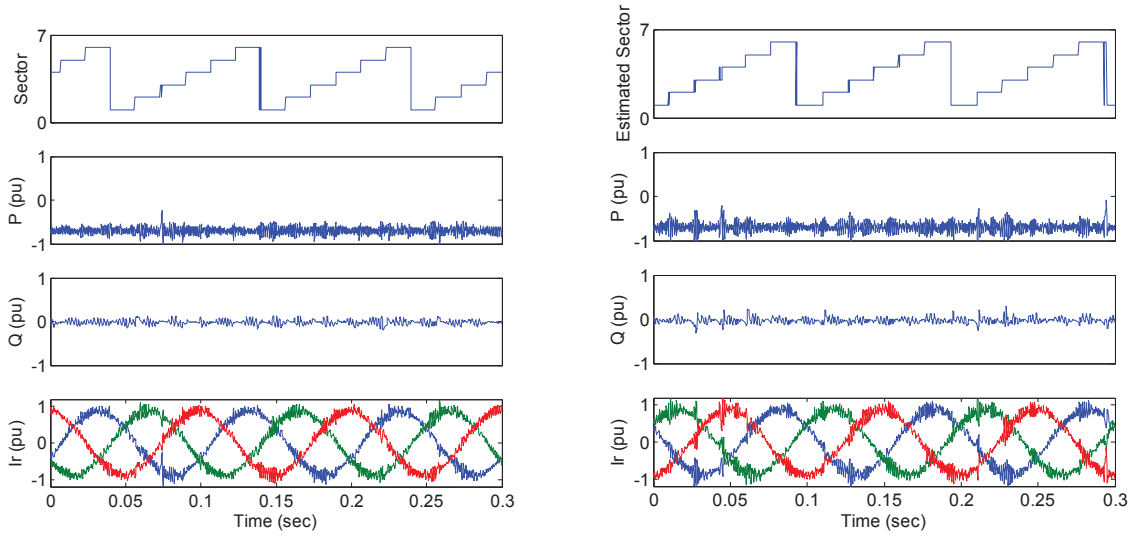

(a) (b)

Fig. 2.26 Experimental performances with and without rotor position sensor. (a) with rotor position sensor, (b) without rotor position sensor.

Fig. 2.26 shows the waveforms of the stator active power, reactive power, and rotor current along with the sector information for P^* = –0.75 pu and Q^* = 0 pu. It can be seen that the rotor flux sector can be correctly estimated and there is very little deterioration in system performance with the proposed sensorless scheme. In order to deeply analyse the updated sector information, Fig. 2.27 shows the details of Fig. 2.26(b) at around 0.24 second. In rotor position sensorless control investigation, the rotor encoder was still installed on the shaft, but its position output was not used in the

system control. Instead, it was used for comparison with the estimated sector values. Fig. 2.27 shows that $f_{11} < 0$ and $f_{22} > 0$ at the $(k\text{-}2)^{th}$, $(k\text{-}1)^{th}$, and k^{th} sampling instances. However, at the $(k+1)^{th}$ instant, f_{22} become negative while f_{11} is still positive. This means that the rotor flux has already stepped forwards into the next sector, as given in Table 2.3 ($\Delta P < 0$ and f_{22} reverses). After comparing the estimated sectors with the actual sectors from encoder, as shown in Fig. 2.27(b), it is verified that they match well. This scheme can also be implemented in Mode 1.

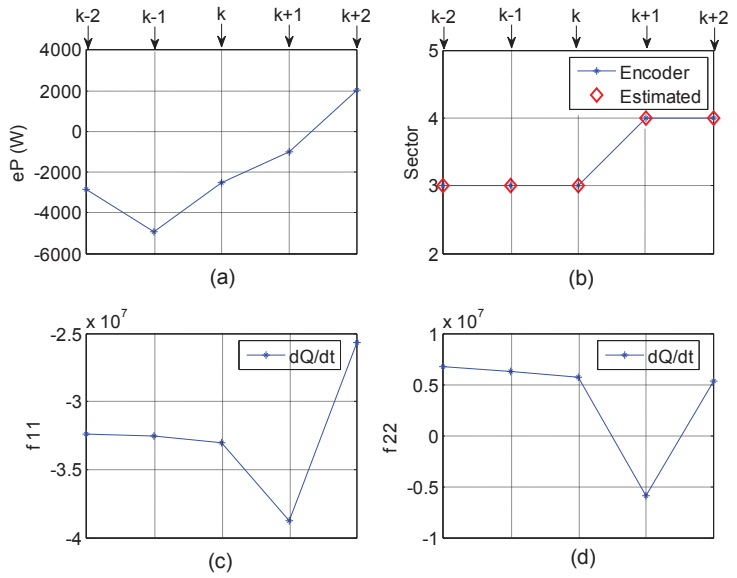

Fig. 2.27 Sensorless scheme validation. (a) active power error, (b) estimated sector, (c) reactive power derivative for the first active vector, (d) reactive power derivative for the second active vector.

2.4 Summary of the Chapter

In this chapter, different wind power system configurations are firstly presented, and then the advantages and disadvantages of each type are comprehensively compared. After that, the state of art of wind power generation techniques is reviewed.

In the latter part of this chapter, a novel predictive direct virtual torque and power control method for DFIG with excellent transient and steady-state performance is proposed. Using this method, a new grid synchronization strategy for a DFIG is presented. Numerical simulation was performed to check the feasibility of the new strategy, and experimental testing done to check the validity. The results show that fast

and smooth grid synchronization was achieved in Mode 1, and flexible power regulation in Mode 2 (after synchronization). The transition between Modes 1 and 2 was simple, fast and smooth since there is no change in the control structure. The influence of one-step delay has been successfully compensated in practical implementation by using a model-based predictive scheme. Finally, by using a sensorless rotor control algorithm, the system reliability is improved.

References

[2.1] S. Sawyer and A. Zervos, "Global Wind 2011 Report," Global Wind Energy Council, 2012.

[2.2] S. Rahman, "Smart grid expectations [In My View]," *Power and Energy Magazine, IEEE,* vol. 7, pp. 88, 84-85, 2009.

[2.3] Y. Zhao, X. D. Zou, Y. N. Xu, Y. Kang, and J. Chen, "Maximal Power Point Tracking under Speed-Mode Control for Wind Energy Generation System with Doubly Fed Introduction Generator," in *Power Electronics and Motion Control Conference, 2006. IPEMC 2006. CES/IEEE 5th International*, 2006, pp. 1-5.

[2.4] Y.Amirat, M.E.H.Benhouzid, B.Bensaker, and R.Wamkeue, "Generators for Wind Energy Conversion System: State of the Art and Coming Attractions," *Electrical Systems,* vol. 3, pp. 26-38, 2007.

[2.5] Z. C. H. Li, "Overview of different wind generator systems and their comparisons," 2007.

[2.6] S. Soter and R. Wegener, "Development of Induction Machines in Wind Power Technology," in *Electric Machines & Drives Conference, 2007. IEMDC '07. IEEE International*, 2007, pp. 1490-1495.

[2.7] H. P. J. Marques, H. A. Gründling, J. R. Pinheiro and H. L. Hey, "A SURVEY ON VARIABLE-SPEED WIND TURBINE SYSTEM," 2002.

[2.8] G. Boardman, J. Zhu, and Q. P. Ha, "Dynamic and steady state modelling of brushless doubly fed induction machines," in *IEEE Proceedings of the Fifth International Electrical Machines and Systems Conference (ICEMS)*, 2001, pp. 412-416.

[2.9] J. Zhu, D. Basic, and G. Boardman, "MODELING AND PERFORMANCE OF A BRUSHLESS DOUBLY FED TWIN STATOR INDUCTION GENERATOR," 2001.

[2.10] A. G. Abo-Khalil and L. Dong-Choon, "MPPT Control of Wind Generation Systems Based on Estimated Wind Speed Using SVR," *Industrial Electronics, IEEE Transactions on,* vol. 55, pp. 1489-1490, 2008.

[2.11] Z. Xuemei, L. Lin, X. Dianguo, and J. Platts, "Sliding Mode MPPT Control of Variable Speed Wind Power System," in *Power and Energy Engineering Conference, 2009. APPEEC 2009. Asia-Pacific*, 2009, pp. 1-4.

[2.12] W. Ping, L. Hongyuan, G. Cuishuang, and T. Chenbin, "MPPT control algorithms for wind power generation based on voltage disturbance," in *Intelligent Control and Automation, 2008. WCICA 2008. 7th World Congress on*, 2008, pp. 7398-7402.

[2.13] S. Baike, B. Mwinyiwiwa, Z. Yongzheng, and O. Boon-Teck, "Sensorless Maximum Power Point Tracking of Wind by DFIG Using Rotor Position Phase Lock Loop (PLL)," *Power Electronics, IEEE Transactions on,* vol. 24, pp. 942-951, 2009.

[2.14] J. Hu, J. Zhu, D. G. Dorrell, Q. Ma, Y. Zhang, and W. Xu, "Control Strategies of Variable-Speed Wind System Under New Grid Code Requirement - A Survey," in *Proc. IEEE IECON Conf.,* pp. 3061–3066, 2010.

[2.15] M. Shahabi, M. R. Haghifam, M. Mohamadian, and S. A. N-Niaki, "Microgrid dynamic performance improvement using a doubly fed induction wind generator," *IEEE Trans. Energy. Convers.,* vol. 24, no. 1, pp. 137–145, Mar 2009.

[2.16] J. Hu, J. Zhu, D. G. Dorrell, Y. Wang, Y. Zhang, W. Xu and Y. Li, "A Novel Control Strategy for Doubly Fed Induction Generator and Permanent Magnet Synchronous Generator during Voltage Dips," in *Proc. IEEE AUPEC Conf.,* pp. 1–6, 2010.

[2.17] V. T. Phan and H. H. Lee, "Control strategy for harmonic elimination in stand-alone DFIG applications with nonlinear loads," *IEEE Trans. Power. Electron.,* vol. 26, no. 9, pp. 2662–2675, September 2011.

[2.18] M. Mohseni, S. M. Islam, "Transient control of DFIG-based wind power plants in compliance with the Australian grid code," *IEEE Trans. Power. Electron.,* vol. 27, no. 6, pp. 2813–2824, June 2012.

[2.19] C. Wessels, F. Gebhardt, F. W. Fuchs, "Fault ride-through of a DFIG wind turbine using a dynamic voltage restorer during symmetrical and asymmetrical grid faults," *IEEE Trans. Power. Electron.,* vol. 26, no. 3, pp. 807–815, March 2011.

[2.20] R. I. Bojoi, L. R. Limongi, D. Roiu, and A. Tenconi, "Enhanced power quality control strategy for single phase inverters in distributed generation systems," *IEEE Trans. Power. Electron.,* vol. 26, no. 3, pp. 798–806, March 2011.

[2.21] R. Pena, J. C. Clare, and G. M. Asher, "Doubly-fed induction generator using back-to-back PWM converters and its application to variable-speed wind-energy

generation," *Inst. Electr. Eng. Proc. Power Appl*., vol. 143, no. 3, pp. 231–241, May 1996.

[2.22] L. Morel, H. Godfroid, A. Mirzaian, and J. M. Kauffmann, "Doubly-fed induction machine: converter optimization and field oriented control without position sensor," *IEE Proc. Electr. Power Appl*., vol. 145, no. 4, pp. 360–368, 1998.

[2.23] R. Datta and V. T. Ranganthan, "A simple position-sensorless algorithm for rotor-side field-oriented control of wound-rotor induction machine," *IEEE Trans. Ind. Electron.,* vol. 48, no. 4, pp. 786–793, August 2001.

[2.24] R. W. De Doncker, S. Muller, and M. Deicke, "Doubly fed induction generator systems for wind turbines," *IEEE Magazine Ind. Appl.,* vol. 8, no. 3, pp. 26–33, May/Jun 2002.

[2.25] G. S. Buja and M. P. Kazmierkowski, "Direct torque control of PWM inverter-fed AC motors – a survey," *IEEE Trans. Ind. Electron.,* vol. 51, no. 4, pp. 744–757, 2004.

[2.26] S. Arnalte, J. Burgos, and J. Rodriguez-Amenedo, "Direct torque control of a doubly-fed induction generator for variable speed wind turbines," *Electric power components and systems*, vol. 30, no. 2, pp. 199–216, 2002.

[2.27] R. Datta and V. T. Ranganathan, "Direct power control of grid-connected wound rotor induction machine without rotor position sensors," *IEEE Trans. Power. Electron.,* vol. 16, no. 3, pp. 390–399, May 2001.

[2.28] L. Xu and P. Cartwright, "Direct active and reactive power control of DFIG for wind energy generation," *IEEE Trans. Energy. Convers.,* vol. 21, no. 3, pp. 750–758, September 2006.

[2.29] Y.-S. Lai and J.-H. Chen, "A new approach to direct torque control of induction motor drives for constant inverter frequency and torque ripple reduction," *IEEE Trans. Energy. Convers.,* vol. 16, no. 3, pp. 220–227, September 2001.

[2.30] C. Lascu and A. M. Trzynadlowski, "Combining the principles of sliding mode, direct torque control, and space-vector modulation in a high-performance sensorless AC drive," *IEEE Trans. Ind. App.,* vol. 40, no. 1, pp. 170–177, January/February 2004.

[2.31] G. Abad, M. A. Rodriguez, and J. Poza, "Two-level VSC based predictive direct torque control of the doubly fed induction machine with reduced torque and flux

ripples at low constant switching frequency," *IEEE Trans. Power. Electron.,* vol. 23, no. 3, pp. 1050–1061, May 2008.

[2.32] D. Zhi, L. Xu, and B. W. Williams, "Model-based predictive direct power control of doubly fed induction generators," *IEEE Trans. Power. Electron.,* vol. 25, no. 2, pp. 341–351, February 2010.

[2.33] J. Hu, J. Zhu, Y. Zhang, Q. Ma, and Y. Guo, "Simple and Robust Predictive Direct Control of DFIG with Low Constant Switching Frequency and Reduced Torque and Flux Ripples," in *Proc. IEEE Int. Electric Machines and Drives Conf.* 2011*,* pp. 781–786.

[2.34] J. Hu, L. Shang, Y. He, and Z. Zhu, "Direct active and reactive power regulation of grid-connected DC/AC converters using sliding mode control approach," *IEEE Trans. Power. Electron.,* vol. 26, no. 1, pp. 210–222, January 2011.

[2.35] J. Yang, J. E. Fletcher and J. O'Reilly, "A Series-Dynamic-Resistor-Based Converter Protection Scheme for Doubly-Fed Induction Generator During Various Fault Conditions" *IEEE Trans. Energy Convers*., vol. 25, no. 2, pp 422 – 432, June 2010.

[2.36] G. Yuan, J. Chai, and Y. Li, "Vector control and synchronization of doubly fed induction wind generator system," in *Proc. 4th Int. Power Electronic and Motion Control Conf.*, 2004, vol. 2, pp. 886–890.

[2.37] F. Blaabjerg, R. Teodorescu, M. Liserre, and A. V. Timbus, "Overview of control and grid synchronization for distributed power generation systems," *IEEE Trans. Ind. Electron.,* vol. 53, no. 5, pp. 1398–1409, Oct 2006.

[2.38] X. Zhang, D. Xu, Y. Lang, and H. Ma, "Study on stagewise control of connecting dfig to the grid," in *Proc. CES/IEEE 5th Int. Power Electronics and Motion Control Conf., 2006,* vol. 1, 2006, pp. 1–5.

[2.39] J. Park, K. Lee, and D. Kim, "Control method of a doubly-fed induction generator with automatic grid synchronization," in *Proc. IEEE IECON Conf.,* 2006, pp. 4254–4259.

[2.40] G. Iwanski and W. Koczara, "Synchronization and mains outage detection for controlled grid connection of the wind driven variable speed power generation system," in *Proc. IEEE Clean Electrical Power Conf.*, 2007, pp. 585–590.

[2.41] S. Z. Chen, N. C Cheung, K. C. Wong, and J. Wu, "Grid synchronization of doubly-fed induction generator using integral variable structure control," *IEEE Trans. Energy Convers.,* vol. 24, no. 4, pp. 875–883, December 2009.

[2.42] S. A. Gomez and J. L. R. Amenedo, "Grid synchronisation of doubly fed induction generators using direct torque control," in *Proc. IEEE IECON Conf.*, 2002, pp. 3338–3343.

[2.43] J. Arbi, M. J.-B. Ghorbal, I. Slama-Belkhodja, and L. Charaabi, "Direct virtual torque control for doubly fed induction generator grid connection," *IEEE Trans. Ind. Electron.,* vol. 56, no. 10, pp. 4163–4173, October 2009.

[2.44] Manel, J.- B. G, J. Arbi, and S.-B Ilhem, "A novel approach of direct active and reactive power control allowing the connection of the DFIG to the grid," in *Proc. IEEE Power Electronics and Applications Conf.*. 2009, pp. 1–10.

[2.45] P. Cortes, M. P. Kazmierkowski, R. M. Kennel, D. E. Quevedo and J. Rodriguez, "Predictive control in power electronics and drives," *IEEE Trans. Ind. Electron*, vol. 55, no. 12, pp. 4312–4324, December 2008.

[2.46] T. Geyer, G. Papafotiou and M. Morari, "Model predictive direct torque control—Part I: concept, algorithm, and analysis," *IEEE Trans. Ind. Electron.*, vol. 56, no. 6, pp. 1894–1905, June 2009.

[2.47] S. Kouro, P. Cortes, R. Vargas, U. Ammann and J. Rodriguez, "Model predictive control—A simple and powerful method to control power converters," *IEEE Trans. Ind. Electron.,* vol. 56, no. 6, pp. 1826–1838, June 2009.

[2.48] J. Hu, J. Zhu, Y. Zhang, and Y. Guo, "Predictive Direct Power Control of Doubly Fed Induction Generator with Power Ripples Reduction and One Step Delay Compensation for Wind Power Generation," in *Proc. IEEE ICEMS Conf.,* pp. 1–6, 2011.

[2.49] J. Hu, J. Zhu, Q. Ma, and Y. Zhang, "Predictive Direct Virtual Torque Control of Doubly Fed Induction Generator for Grid Synchronization," in *Proc. IEEE ICEMS Conf.,* pp. 1–6, 2011.

[2.50] Y. Zhang and J. Zhu, "A novel duty cycle control strategy to reduce both torque and flux ripples for DTC of permanent magnet synchronous motor drives with switching frequency reduction," *IEEE Trans. Power. Electron.,* vol. 26, no. 10, pp. 3055–3067, October 2011.

[2.51] Y. Zhang, J. Zhu and J. Hu, "Model Predictive Direct Torque Control for Grid Synchronization of Doubly Fed Induction Generator," in *Proc. IEEE IEMDC Conf.,* pp. 765–770, 2011.

[2.52] J. Hu, J. Zhu, and Y. Zhang, *et al*, "Predictive direct control of doubly fed induction generator for grid synchronization in wind power generation," in *Proc. IEEE ECCE Conf.,* pp. 2381–2388, 2011.

[2.53] E. Levi, "Impact of iron loss on behavior of vector controlled induction machines," *IEEE Trans. Ind. Appl*., vol. 31, no. 6, pp. 1287–1296, November/December 1995.

[2.54] S. D. Wee, M. H. Shin, and D. S. Hyun, "Stator-flux-oriented control of induction motor considering iron loss," *IEEE Trans. Ind. Electron*., vol. 48, no. 3, pp. 602–608, June 2001.

[2.55] K. Yamazaki and N. Fukushima, "Iron loss model for rotating machines using direct eddy current analysis in electrical steel sheets," *IEEE Trans. Energy Convers*., vol. 25, no. 3, pp. 633–641, September 2010.

[2.56] F. Wang, J. L. Duarte, M. A. M. Hendrix, "Grid-interfacing converter systems with enhanced voltage quality for microgrid application – concept and implementation," *IEEE Trans. Power. Electron.,* vol. 26, no. 12, pp. 3501–3513, December 2011.

[2.57] Y. Mohamed, H. H. Zeineldin, M. M. M. Salama, R. R. Seethapathy, "Seamless formation and robust control of distributed generation microgrids via voltage control and optimized dynamic power sharing," *IEEE Trans. Power. Electron.,* vol. 27, no. 3, pp. 1283–1294, March 2012.

[2.58] C. Cho, J. Jeon, J. Kim, S. Kwon, K. Park, S. Kim, "Active synchronizing control of a microgrid," *IEEE Trans. Power. Electron.,* vol. 26, no. 12, pp. 3707–3719, December 2011.

[2.59] J. Beerten, J. Verveckken and J. Driesen, "Predictive direct torque control for flux and torque ripple reduction," *IEEE Trans. Ind. Electron*., vol. 57, no. 1, pp. 404–412, January 2010.

CHAPTER 3

SOLAR PHOTOVOLTAIC POWER GENERATION

3.1 Introduction

3.1.1 Principle and configuration of photovoltaic systems

Photovoltaic (PV) technology involves converting solar energy directly into electrical energy by means of solar cells, which are usually manufactured and combined into modules that consist of 36 to 72 cells, depending on the output voltage and current of the module [3.1]. Additionally, the modules can also be grouped together in various quantities and configurations to form arrays with unique voltage and current characteristics [3.2], [3.3].

The performance of a PV array can be affected by many factors, such as temperature, sun light strength, and shading, etc. Fig 3.1 shows the total power output performance of a laboratory PV array from 6:00 am to 8:00 pm in a sunny day (21-10-2011) and a cloudy day (23-10-2011). It can be seen that, in a sunny day, the PV output power increase smoothly in the morning, reached the peak value of about 19 kW at around 2 pm, decreased gradually in the afternoon, and hit the bottom of 0 kW at around 7 pm. However, the output power features an obvious fluctuated characteristic in a cloudy day.

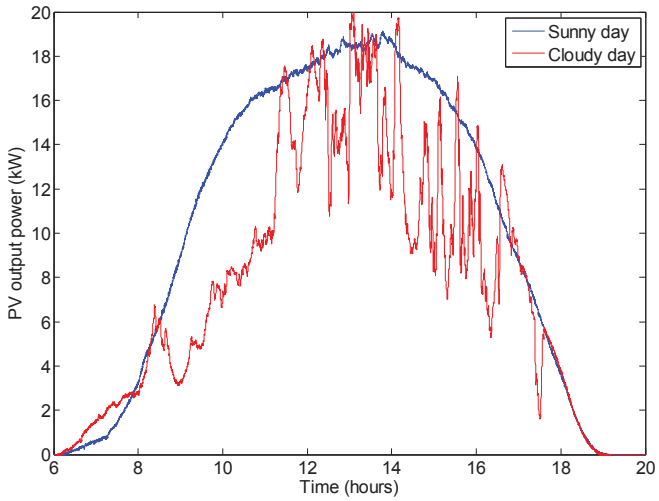

Fig. 3.1 PV output power measured in two different days.

PV systems can be structured into several operational configurations. Each configuration has the basic power electronic interfaces that interconnect the system to the utility grid. Fig. 3.2 shows the configurations where a centralized inverter is used. This has been the most common type of PV installation in the past. PV modules are connected in series and/or parallel and connected to a centralized DC/AC converter. The primary advantage of this design is the fact that if the inverter is most costly part in the installed PV system, this system has the lowest cost design because of the presence of only one inverter. However, the main drawback of this configuration is that the power losses can be high due to the mismatch between the PV modules and the presence of string diodes. Another disadvantage is that this configuration has a single point failure at the inverter, and thus has less reliability.

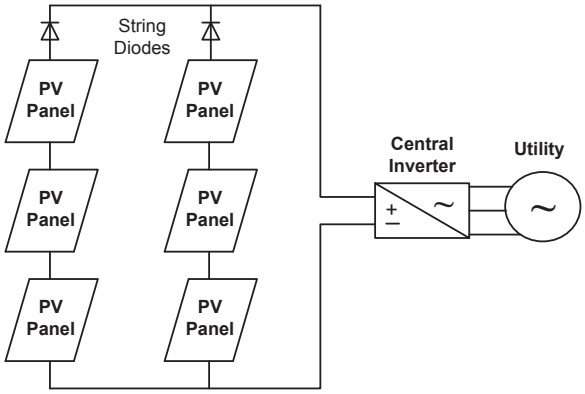

Fig. 3.2 Centralized PV configuration

Fig. 3.3(a) shows the configuration of a string-array PV system. The series of PV panels are connected in the form of a single string. Typically, 15 panels are strung together in series and interconnected through the utility with one inverter per string. The primary advantage of this topology is that there are no losses associated with the string diodes and a maximum power point tracking (MPPT) can be applied for each string. This is especially useful when multiple strings are mounted on fixed surfaces in different operations. The disadvantage to this configuration is the increased cost due to additional inverters.

Fig. 3.3(b) shows the configuration of a multi-string PV system. It has several strings that are interfaced with their own DC/DC inverter for voltage boosting and are then connected to a common DC bus. A common DC/AC inverter is then used for utility interfacing.

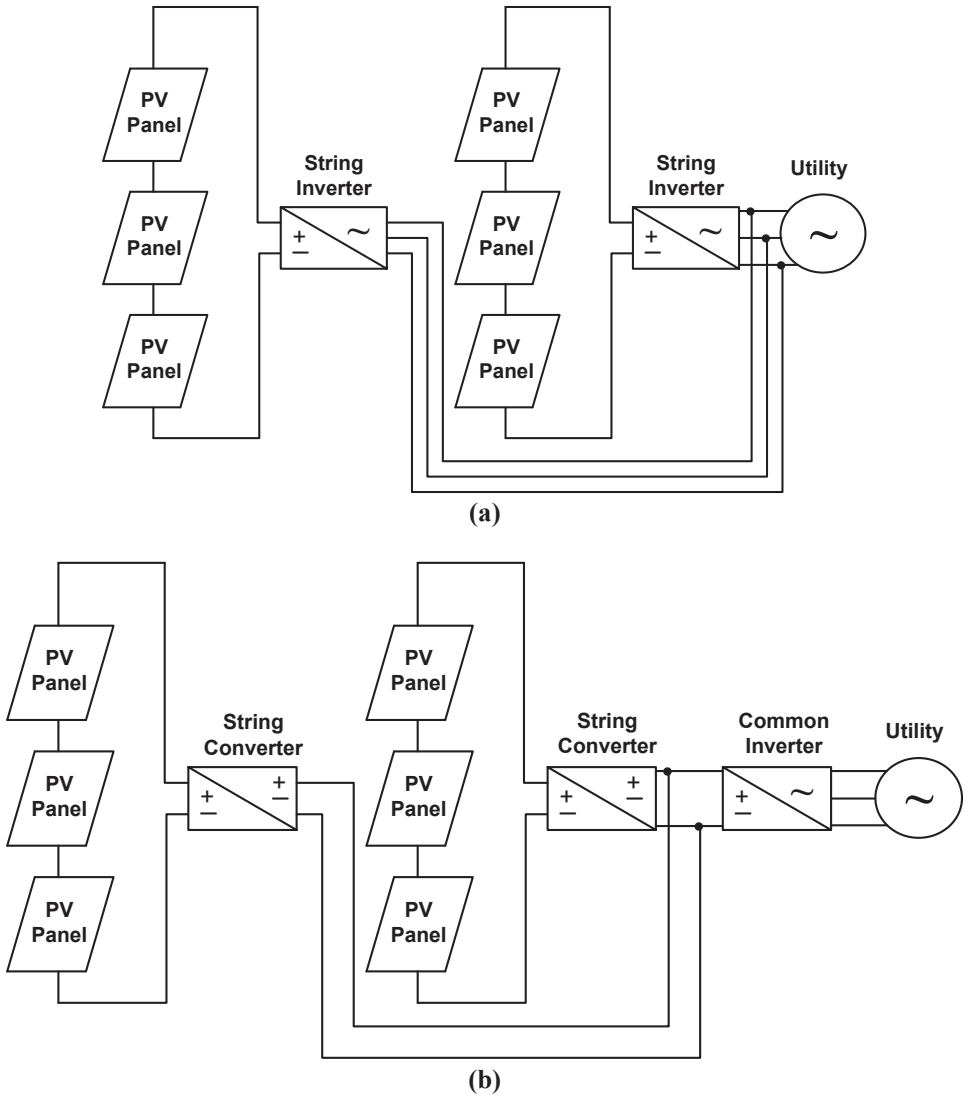

Fig. 3.3(a) PV panels in strings with individual inverters, (b) PV panels in a multi-string configuration

Fig. 3.4 shows a configuration where each PV module has its own inverter. This design is also known as an AC-module. The advantages of this type of configuration are that it is easy to add modules because each module has its own DC/AC inverter and the connection to the utility is made by connecting the inverter AC field wirings together. There is also an overall improvement in system reliability because there is no single-failure for the system. In addition, the power loss of the system is lower due to the reduced mismatch among the modules. This configuration seems to be a promising option for future designs as it can be used as a plug-in device by individuals without specialized knowledge.

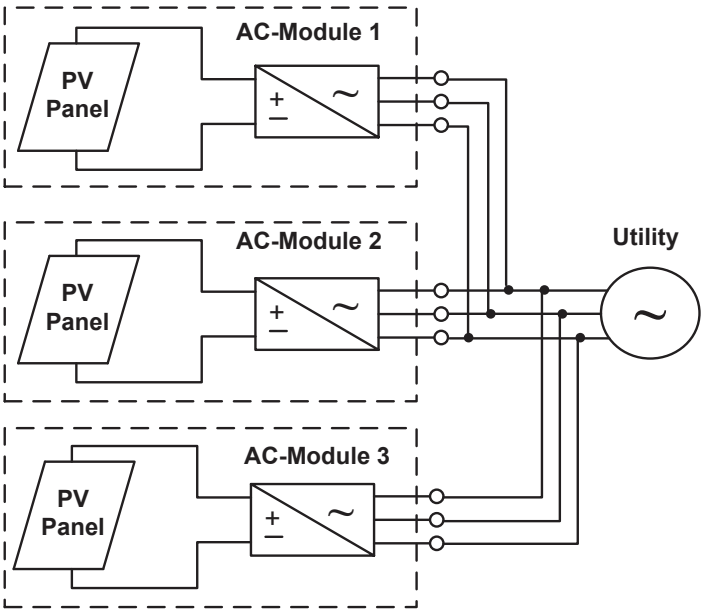

Fig. 3.4 AC-Module power electronics configuration

3.1.2 Power converters and controllers for PV systems

For PV systems, there is no standard PV converter topology. Several useful proposed topologies have been studied and applied [3.4]. The main requirement of power electronic interfaces for the PV systems is to convert the generated DC voltage into a suitable AC for consumer use and utility connection. Generally, the DC voltage magnitude of the PV array is required to be boosted to a higher value by using DC – DC converters before converting them to the utility compatible AC. The DC/AC inverters are then utilized to convert the voltage to AC. Overall, the power electronics topologies for the PV systems can be categorized on the basis of the number of power processing stages, the location of power decoupling capacitors, utilization transformers, and the types of grid interfaces.

A. Single phase – single stage

Fig. 3.5 shows the single-phase single-stage configuration of PV power electronics. It is one of the fundamental topologies for PV system in last decades. The output of the PV array is first connected to a capacitor, which is used to stabilize the DC voltage and filter out the harmonics from the array. The other side on the capacitor is connected to a single-phase full-bridge converter that is connected to a LC filter before connected to

the grid through an isolation transformer. This configuration features several merits including simple structure, low cost, and high reliability. However, severe power losses during partial shadowing are unavoidable because all of the modules are connected to the same MPPT device [3.1].

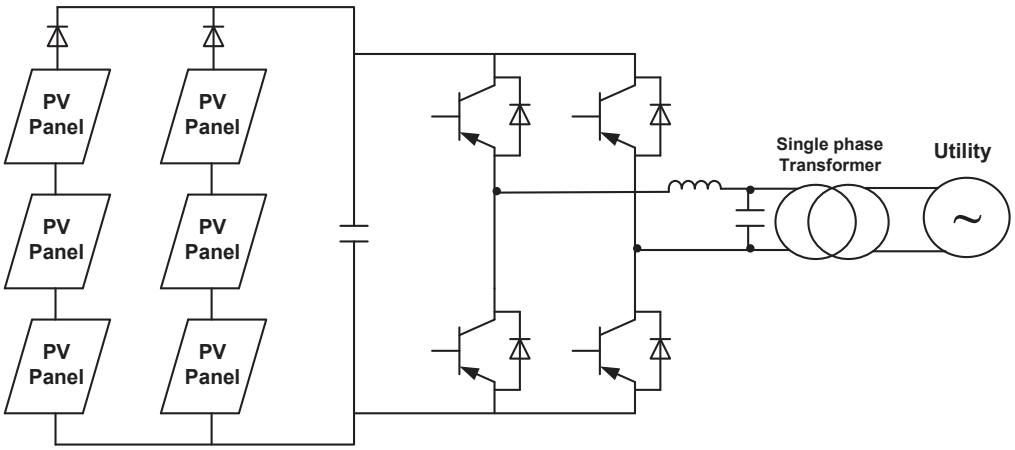

Fig. 3.5 Single-phase single-stage PV power electronics

B. Single phase – Multiple stage

In fact, there is another drawback of the single-phase single-stage configuration that is relatively large size and low efficiency due to the utilization of low-frequency transformers, as shown in Fig. 3.5. In order to address these issues, multistage conversion systems are widely used nowadays. Fig. 3.6 presents a single-phase multistage configuration, which uses a high frequency transformer for a single phase connection to the grid. Since the output of the secondary side of the transformer is high frequency voltage, which cannot be fed back to the grid directly. Therefore, a diode-bride rectifier is employed to convert the high-frequency voltage to DC voltage, and then converted back to AC voltage through an inverter which can match the grid voltage in terms of frequency, phase angle, and amplitude.

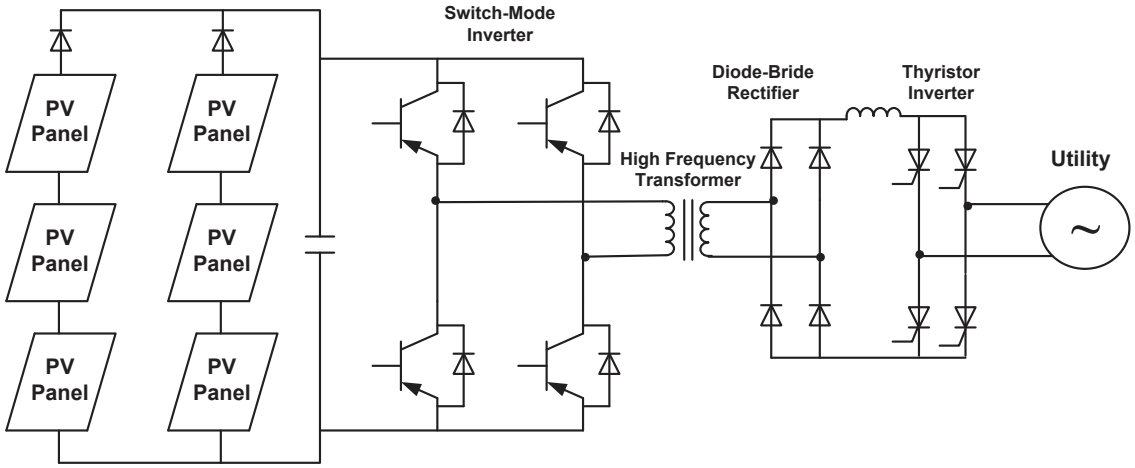

Fig. 3.6 Single-phase multiple-stage PV power electronics

C. Three phase single stage

Recently, the utilization of three-phase inverters in PV system has increased because it is quite suitable for larger system with larger power capacity, this will become more so since the high-voltage high power renewable power system will be the tendency in the near future. Fig. 3.7 shows the three-phase topology for PV system, where a low-frequency three-phase transformer is used. Again, the output of the PV array is connected to a capacitor first before connected to the three-phase inverter. LC filters are also employed here to clear the high frequency harmonics injected into the main grid.

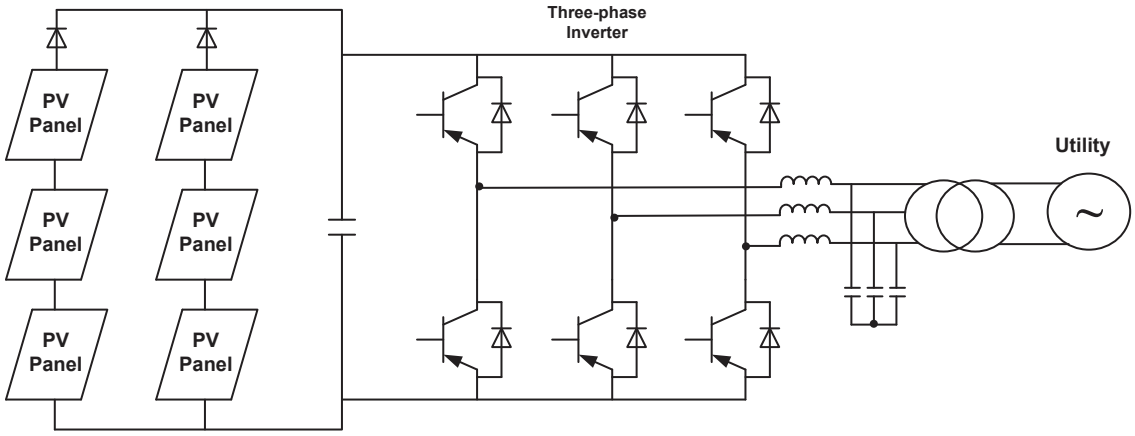

Fig. 3.7 Three-phase PV topology with line-frequency transformer

D. PV Controller

A simplified block diagram of the PV system with the power electronics and control is presented in Fig. 3.8. It consists of a DC/DC converter and a three-phase inverter. The DC/DC converter is based on current-source full-bridge inverter with an embedded

high-frequency transformer and rectifier. The current-source input stage is beneficial since it reduces the requirement for the filter capacitor in parallel with the PV strings. The voltage from the PV string is first converted into a high-frequency AC, and galvanic isolation with voltage boosting is accomplished through the use of a high-frequency transformer. The transformer secondary voltage is then rectified using a full-bridge diode rectifier. After that, the rectified DC is converted into grid compatible AC and connected to the utility by a three-phase voltage-source inverter.

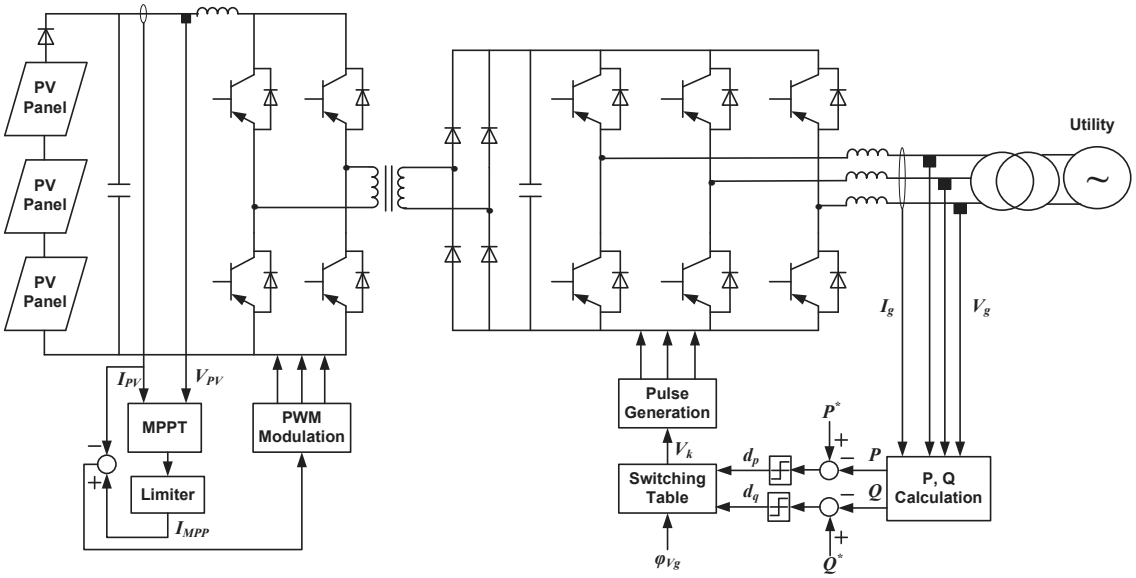

Fig. 3.8 Example of the control scheme for PV systems

Tracking the maximum power point (MPP) of a PV array is usually an essential of a PV system, which will be implemented on DC/DC converter. Over the years, many MPPT methods have been developed and implemented. These methods vary in complexity, required sensors, convergence speed, cost, range of effectiveness, implementation hardware, and popularity, etc. The names of some of these methods are hill climbing, perturb and observe, incremental conductance, fractional open-circuit voltage, fractional short-circuit current, fuzzy logic and neural network control, ripple correlation control, current sweep, DC – link capacitor droop control, load – current or load – voltage maximization, and dP/dV or dP/dI feedback control [3.5].

(1) MPPT control of PV system

A circuit diagram representing the PV cells is illustrated in Fig. 3.9, where the current source I_{pv} represents the photocurrent, I_d the current shunted through the diode, and R_{PVs} and R_{PVsh} are the intrinsic series and shunt resistances of the cell ($R_{sh} >> R_s$).

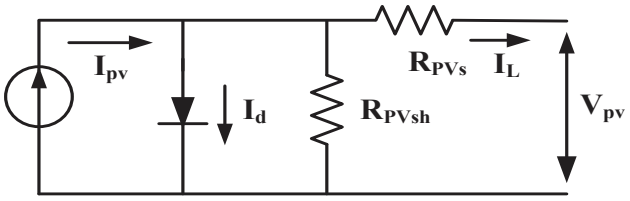

Fig. 3.9 Equivalent circuit of a PV cell

The PV cells are assembled in large units known as PV modules, which are further grouped in a parallel-series configuration to form a PV array. The corresponding mathematical equation that describes the current-voltage characteristics of a PV array can be expressed as [3.6], [3.7]

$$I = N_p I_{pv} - N_p I_{rs}\left[\exp\left(\frac{q}{k\beta A}\frac{V_{dc}}{N_s}\right)-1\right] \tag{3.1}$$

where V_{dc} is the PV array output voltage, I and I_{rs} are the PV array output current and reverse saturation current of a *p-n* junction, respectively, q (=1.602×10^{-19} C) is the unit electric charge, k (=1.38×10^{-23} J/K) the Boltzman's constant, β the p-n junction temperature (in Kelvin), and A the ideality factor. N_s and N_p are the number of cells connected in series and the number of modules connected in parallel, respectively. It is noted that the photocurrent I_{pv} is proportional to the solar irradiation level S and to the cell temperature as

$$I_{pv} = [I_{scr} + k_\beta(\beta - \beta_r)]\frac{S}{100} \tag{2}$$

where β_r is the cell reference temperature, I_{scr} the short-circuit current of one PV cell at the reference temperature and irradiation level, and K_β the temperature coefficient. From (3.1), the power delivered by the PV array can be written as

$$P_{pv} = N_p I_{pv} V_{dc} - N_p I_{rs} V_{dc}\left[\exp\left(\frac{q}{k\beta A}\frac{V_{dc}}{N_s}\right)-1\right] \tag{3.3}$$

Under uniform solar irradiation conditions, PV panels exhibits a unique operating point where PV output power is maximized. Since the PV power characteristic is nonlinear, as shown in Fig. 3.10. It varies with the level of solar irradiation and temperature, which complicates the extraction of maximum power. In order to overcome this problem, several methods for extracting the maximum power have been proposed, which are briefly introduced here.

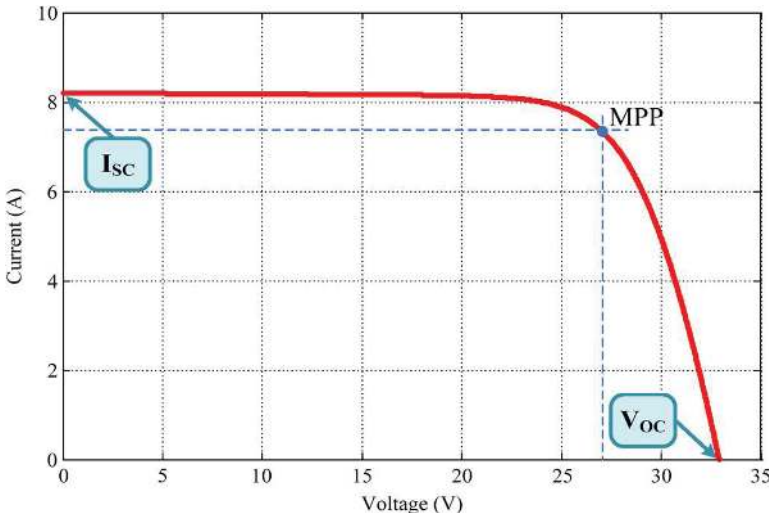

Fig. 3.10 Current versus voltage characteristic of a PV cell. [3.5]

(a) Constant voltage method

Normally the voltage at MPP is around 70% - 80% of the PV open-circuit voltage. Based on this empirical experience, the MPPT can be approximately achieved by controlling the PV output voltage to a specified value. In this method, only the PV voltage is measured, and the control structure is quite simple. However, it must be used in regions where the temperature varies very little because the voltage at the terminals of the module varies when the temperature changes [3.8].

(b) Fixed duty cycle

Another simple approach of MPPT is the fixed duty cycle method. It does not require any feedback, and the load impedance is adjusted only once for the MPP.

(c) MPP locus characterization

The basic principle of this approach is to find a linear relationship between voltage and current at the MPP. This relationship is the tangent line to the MPP locus curve for

the PV current in which the minimum irradiation condition satisfies the sensitivity of the method. Generally the equation given by (3.4) is used to represent the MPP locus curve [3.9]. It is noted that this is just the linear approximation made offline with the PV panel. Besides, it should be updated with the temperature. This can be done by measuring the open-circuit voltage periodically, which means that the interface converter must be disconnected to the PV circuit, resulting in loss of power in these instants [3.9].

$$T_L = \left(\frac{\eta V_T}{I_{MPP}} - N \cdot R_s \right) I_{MPP} + \left[V_{oc} - \eta (V_{Do} + V_T) \right] \tag{3.4}$$

where N is the number of the PV cells, I_{MPP} is the current at MPP, V_T is the temperature voltage, while V_{Do} is the differential voltage.

(d) Beta method

The Beta method is the approximation of the MPP through the equation of an intermediate variable β described as the following [3.10]

$$\beta = \ln\left(\frac{I_{PV}}{V_{PV}} \right) - c \times V_{PV} \tag{3.5}$$

where $c = (q/(\eta \cdot K_B \cdot T \cdot N_s))$ is a constant that depends on the electron charge q, the quality factor of the junction panel η, the Boltzmann constant K_B, temperature T, and the amount of series PV cells N_s.

In this method, the value of β remains almost constant even the operating conditions change. Therefore, β can be continuously calculated using the voltage and current of the panel and inserted on a conventional closed loop with a constant reference. The main drawback of this method is that the PV electrical parameters must be obtained.

(e) Temperature method

One attractive solution is to use a temperature method where the deviation of the MPP due to the variation of temperature can be eliminated [3.11]. In order to fulfill this goal, a low-cost temperature sensor is employed and modifies the MPP algorithm function, maintaining the right track of MPP [3.12].

(f) System oscillation and ripple correlation

This technique uses the oscillations to determine the optimum point of operation, which is quite similar to the hill-climb searching technique of MPPT for wind power

system, as introduced in Chapter 2. At the MPP, the ratio of the amplitude of the oscillation to the average voltage is constant. To implement this method, the doubly grid frequency or the additional low-frequency ripple can be used. However, switching frequencies must be filtered before being acquired in order to avoid wrong switching states and an increase of electromagnetic interference issues [3.13]. Similarly, ripple correlation uses the oscillations in power though all pass filter to obtain the optimal point, i.e., the high-frequency ripples in power and voltage are captured using high-frequency filters, which are then used to compute dP/dV. After that, the sign of this derivative is sent to a signal function to indicate the right region of operation, and an integrator also ensures the MPP [3.14].

(g) P&O and P&O based on PI

The basic idea of the P&O method is to periodically increase or decrease the output terminal voltage of the PV cell and then compare the power obtained in the current cycle with the power of the previous one by checking the sign of dP/dV. If the voltage varies and the power increases, the control system changes the operating point in that direction. Otherwise, it changes the operating point in the opposite direction. After the direction for the change of voltage is obtained, the voltage is varied at a constant rate [3.15], [3.16]. A modified operation can be obtained when the steps are changed according to the distance of the MPP, resulting in higher efficiency.

It is noted that in steady state, the operation point is not altered unless changes in environmental conditions happen. The key is to reduce the dP/dV to zero using a closed-loop control performing the P&O based on PI.

(2) Grid-side inverter control of PV system

As all these MPPT approaches mentioned above are quite mature and already implemented in practical application, therefore, MPPT of PV systems is not the main focus in this chapter. In this chapter, we concentrate on control of the grid-side inverter of the PV system.

In a distributed generation system, there are generally two operation modes, namely, islanded mode and grid-connected mode. In islanded mode, the DG sources and the local loads form an isolated small power system, where the loads are totally powered by the DG units. In this case, the inverters are controlled to convert the DG energy to AC

power for the local loads, by establishing a stable voltage at the point of common coupling (PCC). In islanded operation, generally an inductive/capacitive (LC) filter is required to filter the pulse width modulation (PWM) ripple from the inverters in order to establish a satisfactory voltage waveform. If the power generated within the distributed generation system is greater than the local load demand, these DG units should be able to achieve grid synchronization and connection. A basic requirement here is that the transfer process from islanded operation to grid-connected mode should be as fast as possible, and not have any negative effect on the utility grid or the microgrid [3.17]-[3.20]. After grid connection, the inverters should be controlled to achieve flexible power regulation. The relevant IEEE standard does not currently allow a distributed generation system to actively regulate the voltage at the PCC, and recommends that low-power systems should be disconnected when the grid voltage is lower than 0.85 pu or higher than 1.1 pu, as an anti-islanding requirement [3.21], [3.22]. Despite this, in the future, if individual distributed generation systems like microgrids can be allowed to flexibly regulate active and reactive power, they could also be used to provide voltage support and power quality improvement at the system low voltage distribution level [3.23]-[3.25].

Some recent work has investigated the control of inverters in islanded operation with a particular focus on uninterruptible power supply (UPS) application, including deadbeat control [3.26], [3.27], adaptive control [3.28], multiloop feedback control [3.29]-[3.31], etc. Most of these schemes use the output voltage and currents with outer and inner control loops, requiring proportional-integral (PI) regulators, which complicate the control system, and require significant tuning effort in practical implementation. Recently a model predictive control strategy was proposed to control inverters in islanded operation [3.32]. In this work, there is no need for internal current-control loops, no modulators, and the scheme is easy to implement.

Some effort has also been paid to grid-connected operation. Direct power control (DPC), derived from direct torque control (DTC) of AC machines, has become one of the most popular control strategies of grid-connected inverters because of its simplicity and excellent dynamic response. However, large power ripple is the main drawback of the conventional switching DPC, leading to distorted line currents [3.33]-[3.35]. Recently some improved DPC methods have been developed for better performance [3.36]-[3.38]. More recently, predictive control techniques appear to be an attractive alternative for the control of power converters, among which model predictive control

(MPC) has attracted much attention, predominantly because it has a flexible control scheme that allows the easy inclusion of system constraints and nonlinearities. In this control, a model is used to predict the system behavior, and a cost function is employed as a criterion to select the optimal switching states. The control objectives of MPC can vary considerably according to the applications. For example, the control objective is the inverter output voltage for an UPS system in [3.32], while in other applications, the objectives become the active and reactive powers in [3.39] and [3.40] for rectifiers, the currents in [3.41] and [3.42] for inverters, and the electromagnetic torque in [3.43], [3.44] for electric drives. Despite these systems, so far the literature reports very little on flexible power regulation for grid-connected inverters using MPC strategies.

Though many control methods have been developed to control inverters for distributed generation systems, the majority of these methods only focus on one specific operation mode, and the literature seldom presents a general control strategy of inverters targeted at microgrid applications. Here we propose a MPC strategy of inverters for PV systems in microgrid application, which is sufficiently flexible to achieve islanded operation, seamless transfer, and grid-connected operation.

3.2 Islanded Operation

3.2.1 System model

For a three-phase two-level inverter, determined by the switching states, the inverter output voltage $\boldsymbol{V}_i$ can be controlled to eight vectors, as shown in Fig. 3.11, which can be expressed in complex space vectors as

$$\boldsymbol{V}_i = \begin{cases} \frac{2}{3} V_{dc} e^{j(i-1)\frac{\pi}{3}} & (i = 1 \cdots 6) \\ 0 & (i = 0, 7) \end{cases} \tag{3.6}$$

A three-phase inverter based PV system considered in this paper is shown in Fig. 3.12.

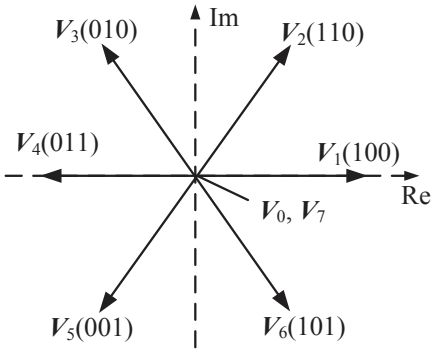

Fig. 3.11 Inverter possible output voltage vectors

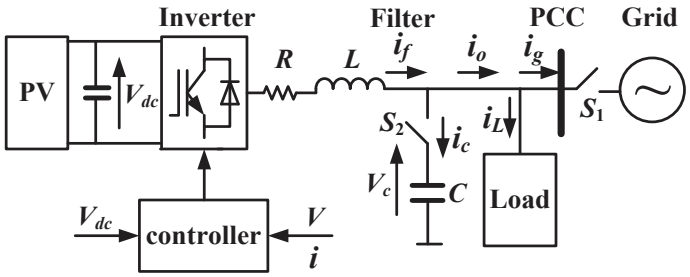

Fig. 3.12 One-phase model of inverter-based PV system

In islanded operation, the static transfer switch S_1 is off while the bypass switch S_2 is on. The PV system supplies the power to the local load. In this scenario, the dynamic behavior of the capacitor of the LC filter can be expressed as

$$C\frac{d\boldsymbol{V}_c}{dt} = \boldsymbol{i}_f - \boldsymbol{i}_L \tag{3.7}$$

where C is the filter capacitance, $\boldsymbol{V}_c$ the capacitor voltage vector, $\boldsymbol{i}_f$ the inductor current vector, and $\boldsymbol{i}_L$ the load current vector ($\boldsymbol{i}_o = \boldsymbol{i}_L$). On the other hand, the behavior of the inductor of the LC filter can be described as

$$\boldsymbol{V}_i = \boldsymbol{V}_c + \boldsymbol{i}_f R + L\frac{d\boldsymbol{i}_f}{dt} \tag{3.8}$$

where R and L are the filter resistance and filter inductance, respectively.

3.2.2 Voltage control in islanded mode

A. Basic principle of MPC

Generally the MPC controller can be divided into three components, namely, system predictive model, cost function and parameters design [3.44], as illustrated in Fig. 3.13. Firstly, MPC strategies are usually formulated in a discrete-time setting with a fixed sampling interval. Thus the system model can be expressed as a state-space model, the output of which is determined by the input, the current state of the model, and the discrete interval. In this way, the future behavior of the system can be predicted until a certain horizon of time. Secondly, the power converter or drive control problem can be defined as the determination of an appropriate control action that will drive a generic system variable $x(t)$ as close as possible to a desired reference value $x^*(t)$. Therefore, a cost function over a finite horizon of length N is utilized to evaluate each switching state, the one minimizing the error between $x(t)$ and $x^*(t)$ will be selected for the next sampling period. Finally, as MPC allows the easy inclusion of system constraints and nonlinearities of the system by revising the cost function, a proper weighting factors selection is essential to obtain satisfactory performance by taking different control objectives into account. In addition, sampling interval, horizon length N, and constraints selection should also be considered in parameters design, according to different applications.

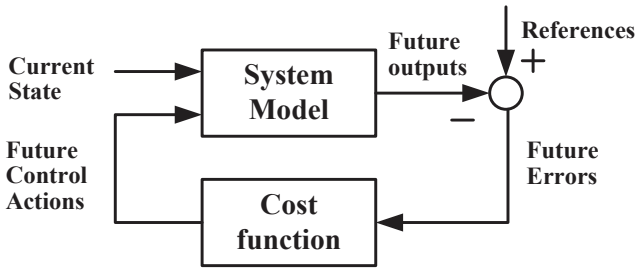

Fig. 3.13 Basic principle of MPC

B. Voltage control based on MPC

For voltage control in islanded mode, the inverter should be controlled to establish a stable PCC voltage for the local loads without the power supply from the grid, therefore, the essential of voltage control based on MPC is to predict the future behavior of the capacitor voltage V_c. The block diagram of the voltage control based on MPC is illustrated in Fig. 3.14.

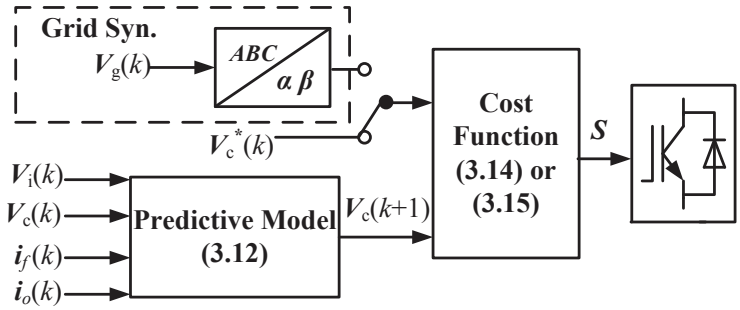

Fig. 3.14 Block diagram of voltage control

Combining (3.7) and (3.8), the system LC filter can be rewritten as a state-space system as

$$\frac{d\boldsymbol{x}}{dt} = A\boldsymbol{x} + BV_i + B_d\boldsymbol{i}_o \tag{3.9}$$

where

$$\boldsymbol{x} = \begin{bmatrix} \boldsymbol{i}_f \\ \boldsymbol{V}_c \end{bmatrix} \tag{3.10}$$

$$A = \begin{bmatrix} -R/L & -1/L \\ 1/C & 0 \end{bmatrix}$$

$$B = \begin{bmatrix} 1/L \\ 0 \end{bmatrix}$$

$$B_d = \begin{bmatrix} 0 \\ -1/C \end{bmatrix}$$

Since the sampling time T_s is very small, assume

$$e^{AT_s} = 1 + AT_s + \frac{(AT_s)^2}{2!} + \cdots + \frac{(AT_s)^n}{n!} \approx 1 + AT_s \tag{3.11}$$

Therefore, the discrete-time model of the filter of (3.7) for a sampling time T_s can be expressed as [3.32]

$$\boldsymbol{x}(k+1) = A_q \boldsymbol{x}(k) + B_q \boldsymbol{V}_i(k) + B_{dq} \boldsymbol{i}_o(k) \tag{3.12}$$

$$A_q = e^{AT_s}$$

$$B_q = \int_0^{T_s} e^{A\tau} d\tau$$

$$B_{dq} = \int_0^{T_s} e^{A\tau} B_d d\tau$$

Therefore, the capacitor voltage at $(k+1)^{th}$ instant can be predicted as

$$V_c(k+1) = V_c(k) + e^{T_s/C} i_f(k) + \frac{C(e^{T_s/C} - 1)}{L} V_i(k) - \frac{T_s}{C} i_o(k) \tag{3.13}$$

To minimize the error in the PCC voltage, a cost function

$$J = \sqrt{(V_{c\alpha}^* - V_{c\alpha}^{k+1})^2 + (V_{c\beta}^* - V_{c\beta}^{k+1})^2} \tag{3.14}$$

where $V_{c\alpha}$ and $V_{c\beta}$ are the real and imaginary components of the PCC voltage, respectively, is used to evaluate the possible voltage vectors.

C. Seamless transfer

According to (3.14), the PCC voltage can track its reference because the α and β components are tightly controlled using the cost function (3.14). Based on this analysis, it can be expected that the grid synchronization can be achieved by replacing the PCC referenced voltage $\boldsymbol{V}_c^*$ with the grid voltage $\boldsymbol{V}_g$, as illustrated in Fig. 3.14. Therefore, the cost function can be revised as

$$J = \sqrt{(V_{g\alpha}^* - V_{c\alpha}^{k+1})^2 + (V_{g\beta}^* - V_{c\beta}^{k+1})^2} \tag{3.15}$$

Using (3.15), the PCC voltage can match the grid voltage in terms of phase angle, amplitude and frequency tightly. When the grid synchronization process is completed, the PV system is ready for grid connection.

D. Discrete-time digital implementation of MPC

It is noted that one-step delay will be caused by the time needed for performing the calculation in digital implementation. It is necessary to compensate this one step delay for model predictive control. Otherwise, the system performance will be deteriorated [3.40], [3.41]. This has been discussed in details using Fig. 2.15 of Chapter 2.

One of the most effective methods to predict the system state in the next time instant is model based prediction. In islanded operation, $\boldsymbol{V}_c^{k+1}$ can be first predicted using (3.13), and similarly, $\boldsymbol{V}_c^{k+2}$ can be predicted with $\boldsymbol{V}_c^{k+1}$ as a new initial state and $\boldsymbol{V}_i^{k+1}$ as input using (3.13) again. In order to eliminate the one-step delay influence, in islanded operation, the cost function (3.14) should be revised as

$$J = \sqrt{(V_{c\alpha}^{*} - V_{c\alpha}^{k+2})^2 + (V_{c\beta}^{*} - V_{c\beta}^{k+2})^2} \tag{3.16}$$

In grid synchronization, the cost function (3.15) should be revised as

$$J = \sqrt{(V_{g\alpha}^{*} - V_{c\alpha}^{k+2})^2 + (V_{g\beta}^{*} - V_{c\beta}^{k+2})^2} \tag{3.17}$$

3.3 Grid-connected Operation

Current IEEE standards do not allow a distributed generation system to actively regulate the voltage at the point of common coupling (PCC), but in the future, if individual DG systems are allowed to flexibly regulate active and reactive power, they can also be used to provide voltage support and improve power quality at the system low voltage distribution level [3.23]-[3.25]. In this case, flexible power regulation capability for a DG unit becomes more and more significant. Here, after the PV system is connected to the grid, the inverter should be controlled to achieve flexible power regulation. For the predictive approaches, here, a MPC strategy for grid-connected inverter is developed.

3.3.1 Flexible power regulation

In grid-connected operation, the static transfer switch S_1 is on while the bypass switch S_2 is off. The inverter is connected to the grid through the line inductor, and the

PV system supplies the power to the local load together with the grid. The excess power generated by the PV system will be exported to the grid.

In grid-connected mode, the mathematical model of the system can be expressed as

$$\boldsymbol{i}_f = \boldsymbol{i}_o \tag{3.18}$$

$$\boldsymbol{i}_o = \boldsymbol{i}_L + \boldsymbol{i}_g \tag{3.19}$$

$$\boldsymbol{V}_i = \boldsymbol{V}_g + \boldsymbol{i}_o R + L\frac{d\boldsymbol{i}_o}{dt} \tag{3.20}$$

where $\boldsymbol{V}_\mathrm{g}$ is the grid voltage vector, and $\boldsymbol{i}_\mathrm{g}$ the current vector injected into the grid. On the other hand, the inverter instantaneous output active and reactive powers can be written as

$$P = \frac{3}{2}\mathrm{Re}\{\boldsymbol{V}_g \boldsymbol{i}_o^*\} = \frac{3}{2}\left(V_{g\alpha} i_{o\alpha} + V_{g\beta} i_{o\beta}\right) \tag{3.21}$$

$$Q = \frac{3}{2}\mathrm{Im}\{\boldsymbol{V}_g \boldsymbol{i}_o^*\} = \frac{3}{2}\left(V_{g\beta} i_{o\alpha} - V_{g\alpha} i_{o\beta}\right) \tag{3.22}$$

where * denotes conjugate of the vector. The active and reactive power derivatives can be derived from (3.21) and (3.22) as

$$\frac{dP}{dt} = \frac{3}{2}\left(\frac{dV_{g\alpha}}{dt} i_{f\alpha} + V_{g\alpha}\frac{di_{f\alpha}}{dt} + \frac{dV_{g\beta}}{dt} i_{f\beta} + V_{g\beta}\frac{di_{f\beta}}{dt}\right) \tag{3.23}$$

$$\frac{dQ}{dt} = \frac{3}{2}\left(\frac{dV_{g\beta}}{dt} i_{f\alpha} + V_{g\beta}\frac{di_{f\alpha}}{dt} - \frac{dV_{g\alpha}}{dt} i_{f\beta} - V_{g\alpha}\frac{di_{f\beta}}{dt}\right) \tag{3.24}$$

Assume sinusoidal and balanced grid line voltage, or

$$\boldsymbol{V}_g = V_g + jV_g = |\boldsymbol{V}_g| e^{j\omega t} \tag{3.25}$$

where ω is the grid voltage frequency. The following expression can be deduced from (3.25) as

$$\frac{dV_{g\alpha}}{dt} = -\omega \cdot V_{g\beta} \tag{3.26}$$

$$\frac{dV_{g\beta}}{dt} = \omega \cdot V_{g\alpha} \tag{3.27}$$

On the other hand, in grid-connected mode, (3.8) becomes

$$\boldsymbol{V}_i = \boldsymbol{V}_g + \boldsymbol{i}_f R + L\frac{d\boldsymbol{i}_f}{dt} \tag{3.28}$$

The instantaneous active and reactive power derivations can then be obtained by substituting (3.26), (3.27) and (3.28) into (3.23) and (3.24) as

$$\frac{dP}{dt} = -\frac{R}{L}P - \omega Q + \frac{3}{2L}\left(\mathrm{Re}\left(\boldsymbol{V}_g \boldsymbol{V}_i^*\right) - \left|\boldsymbol{V}_g\right|^2\right) \tag{3.29}$$

$$\frac{dQ}{dt} = \omega P - \frac{R}{L}Q + \frac{3}{2L}\mathrm{Im}\left(\boldsymbol{V}_g \boldsymbol{V}_i^*\right) \tag{3.30}$$

The predictive power at the end of the sampling period T_s can be expressed as

$$P^{k+1} = T_s\left[-\frac{R}{L}P - \omega Q + \frac{3}{2L}\left(\mathrm{Re}\left(\boldsymbol{V}_g \boldsymbol{V}_i^*\right) - \left|\boldsymbol{V}_g\right|^2\right)\right] + P^k \tag{3.31}$$

$$Q^{k+1} = T_s\left[\omega P - \frac{R}{L}Q + \frac{3}{2L}\mathrm{Im}\left(\boldsymbol{V}_g \boldsymbol{V}_i^*\right)\right] + Q^k \tag{3.32}$$

However, it can be seen that the prediction based on power derivatives using (3.31) and (3.32) are very complicated, making it not easy to implementation. Here, a simpler prediction scheme is developed. The discrete-time model of (3.28) can be expressed as

$$\boldsymbol{i}_f(k+1) = T_s\left(\boldsymbol{V}_i(k) - \boldsymbol{V}_g(k) - \boldsymbol{i}_f(k)R\right)/L + \boldsymbol{i}_f(k) \tag{3.33}$$

Assuming the constant grid voltage during the sampling period, $P(k+1)$ and $Q(k+1)$ can then be calculated by substituting (3.33) into (3.21) and (3.22).

Then evaluate the effects of each voltage vector on active and reactive power and select the one producing the least power ripples according to a specific cost function. In this work, the cost function is defined as

$$J = \sqrt{(P^* - P^{k+1})^2 + (Q^* - Q^{k+1})^2} \tag{3.34}$$

The control block of grid-connected operation is shown in Fig. 3.15.

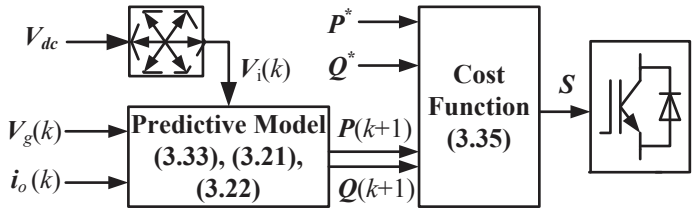

Fig. 3.15 Block diagram of MPC-based power regulation

Once again, as explained previously, one-step delay influence needs to be eliminated. Similar to the previous section, a two-step prediction is employed. $\boldsymbol{i}_f^{k+1}$ is first obtained from (3.28) and then similarly, $\boldsymbol{i}_f^{k+2}$ can be predicted with $\boldsymbol{i}^{k+1}$ as new initial state and $\boldsymbol{V}_i^{k+1}$ as the input. Finally P^{k+2} and Q^{k+2} can be obtained from (3.21) and (3.22). Consequently, the cost function in (3.34) should be revised as follows

$$J = \sqrt{(P^* - P^{k+2})^2 + (Q^* - Q^{k+2})^2} \tag{3.35}$$

3.3.2 Switching frequency reduction

In MPC, the most appropriate vector is chosen based on an optimization criterion. However, this depends on whether the state of the system is transient or steady [3.42]. In dynamic response, the power error should be minimized as much as possible in order to obtain fast dynamics. Then evaluate the effects of each voltage vector on active and reactive power and select the one producing the least power ripples according to a specific cost function. In steady state, the goal is to obtain the minimum possible state changes in order to maximally reduce the switching frequency. In power conversion, particularly in high-power applications, the efficiency is essential. Without deteriorating the system performance, the lower the switching frequency, the lower the switching power loss, i.e. the higher the efficiency.

In this work, in order to reduce the switching frequency, the expression of cost function (3.35) can be revised as

$$\begin{aligned} J = &\sqrt{(P^* - P^{k+2})^2 + (Q^* - Q^{k+2})^2} \\ &+ \lambda_2 \left(\sum_{i=a,b,c} \left| D_i^{k+1} - D_i^k \right| \right) \end{aligned} \tag{3.36}$$

where $D_{\mathrm{i}}^{\mathrm{k+1}}$ and $D_{\mathrm{i}}^{\mathrm{k}}$ represent the switching state of the rectifier leg i (i=a,b,c) at the current and the next control periods, respectively, D_{i} = 0 or 1, with 0 meaning that the upper transistor is off and the lower one is on, while 1 indicates the inverse switching state, and λ_2 is the weighting factor. The first term in (3.36) is dedicated to achieve power ripple reduction and reference tracking, and the second term contributes to the objective of switching frequency reduction. A large value of the weighting factor λ_2 implies a greater priority to this objective. Therefore, by defining the cost function as (3.36), the switching frequency can be taken into account. One should bear in mind that

eight possible vectors should be evaluated in (3.36) for switching frequency reduction, although only seven possible vectors would be enough for (3.34) because the effects of $\boldsymbol{V}_0$ and $\boldsymbol{V}_7$ are the same without considering switching frequency reduction.

3.4 Numerical Simulation and Experimental Verification

3.4.1 Numerical simulation

The proposed control strategy for inverters is tested in simulation using MATLAB/Simulink. The system parameters are listed in Table 3.1. At 0.05 s, the control system starts to operate, and the grid synchronization begins at 0.15 s. The inverter is connected to the grid at 0.2 s with P^* = 0 W and Q^* = 0 VAR initially.

TABLE 3.1 System Parameters of the PV System

Line resistance		R	0.51 Ω
Line inductance		L	4.8 mH
Line capacitor		C	36 uF
Phase-phase Voltage		e	133 V(rms)
Grid voltage frequency		f	50 Hz
DC-link voltage		V_{dc}	250 V
Sampling period		Ts	40 μs
Local load	R_L		864 W

A. Voltage control in islanded mode

Fig. 3.16 shows the PCC voltage and load current in islanded operation. It can be seen that a stable PCC voltage is established very quickly, and it is sinusoidal with low distortion (THD = 2.54%). The grid synchronization process and grid connection are presented in Fig. 3.17. From top to bottom, the waveforms are PCC voltage, grid voltage, and inverter output currents, respectively. It can be seen that the PCC voltage can match the grid voltage in less than 1 ms once the grid synchronization algorithm starts to operate. After the PCC voltage is synchronized with the grid voltage in terms of amplitude, frequency and phase angle, the PV system is connected to the grid through the static transfer switch and the capacitor of the LC filter is bypassed at 0.15 s.

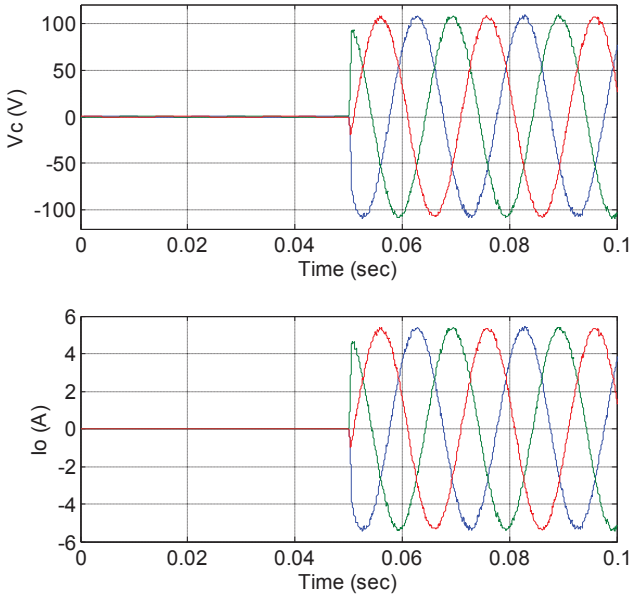

Fig. 3.16 Simulation results of PCC voltage and load current.

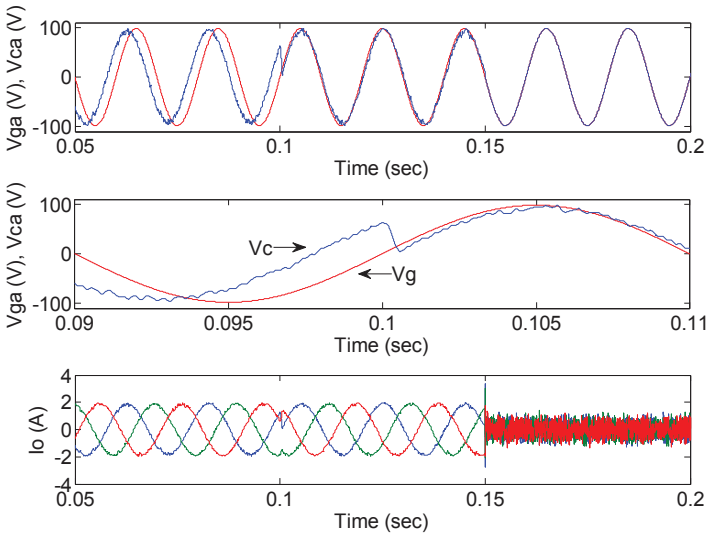

Fig. 3.17 Simulation results of grid synchronization and connection

B. Flexible power regulation in grid-connected mode

Since the conventional switching table based direct power control (SDPC) [3.34] has had a significant impact and is commonly used, we use it as a benchmark to compare with the proposed MPC strategy.

Fig. 3.18 compares the system dynamic responses during various active and reactive power steps for the SDPC and the proposed MPC strategy, respectively. Initially the

reactive power is set to 0 VAR while the active power is stepped from 0 W to -2 kW at 0.22 s and back to 0 W at 0.24 s. After that, the active power is kept at 0 W while the reactive is stepped to 1 kVAR and -1 kVAR, respectively. Because of the merit of direct control method, SDPC presents excellent transient performance, as shown in Fig. 3.18(a). On the other hand, the proposed MPC strategy also shows excellent dynamic response. The proposed MPC strategy presents even better references tracking ability than that of SDPC around 0.24 s and around 0.26 s, as shown in Fig. 3.18(b).

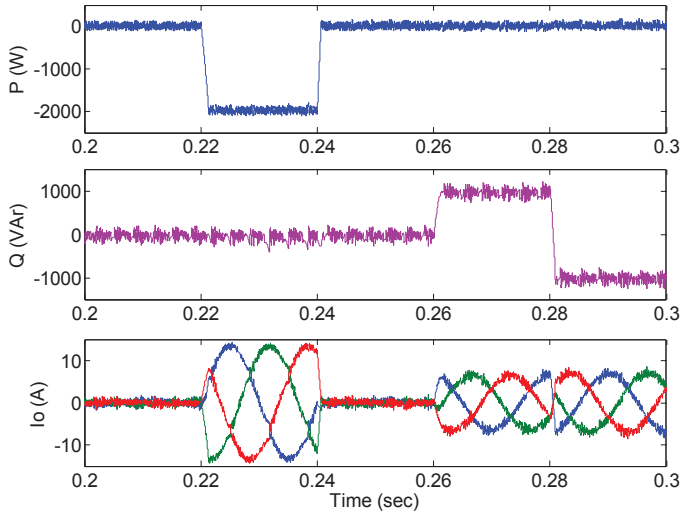

(a)

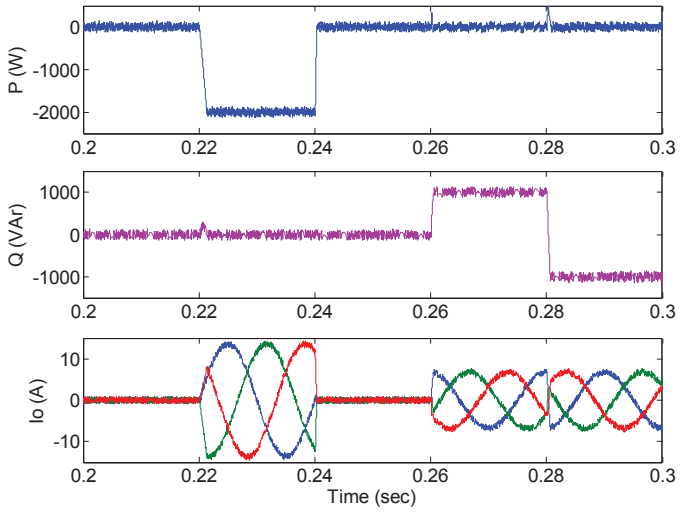

(b)

Fig. 3.18 Simulation results of flexible power regulation. (a) SDPC, (b) proposed MPC strategy.

3.4.2 Experimental verification

The proposed control strategy has been further validated by experiments using a laboratory PV system setup. The hardware configuration is shown in Fig. 3.19. It consists of the following devices: a Semikron intelligent power module (IPM) as the inverter, a TMS320F28335 floating-point DSP used for the control, a XANTREX DC power supply used to simulate the PV panels, a three-phase LC filter, and a three-phase isolated transformer to increase the inverter output voltage to 415V. The system parameters are the same as simulation.

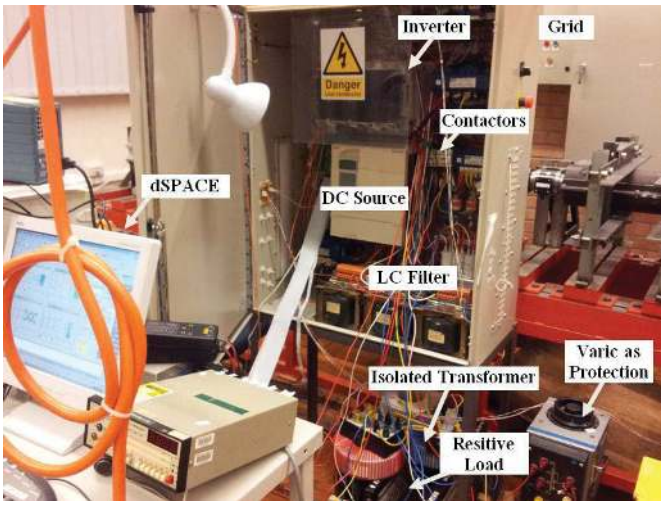

Fig. 3.19 Laboratory test bench.

A. Islanded mode

In the islanded operation, the static transfer switch S1 is off while the bypass switch S2 is on. Fig. 3.20 presents the experimental results of islanded operation. From top to bottom, the curves are PCC voltage, load current, and inductor current of the *LC* filter, respectively. It can be seen that the experimental results are in good agreement with the simulation. The PCC voltage was established quickly and is very stable. Due to the resistive load, the load current is proportional to the PCC voltage. The inductor current presents high-frequency harmonics which are attenuated by the filter.

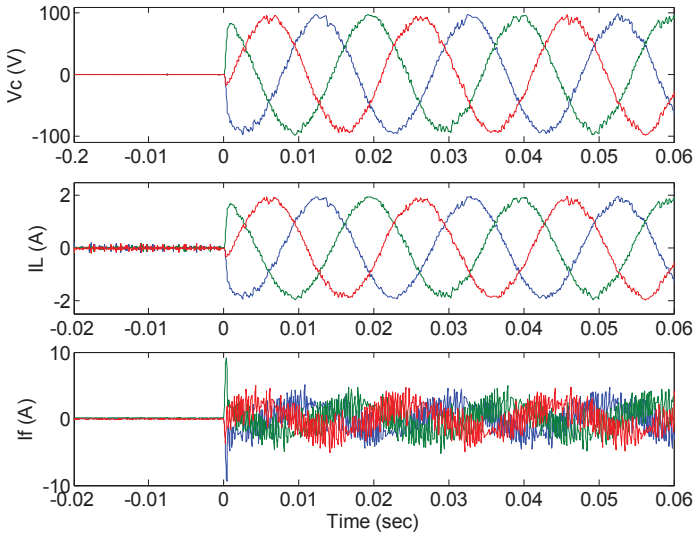

Fig. 3.20 Experimental results of islanded mode.

Fig. 3.21 shows the waveforms of the PCC voltage and grid voltage. Once the grid synchronization process begins, the two curves are in close agreement in phase, frequency, and magnitude.

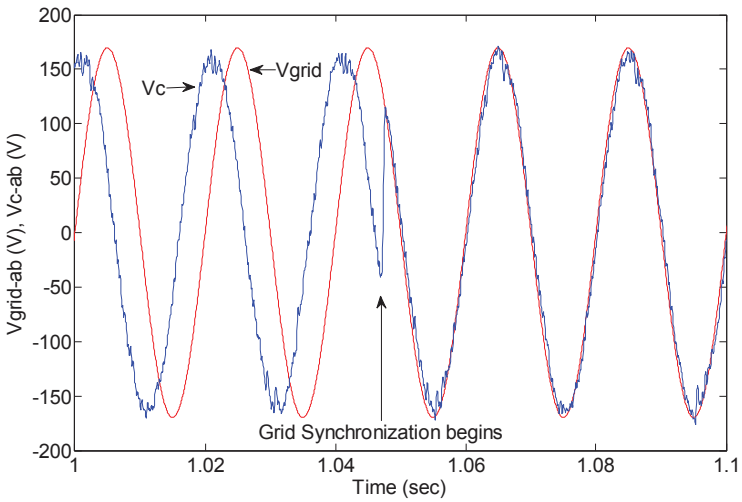

Fig. 3.21 Experimental results of grid synchronization.

B. Grid-connected mode

After the successful grid connection, the PV system can switch to the flexible power regulation mode; i.e. the PV system can supply power to the local load and the grid flexibly. If the power generated is less than the local load demand, more power would be imported from the grid. On the other hand, if the power generated is larger than the

local load demand, the excess will be exported to the grid. Fig. 3.22(a)-(d) show the dynamic response of SDPC and the proposed MPC strategy. Again, it can be seen the experimental results are in good agreement with the simulation, and both methods present excellent transient performance. It should be noted that the active and reactive powers shown in Fig. 3.22 are the PV inverter output power, not the power exchanged between the main grid and the microgrid. For example, in Fig. 3.22(a) and Fig. 3.22(c), the PV system generated 2 kW active power (-2 kW means power is flowing out from the PV system), the local load consumed $\sqrt{3} \times (120 / R_L)^2 = 288$ W active power, and there is about 1.712 kW active power fed to the grid from the PV system.

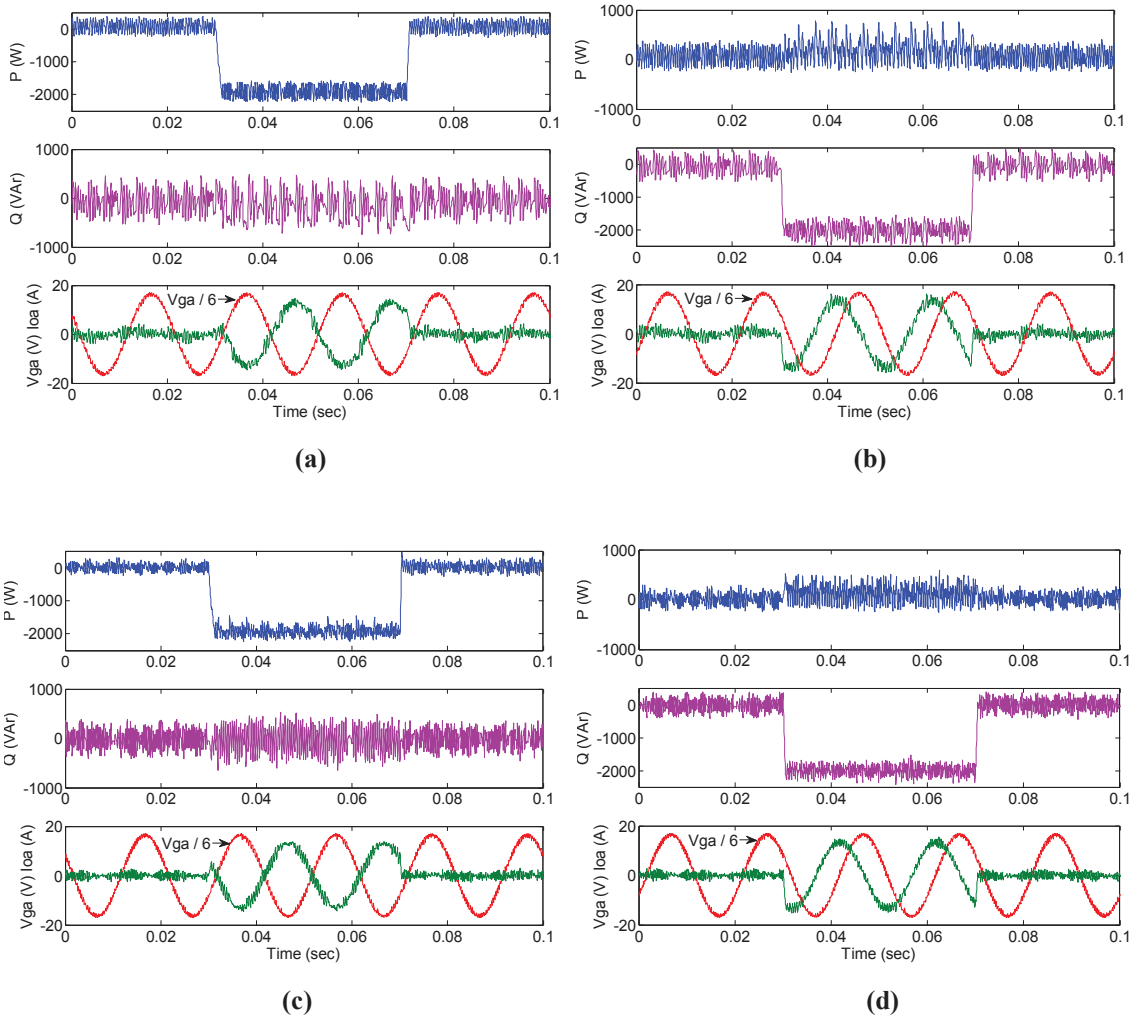

Fig. 3.22 Experimental results of flexible power regulation. (a) active power steps of SDPC, (b) reactive power steps of SDPC, (c) active power steps of proposed MPC strategy, (d) reactive power steps of proposed MPC strategy.

C. Comprehensive comparison

In order to obtain a better understanding of the whole proposed MPC strategy, the quantitative results of the different strategies are summarized in Table 3.2. Firstly, compared to SDPC, the MPC controller selects the most appropriate voltage vector based on a cost function rather than choosing the vector according to a look-up table. It can be seen that the performance of the proposed MPC strategy using (3.34) is better than that of SDPC, which is as expected. After the one-step delay compensation scheme is employed, i.e. using (3.35), the system performance is improved greatly, and is much better than that of SDPC. Furthermore, if the switching frequency reduction is also introduced to the cost function, i.e. using (3.36), the average switching frequency is reduced considerably to only 1053 Hz. It is noted that an additional term can be added to the cost function (3.36) to reduce the power ripples while low switching frequency can be maintained [3.45], which is not discussed in detail here.

TABLE 3.2 Quantitative Comparison of Steady-state Performance of PV System

Strategy	f_s (Hz)	f_{sw} (Hz)	THD (%)	P_{rip} (W)	Q_{rip} (Var)
STDPC	20 k	3018	9.35	80.68	115.23
MPC (3.34)	20 k	2450	9.01	97.55	98.43
MPC (3.35)	20 k	3164	6.02	70.71	82.94
MPC (3.36)	20 k	1053	25.59	379.64	172.29

Finally, it is worth mentioning that the optimization of the weighting factor λ_2 and λ_3 is out of scope of this research. This specific research topic combined with the knowledge of mathematics and optimization design is investigated in some other research areas such as [3.46].

3.5 Summary of the Chapter

This Chapter proposes a model predictive control strategy for PV system inverters. The first contribution of this work is that this strategy can be used as a general control approach in microgrid applications in terms of islanded mode, grid synchronization, and grid-connected operation. By changing the cost function appropriately, different control objectives can be fulfilled. In the islanded mode, the control objectives are the α and β components of the voltage. In order to achieve grid connection, the voltage reference in

the cost function can be replaced by the grid voltage without changing the control structure. After connecting to the grid, the system can be controlled to generate flexibly any amount of active and reactive power within its capacity. The second contribution of this work is to develop a suitable one-step delay compensation scheme for this proposed model predictive control strategy, which is very useful in practical digital implementation. Last but not the least, an effective switching frequency reduction algorithm is proposed, which is very attractive for maximizing the efficiency of large capacity renewable energy generation systems.

References

[3.1] W. Kramer. S. Chakraborty, B. Kroposki, and H. Thomas, *Advanced Power Electronic Interfaces for Distributed Energy Systems – Part 1: Systems and Topologies*, Technical Report, NREL/TP-581-42672, March 2008.

[3.2] K. H. Hussein, I. Muta, T. Hoshino, and M. Osakada, "Maximum photovoltaic power tracking: An algorithm for rapidly changing atmospheric conditions," *Proc. Inst. Elect. Eng., Gen., Transm., Distrib.,* vol. 142, no. 1, pp. 59–64, 1995.

[3.3] A. Yazdani and P. P. Dash, "A control methodology and characterization of dynamics for a photovoltaic (PV) system interfaced with a distribution network," *IEEE Trans. Power. Delivery.,* vol. 24, no. 3, pp. 1538–1551, 2009.

[3.4] B. Kjaer, J. K. Pedersen, and F. Blaabjerg, "A review of single-phase grid-connected inverters for photovoltaic modules," *IEEE Trans. Ind. Appl.,* vol. 41, no. 5, pp. 1292-1306, Sep./Oct. 2005.

[3.5] M. A. G. de. Brito, L. Galotto, L. P. Sampaio, G. de A. Melo, and C. A. Canesin, "Evaluation of the main MPPT techniques for photovoltaic applications," *IEEE Trans. Ind. Electron.,* vol. 60, no. 3, pp. 1156-1167, 2013.

[3.6] K. H. Hussein, I. Muta, T. Hoshino, and M. Osakada, "Maximum photovoltaic power tracking: An algorithm for rapidly changing atmospheric conditions," *Proc. Inst. Elect. Eng., Gen., Transm., Distrib.,* vol. 142, no. 1, pp. 59–64, 1995.

[3.7] A. Yazdani and P. P. Dash, "A control methodology and characterization of dynamics for a photovoltaic (PV) system interfaced with a distribution network," *IEEE Trans. Power. Delivery.,* vol. 24, no. 3, pp. 1538–1551, 2009.

[3.8] A. Pandey, N. Dasgupta, and A. K. Mukerjee, "A simple single-sensor MPPT solution," *IEEE Trans. Power. Electron.,* vol. 22, no. 6, pp. 698-700, 2007.

[3.9] V. V. R. Scarpa, S. Buzo, and G. Spiazzi, "Low complexity MPPT technique exploiting the effect of the PV module MPP locus characterization," *IEEE Trans. Ind. Electron.,* vol. 56, no. 5, pp. 1531-1538, 2009.

[3.10] S. Jain and V. Agarwal, "A new algorithm for rapid tracking of approximate maximum power point in photovoltaic systems," *IEEE Power. Electron. Lett.,* vol. 2, no. 1, pp. 16-19, 2004.

[3.11] M. Park and I. A. Yu, "Study on the optimal voltage for MPPT obtained by surface temperature of solar cell," in *Proc. IEEE IECON.,* 2004, pp. 2040-2045.

[3.12] R. F. Coelho, F. M. Concer, and D. C. Martins, "A MPPT approach based on temperature measurements applied in PV systems," in *Proc. IEEE ICSET.,* 2010, pp. 1-6.

[3.13] B. M. Ho and H. S. Chung, "An integrated inverter with maximum power tracking for grid-connected PV systems," *IEEE Trans. Power Electron.,* vol. 20 no. 4, pp. 953-962, 2005.

[3.14] D. Casadei, G. Grandi, and C. Rossi, "Single-phase single-stage photovoltaic generation system based on a ripple correlation control maximum power point tracking," *IEEE Trans. Energy Convers.,* vol. 21, no. 2, pp. 562-568, 2006.

[3.15] N. Femia, G. Petrone, G. Spanuolo, and M. Vitelli, "Optimization of perturb and observe maximum power point tracking method," *IEEE Trans. Power Electron.,* vol. 20, no. 4, pp. 963-73, 2005.

[3.16] T. Esram and P. L. Chapman, "Comparison of photovoltaic array maximum power point tracking techniques," *IEEE Trans. Energy Convers.,* vol. 22, no. 2, pp. 439-449, 2007.

[3.17] F. Blaabjerg, R. Teodorescu, Z. Chen, and M. Liserre, "Overview of control and grid synchronization for distributed power generation," *IEEE Trans. Ind. Electron.,* vol. 53, no. 5, pp. 1398-1409, 2006.

[3.18] Z. Yao, L. Xiao, and Y. Yan, "Seamless transfer of single-phase grid-interactive inverters between grid-connected and stand-alone modes," *IEEE Trans. Power Electron.,* vol. 25, no. 6, pp. 1597-1603, June 2010.

[3.19] P. Rodriguez, A. Luna, R. S. Munoz-Aguilar, I. Etxeberria-Otadui, R. Teodorescu, and F. Blaabjerg, "A stationary reference frame grid synchronization system for three-phase grid-connected power converters under adverse grid

conditions," *IEEE Trans. Power Electron.,* vol. 27, no. 1, pp. 99-112, January 2012.

[3.20] J. Kwon, S. Yoon, and S. Choi, "Indirect current control for seamless transfer of three-phase utility interactive inverters," *IEEE Trans. Power Electron.,* vol. 27, no. 2, pp. 773-781, February 2012.

[3.21] IEEE Standard for Interconnecting Distributed Resources With Electric Power Systems, IEEE Std. 1547-2003.

[3.22] IEEE Guide for Monitoring, Information Exchange, and Control of Distributed Resources Interconnected With Electric Power Systems, IEEE 1547.3-2007, 2007.

[3.23] F. Wang, J. L. Duarte, M. A. M. Hendrix, "Grid-interfacing converter systems with enhanced voltage quality for microgrid application – concept and implementation," *IEEE Trans. Power. Electron.,* vol. 26, no. 12, pp. 3501–3513, December 2011.

[3.24] R. I. Bojoi, L. R. Limongi, D. Roiu, and A. Tenconi, "Enhanced power quality control strategy for single phase inverters in distributed generation systems," *IEEE Trans. Power. Electron.,* vol. 26, no. 3, pp. 798–806, March 2011.

[3.25] M. Shahabi, M. R. Haghifam, M. Mohamadian, and S. A. Nabavi-Niaki, "Microgrid dynamic performance improvement using a doubly fed induction wind generator," *IEEE Trans. Energy. Convers.,* vol. 24, no. 1, pp. 137-145, March 2009.

[3.26] O. Kukrer, "Deadbeat control of a three-phase inverter with an output LC filter," *IEEE Trans. Power. Electron.,* vol. 11, no. 1, pp. 16–23, Jan. 1996.

[3.27] P. Mattavelli, "An improved deadbeat control for UPS using disturbance observers," *IEEE Trans. Ind. Electron.,* vol. 52, no. 1, pp. 206-212, Feb. 2005.

[3.28] M. N. Marwali and A. Keyhani, "Control of distributed generation systems – Part I: Voltage and currents control," *IEEE Trans. Power. Electron.,* vol. 19, no. 6, pp. 1541–1550, Nov. 2004.

[3.29] M. Abdel-Rahim and J. E. Quaicoe, "Analysis and design of a multiple feedback loop control strategy for single-phase voltage-source UPS inverters," *IEEE Trans. Power Electron.,* vol. 11, no. 4, pp. 532-541, 1996.

[3.30] P. C. Loh, M. J. Newman, D. N. Zmood, and D. G. Holmes, "A comparative analysis of multiloop voltage regulation strategies for single and three-phase UPS systems," *IEEE Trans. Ind. Electron.,* vol. 18, no. 5, pp. 1176-1185, Sep. 2003.

[3.31] P. C. Loh and D. G. Holmes, "Analysis of multiloop strategies for LC/CL/LCL-filtered voltage-source and current-source inverters," *IEEE Trans. Ind. Appl*., vol. 41, no. 2, pp 644-654, Mar./Apr. 2005.

[3.32] P. Cortés, G. Ortiz, J. I. Yuz, J. Rodríguez, S. Vazquez, and L. G. Franquelo, "Model predictive control of an inverter with output LC filter for UPS applications," *IEEE Trans. Ind. Electron.,* vol. 56, no. 6, pp. 1875-1883, 2009.

[3.33] T. Ohnishi, "Three phase PWM converter/inverter by means of instantaneous active and reactive power control," *in Proc. IEEE Int. Conf. Ind. Electron., Control Instrum.(IECON),* 1991*,* vol. 1, pp. 819-824.

[3.34] Noguchi. H. Tomiki, S. Kondo and I. Takahashi, "Direct power control of PWM converter without power-source voltage sensors," *IEEE Trans. Ind. Appl*., vol. 34, pp 473-479, 1998.

[3.35] M. Malinowski, M. P. Kazmierkowski and A. M. Trzynadlowski, "A comparative study of control techniques for PWM rectifiers in AC adjustable speed drives," *IEEE Trans. Power Electron.,* vol. 18, no. 6, pp. 1390-1396, 2003.

[3.36] J. Alonso-Martinez, J. Eloy-Garcia, and S. Arnaltes, "Table-based direct power control: A critical review for microgrid applications," *IEEE Trans. Power Electron.,* vol. 25, no. 12, pp. 2949-2916, December 2010.

[3.37] D. Zhi, L. Xu, and B. W. Williams, "Improved direct power control of grid-connected DC/AC converters," *IEEE Trans. Power Electron.,* vol. 24, no. 5, pp. 1280-1292, 2009.

[3.38] J. Hu, L. Shang, Y. He, and Z. Zhu, "Direct active and reactive power regulation of grid-connected DC/AC converters using sliding mode control approach," *IEEE Trans. Power Electron.,* vol. 26, no. 1, pp. 210-222, Jan. 2011.

[3.39] P. Cortes, J. Rodriguez, P. Antoniewicz, and M. Kazmierkowski, "Direct power control of an AFE using predictive control," *IEEE Power Electron.,* vol. 23, no. 5, pp. 2516-2523, 2008.

[3.40] J. Hu, J. Zhu, G. Platt, and D. G. Dorrell, "Model-predictive direct power control of AC/DC converters with one step delay compensation," *in Proc. IEEE IECON Conf.,* 2012, pp. 4874-4879.

[3.41] J. Rodriguez, J. Pontt, C. A. Silva, P. Correa, P. Lezana, P. Cortes, and U. Ammann, "Predictive current control of a voltage source inverter," *IEEE Trans. Ind. Electron*, vol. 54, no. 1, pp. 495-503, Feb. 2007.

[3.42] M. Preindl, E. Schaltz, and P. Thogersen, "Switching frequency reduction using model predictive direct current control for high-power voltage sources inverters," *IEEE Trans. Ind. Electron.,* vol. 58, no. 7, pp. 2826-2835, 2011.

[3.43] T. Geyer, G. Papafotiou, and M. Morari, "Model predictive direct torque control – Part I: concept, algorithm, and analysis," *IEEE Trans. Ind. Electron.,* vol. 56, no. 6, pp. 1894-1905, 2009.

[3.44] P. Cortes, M. P. Kazmierkowski, R. M. Kennel, D. E. Quevedo and J. Rodriguez, "Predictive control in power electronics and dirves," *IEEE Trans. Ind. Electron.*, vol. 55, no. 12, pp. 4312-4324, 2008.

[3.45] J. Hu, J. Zhu, G. Platt and D. G. Dorrell, "Multi-objective model-predictive control for high power converters," *IEEE Trans. on Energy Conversion,* vol. 28, no. 3, pp. 652-663, Sep. 2013.

[3.46] S. Thielemans, T. J. Vyncke, and J. Melkebeek, "Weight factor selection for model-based predictive control of a four-level flying-capacitor inverter," *IET. Power. Electron.,* vol. 5, no. 3, pp. 323-333, 2012.

CHAPTER 4

MULTI-OBJECTIVE MODEL-PREDICTIVE CONTROL FOR HIGH POWER CONVERTERS

4.1 Introduction

Effective performance control strategies for electrical drives and power converters have been an ongoing research subject for several decades. With the development of more forms of electric transportation, this is becoming more so [4.1]. The direct torque control (DTC) has become a powerful control scheme since its first proposal in 1980s [4.2]-[4.5]. Because of its fast transient performance, simple control structure and robustness, DTC has been further utilized in renewable energy applications [4.6], [4.7]. Among the control techniques used in power converters, the direct power control (DPC), which is adapted from DTC for AC machines, has become one of the most popular control strategies, again, because of its robustness and simplicity [4.8]-[4.12]. In the conventional switching table based DPC (SDPC), the converter states are chosen by using a switching table, which is constructed from the instantaneous errors between the estimated and the referenced values of active and reactive power. Unlike the voltage oriented control (VOC), it does not need internal current loops and modulators, and thus the coordinate transformation is also eliminated. However, the main drawback is the large power ripples, leading to distorted line currents.

Predictive control appears to be an attractive alternative for the control of power converters because it has excellent steady-state and dynamic responses. Several kinds of control schemes have been developed under the name of predictive control, such as deadbeat predictive control, hysteresis-based predictive control, trajectory-based predictive control and model-predictive control (MPC) [4.13]-[4.28].

MPC is a flexible control scheme that allows the easy inclusion of system constraints and nonlinearities, and has raised much interest in recent years [4.19]-[4.28]. In this control, a model is used to predict the system behavior, and a cost function is employed as a criterion to select the optimal switching states. The control objectives of MPC can vary considerably according to the application. The cost function defined in [4.19] was employed to evaluate the effects of each voltage vector in order to select the one which

minimized the error of the output voltage. This was for an inverter-based UPS system. In other systems, the minimizing objectives are the active and reactive powers in [4.20] and [4.21], the currents in [4.22] to [4.25] and the electromagnetic torque in [4.26] and [4.27]. In addition to defining different cost functions, MPC can also include different norms, multiple constraints and nonlinearities to improve the system performance. The key is to choose the correct weighting factors to get a reasonable tradeoff between the various control objectives [4.28].

In high power applications, such as flexible alternating current transmission systems (FACTS) [4.29], high voltage direct current (HVDC) transmission systems [4.30], and large capacity renewable energy (wind and PV) systems [4.31], [4.32], low switching frequencies are employed to reduce the switching losses. However, it is of very high priority to control the power converters intelligently to maintain high power quality in the current. This is important in a distributed power generation system, and also in the micro and smart grids in the future [4.33][4.34].

High power converters for distributed generation need a grid-friendly operation, low harmonic conductive electromagnetic emission for low electromagnetic interference, and at the same time converters must be controlled with low switching frequency in order to reduce the commutation losses. The power-switching devices used in these converters, such as high-voltage insulated-gate bipolar transistor (IGBT) and integrated-gate commutated thyristor (IGCT), are capable of switching at a modest frequency of 3-5 kHz. In high-power applications, it is often desirable to switch at even lower frequencies for lower switching power losses and higher power-handling capability. Proper selection of the switching frequency and PWM scheme is critical in minimizing harmonics and imbalance, and therefore, to achieve the desired system performance and to avoid costly and complex filters.

The literature reports very little on MPC with switching frequency reduction. Switching frequency reduction was introduced in [4.22] and [4.23] for current control of a neutral-point-clamped (NPC) multi-level converter and a three-phase two level voltage source inverter, respectively, and they are of relevance here. By predicting the times of switching over a one-step receding horizon, the transistor commutations can be reduced. Similarly, this method was applied in [4.35] for the control of a matrix converter and in [4.36] for a three-phase two-level inverter. However, the introduction of switching frequency reduction without performance deterioration in MPC needs further investigation in order to take into account the computing power required to

evaluate the cost function with various constrains, especially with high sampling frequency.

4.2 Multi-Objective Model-Predictive Control

A three-phase two-level AC/DC converter, as shown in Fig. 4.1, is used as an example to illustrate the proposed multi-objective model predictive control (MOMPC) strategy. Three IGBT half-bridge units are connected to the main grid via a choke consisting of three series-connected inductors L and resistors R. On the DC side, a purely resistive load R_L is connected to the IGBT bridge with a capacitor C in parallel. The converter input voltage can be expressed as the complex space vectors where

$$\boldsymbol{V}_i = \begin{cases} \frac{2}{3} V_{dc} e^{j(i-1)\frac{\pi}{3}} & (i = 1 \cdots 6) \\ 0 & (i = 0, 7) \end{cases} \tag{4.1}$$

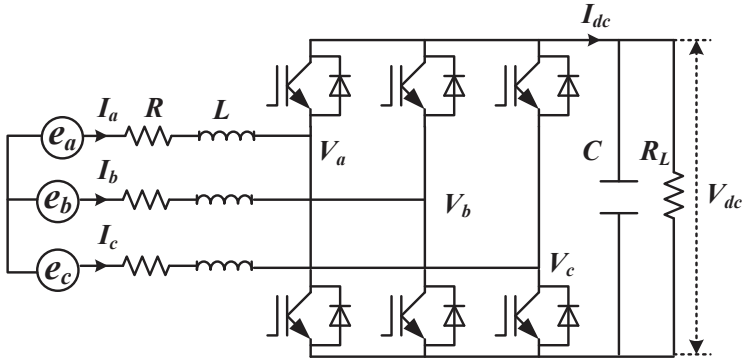

Fig. 4.1 AC/DC converter structure

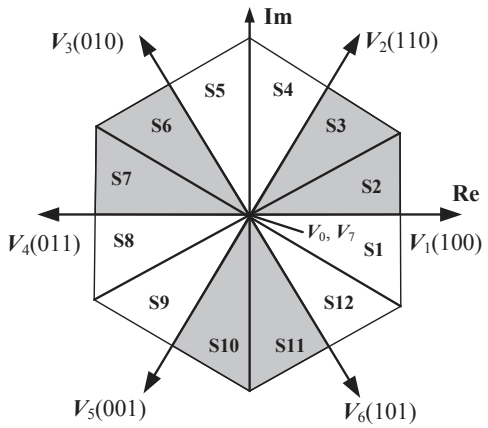

Fig. 4.2 Possible voltage vectors.

Depending on the switching states, there exists seven space voltage vectors: $\boldsymbol{V}_i$ (i = 1, 2,…,7). Note that $\boldsymbol{V}_0 = \boldsymbol{V}_7$, as shown in Fig. 4.2. Consequently, the mathematical model of the converter can be described in the stationary α-β coordinates as

$$\boldsymbol{e}_{\alpha\beta} = L\frac{d\boldsymbol{I}_{a\beta}}{dt} + R\boldsymbol{I}_{a\beta} + \boldsymbol{V}_{\alpha\beta} \tag{4.2}$$

$$C\frac{dV_{dc}}{dt} = \frac{3}{2}\left(\boldsymbol{I}_\alpha D_\alpha + \boldsymbol{I}_\beta D_\beta\right) - I_L \tag{4.3}$$

where $\boldsymbol{e}_{\alpha\beta}$ is the three-phase input voltage vector, $\boldsymbol{V}_{\alpha\beta}$ the converter input voltage vector, $\boldsymbol{I}_{\alpha\beta}$ the line current vector, $\boldsymbol{I}_L$ the DC load current, and D_α and D_β are the switching states (0 = off, 1 = on). The active and reactive power supplied to the grid (which may go negative) can be calculated by

$$P = \frac{3}{2}\mathrm{Re}\{eI^*\} = \frac{3}{2}\left(e_\alpha I_\alpha + e_\beta I_\beta\right) \tag{4.4}$$

$$Q = \frac{3}{2}\mathrm{Im}\{eI^*\} = \frac{3}{2}\left(e_\beta I_\alpha - e_\alpha I_\beta\right) \tag{4.5}$$

4.2.1 Concept of MOMPC

A. Conventional switching table based DPC (SDPC)

Since SDPC is a widely employed and accepted control strategy, it is used as a benchmark reference for the proposed MOMPC in this work. Fig. 4.3 illustrates the SDPC scheme, where the reference active power P^* is delivered from the PI DC voltage regulator while the referenced reactive power Q^* is generally set to zero for unity power factor. The digitized signals d_P and d_Q are then generated by two fixed-band hysteresis comparators using the tracking errors between the estimated and referenced values of the active and reactive powers. The converter switching signals are then selected from a look-up switching table (Table 4.1) according to d_Q, and d_P and the position of system input voltage vector $\boldsymbol{e}_{\alpha\beta}$ in the α-β plane, which has 12 sectors (Fig. 4.2).

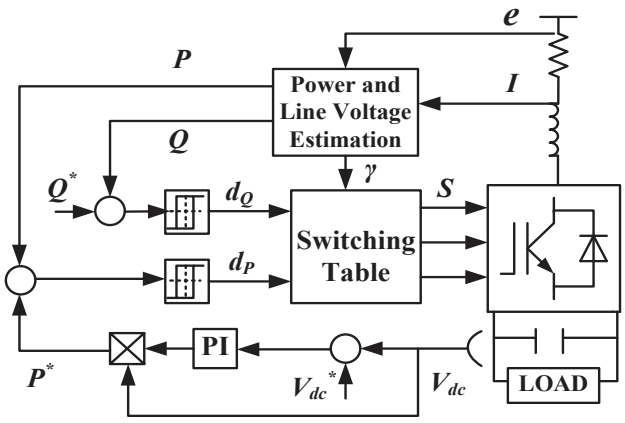

Fig. 4.3 Control block of SDPC

TABLE 4.1 Switching Table of Conventional SDPC

d_P	d_Q	S1	S2	S3	S4	S5	S6	S7	S8	S9	S10	S11	S12
1	0	V_6	V_7	V_1	V_0	V_2	V_7	V_3	V_0	V_4	V_7	V_5	V_0
	1	V_7	V_7	V_0	V_0	V_7	V_7	V_0	V_0	V_7	V_7	V_0	V_0
0	0	V_6	V_1	V_1	V_2	V_2	V_3	V_3	V_4	V_4	V_5	V_5	V_6
	1	V_1	V_2	V_2	V_3	V_3	V_4	V_5	V_5	V_5	V_6	V_6	V_1

An in-depth analysis of the SDPC switching table reveals that the voltage vector selected is not necessarily the best one to correct the power errors in some sectors. For example, V_7 is selected using the table if $d_P > 0$ and $d_Q > 0$ in sector S1. However, the reactive power derivative (or "slope") of V_7 is near zero, which means that activating V_7 just keeps the reactive power constant rather than increases it, resulting in large power ripples and current distortion. In this case, the more suitable vector to control the power is V_3 rather than V_7.

B. Basic principle of MPC

Fig. 4.4 shows a block diagram of the MPC. The key to the scheme is the prediction of power at the $(k+1)^{th}$ sampling instant for different voltage vectors. This assumes that an optimal voltage vector is able to minimize the power ripple effectively when applied during the interval between the k^{th} and $(k+1)^{th}$ instants.

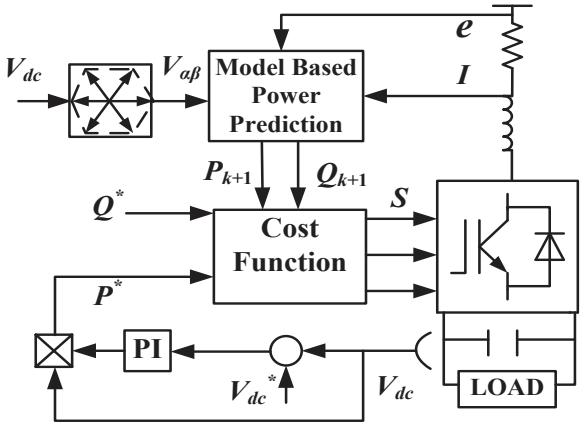

Fig. 4.4 Basic principle of MPC

The active and reactive power derivatives can be obtained from (4.4) and (4.5) as

$$\frac{dP}{dt}=\frac{3}{2}\left(\frac{de_\alpha}{dt}I_\alpha+e_\alpha\frac{dI_\alpha}{dt}+\frac{de_\beta}{dt}I_\beta+e_\beta\frac{dI_\beta}{dt}\right) \tag{4.6}$$

$$\frac{dQ}{dt}=\frac{3}{2}\left(\frac{de_\beta}{dt}I_\alpha+e_\beta\frac{dI_\alpha}{dt}-\frac{de_\alpha}{dt}I_\beta-e_\alpha\frac{dI_\beta}{dt}\right) \tag{4.7}$$

Assume sinusoidal and balanced line voltages, i.e.

$$\boldsymbol{e}=e_\alpha+je_\beta=|\boldsymbol{e}|e^{j\omega t} \tag{4.8}$$

It can be deduced that

$$\frac{de_\alpha}{dt}=-\omega\cdot e_\beta \tag{4.9}$$

$$\frac{de_\beta}{dt}=\omega\cdot e_\alpha \tag{4.10}$$

Substituting (4.2), (4.9) and (4.10) into (4.6) and (4.7) yields

$$\frac{dP}{dt}=-\frac{R}{L}P-\omega Q+\frac{3}{2L}\left(|\boldsymbol{e}|^2-\mathrm{Re}\left(\boldsymbol{eV}^*\right)\right) \tag{4.11}$$

$$\frac{dQ}{dt}=\omega P-\frac{R}{L}Q-\frac{3}{2L}\mathrm{Im}\left(\boldsymbol{eV}^*\right) \tag{4.12}$$

The active and reactive power at the $(k+1)^{th}$ sampling instant can then be obtained as

$$P^{k+1}=T_s\left[-\frac{R}{L}P^k-\omega Q^k+\frac{3}{2L}\left(|\boldsymbol{e}|^2-\mathrm{Re}\left(\boldsymbol{eV}^*\right)\right)\right]+P^k \tag{4.13}$$

$$Q^{k+1}=T_s\left[\omega P^k-\frac{R}{L}Q^k-\frac{3}{2L}\mathrm{Im}\left(\boldsymbol{eV}^*\right)\right]+Q^k \tag{4.14}$$

where T_s is the time length of sampling period

By evaluating the effects of each voltage vector on the active and reactive powers according to a specific cost function, the voltage vector that produces the least power ripple can be determined. In the rectifier control, the control objectives are chosen as the DC-link voltage and the power factor of the AC input, which can be regulated by controlling the active power P and reactive power Q, respectively. Therefore, the cost function can be defined as

$$J = \sqrt{(P^* - P^{k+1})^2 + (Q^* - Q^{k+1})^2} \tag{4.15}$$

C. Multi-objective MPC concept

In MPC, the most appropriate vector is chosen by an optimization criterion. This, however, depends largely on whether the system is in a transient or steady-state [4.23]. That is, the control objectives will be different for different operations. As a matter of fact, even when the system is running in one operation, there are several aspects, or multiple objectives, to be considered in order to obtain a good performance. The proposed MOMPC concept is illustrated schematically in Fig. 4.5. In a dynamic state operation, the power error should be minimized as fast as possible in order to obtain a fast dynamic response. The effects of each voltage vector on active and reactive power will then be evaluated and the one producing the least power ripple will be chosen according to a specific cost function.

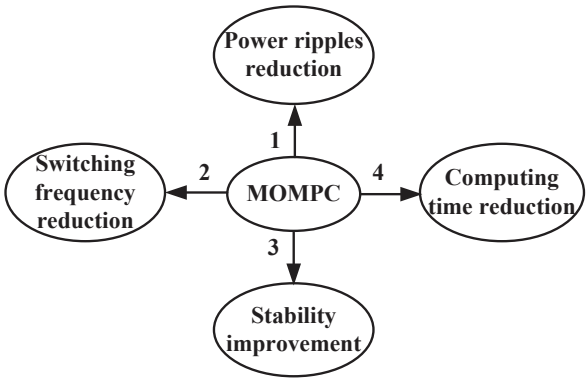

Fig. 4.5 Schematic illustration of MOMPC concept

In a steady state operation, the converter switching behaviour should be optimized to reduce the switching losses which account for a large amount of the total converter losses in high power applications. The cost function should then be revised to take into account the switching frequency. However, if the switching frequency is reduced too much, the system stability will deteriorate. It is necessary to add another component in the cost function to improve the system stability. This leads to an increased computational burden because of the large increase in the number of admissible switching sequences. Hence, the reduction of computing time becomes an important point to address in MOMPC implementation.

4.2.2 Discrete-time digital implementation

It should be noted that compensating for the one step delay is essential for MPC to avoid system performance deterioration [4.38], [4.39], as explained in Chapter 3 previously. Model-based prediction can be an effective method to predict the system state in the next sampling instant. Here, (4.2) is used to obtain a prediction of line current $\boldsymbol{I}^{k+1}$, which will then be substituted into (4.4) and (4.5) to obtain P^{k+1} and Q^{k+1}. However, for cost-function-based predictive control, after P^{k+1} and Q^{k+1} are obtained, seven voltage vectors will be evaluated and the one making $\boldsymbol{x}^{k+2}$ closest to $\boldsymbol{x}^*$ will be chosen. Therefore, to incorporate one-step delay compensation with cost-function-based predictive control, two-step prediction is required. $\boldsymbol{I}^{k+1}$ is first obtained from (4.2) and then similarly $\boldsymbol{I}^{k+2}$ can be predicted with $\boldsymbol{I}^{k+1}$ as a new initial state and $\boldsymbol{V}_i^{k+1}$ as the input. Finally, P^{k+2} and Q^{k+2} can be obtained from (4.4) and (4.5), and consequently the cost function of (4.15) should be revised as

$$J = \sqrt{(P^* - P^{k+2})^2 + (Q^* - Q^{k+2})^2} \tag{4.16}$$

Because the directly controlled variables of the rectifier are the active and reactive power, the one step delay influence can be compensated for when (4.16) is implemented even when other norms or components are included. Therefore, the inclusion of more control objectives for the MOMPC should be based on modification of (4.16).

4.2.3 Switching frequency reduction

In steady-state, the goal of the control is to obtain the minimum possible state changes in order to reduce the switching frequency. In power conversion, especially in high power applications, high efficiency is very important. Less power is lost when the switching frequency is reduced provided the system stability is maintained. Lower dynamic response may be acceptable if it leads to a reduction in average switching frequency. Fig. 4.6 shows the possible vector switching paths for a three-phase two-level power converter. Assuming the switching state is "000" it can be seen that there are four types of possible switching paths according to the number of IGBT leg switches; i.e. no switching, one-state change, two-state change, and three-state change. For example, if the next switching state is "110", the total number of leg switches is two. For the sake of switching frequency reduction, the switching path which causes least leg switches is preferred.

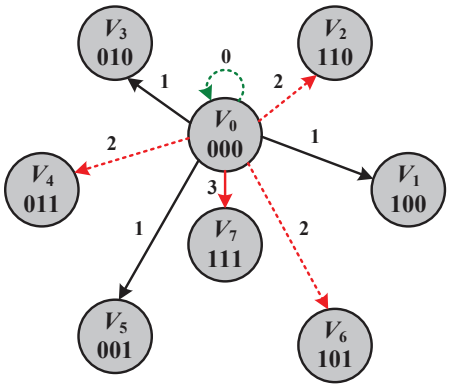

Fig. 4.6 Switching paths of vectors: the green dashed lines standing for no switching, the black solid lines one-state change, the red dashed lines two-state change, the red solid lines three-state change.

In order to reduce the switching frequency, the expression of the cost function (4.16) can be revised to

$$J = \sqrt{(P^* - P^{k+2})^2 + (Q^* - Q^{k+2})^2} + \lambda_2 \left(\sum_{i=a,b,c} \left| D_i^{k+1} - D_i^k \right| \right) \tag{4.17}$$

where D_i^k and D_i^{k+1} represent the switching state of the i phase (i=a,b,c) rectifier leg in the current and the next control periods, respectively. D_i = 0 or 1 where 0 means that the

upper transistor is off and the lower one is on, and 1 reverses this switching state. λ_2 is the weighting factor. The first term in (4.17) reduces the real and reactive power ripple and the reference tracking, while the second term contributes to switching frequency reduction. A large value for the weighting factor λ_2 implies a higher priority for this objective. Therefore, by defining the cost function as (4.17), the switching frequency can be taken into account. It should be borne in mind that eight possible vectors should be evaluated in (4.17) because $\boldsymbol{V}_0$ and $\boldsymbol{V}_7$ are different vectors for switching frequency reduction, whereas only seven possible vectors are evaluated in (4.16) because the effects of $\boldsymbol{V}_0$ and $\boldsymbol{V}_7$ are the same.

4.2.4 System stability improvement

In (4.17), if λ_2 is too large; i.e. the switching frequency reduction is more aggressive than necessary, the system stability will deteriorate, resulting in excessively large currents and power ripples. This phenomenon can be explained by the following example. Assume $\boldsymbol{V}_0$ is the voltage vector applied during the interval between k^{th} and $(k+1)^{th}$ sampling instant, and $\boldsymbol{V}_2$, $\boldsymbol{V}_1$, and $\boldsymbol{V}_0$ are the three best vectors for the correction of the power tracking errors in the next sampling period. However, the three best vectors to reduce the switching frequency are $\boldsymbol{V}_0$, $\boldsymbol{V}_1$, and $\boldsymbol{V}_2$. If λ_2 is set to a very large value, $\boldsymbol{V}_0$ is selected, which will cause large power ripple. A further analysis reveals that the better performance of one objective is achieved at the expense of compromising the performance of the other objectives when it is led unchanged (4.17).

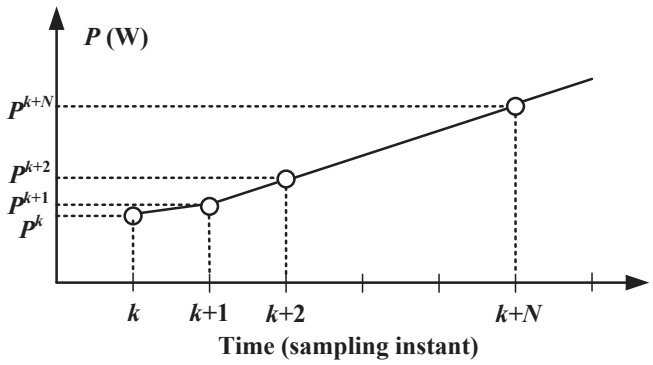

Fig. 4.7 Active power trajectories and switching position with N-step prediction.

Using the principles of MPC, a further development is to predict the behavior of the variables up to certain future point in time. Controlling the error at the next N (N >1) instants will help to stabilize the system when λ_2 is too large. This is different from the model-based predictions for P^{k+2} and Q^{k+2} with horizon N = 1 as discussed in Section 4.2.2. This is also different from the method presented in [4.26] with N >1, where the variable is predicted every step from 1 to N. Instead, here, the input power of the rectifier at the $(k+N)^{th}$ instant is predicted from the value at the $(k+1)^{th}$ and $(k+2)^{th}$ instants using linear extrapolations. This is similar to [4.40] and [4.41]. To visualize this prediction theory, Fig. 4.7 depicts an example of the active power trajectory and the switching position with N-step prediction. The active and reactive power at the $(k+N)^{th}$ instant can be predicted as

$$P^{k+N} = P^{k+1} + (N-1)(P^{k+2} - P^{k+1}) \tag{4.18}$$

$$Q^{k+N} = Q^{k+1} + (N-1)(Q^{k+2} - Q^{k+1}) \tag{4.19}$$

where P^{k+1}, Q^{k+1}, P^{k+2}, and Q^{k+2} can be obtained by using the method presented in Section IV. Consequently, the cost function (4.17) can be further revised to

$$\begin{aligned} J = & \sqrt{(P^* - P^{k+2})^2 + (Q^* - Q^{k+2})^2} \\ & + \lambda_2 \left(\sum_{i=a,b,c} \left| D_i^{k+1} - D_i^k \right| \right) \\ & + \lambda_3 \left(\left| P^* - P^{k+N} \right| + \left| Q^* - Q^{k+N} \right| \right) \end{aligned} \tag{4.20}$$

where λ_3 is the weighting factor of the component in charge of system stability. Using the linear extrapolation for the prediction horizon, where N is larger than 2, it is feasible, especially when the sampling period is very short. Here, N = 5.

4.2.5 Computational time reduction

Calculating a cost function that contains several norms, e.g. (4.20), can be very time consuming although the computing power of microprocessors has increased dramatically in recent years. When the computing time T_c is greater than the sampling period T_s, the computation of the cost function cannot be completed. This delay in computation of the steps caused by slow computation can cause significant system performance deterioration. Therefore, steps must be taken to reduce the computing time when implementing the MOMPC strategy. It is worth mentioning that for almost any control algorithm, the computing time can be more or less reduced by machine code

optimization after the control strategy has been programmed. This can be done using procedures such as setting a global variable for a calculation that is used frequently, and using multiplication instead of division if possible. Instead of using the commonly used methods like the machine code optimization, this work presents a computing time reduction method by revising the control strategy itself.

The new method is based on a hypothesis that the time demanded for the prediction of all the possible errors might be unnecessary. To control a three-phase two-level converter, it may be sufficient just to evaluate some of the eight switching states instead of all of them in the cost function in order to find the optimal vector for the next sampling period. For example, if the system input voltage vector $\boldsymbol{e}$ is within Sector S2 or S3, as shown in Fig. 4.2, $\boldsymbol{V}_1$ and $\boldsymbol{V}_2$ will be probably used while $\boldsymbol{V}_4$ and $\boldsymbol{V}_5$ are barely be used for power ripple reduction. The switching state transfers from $\boldsymbol{V}_1$ (or $\boldsymbol{V}_2$) to $\boldsymbol{V}_4$ (or $\boldsymbol{V}_5$) requires switching of at least two IGBT legs, which is not the priority for switching frequency reduction. Therefore, in the cost function, only six vectors are evaluated according to the position of system input voltage vector $\boldsymbol{e}$. Similarly, $\boldsymbol{V}_5$ and $\boldsymbol{V}_6$ will not be evaluated if $\boldsymbol{e}$ is located in S4 or S5, and so on. Consequently, the computing time can be reduced by almost 25% without causing any apparent performance deterioration. This effect can be more significant when the sampling frequency is high.

4.3 Numerical Simulation and Experimental Verification

4.3.1 Numerical simulation

To check the feasibility of the proposed MOMPC, it is compared with the CDPC using simulation in the MATLAB/Simulink environment. The system parameters are listed in Table 4.2. For simplicity, the CDPC methods without and with one-step delay compensation are denoted as “SDPC.I” and “SDPC.II”, and the MOMPC methods using (4.15), (4.16), (4.17), and (4.20) as cost functions are denoted as “MOMPC.I”, “MOMPC.II”, “MOMPC.III”, and “MOMPC.IV”, respectively. The MOMPC using (4.20) as the cost function and implemented by the proposed computing time reduction method is denoted as “MOMPC.V”.

TABLE 4.2 Parameters of the MOMPC System in Simulation

Resistance of Choker	R	0.25 Ω
Inductance of Choker	L	10 mH
DC-link capacitor	C	470 uF
Load resistance	R_L	100 Ω
Phase-phase Voltage	e	120 V(rms)
Source voltage frequency	f	50 Hz
DC-link voltage	V_{dc}	300 V
Sampling period	Ts	50 μs

The reference DC-link voltage V_{dc}* is set to be 300 V, and the reference reactive power Q* is set to 0 VAR for unity power factor operation. Fig. 4.8 shows the steady-state performance of the SDPC: (a) without and (b) with one-step delay compensation. From top to bottom, the curves are the active power (P), reactive power (Q), phase a voltage (e_a/10), three-phase AC line currents (I), and the average switching frequency (f_{sw}). The average switching frequency is calculated by counting the total commutation instants of a phase leg during a fixed period and then divided by 2. It can be seen that the power ripple is reduced and the line currents are more sinusoidal after introducing the one-step delay compensation, but the switching frequency increases from (a) about 1.6 kHz up to (b) 5.1 kHz.

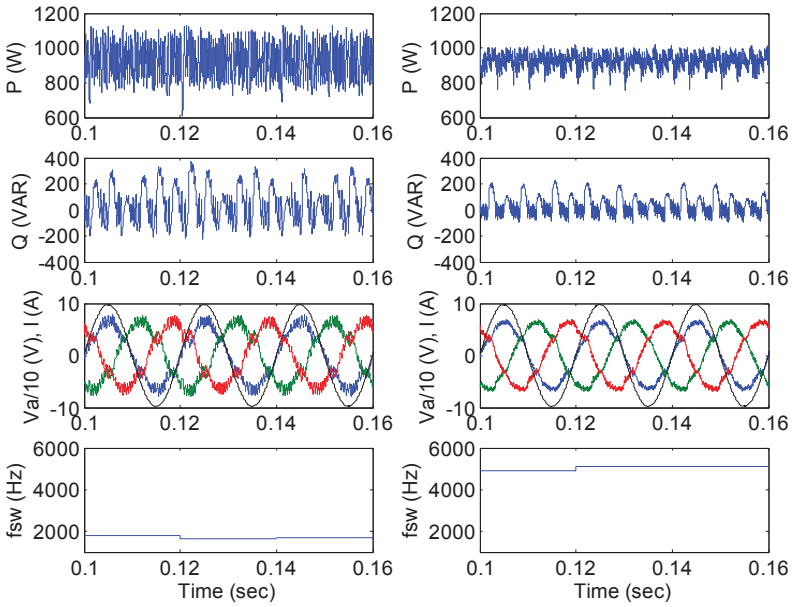

Fig. 4.8 Simulated steady-state performance. (a) SDPC.I, and (b) SDPC.II.

Fig. 4.9 shows the steady state performance of MOMPC.I and MOMPC.II. It can be seen that compared with SDPC.I and SDPC.II, MOMPC.I and MOMPC.II yield much smaller power ripple and more sinusoidal line currents with a significant increase of the switching frequency after the introduction of one step delay compensation.

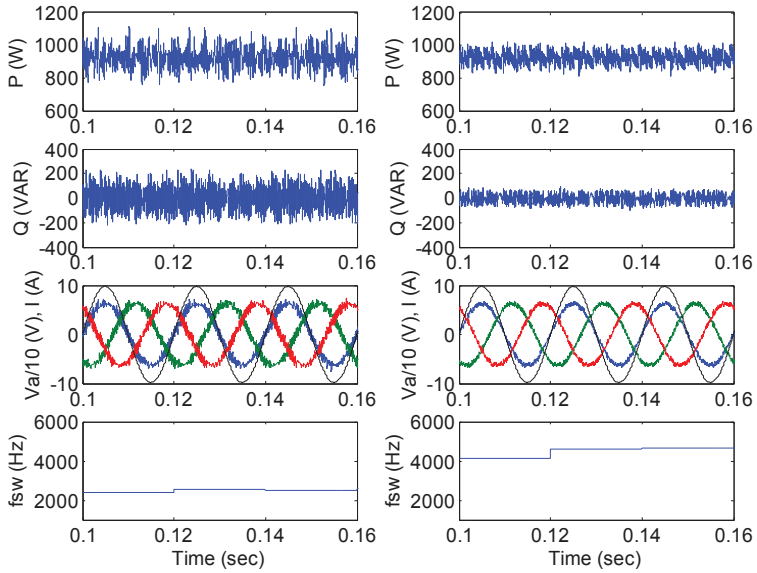

Fig. 4.9 Simulated steady-state performance. (a) MOMPC.I, and (b) MOMPC.II.

Fig. 4.10(a) demonstrates the effects of the switching frequency reduction strategy in MOMPC.III. It can be seen that the switching frequency is reduced from 4.6 kHz (shown in Fig. 4.9(b)) to about 2.2 kHz. However, the power ripple increases significantly due to aggressive switching frequency reduction, resulting in distorted line currents.

Fig. 4.10(b) shows the switching frequency reduction that can be achieved without system performance deterioration by the introduction of a linear extrapolation component in the cost function. As shown, MOMPC.IV yields much lower power ripple and much more sinusoidal line current with a switching frequency of only 2.8 kHz.

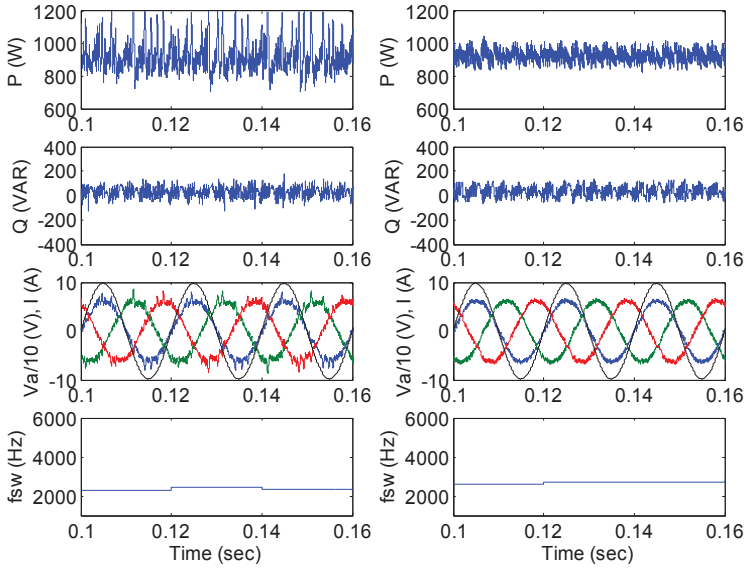

Fig. 4.10 Simulated steady state performance. (a) MOMPC.III, λ_2=70, and (b) MOMPC.IV, λ_2=70, λ_3=0.12.

4.3.2 Experimental verification

The proposed MOMPC strategy was tested experimentally on a scale-down laboratory AC/DC converter system, which uses a Semikron intelligent power module (IPM). The hardware setup is shown in Fig. 4.11. A TMS320F28335 floating-point DSP was used for the control. The controller was designed so that the control functions are interrupt driven. After completing the A/D conversion (ADC), an interrupt is generated and the program enters the interrupt service routine (ISR). The ADC start occurs using the period interrupt of the PWM. Therefore, the ISR runs once in each PWM cycle and is used to compute the switching state for the next cycle. The time consumption of ADC is less than 300 ns. The system variables are controlled using Real Time Data Exchange (RTDX) communication between the DSP and PC. The converter input active and reactive power are displayed through digital to analog conversion (DAC) ranged from 0 V – 5 V with 1 V represents 60 (W or VAR) and 2.5 V corresponding to 0 (W or VAR). The system parameters of the experimental test are listed in Table 4.3.

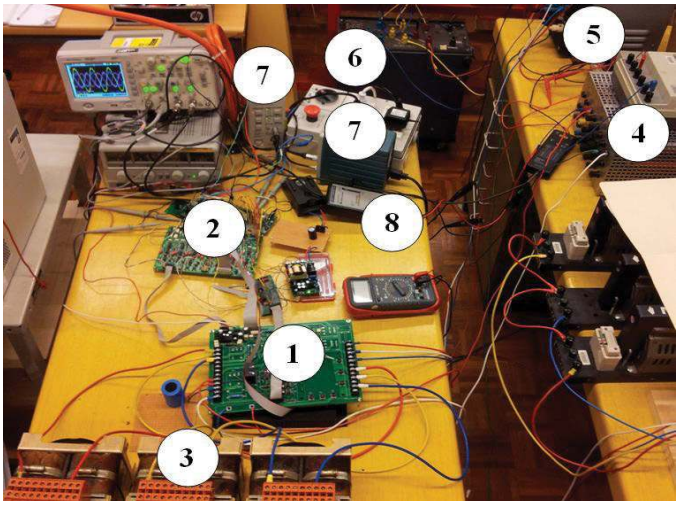

Fig. 4.11 Laboratory test bench: (1) Semikron intelligent power module based AC/DC converter, (2) control unit, (3) inductors, (4) DC resistive load, (5) three-phase auto-transformer, (6) three-phase isolated transformer, (7) Tektronix current probe, and (8) voltage probe.

TABLE 4.3 Parameters of the MOMPC System in Experiment

Resistance of Choker	R	0.51 Ω
Inductance of Choker	L	22 mH
DC-link capacitor	C	680 uF
Load resistance	R_L	150 Ω
Phase-phase Voltage	e	50 V(rms)
Source voltage frequency	f	50 Hz
DC-link voltage	V_{dc}	120 V
Sampling period	Ts	50 μs

Fig. 4.12 compares the experimental results of different control methods. It can be seen that experimental results are in good agreement with the simulation (Fig. 4.8 and Fig. 4.9). The input voltage is in phase with the input current for all the methods because the reactive power reference Q^* is set to zero for unit power factor operation. After integrated the one-step delay compensation scheme into the SDPC, the active power and reactive power ripples are reduced, resulting in improved line currents, as shown in Fig. 4.12(a) and Fig.4.12(b). On the other hand, MOMPC presents less power ripple and a more stable DC-link voltage. Overall, better performances in terms of line current THD, active and reactive power ripples are achieved by MOMPC compared with SDPC, and one-step delay compensation further improves the performance, as illustrated in Fig. 4.12(c) and (d).

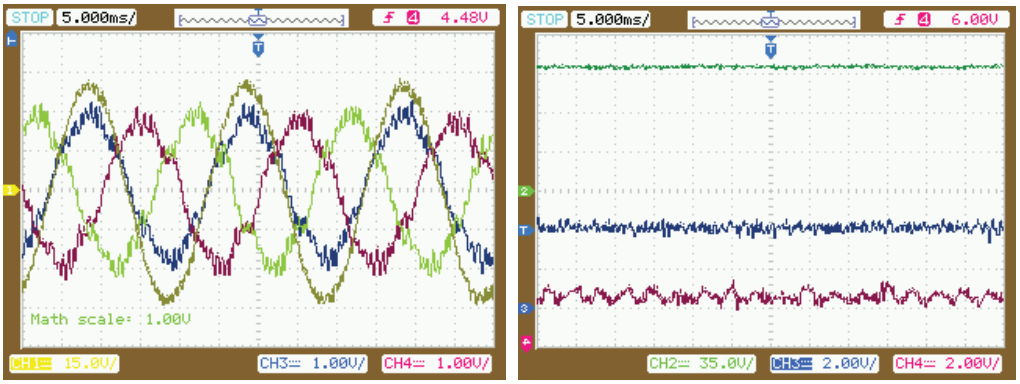

(a)

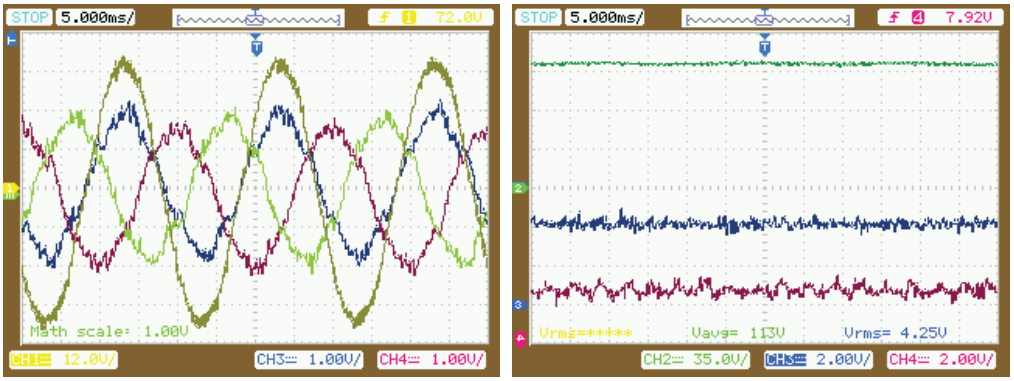

(b)

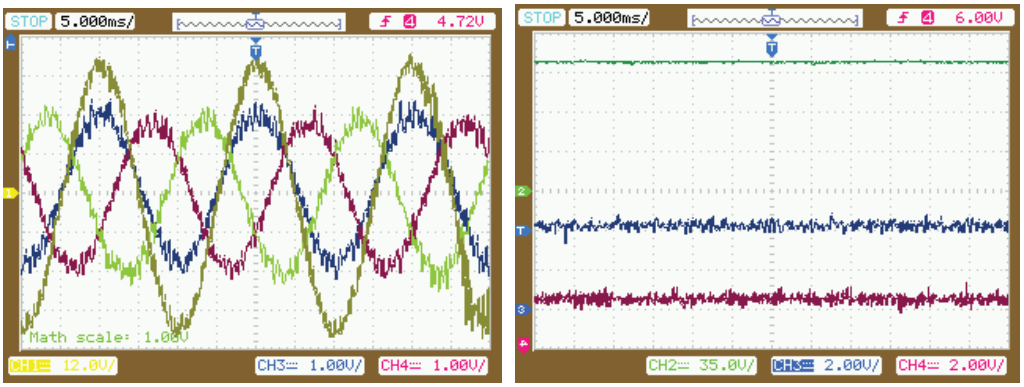

(c)

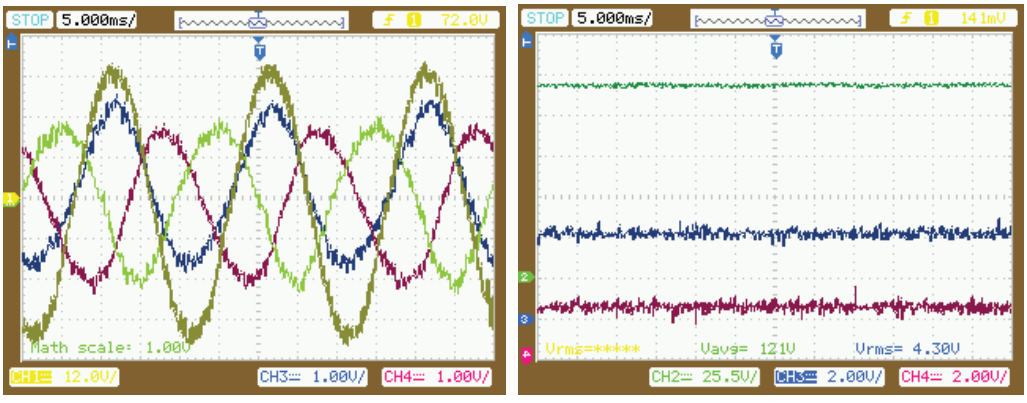

(d)

Fig. 4.12 Experimental results. Left: CH1-grid phase A voltage, CH3 and CH4-converter input currents; Right: CH2-DC-link voltage, CH3-active power, CH4-reactive power. (a) SDPC.I, THD =

16.68%, f_{sw} = 1562 Hz, (b) SDPC.II, THD = 11.04%, f_{sw} = 5017 Hz, (c) MOMPC.I, THD = 11.72%, f_{sw} = 2439 Hz, (d) MOMPC.II, THD = 7.16%, f_{sw} = 4482 Hz.

In order to demonstrate the effectiveness of frequency reduction algorithm and obtain the visual comparison, the PWM signals are also plotted. Fig. 4.13 presents the results of frequency reduction and system stability improvement. After adding the component of frequency reduction to the cost function, i.e. using (4.17), the average switching frequency is reduced considerably. However, the converter input currents are severely distorted and the system becomes fluctuating due to the aggressive switching frequency reduction. In order to stabilize the system, another norm is added to the cost function. After using (4.20), the system can be stabilized while the switching frequency is also reduced, compared to that of SDPC.

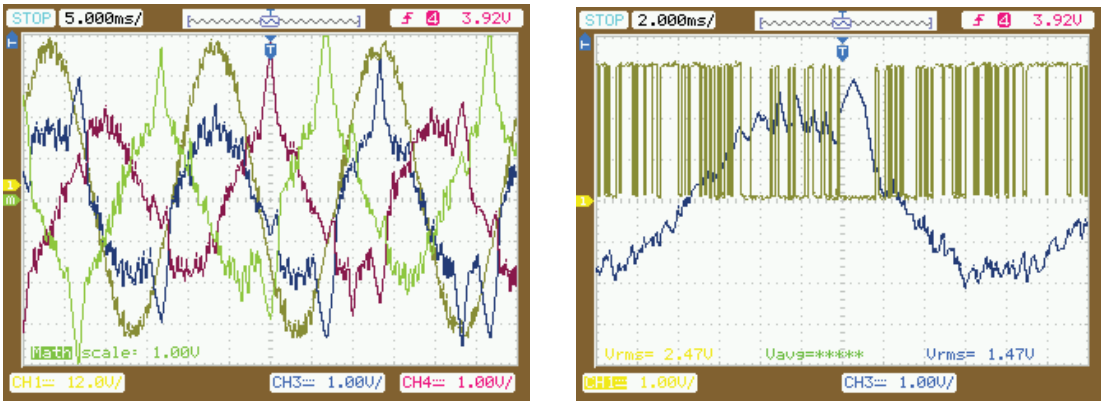

(a)

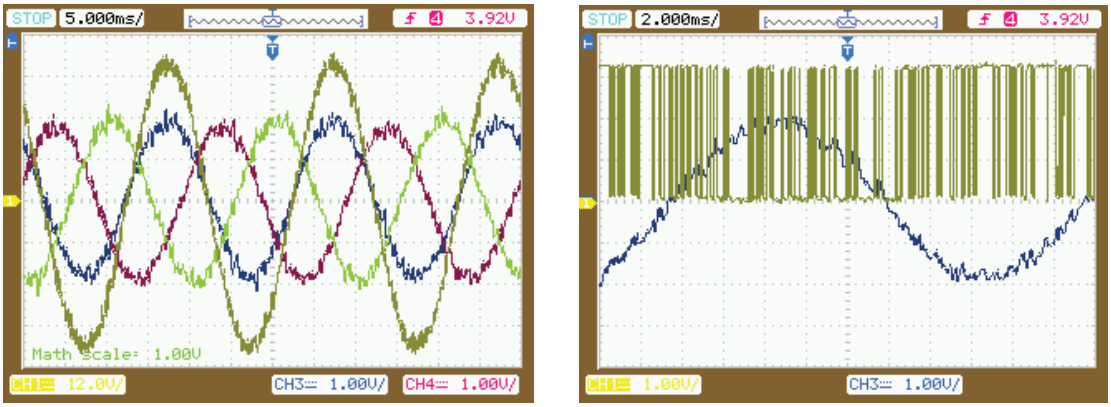

(b)

Fig. 4.13 Experimental results of frequency reduction scheme and system stability improvement. Left: CH1-grid phase A voltage, CH3 and CH4-converter input currents; Right: CH1-PWM signals of upper leg of phase A, CH3-phase A current, (a) MOMPC.III, λ_2=70, THD = 14.38%, f_{sw} = 1953 Hz, (b) MOMPC.IV, λ_2=70, λ_3=0.12, THD = 7.75%, f_{sw} = 2638 Hz.

Fig. 4.14 shows the results of MOMPC.V, i.e. (4.20) is used and the computing time reduction algorithm is employed. It can be seen that the system performance is almost the same as that of MOMPC.IV, while the power ripples are reduced, and the line currents are much more sinusoidal, compared to CDPC, which validates the effectiveness of the proposed MOMPC strategy.

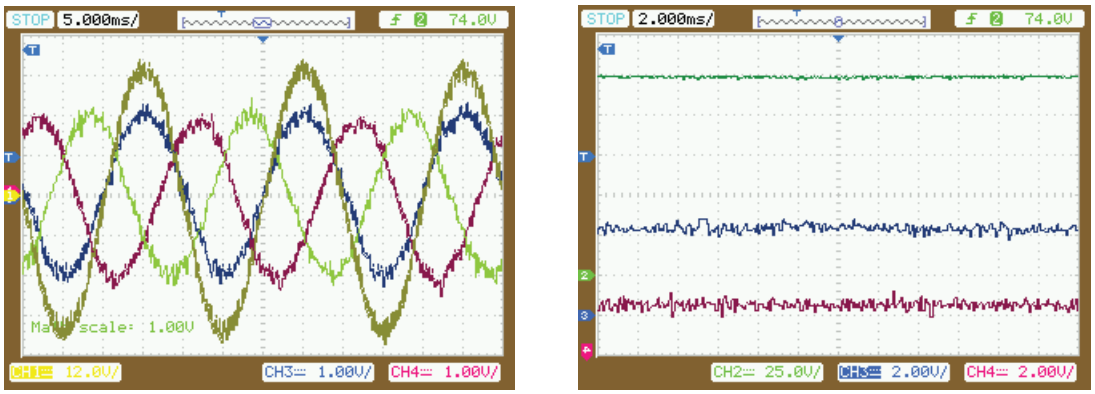

Fig. 4.14 Experimental results of computing time reduction algorithm MOMPC.V, CH1: grid phase A voltage, CH3 and CH4: converter input currents; CH2: DC-link voltage, CH3: and active, CH4: reactive power,λ_2=70, λ_3=0.12, THD = 7.89%, f_{sw} = 2623 Hz.

Fig. 4.15 compares the line current spectra of various control strategies. It can be seen that the SDPC strategies yields more low-order harmonics (Figs. 4.15(a) and (b)) whereas the MOMPC strategies have a relatively broad harmonic spectrum with smaller low-order harmonics (Figs. 4.15(c)-(f)). A further observation of the MOMPC strategies reveals that MOMPC.I and MOMPC.II present similar spectra, while the spectrum of MOMPC.III contains more low-order harmonics, and MOMPC.IV appears to be better with smaller harmonics, compared to MOMPC.III. It can be seen that the performances of MOMPC.IV and MOMPC.V are only slightly degraded compared with MOMPC.II, but still much better than that of SDPC.II.

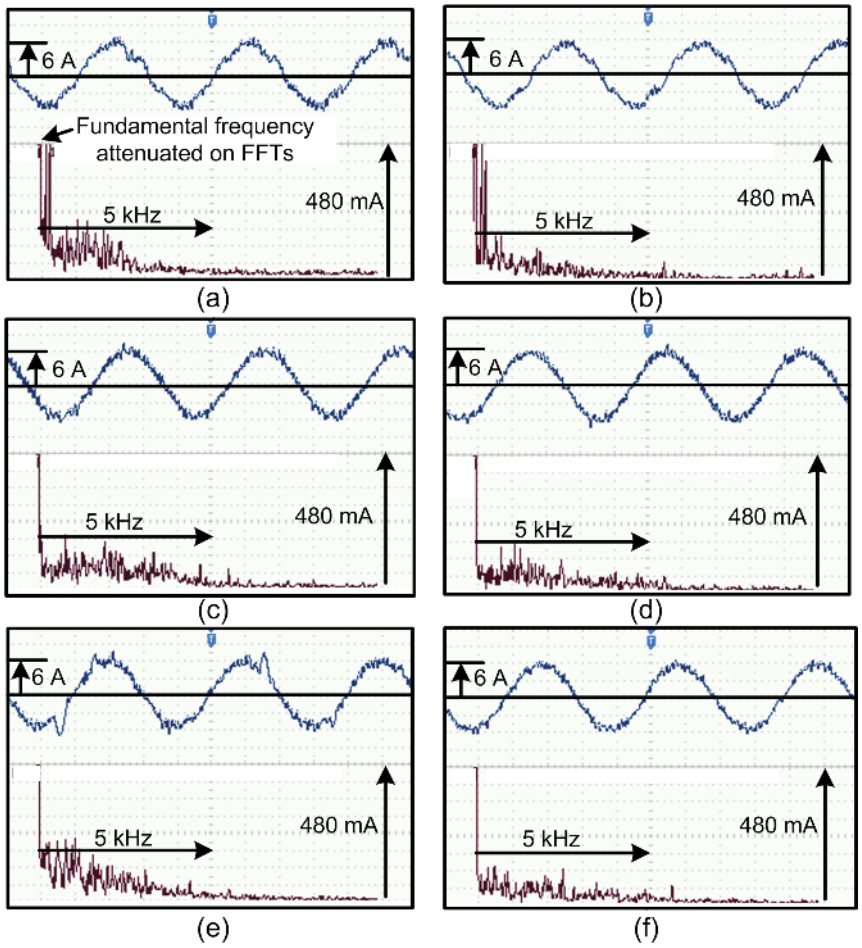

Fig. 4.15 Line current spectrum, 60 mA/div, 1 kHz/div, Sa=20 kSa, (a) SDPC.I, (b) SDPC.II, (c) MOMPC.I, (d) MOMPC.II, (e) MOMPC.III, (f) MOMPC.IV.

The dynamic responses of SDPC and the proposed MOMPC strategy are shown in Fig. 4.16 and Fig. 4.17, respectively. In this test, the outer DC-link voltage control loop is open, the active power P^* steps up from 50 W to 100 W and steps back to 50 W shortly. It can be observed that the SDPC presents excellent tracking ability with only around 10 ms responding time, owning to the fact that no PI regulators and PWM modulators are used in direct control approaches. For the proposed MOMPC strategy, it takes only around 3 ms from 50 W to 100 W and around 10 ms from 100 W back to 50 W, featuring even better transient performance than SDPC.

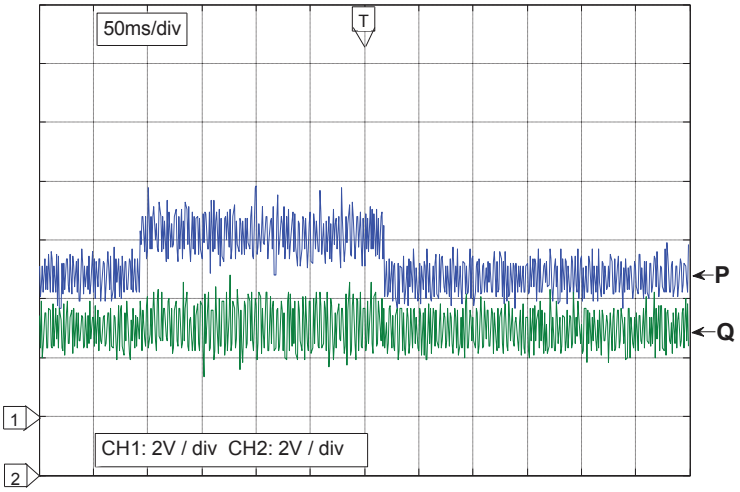

(a)

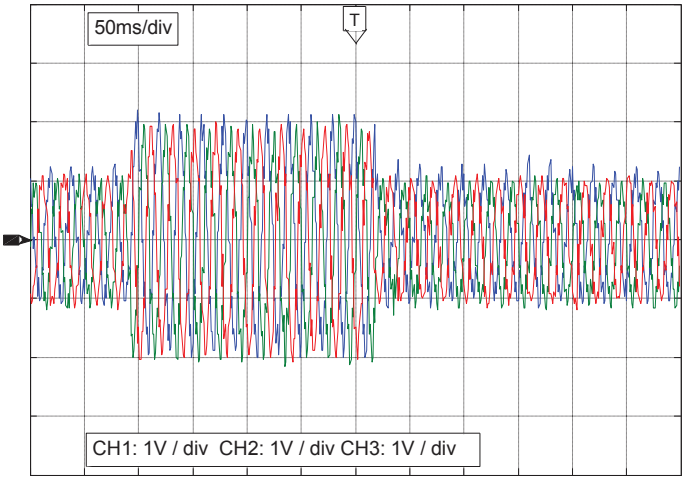

(b)

Fig. 4.16 Experimental results of dynamic response of SDPC.II, (a) active and reactive power, (b) three-phase input currents.

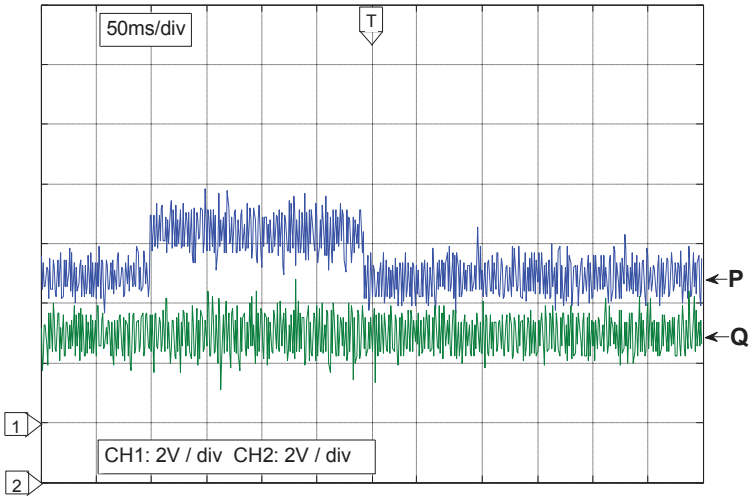

(a)

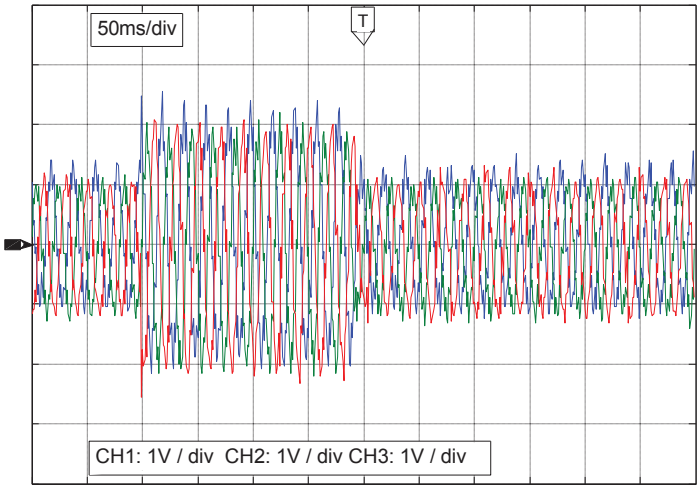

(b)

Fig. 4.17 Experimental results of dynamic response of MOMPC.V, (a) active and reactive power, (b) three-phase input currents.

4.4 Summary of the Chapter

In this Chapter, a new MOMPC strategy has been proposed. By using the system model to predict the behavior of system variables, a cost function is employed as a criterion to select the optimal switching states. The main contribution of MOMPC is the considerable reduction of the average switching frequency, which makes it very significant for high power applications, such as larger-scale wind power generation systems and HVDC transmission systems. In addition, in order to improve system stability, an *N*-step linear extrapolation method is proposed and included in the cost function. Finally, a new method is proposed to simplify the implementation of control algorithm for effective reduction of the computing time.

The proposed MOMPC method presents excellent steady-state and dynamic performances. This takes into account different control objectives by revising the cost function flexibly and correctly, which makes this method very attractive in terms of controlling power converters and in the development of micro and smart grids.

References

[4.1] B. Fahimi and J. Wang, "Electric transportation – a transformation around the globe," *IEEE Magazine. Power & Energy*, vol. 9, no. 4, pp 14-16, June 2011.

[4.2] I. Takahashi and T. Noguchi, "A new quick-response and high efficiency control strategy of an induction machine," *IEEE Trans. Ind. Appl*., vol. IA-22, pp 820-827, 1986.

[4.3] "Direct torque control – The world's most advanced AC drive technology," ABB Finland, Helsinki, Tech. Guide 1, 1996.

[4.4] K-B. Lee, S-H. Huh, J-Y. Yoo, and F. Blaabjerg, "Performance improvement of DTC for induction motor-fed by three-level inverter with an uncertainty observer using RBFN," *IEEE Trans. Energy. Convers*., vol. 20, no. 2, pp. 276–283, June 2005.

[4.5] S. M. A. Cruz, H. A. Toliyat, and A. J. Marques, "DSP implementation of the multiple reference frames theory for the diagnosis of stator faults in a DTC induction motor drive," *IEEE Trans. Energy. Convers*., vol. 20, no. 2, pp. 329–335, June 2005.

[4.6] J. Arbi, M. J.-B. Ghorbal, I. Slama-Belkhodja, and L. Charaabi, "Direct virtual torque control for doubly fed induction generator grid connection," *IEEE Trans. Ind. Electron.,* vol. 56, no. 10, pp. 4163–4173, October 2009.

[4.7] G. Abad, M. A. Rodriguez, J. Poza, and J. M. Canales, "Direct torque control for doubly fed induction machine-based wind turbines under voltage dips and without crowbar protection," *IEEE Trans. Energy. Convers*., vol. 25, no. 2, pp. 586–588, June 2010.

[4.8] Noguchi. H. Tomiki, S. Kondo and I. Takahashi, "Direct power control of PWM converter without poewr-source voltage sensors," *IEEE Trans. Ind. Appl*., vol. 34, pp 473-479, 1998.

[4.9] M. Malinowski, M. P. Kazmierkowski, S. Hansen, F. Blaabjerg, and G. D. Marques, "Virtual-flux-based direct power control of three-phase PAWM rectifier," *IEEE Trans. Ind. Appl.,* vol. 37, no. 4, pp. 1019-1027, 2001.

[4.10] M. Malinowski, M. P. Kazmierkowski and A. M. Trzynadlowski, "A comparative study of control techniques for PWM rectifiers in AC adjustable speed drives," *IEEE Trans. Power Electron.,* vol. 18, no. 6, pp. 1390-1396, 2003.

[4.11] L. Xu and P. Cartwright, "Direct active and reactive power control of DFIG for wind energy generation," *IEEE Trans. Energy. Convers.,* vol. 21, no. 3, pp. 750–758, September 2006.

[4.12] D. Zhi and L. Xu, "Direct power control of DFIG with constant switching frequency and improved transient performance," *IEEE Trans. Energy. Convers.,* vol. 22, no. 1, pp. 110-118, March 2007.

[4.13] P. Cortés, M. P. Kazmierkowsik, R. M. Kennel, D. E. Qeuvedo, and J. Rodríguez, "Predictive control in power electronics and drives," *IEEE Trans. Ind. Electron.,* vol. 55, no. 12, pp. 4312-4321, 2008.

[4.14] S. A. Larrinaga, M. A. Rodriguez, E. Oyarbide and J. R. T. Apraiz, "Predictive control strategy for DC/AC converters based on direct power control," *IEEE Trans. Ind. Electron.,* vol. 54, no. 3, pp. 1261-1271, June 2007.

[4.15] P. Antoniewicz and M. P. Kazmierkowski, "Virtual-flux-based predictive direct power control of AC/DC converters with online inductance estimation," *IEEE Trans. Ind. Electron.,* vol. 55, no. 12, pp. 4381-4390, December 2008.

[4.16] G. Abad, M. A. Rodriguez, and J. Poza, "Two-level VSC-based predictive direct power control of the doubly fed induction machine with reduced power ripple at low constant switching frequency," *IEEE Trans. Energy. Convers.,* vol. 23, no. 2, pp. 570–580, June 2008.

[4.17] P. Antoniewicz and M. P. Kazmierkowski, "Virtual-flux-based predictive direct power control of AC/DC converters with online inductance estimation," *IEEE Trans. Ind. Electron.,* vol. 55, no. 12, pp. 4381-4390, December 2008.

[4.18] D. Zhi, L. Xu, and B. W. Williams, "Model-based predictive direct power control of doubly fed induction generators," *IEEE Trans. Power Electron.,* vol. 25, no. 2, pp. 341-351, February 2010.

[4.19] P. Cortés, G. Ortiz, J. I. Yuz, J. Rodríguez, S. Vazquez, and L. G. Franquelo, "Model predictive control of an inverter with output LC filter for UPS applications," *IEEE Trans. Ind. Electron.,* vol. 56, no. 6, pp. 1875-1883, 2009.

[4.20] P. Cortes, J. Rodriguez, P. Antoniewicz, and M. Kazmierkowski, "Direct power control of an AFE using predictive control," *IEEE Trans. Power Electron.,* vol. 23, no. 5, pp. 2516-2523, September 2008.

[4.21] J. Hu, J. Zhu, G. Platt and D. G. Dorrell, "Model-Predictive direct power control of AC/DC converters with one step delay compensation," in *Proc. IEEE IECON Conf.,* pp. 4874–4879, 2012.

[4.22] R. Vargas, P. Cortes, U. Ammann, J. Rodriguez, and J. Pontt, "Predictive control of a three-phase neutral-point-clamped inverter," *IEEE Trans. Ind. Electron.,* vol. 54, no. 5, pp. 2697-2705, October 2007.

[4.23] M. Preindl, E. Schaltz, and P. Thogersen, "Switching frequency reduction using model predictive direct current control for high-power voltage sources inverters," *IEEE Trans. Ind. Electron.,* vol. 58, no. 7, pp. 2826-2835, 2011.

[4.24] S. Mariethoz and M. Morari, "Explicit model-predictive control of a PWM inverter with an LCL filter," *IEEE Trans. Ind. Electron.,* vol. 56, no. 2, pp. 389-399, February 2009.

[4.25] S. Kouro, P. Cortés, R. Vargas, U. Ammann, and J. Rodríguez, "Model predictive control – a simple and powerful method to control power converters," *IEEE Trans. Ind. Electron.,* vol. 56, no. 6, pp. 1826-1838, 2009.

[4.26] T. Geyer, G. Papafotiou, and M. Morari, "Model predictive direct torque control – Part I: concept, algorithm, and analysis," *IEEE Trans. Ind. Electron.,* vol. 56, no. 6, pp. 1894-1905, 2009.

[4.27] T. Geyer, "Computationally efficient model predictive direct torque control," *IEEE Trans. Power Electron.,* vol. 26, no. 10, pp. 2804-2816, October 2011.

[4.28] S. Thielemans, T. J. Vyncke, and J. Melkebeek, "Weight factor selection for model-based predictive control of a four-level flying-capacitor inverter," *IET. Power. Electron.,* vol. 5, no. 3, pp. 323-333, 2012.

[4.29] X. Jiang, X. Fang, J. H. Chow, Abdel-Aty Edris, M. Parisi, and L. Hopkins, "A novel approach for modeling voltage-sourced converter-based FACTS controllers," *IEEE Trans. Power. Del.,* vol. 23, no. 4, pp. 2591–2598, October 2008.

[4.30] Z. Miao, L. Fan, D. Osborn, and S. Yuvarajan, "Wind farms with HVDC delivery in inertial response and primary frequency control," *IEEE Trans. Energy. Convers.,* vol. 25, no. 4, pp. 1171–1178, December 2010.

[4.31] F. Blaabjerg, "Power electronics in renewable energy systems," Tutorial in *SAAEI'06 Conf.* 2006.

[4.32] Z. Chen, J. M. Guerrero, and F. Blaabjerg, "A review of the state of the art of power electronics for wind turbines," *IEEE Trans. Power Electron.,* vol. 24, no. 8, pp. 1859-1875, August 2009.

[4.33] J. Wang, Q. Huang, W. Sung, Y. Liu, and B. J. Baliga, "Smart grid technologies," *IEEE Magazine. Ind. Electron*., pp. 16–23, June 2009.

[4.34] H. Farhangi, "The path of the smart grid," *IEEE Magazine. Power & Energy*., vol. 4, no. 1, pp. 18–28, January/February 2010.

[4.35] S. Muller, U. Ammann, and S. Rees, "New time-discrete modulation scheme for matrix converters," *IEEE Trans. Ind. Electron*., vol. 52, no. 6, pp. 1607–1615, December 2005.

[4.36] J. Rodriguez, J. Pontt, C. Silva, P. Correa, P. Lezana, P. Cortes, and U. Ammann, "Predictive current control of a voltage source inverter," *IEEE Trans. Ind. Electron*., vol. 54, no. 1, pp. 495–503, February 2007.

[4.37] A. Bouafia, J. P. Gaubert andF. Krim, "Analysis and design of new switching table for direct power control of three-phase PWM rectifier," in *Proc. IEEE Int. Power Electronics and Motion Control Conf. EPE-PEMC*' 08, pp. 1-6, 2008. .

[4.38] P. Cortes, J. Rodriguez, D. E. Quevedo, and C. Silva, "Predictive current control strategy with imposed load current spectrum," *IEEE Trans. Power Electron.,* vol. 23, no. 2, pp. 612-618, March 2008.

[4.39] J. Beerten, J. Verveckken and J. Driesen, "Predictive direct torque control for flux and torque ripple reduction," *IEEE Trans. Ind. Electron*., vol. 57, no. 1, pp. 404–412, January 2010.

[4.40] H. Zhang and R. P. Paul, "A parallel inverse kinematics solution for robot manipulators based on multiprocessing and linear extrapolation," *IEEE Trans. Robotics Automat.,* vol. 7, no. 5, pp. 660-669, October 1991.

[4.41] Y. Zhang, J. Zhu, and W. Xu, "Predictive torque control of permanent magnet synchronous motor drive with reduced switching frequency," in *Proc. IEEE Int. Electrical Machines and System Conf. 2010*, pp. 1-6.

CHAPTER 5

SMART MICROGRID SYSTEM CONTROL

5.1 Introduction

As the demand for electricity power keeps rising these years, the existing electricity power system is undergoing a major transformation. Due to the limitation of delivery capability and the increase in power demand, it is getting more and more stressed. Generally, the main drawbacks of the existing power systems can be summarized as followings [5.1]:

A. *Inefficiency:* Almost 8% of the total power is lost along transmission lines while only one-fifth of its generation capacity exists to meet the peak demand.
B. *Domino-effect failures:* It is a strictly hierarchical system where power plants at the top of the chain ensure power delivery to customers' loads at the bottom of the chain. In other words, the power flows in only one direction, which will leads to large-scaled blackout triggered by power plants intermittence or even transmission lines problems. The most well-known failure occurred in August 2003, when 50 million customers in the USA and Canada lost power for up to two days due to cascading events.
C. *Instability:* The unprecedented fluctuation of demand for electrical power, coupled with increasing penetration level of DGs and lagging investments in the electrical power infrastructure, has decreased system stability.

In order to address the issues of the existing electricity grid mentioned above and at the same time exploit the renewable energy sources effectively, the next generation electricity grid known as the "Smart Grid" was proposed recently. At the generation level, it is expected to emerge as a well-planned plug and play integration of smart microgrids. At the distribution and transmission level, the smart grid integrates small microgrids through dedicated highways for command, data, and power exchanges. Therefore, the efficiency, reliability, and security of the grid can be improved greatly by dynamic optimization of electric-system operations, maintenance, and planning. The

smart grid can thus be thought of as a platform where both supply and demand sides meet [5.2]-[5.4].

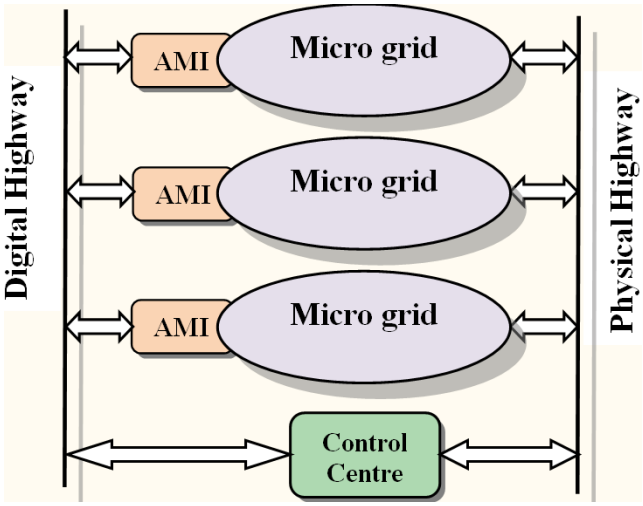

Fig. 5.1 Smart grid topology

Fig. 5.1 shows a smart grid topology, it is seen that there are two transmission lines throughout the smart grid, i.e. the digital highway and the physical highway. The information from the smart meters and fault diagnosis monitors is collected by advanced metering infrastructure (AMI) system, and is then sent to the control center through digital highway. The control center controls the electronic device to optimize the power flow and heal the grid faults in physical highway. Since smart grid is an electricity network that can intelligently integrate the actions of many microgrids, the distinct advantage compared to the conventional power grid is that it can efficiently deliver sustainable, economic and secure electricity supplies. It is noted that the smart grid would and should coexist with the existing electricity grid, and it is required to be self-healing and resilient to system anomalies.

Although much attention has been drawn from all over the world, the development of smart grids is still in the pilot stage. Generally, the key technologies and challenges of smart grids can be summarized as:

- **Power Electronics Control Technology**

Control strategies of power electronics with excellent steady-state and dynamic performance are very important in active and reactive power regulation, current, voltage and frequency control. Though some methods have been proposed such as improved

droop control (to be investigated in Section 5.3), for larger microgrids with numerous inverters, the depth of available literature is less comprehensive and doubts remain as to the scalability of techniques proposed for small-scale systems.

- **New Semiconductor Device**

Silicon-based semiconductor device is reaching its physical limits in power handling and switching frequency capability. Seeking new materials technology is very exigent for smart grid. As the need for renewable energy technologies, energy storage technologies, and smart grid technologies has grown in recent years, power semiconductor devices with high-voltage, high-frequency, and high temperature operation capability is required.

- **Information Technology**

Increasing numbers of smart grid deployments are using the internet technologies, broadband communication, and nondeterministic communication environments. Advanced technique of huge data processing is essential in information collection and energy management within the smart grid.

- **Security and Privacy Issues**

As the grid incorporates smart metering and load management, user and corporate privacy is increasingly becoming an issue. For example, will the power utilities be able to control the customer load without the customer's prior permission? Will the private power consumption information be stolen by cyber-hacker with illegal motivation? Could the electricity consumption patterns lead to disclosure of not only how much energy customers use but also when they are at home, at work, or traveling? These are the security and privacy issues need to be concerned under the construction of the next generation smart grid.

5.2 Smart Microgrid Topology

From the power distribution perspective, to mitigate the negative influences on the grid and incorporate effectively the renewable generations, it is a good idea to combine the local utilization, energy storage, and distributed generation to form a grid-friendly distributed generation system, namely microgrid. In addition, considering that most of

the power outages and disturbances take place in the distribtution network, and therefore, the first step towards the smart grid should start at the bottom of the chain, in the microgrid system.

Based on this background, the next-generation electricity grid is expected to address the major shortcomings of the existing grid. The microgrid is one of such systems, in which the distributed power generation is controlled not only to provide power but also to stabilize the fluctuation caused by the renewable energy sources, such as wind power and photovoltaic. Microgrid system is currently a conceptual solution to fulfil the commitment of reliable power delivery for future power system, which can address issues related to operation, control and stability of the system. Renewable power sources such as wind and hydro offer the best potential for emission free power for future microgrid systems.

Fig. 5.2 shows a typical microgrid application for households, where the PV panels are generally installed on the roof of the houses, an energy storage system (ESS) is also utilized to absorb the surplus energy when the production is greater than the power consumption.

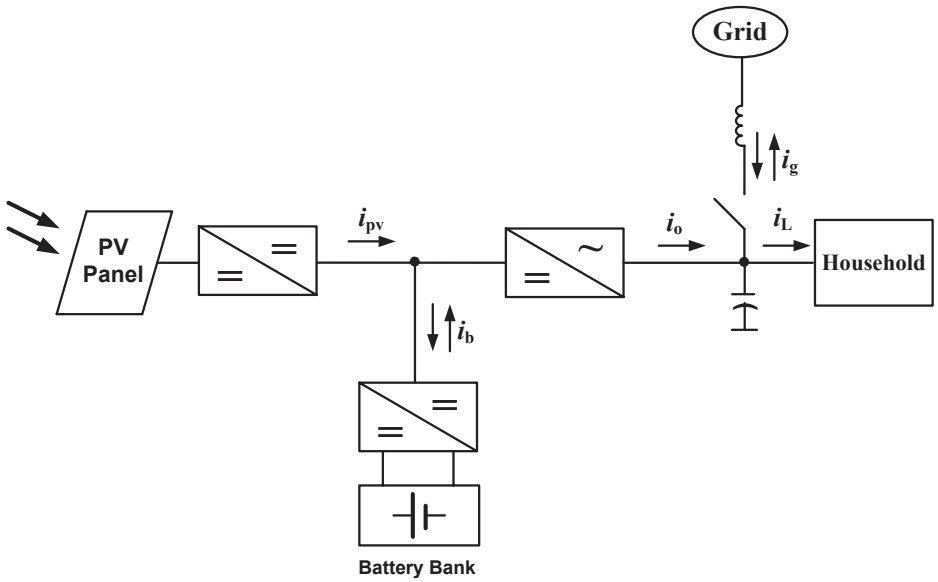

Fig. 5.2 Schematic diagram of a simplified microgrid system

In such a small power system, the DC output of the PV panel is connected to the common DC bus through a DC/DC converter that is used to achieve MPPT, as explained in Chapter 3. On the other hand, an energy storage device, such as the battery bank, is used to smooth the gap between the generation and consumption. It is

interfaced to the common DC bus through a DC/DC converter which allows the bi-directional power flows for battery charging and discharging. The other side on the common DC bus is connected to a DC/AC converter that is connected to an LC filter before connected to the household electric appliances or the utility grid.

For the smart operation of a microgrid system, all the DG units should be able to participate in the optimized control mechanism, from the perspectives of both the loads and the utility grid. Generally the basic requirements for a microgrid to achieve smart operation can be described as:

- Provide high quality power for the loads, i.e., establish a stable output voltage regardless of intermittent power generation and the fluctuated power demand

- Provide utility grid support such as voltage boost and frequency stabilization during grid faults, by exploiting the STATCOM capability of the power electronics within the microgird.

Fig. 5.3 shows a microgrid system with several DG sources at the Commonwealth Scientific and Industrial Research Organisation (CSIRO), Australia. It consists of three control levels. The first level is the DC microgrid including a small capacity wind turbine (WT), PV panel and a battery bank, which are connected to a DC point of common coupling (PCC). At the second level, single-phase inverters are used to interface PVs to the 240V AC PCC while a WT and a gas micro-turbine (MT) supply power to this AC common bus through three-phase converters. A load bank controlled in a binary system is utilized to simulate the fluctuated profile of power consumption. There are also wind turbines, PVs and gas MT with higher capacity at the third level, which is not shown here. In this distributed generation system, the gas MT not only provide a voltage signal to which all other inverters can synchronize to, but also control the voltage and frequency of AC PCC. The control of the DGs and the data acquisition are fulfilled through a supervisory control and data acquisition (SCADA) system.

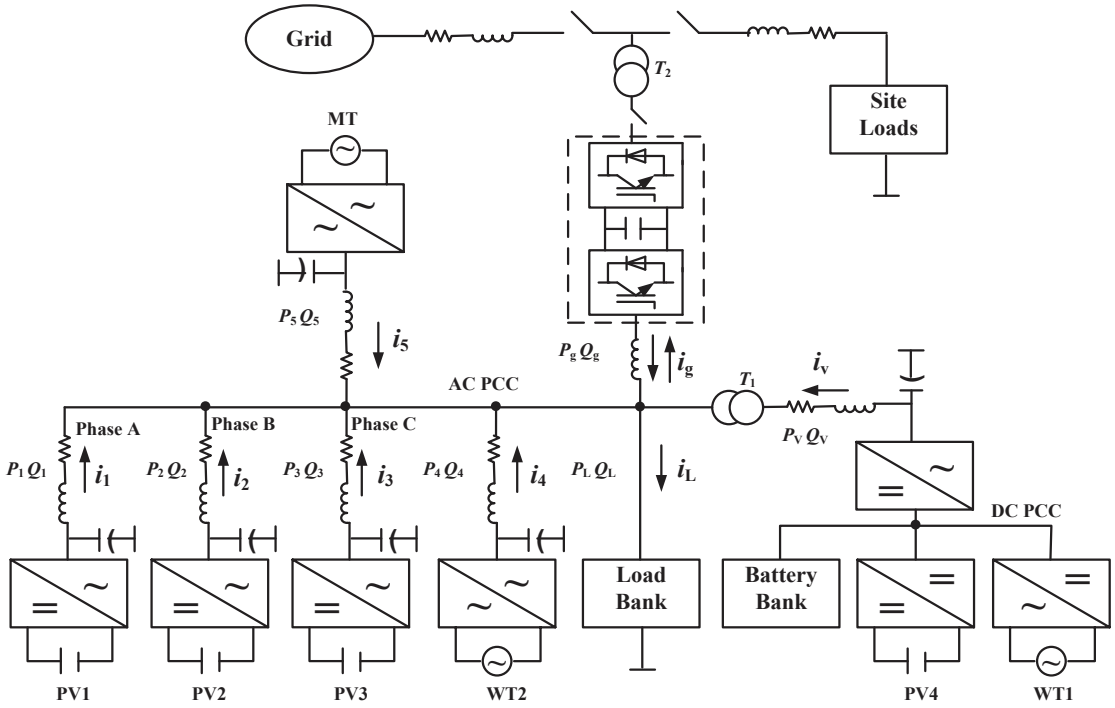

Fig. 5.3 Microgrid configuration in energy centre of CSIRO

In such a system, the major part of the electricity produced by DGs is consumed locally, and the excess will be exported to the grid. If the load is greater than local generation, more power can be obtained from the grid. Besides, it can operate in islanded mode in which electricity power can continue to be supplied to the load bank. The control centre will coordinate/dispatch the generators and energy storage devices according to the demands of the local consumption. The main objectives of this microgrid are to exploit the renewable energy effectively and efficiently [5.5].

Fig. 5.4 shows a proposed microgrid system being built at the University of Technology, Sydney (UTS). Fig. 5.4(a) is the configuration of this microgrid while Fig. 5.4(b) is the laboratory hardware system of this microgrid. In this microgrid, there are distributed generation units including doubly-fed induction generator (DFIG) based wind power system, photovoltaic (PV), and proton exchange membrane (PEM) fuel cell. In addition, there is a charging/discharging battery based ESS to absorb the fluctuation between power generation and power consumption. The real-time information such as voltage and current of each DG unit and the point of common coupling (PCC) at common AC bus are monitored by a radio frequency (RF) module which is sent to the control centre through wireless transmission. The control centre will then determine the future behaviours of the microgrid in order to obtain the optimized power flow and

power quality, according to the current real-time information. After that, the control centre will deliver the control commands to control the power converters of each DG units.

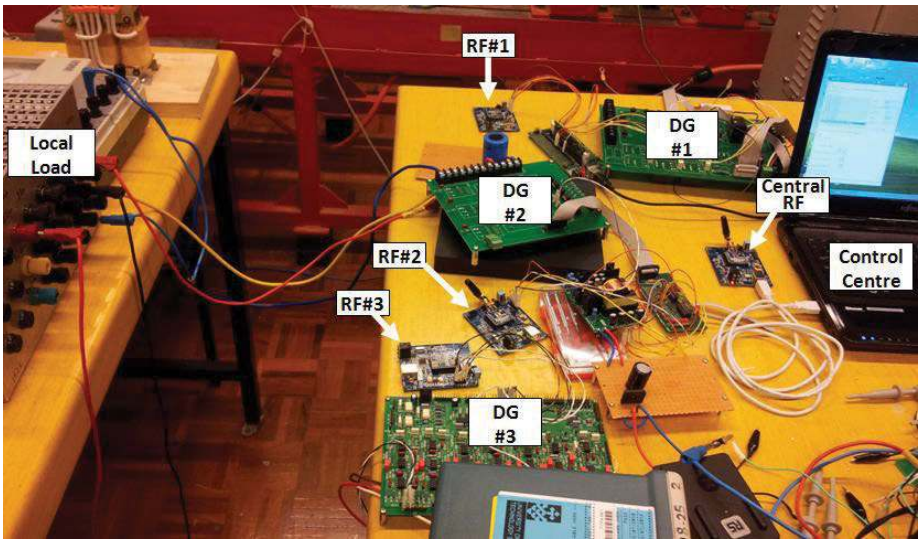

(a)

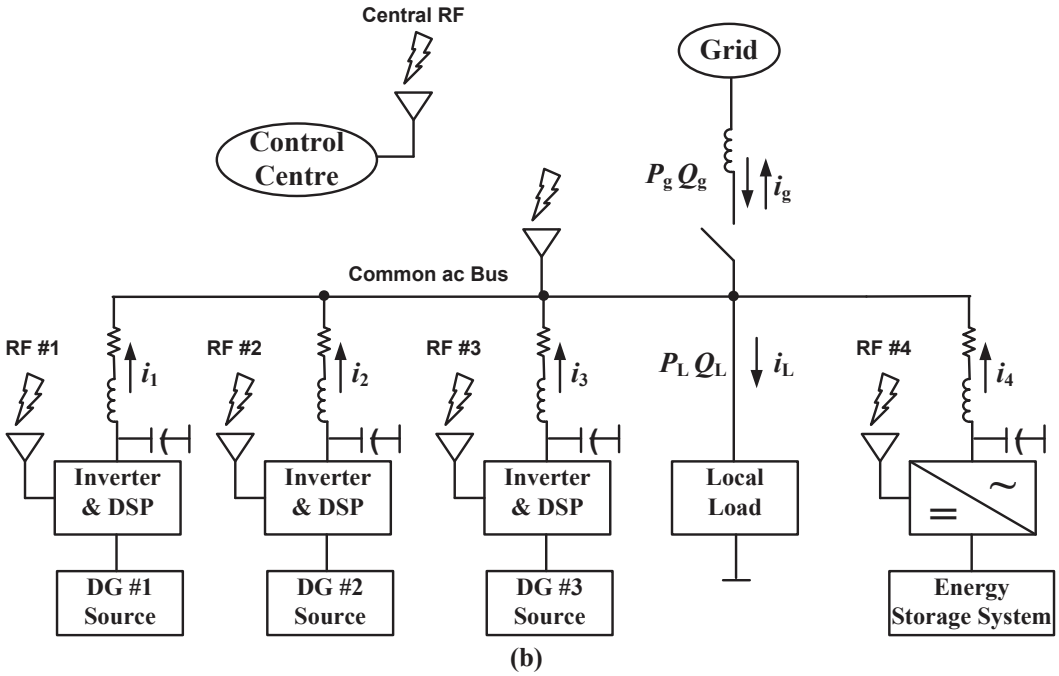

(b)

Fig. 5.4 Smart microgrid, (a) laboratory setup, (b) schematic topology.

The proposed microgrid system can operate in both grid-connected and islanded modes, which integrates the following features:

(1) It incorporates distributed generations capable of meeting local demand as well as feeding the unused energy back to the electricity grid. Such distributed

generations are known as co-generators and often use renewable sources of energy, such as wind and solar.

(2) It services a variety of loads, including residential, office and the whole building.

(3) The control centre will coordinate/dispatch the generators and energy storage devices according to the demands of the local consumption. Therefore, it can smooth the intermittent performance of renewable energy sources and the fluctuating profile of the loads.

(4) It incorporates smart sensors capable of measuring a multitude of consumption parameters (e.g. active power, reactive power, voltage, current, demand and so on) with acceptable precision and accuracy.

(5) It incorporates RF modules capable of sending the real-time information of power generation and consumption and receiving control demands through wireless transmission, which makes it very useful in the applications where long wire interconnection is impractical, such as rural areas and large high-tech building in cities considering the reduction of cost and space.

(6) It can also participate in the voltage support and power quality improvement for the utility grid.

5.3 Control of Parallel Connected Inverters in Microgrids

In order to propose appropriate control strategies for the microgrids, it is necessary to study the operating mechanism between DGs, which will provide insights into the performance of the methods. With a non-radial system configuration due to the presence of DG units, the power control complexity for a microgrid is substantially increased, and the “plug and play” feature is the key to ensure that the installation of additional DG units will not change the control strategies of DG units already in the microgrid. To realize this “plug and play” characteristic, many control techniques have been developed, which can be categorized into two main groups, namely active load sharing method and droop control method, as introduced in Chapter 1. The first one is derived from control approaches of parallel DC/DC converters and UPS, such as centralized [5.6], average load sharing [5.7], and circular chain control [5.8]. However, these

methods need intercommunication lines between DGs to achieve output-voltage regulation and power sharing, which can deteriorate the system stability and reliability.

The second type of control technique of parallel DGs is the droop control without control wire interconnections, which has been commonly used for active and reactive power regulation in microgrids recently [5.9]-[5.15]. In this method, an artificial droop characteristics is introduced, and the active and reactive power supplied by the DGs can be controlled by adjusting the output voltage frequency and amplitude, respectively, according to a pre-defined manner. Therefore, the DGs can meet the new load requirements in a manner determined by its frequency and voltage droop characteristics, which is similar to the power system theory where a generator connected to the utility drops its frequency when the power required increases.

With this technique, the active and reactive power sharing by the inverters is automatic achieved by adjusting the output voltage frequency and amplitude. In order to fix the reference voltage generated by the droop controller, generally a multiloop control scheme is implemented, where an inner inductor current feedback loop and outer filter capacitor voltage feedback loop are used.

Recently much attention has been paid to improve the voltage droop method to obtain better transient performance and more accurate power sharing. For example, better transient response was obtained by introducing derivative-integral terms. The power sharing accuracy was enhanced by employing a virtual power frame transformation or virtual output impedance. In some applications, an angle controller was proposed to minimize frequency variation by drooping the inverter output voltage angle instead of the frequency. For the improvement of the voltage quality, the voltage deviation caused by droop method is compensated by a multilayer control strategy.

5.3.1 Voltage droop method

A. Voltage droop for power sharing

Fig. 5.5 shows the equivalent circuit of DGs connected to a common AC bus through inverters.

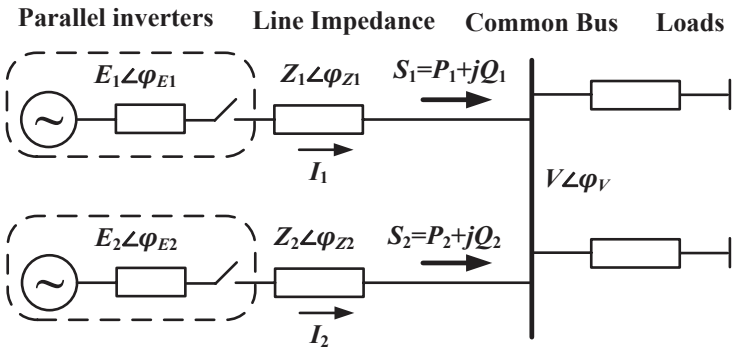

Fig. 5.5 Equivalent circuit of parallel-inverters-based microgrid

The active and reactive power flow from the DG to the common AC bus can be expressed as [5.16]

$$P=\frac{E^2\cos\varphi_Z-EV\cos(\varphi_E-\varphi_V+\varphi_Z)}{Z} \tag{5.1}$$

$$Q=\frac{E^2\sin\varphi_Z-EV\sin(\varphi_E-\varphi_V+\varphi_Z)}{Z} \tag{5.2}$$

where E and V are the magnitudes of the inverter output voltage and AC common bus voltage, Z is the line impedance. For a purely inductive line impedance, the line resistance may be neglected, i.e. φ_Z=90°, and thus (5.1) and (5.2) become

$$P=\frac{EV\sin(\varphi_E-\varphi_V)}{X} \tag{5.3}$$

$$Q=\frac{E^2-EV\cos(\varphi_E-\varphi_V)}{X} \tag{5.4}$$

where X is the line reactance.

Further, considering that the phase angle difference $\delta=\varphi_E-\varphi_V$ is typically small, we can assume $\sin(\delta)=\delta$ and $\cos(\delta)=1$, and consequently,

$$P=\frac{EV\delta}{X} \tag{5.5}$$

$$Q=\frac{E(E-V)}{X} \tag{5.6}$$

As a consequence, the flow of active power is linearly dependent on the phase angle difference (δ) and the flow of reactive power is linearly dependent on the voltage magnitude difference (E-V). At this point, similar to the power system theory where a

generator connected to the utility drops its frequency when the power required increases, and a voltage and frequency droop control method for microgrid can be defined as

$$\omega = \omega^* - m(P - P^*) \tag{5.7}$$

$$E = E^* - n(Q - Q^*) \tag{5.8}$$

where, P^* and Q^* are the desired active and reactive power, ω^* and E^* the inverter normal output frequency and voltage amplitude, and m and n the slopes of the droop characteristics. Fig. 5.6 depicts the droop characteristics. For example, in P- ω droop control, the active power demand changes in load can be taken up by the DGs in a predetermined manner and the wireless control of parallel inverters is achieved with the utilization of system frequency as a communication link within a microgrid.

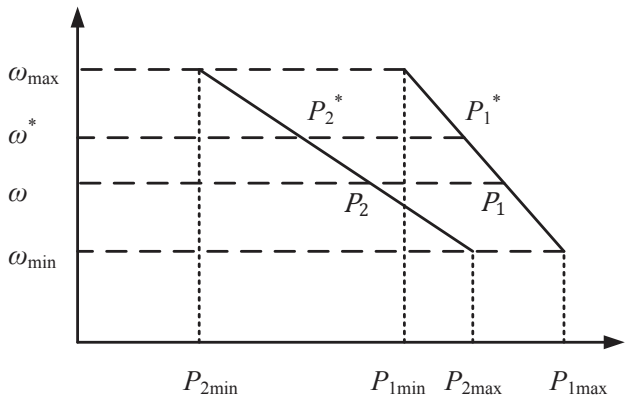

(a)

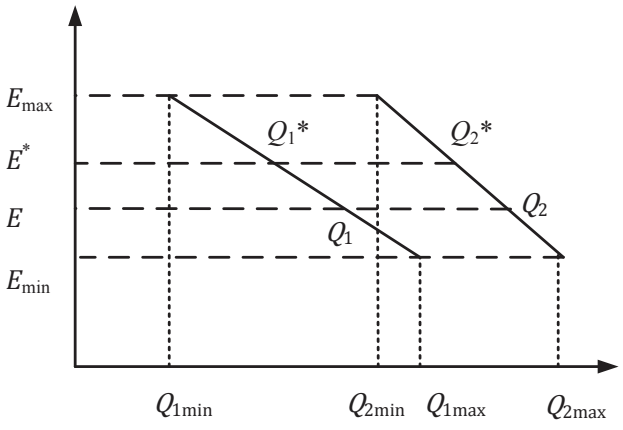

(b)

Fig. 5.6 Droop characteristics, (a) *P* - ω droop characteristics, (b) *Q* - *E* droop characteristics.

It is worth mentioning that this method is subject to two particular problems as follows:

Power coupling: (5.5) and (5.6) are derived based on the assumption that the line impedance is mainly inductive. However, in some cases, line resistance cannot be neglected, especially in a low-voltage microgrid. As a result, the change of δ and E can affect both the active and reactive power flows, which can be explained from (5.1) and (5.2).

Slopes selection: Even the power coupling can be avoided with improved strategies such as virtual power frame transformation or virtual output impedance. The tradeoff between the power sharing accuracy and the voltage frequency and magnitude deviation should be taken into account in the selection of m, n.

B. Multi-loop feedback control of inverters

After the droop controller is design, the inverters should be controlled to produce the specified voltage reference from the droop controller. Regarding to the inverter control, many control techniques have been developed for power inverters in the last few decades, such as multi-loop feedback control [5.17], [5.18], direct flux control [5.19] and direct power control [5.20], [5.21]. Since the output of the droop controller is the voltage reference, the multi-loop feedback control is very suitable to be applied here because it can be used to generate an output voltage with a specified frequency and amplitude within the inverter capacity.

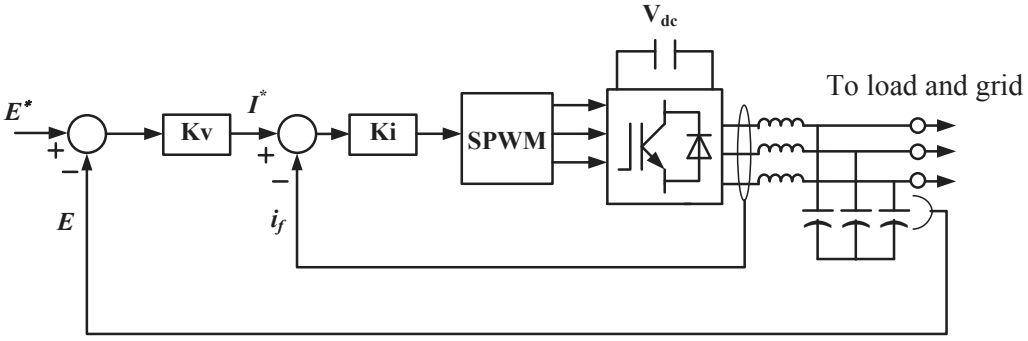

Fig. 5.7 Control block of voltage and current feedback control.

Fig. 5.7 shows the voltage and current feedback control diagram, which including the inner current control loop and the outer voltage control loop. In the voltage control loop, a proportional compensator is used to force the inverter output voltage to track their reference values. The outputs of this voltage compensator together with the inner filter inductor currents are then fed to an inner current compensator to produce modulating signals for the sinusoidal pulse-width modulator (SPWM). This control technique features simple structure and quick transient response though tuning effort of PI regulators is required.

C. Microgrid control

The microgrid can operate in grid-connected or islanded mode. In the grid-connected operation, the DGs together with the utility grid supply power to the local loads. If the power generation is greater than the load consumption, the excess will be injected into the grid. On the other hand, if the power generation is smaller than the load demand, more power will be imported from the grid. In the islanded operation, the DGs should be able to provide a stable voltage at PCC and pick up the loads automatically. In addition, the microgrid should be re-connected to the utility grid seamlessly when the grid is available.

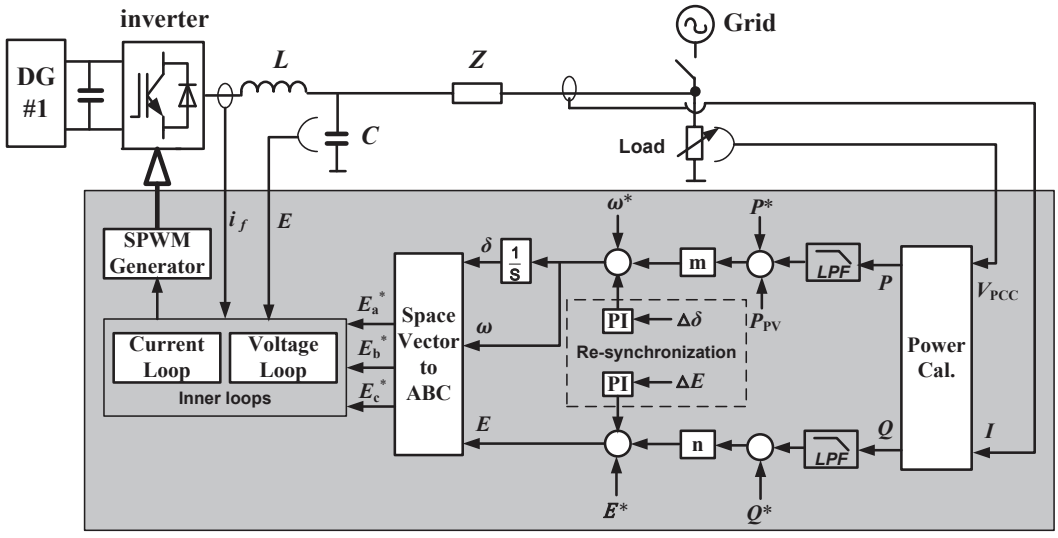

Fig. 5.8 Control diagram of the whole microgrid control based on voltage droop method.

Fig 5.8 illustrates the control strategy of microgirds, which consists of an outer droop controller and the inner inverter controller. To control the parallel inverters, the instantaneous active and reactive powers are firstly calculated from the PCC voltage and the inverter output current. The measured powers are then delivered into a droop controller to achieve proper power sharing between DGs. Next, the voltage reference from the droop controller is sent to the inner voltage/current loop, which utilizes the multi-loop feedback control technique to control the inverter to produce this specified voltage reference, as depicted previously.

In the islanded mode, the static transfer switch (STS) disconnects the microgrid from the main grid, and the total power demand of the load is supplied by the DGs. With any load change, each DG must regulate its frequency and magnitude of output voltage to meet the new load requirement in a predetermined droop characteristic. In the grid-connected mode, the microgrid frequency is fixed to the utility frequency. The DG units are supplying their rated active and reactive powers at rated frequency and voltage. When the load requirement is less than the rated capacity of the DGs, the excess power flows to the utility. In contrast, when the load requirement is greater than the rated capacity of the DGs, more power would be imported from the utility.

On the other hand, a smooth transfer between the grid-connected and islanded modes is also essential for the reliability of a microgrid. Here, a simple synchronization scheme is developed. As shown in Fig. 5.7, in the re-synchronization compensator, the amplitude error ΔE and the phase error $\Delta\delta$ of the grid voltage and the PCC voltage are delivered to a PI regulator, respectively. The outputs of these two regulators are fed into the outputs of the droop controller. In this way, the PCC voltage can track the grid voltage closely. Once the grid synchronization process is completed, the microgrid is ready for the grid connection.

D. Numerical simulation

The performance of the control strategy has been tested in simulation using Matlab/Simulink. A microgrid with two identical DG units, as shown in Fig. 5.5, is employed. In this simulation, there is one local load connected to each DG unit and one common load connected to common AC bus, the microgrid is connected to utility through a STS. The system parameters are listed in Table 5.1 [5.11].

TABLE 5.1 System Parameters of Microgrid Using Voltage Droop Method

Nominal utility voltage	380 V	ω^*	50 Hz
Switching frequency	2 kHz	ω_{min}	48.5 Hz
DC source voltage	1000 V	E^*	310 V
Filter inductance	0.9 mH	E_{min}	290 V
Filter capacitance	250 μF	P_1^*	35 kW
Line impedance	0.05 Ω, 1.6 mH	Q_1^*	15 kVar
Rating of each DG	70 kVA	P_2^*	30 kW
Rating of Load 1	30 kW, 10 kVar	Q_2^*	10 kVar
Rating of Load 2	20 kW, 6 kVar	m_1, n_1	-3/7e4, -4/8e4
Rating of common load	13 kW, 10 kVar	m_2, n_2	-3/1.1e4, -1/3e3

At the beginning, the microgrid operates in the islanded mode. Fig. 5.9 shows the active and reactive power sharing within the microgrid. P_1, P_2, and P_g denote the active power output from DG1 and DG2, and the active power flowing from the utility, respectively. On the other hand, Q_1, Q_2, and Q_g denote the reactive power output from DG1 and DG2, and the reactive power flowing from the utility, respectively. In islanded mode, DG1 and DG2 together supply all the active and reactive power required by the local loads and the common load according to their frequency and voltage droop characteristics. It can be seen that DG1 carries a larger share of active power since it has a stiffer slope while P_g=0 W and Q_g=0 VAR. At 0.1 s, the power consumption of local load 1 raises to its rated value (30 kW, 10 kVAR), DG1 and DG2 increase the output power automatically to meet the new power requirement. The DG output current and the grid current are shown in Fig. 5.10.

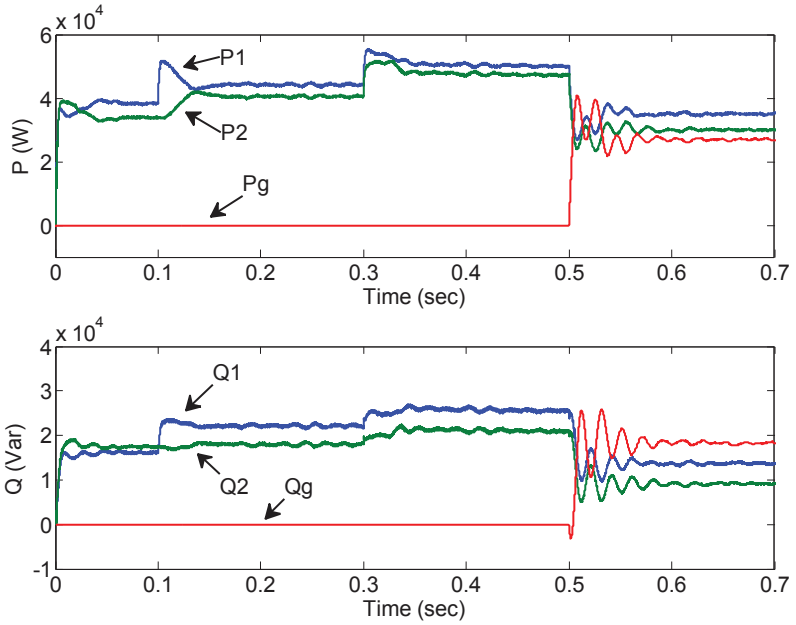

Fig. 5.9 Power flows within microgrid.

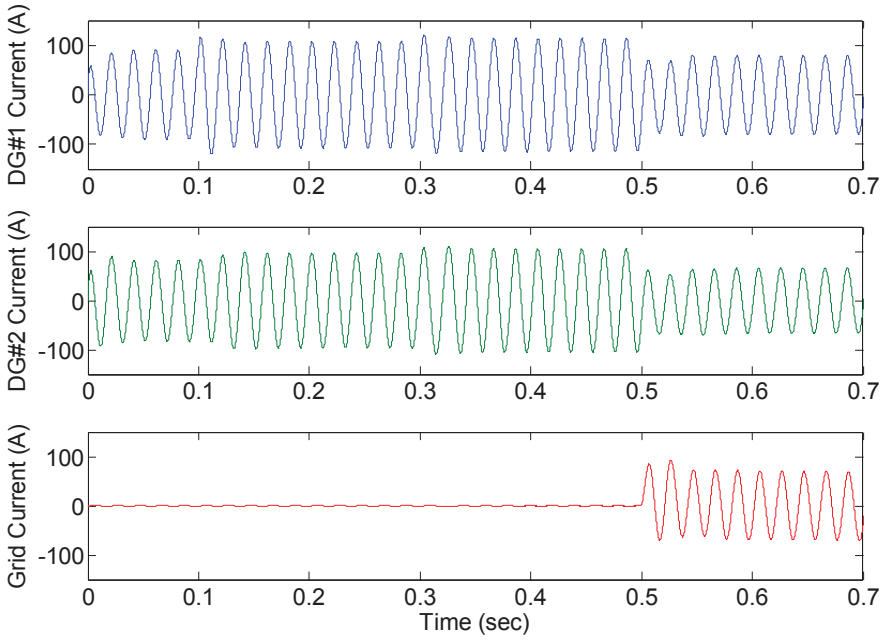

Fig. 5.10 Per phase current within the microgrid.

At 0.3 s, the microgrid starts to synchronize, the increase in both active and reactive output power of DGs can be observed during the process of synchronization. After reconnection (0.5 s) of the microgrid and utility, it is seen that the output powers of DG1 and DGs drop back to their referenced dispatched values (P_1^*, Q_1^*, P_2^*, and Q_2^*) because part of the power flows from the utility in grid-connected mode.

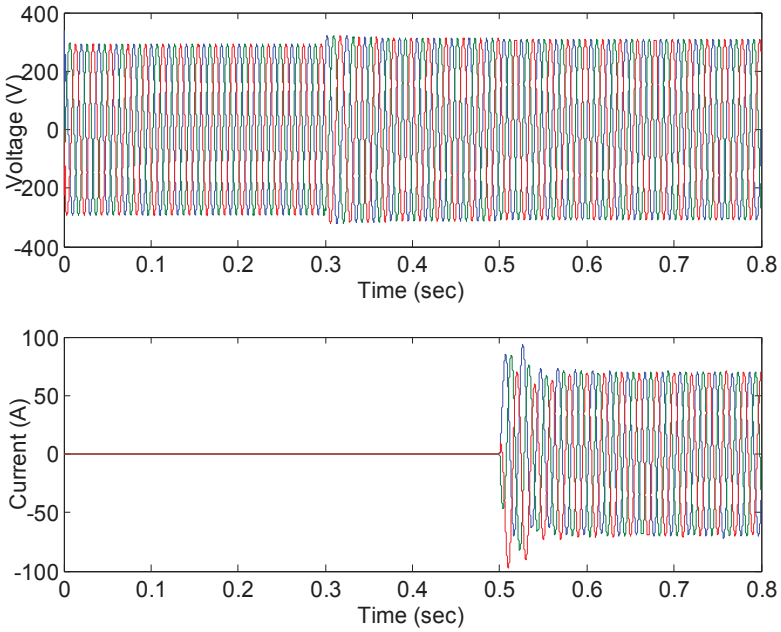

Fig. 5.11 Response of voltage and AC common bus and current through STS

The dynamic response of AC common bus voltage and STS current can be found in Fig. 5.11. The AC common bus voltage is very stable during the grid connection process while slight overshoot current can be observed in the STS at 0.5 s. The synchronization process can be observed in Fig. 5.12, the AC common bus voltage can track the utility grid voltage in less than 100 ms in terms of frequency, magnitude and phase angle, which guarantees the smooth and fast transition from the islanded mode to the grid connected mode.

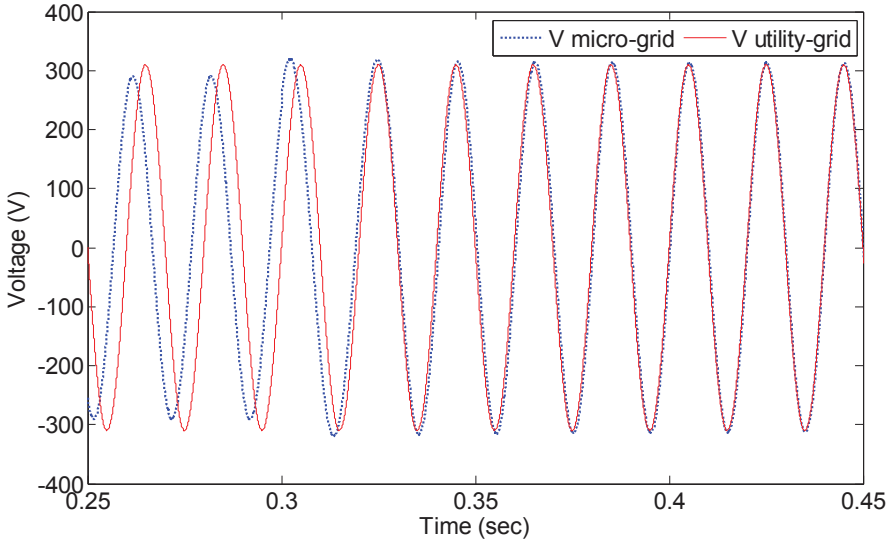

Fig. 5.12 Synchronization of micro- and utility-grids.

5.3.2 Flux droop method

The droop method illustrated in the previous section droops the voltage, i.e. the active and reactive power sharing by the inverters is achieved by adjusting the output voltage frequency and amplitude. To produce the specified voltage from the droop controller, generally a multi-loop control scheme is implemented, where an inner filter inductor current feedback loop and outer filter capacitor voltage feedback loop are used [5.22]-[5.24]. However, PI regulators are required, which complicate the control system. Besides, much tuning effort is needed to obtain system stability, which makes it not easy to be implemented in practical. In [5.9], the voltage and frequency from the droop controller are delivered to the frequency controller and voltage controller respectively to produce the referenced inverter flux, and the inverter is then controlled to generate this specified flux using a direct flux method. However, this strategy is very complicated and the system performance is compromised.

Recently, much attention has been paid to improve the voltage droop method to obtain better transient performance and more accurate power sharing. For example, better transient response was obtained by introducing the derivative-integral terms [5.10], [5.25]-[5.27]. The power sharing accuracy was enhanced by employing a virtual power frame transformation or virtual impedance [5.12], [5.13]. In [5.28], an angle controller was proposed to minimize frequency variation by drooping the inverter output voltage angle instead of the frequency. The voltage deviation caused by droop method is compensated by a multilayer control strategy in [5.29] and [5.30]. However, all these methods are developed based on the voltage droop, i.e. on the $\omega - P$ and $V - Q$ characteristics, and therefore, the conventional multi-feedback loops are unavoidable.

Here, an alternative droop method is developed that active and reactive power sharing can be achieved as well as the conventional voltage droop control, and at the same time the control system can be simplified without multi-feedback loops and the complex PI controllers. This is the initial motivation of this work.

A. Proposed flux droop control

In the conventional droop method, the control loop makes tight adjustment over the output voltage frequency and amplitude of the inverter, in order to compensate the active and reactive power unbalances. A question needs to be answered is if there are

any other droop methods to achieve load sharing rather than voltage droop. In this section, the mathematical relation between the inverter flux and the active and reactive powers drawn to the common AC bus will be deduced, based on which a new droop method will be proposed.

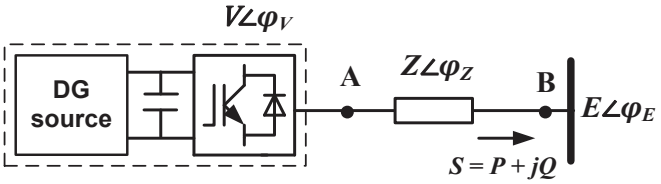

Fig. 5.13 Equivalent circuit of a DG unit connected to a common AC bus

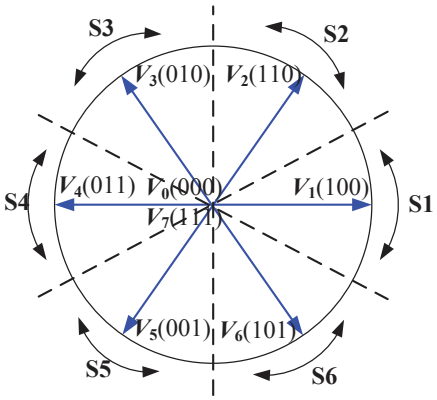

Fig. 5.14 Possible voltage vectors generated by the inverter

A DG unit connected to a common AC bus through a power inverter is shown in Fig. 5.13. The three-phase two level inverter output voltage can be expressed in complex space vectors as

$$\boldsymbol{V}_i = \begin{cases} \frac{2}{3} V_{dc} e^{j(i-1)\frac{\pi}{3}} & (i = 1 \cdots 6) \\ 0 & (i = 0, 7) \end{cases} \tag{5.9}$$

Determined by the switching states, $\boldsymbol{V}_\mathrm{i}$ can be controlled to eight space voltage vectors, as shown in Fig. 5.14. The mathematical equation of the system equivalent circuit can be described as

$$\boldsymbol{V} = R\boldsymbol{I} + L\frac{d\boldsymbol{I}}{dt} + \boldsymbol{E} \tag{5.10}$$

$$\boldsymbol{S} = P + jQ = \boldsymbol{I}^* \boldsymbol{E} \tag{5.11}$$

where $\boldsymbol{V}$, $\boldsymbol{E}$, and $\boldsymbol{I}$ are the inverter output voltage vector, the common AC bus voltage vector, the line current vector, respectively, R is the line resistance, L the line inductance, P and Q are the active and reactive powers flow to the common AC bus, and * denotes the complex conjugate. Similar to the flux definition in an electrical machine, the flux vector of the inverter at node A and the flux vector at node B can be defined as

$$\boldsymbol{\psi}_V = \int_{-\infty}^{t} \boldsymbol{V} d\tau \tag{5.12}$$

$$\boldsymbol{\psi}_E = \int_{-\infty}^{t} \boldsymbol{E} d\tau \tag{5.13}$$

Subsequently, the inverter flux vector and the flux vector at node B can be written as

$$\varphi_{fV} = \varphi_V - \frac{\pi}{2} \tag{5.14}$$

$$|\boldsymbol{\psi}_V| = \frac{|\boldsymbol{V}|}{\omega} \tag{5.15}$$

$$\varphi_{fE} = \varphi_E - \frac{\pi}{2} \tag{5.16}$$

$$|\boldsymbol{\psi}_E| = \frac{|\boldsymbol{E}|}{\omega} \tag{5.17}$$

where φ_{fV} and φ_{fE} are the phase angles of the inverter flux vector ψ_V and the node B flux vector ψ_E, respectively, while φ_V and φ_E are the phase angles of the inverter output voltage vector $\boldsymbol{V}$ and the node B voltage vector $\boldsymbol{E}$, respectively, and ω is the angular frequency of the voltages. As in most practical cases, the line impedance is mainly inductive, and if neglecting the line resistance, combining (5.10), (5.12) and (5.13) yields

$$\boldsymbol{I} = \frac{1}{L}(\boldsymbol{\psi}_V - \boldsymbol{\psi}_E) \tag{5.18}$$

Substituting (5.18) into (5.11), we can obtain

$$S = \frac{1}{L}(\boldsymbol{\psi}_V - \boldsymbol{\psi}_E)^* \boldsymbol{E} \tag{5.19}$$

Substituting (5.14), (5.16) and (5.17) into (5.19) yields

$$S = \frac{1}{L}(|\boldsymbol{\psi}_V| e^{j(\varphi_V - \frac{\pi}{2})} - |\boldsymbol{\psi}_E| e^{j(\varphi_E - \frac{\pi}{2})})^* \omega |\boldsymbol{\psi}_E| e^{j\varphi_E} \tag{5.20}$$

Consequently, the apparent power flows from the DG unit to the common AC bus can be derived as

$$S=\frac{\omega}{L}\left[|\boldsymbol{\psi}_E||\boldsymbol{\psi}_V|\sin(\varphi_V-\varphi_E)+j\left(|\boldsymbol{\psi}_E||\boldsymbol{\psi}_V|\cos(\varphi_V-\varphi_E)-|\boldsymbol{\psi}_E|^2\right)\right] \tag{5.21}$$

Therefore, the active power and reactive power can be expressed as

$$P=\frac{\omega}{L}|\boldsymbol{\psi}_E||\boldsymbol{\psi}_V|\sin\delta \tag{5.22}$$

$$Q=\frac{\omega}{L}\left(|\boldsymbol{\psi}_E||\boldsymbol{\psi}_V|\cos\delta-|\boldsymbol{\psi}_E|^2\right) \tag{5.23}$$

where $\delta = \varphi_{fV} - \varphi_{fE}$. Since typically δ is very small, we can assume $\sin(\delta) = \delta$ and $\cos(\delta) = 1$, and consequently obtain

$$P=\frac{\omega}{L}|\boldsymbol{\psi}_E||\boldsymbol{\psi}_V|\delta \tag{5.24}$$

$$Q=\frac{\omega|\boldsymbol{\psi}_E|}{L}\left(|\boldsymbol{\psi}_V|-|\boldsymbol{\psi}_E|\right) \tag{5.25}$$

Therefore, the flow of active power is proportional to the flux phase angle difference δ and the flow of reactive power is proportional to the flux magnitude difference ($|\boldsymbol{\psi}_V|$ - $|\boldsymbol{\psi}_E|$). Based on the analysis above, we propose a new droop method by drooping the inverter output flux and flux angle as

$$\delta=\delta^*-m(P^*-P) \tag{5.26}$$

$$|\boldsymbol{\psi}_V|=|\boldsymbol{\psi}_V|^*-n(Q^*-Q) \tag{5.27}$$

where δ * is the nominal phase angle difference of $\boldsymbol{\psi}_V$ and $\boldsymbol{\psi}_E$, $|\boldsymbol{\psi}_V|$* is the nominal amplitude of the inverter flux, P* and Q* are the power rating of the DG unit, and m and n are the slopes of the $P - \delta$ characteristics and the $Q - |\boldsymbol{\psi}_V|$ characteristics, respectively. For illustration, consider the $P - \delta$ droop characteristics as shown in Fig. 5.15 for a microgrid containing two-DGs, the active power is dispatched between these two DGs by drooping their own flux angle difference δ automatically. Once the load changes, the power outputs of both DG units will immediately be changed in accordance with their droop characteristics to supply power to all critical loads at a new steady-state of δ.

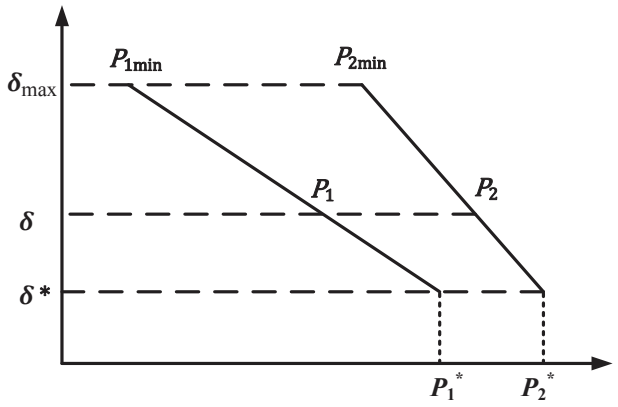

Fig. 5.15 P – δ characteristic

B. Small signal analysis

In order to show the system stability and the transient response, a small-signal analysis is provided, allowing the designer to adjust the control parameters. The small-signal dynamics of the $P-\delta$ droop controller can be obtained by linearizing (5.22) and (5.26) as

$$\Delta\delta(s) = \Delta\delta^*(s) - m(\Delta P^*(s) - \Delta P(s)) \tag{5.28}$$

$$\Delta P(s) = G_p \cdot \Delta\delta(s) \tag{5.29}$$

where

$$G_p = \frac{\omega}{L}|\boldsymbol{\psi}_E||\boldsymbol{\psi}_V|\cos\delta$$

Modeling the low-pass filters with a first-order approximation for the instantaneous active power calculation, the $P-\delta$ droop controller equivalent circuit of the small signal model can be illustrated as shown in Fig. 5.16, where Δ denotes the perturbed values, and ω_c is the cut-off angular frequency of the low-pass filters.

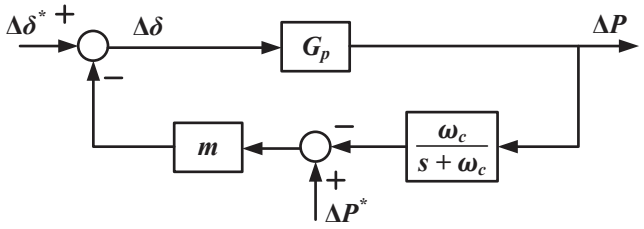

Fig. 5.16 Equivalent circuit of small signal model of the P – δ droop controller

By deriving the closed loop transfer function using ΔP as output and $\Delta\delta^*$ and ΔP^* as input according to the principle of superposition, one can obtain

$$\Delta P(s) = \frac{G_p(s+\omega_c)}{s+\omega_c-\omega_c mG_p}\Delta\delta^*(s) - \frac{mG_p(s+\omega_c)}{s+\omega_c-\omega_c mG_p}\Delta P^*(s) \tag{5.30}$$

The characteristic equation can be derived from (5.30) as

$$s+\omega_c-\omega_c mG_p = 0 \tag{5.31}$$

Subsequently, the eigenvalue of (5.31) can be expressed as

$$\lambda_p = \omega_c(mG_p - 1) \tag{5.32}$$

Similarly, the small-signal dynamics of the $Q - |\psi_V|$ droop controller can be obtained by linearizing (5.23) and (5.27) as

$$\Delta|\psi_V|(s) = \Delta|\psi_V|^*(s) - n(\Delta Q^*(s) - \Delta Q(s)) \tag{5.33}$$

$$\Delta Q(s) = G_q \cdot \Delta|\psi_V|(s) \tag{5.34}$$

where

$$G_q = \frac{\omega}{L}|\psi_E|\cos\delta$$

Modeling the low-pass filters with a first-order approximation for the instantaneous reactive power calculation, the $Q - |\psi_V|$ droop controller equivalent circuit of the small signal model can be illustrated as shown in Fig. 5.17.

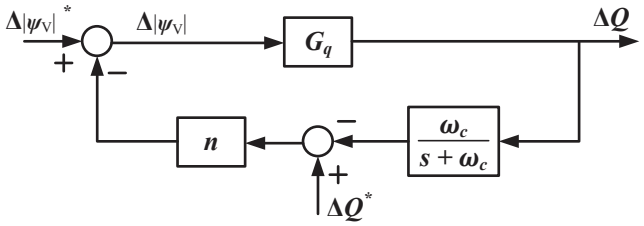

Fig. 5.17 Equivalent circuit of small signal model of the $Q - |\psi_V|$ droop controller

By deriving the closed loop transfer function using ΔQ as output and $\Delta|\psi_V|^*$ and ΔQ^* as input according to the principle of superposition, one can obtain

$$\Delta Q(s) = \frac{G_q(s+\omega_c)}{s+\omega_c-\omega_c nG_q}\Delta|\psi_V|^*(s) - \frac{nG_q(s+\omega_c)}{s+\omega_c-\omega_c nG_q}\Delta Q^*(s) \tag{5.35}$$

The characteristic equation can be derived from (5.35) as

$$s + \omega_c - \omega_c n G_q = 0 \tag{5.36}$$

Subsequently, the eigenvalue of (5.36) can be expressed as

$$\lambda_q = \omega_c (n G_q - 1) \tag{5.37}$$

According to (5.32) and (5.37), it can be seen that the eigenvalues placement of system varies with the droop slopes m and n, illustrating the stability limits which can be used to adjust the transient response of the system.

C. Coefficients selection

Besides to ensure the system stability, the selection of the slopes m and n should also take into account the tradeoff between the power sharing accuracy and the flux deviation, which in return will influence the voltage and frequency deviation. Consider the system stability analysis based on the small signal model previously, and here m and n are chosen to ensure steady state and system stability as

$$m = \frac{\delta^* - \delta_{\max}}{P^* - P_{\min}} \tag{5.38}$$

$$n = \frac{|\boldsymbol{\psi}_V|^* - |\boldsymbol{\psi}_V|_{\max}}{Q^* - Q_{\min}} \tag{5.39}$$

Since the power ratings of DGs and the nominal flux amplitude and phase angle difference are generally fixed for a given microgrid, consequently, the design of m and n is to adjust $\delta_{\max}$, $P_{\min}$, $|\boldsymbol{\psi}_V|_{\max}$, and $Q_{\min}$, taking into account the system ability, power sharing accuracy and the flux deviation.

D. Direct flux control of inverters

After the flux reference is obtained from the droop controller, the inverter is controlled to produce this specific flux in order to achieve proper power sharing between DG units. For the voltage droop method, the voltage reference from the droop controller is generally controlled using multi-loops approaches, i.e., outer voltage and inner current feedback control. For the proposed flux droop method, direct flux control strategy can be employed to generate this specific flux reference since it has been shown to have good dynamic and steady state response [5.9], [5.31].

In direct flux control, two variables that are controlled directly by the inverter are $|\boldsymbol{\psi}_V|$ and δ, in other words, the vector $\boldsymbol{\psi}_V$ is controlled to have a specified magnitude and a specified position relative to the vector $\boldsymbol{\psi}_E$. For the conventional switching-table-based direct flux control strategy (SDFC), the signals d_F and d_A are first generated by two hysteresis comparators according to the tracking errors between the estimated and referenced values of $|\boldsymbol{\psi}_V|$ and δ. The voltage vector is then selected from a look-up table according to d_F, d_A and the inverter flux position φ_{fV}. The switching selection of direct flux control is shown in Table 5.2 [5.9], where d_F equal to 1 if $|\boldsymbol{\psi}_V|^* > |\boldsymbol{\psi}_V|$, d_F equal to 0 if $|\boldsymbol{\psi}_V|^* < |\boldsymbol{\psi}_V|$; d_A equal to 1 if $\delta^* > \delta$, d_A equal to 0 if $\delta^* < \delta$. k is the sector number in the $\alpha - \beta$ plane given by the inverter flux position given by φ_{fV}, as depicted in Fig. 5.13. In this way, $|\boldsymbol{\psi}_V|$ and δ_p are controlled within specified hysteresis bands by means of inverter switching, and therefore, the locus of inverter flux vector is regulated along an approximate circular path.

TABLE 5.2 Vector Selection Strategy of DFC

	Vector
$d_F = 1$	$\boldsymbol{V}_{k+1}$
$d_F = 0$	$\boldsymbol{V}_{k+2}$
Zero vector is applied to when $d_A = 1$	

E. Proposed flux droop control strategy of microgrids

In this section, we will develop a whole control strategy for microgrids. Fig. 5.18 shows the block diagram of the control strategy of one inverter connected to the microgrid, including two control blocks, which are the proposed flux droop control and the proposed MPDFC strategy.

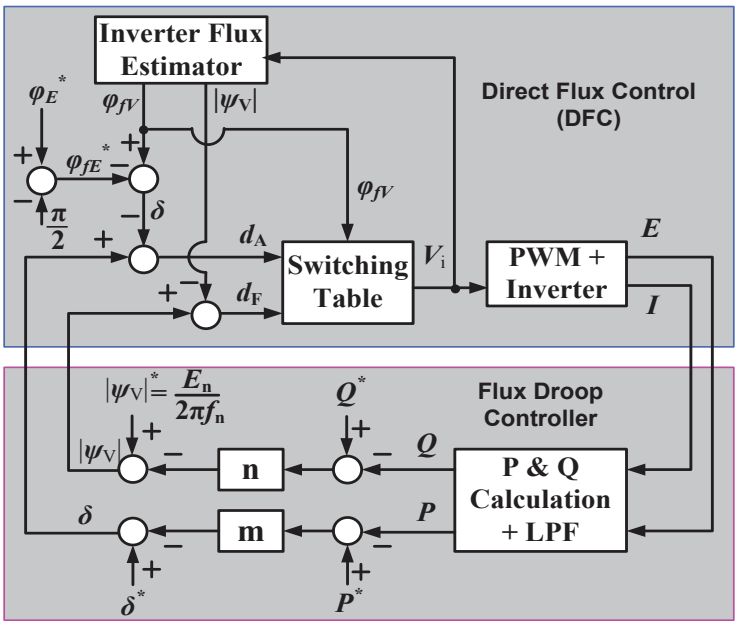

Fig. 5.18 Block diagram of the proposed flux droop control strategy of micrigrods

In the flux droop control, the active and reactive powers P and Q supplied by the DGs to the load are calculated from the line current $\boldsymbol{I}$ and load-side voltage $\boldsymbol{E}$ using (5.11) and delivered to the low-pass filters (LPF). The average values of instantaneous powers are then sent to the flux droop characteristics using (5.26) and (5.27) to obtain the specific inverter flux. In the MPDFC block, the inverter flux is firstly estimated from the current inverter switching states [5.35]. In the flux droop control, the active and reactive powers P and Q supplied by the DGs to the load are calculated from the line current $\boldsymbol{I}$ and load-side voltage $\boldsymbol{E}$, and then sent to the flux droop characteristics to obtain the specific inverter flux. Finally the inverter is controlled to generate this flux reference using the DFC approach.

F. Numerical simulation

Fig. 5.19 shows the test system of a two-DG islanded microgrid, which is identical to the one introduced in [5.9]. The system parameters are listed in Table 5.3. The test was carried out using MATLAB/Simulink. The system sampling frequency is 20 kHz, and the average switching frequency of each inverter is 3.235 kHz. The load resistance R_{E2} is decreased suddenly to half its values at 0.2 s.

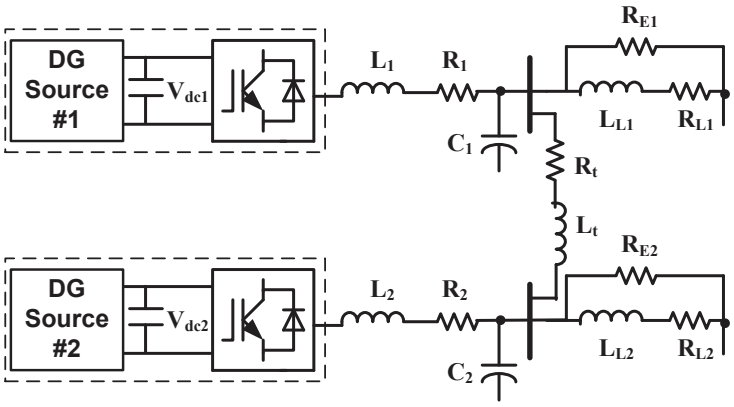

Fig. 5.19 Microgrid structure under study

TABLE 5.3 System Parameters of Microgrid Using Flux Droop Method

Item	Symbol	Value	Unit
Line inductance	L_1, L_2	8	mH
Line resistance	R_1, R_2	0.05	Ω
Filter Capacitance	C_1, C_2	150	uF
Load inductance	L_{L1}, L_{L2}	40	mH
Load resistance	R_{L1}, R_{L2}	16	Ω
Load resistance	R_{E1}, R_{E2}	30	Ω
Tie-line inductance	L_t	6	mH
Tie-line resistance	R_t	0.4	Ω
Nominal line to line Voltage	E_n	3.6	kV rms
Nominal frequency	f_n	60	Hz
DGs output DC voltage	V_{dc1}, V_{dc2}	10	kV
Cut-off angular frequency	ω_c	10	rad/s
Nominal inverter flux amplitude	$\lvert\psi_V\rvert^*$	7.797	Wb
Nominal flux angle difference	δ^*	0.2	rads
Nominal active power of DG #1	P_1^*	0.75	MW
Nominal reactive power of DG #1	Q_1^*	0.2	MVAr
Nominal active power of DG #2	P_2^*	0.6	MW
Nominal reactive power of DG #2	Q_2^*	0.1	MVAr
Slope of $P-\delta$ droop of DG #1	m_1	-2.67×10^{-7}	rad/W

Slope of $Q - \|\psi_V\|$ droop of DG #1	n_1	-2.65×10^{-7}	Wb/VAr
Slope of $P - \delta$ droop of DG #2	m_2	-3.33×10^{-7}	rad/W
Slope of $Q - \|\psi_V\|$ droop of DG #2	n_2	-9.55×10^{-7}	Wb/VAr

Fig. 5.20(a) shows the power sharing. It can be seen that the two DGs can take up the load changes immediately. The system reaches a new steady-state within only 10 ms, and DG #1 carries a larger share of active power because it has a stiffer slope. Fig. 5.20(b) shows the details of the proposed flux droop control algorithm. It can be found that δ was decreased automatically in order to increase the active power output when the load changes, while no obvious change in $|\psi_V|$ can be observed since there is no reactive power change in the load demand. Because of the excellent dynamic performance of the DFC strategy, the actual values of $|\psi_V|$ and δ (blue curves) are well tracking the references (red curves) from the output of the flux droop controller. Fig. 5.21 presents the line-to-line voltage across the capacitor C_1 of DG #1, and as shown, it is very sinusoidal and stable before and after load is changed.

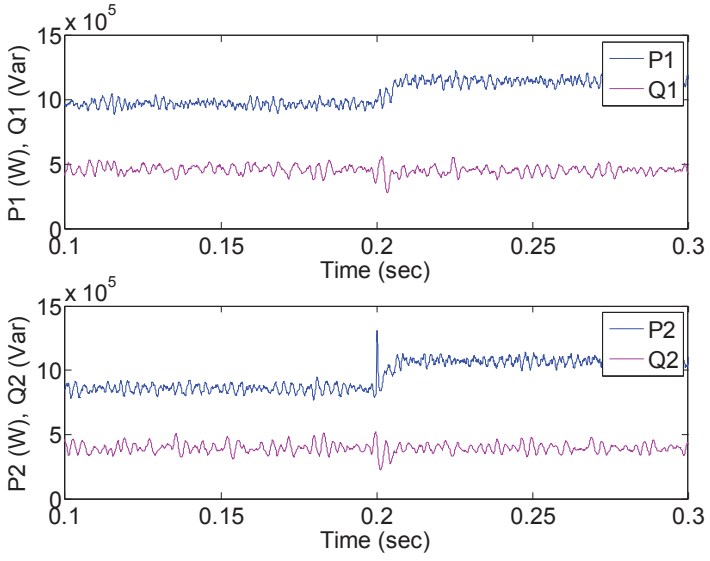

(a)

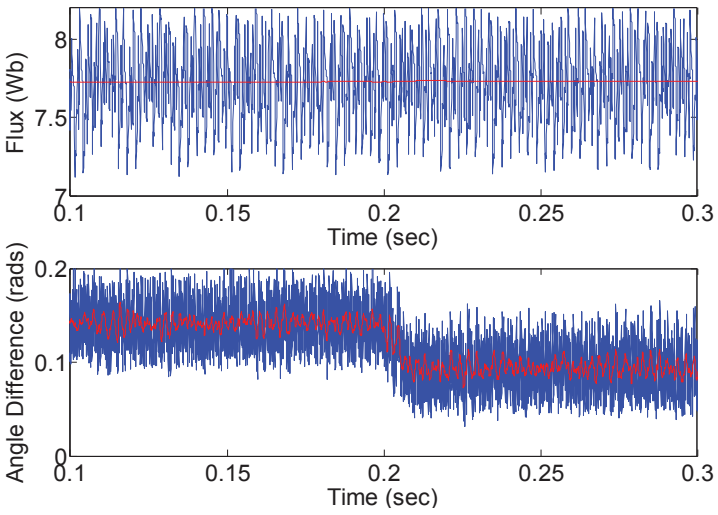

(b)

Fig. 5.20 Dynamic performance of power sharing

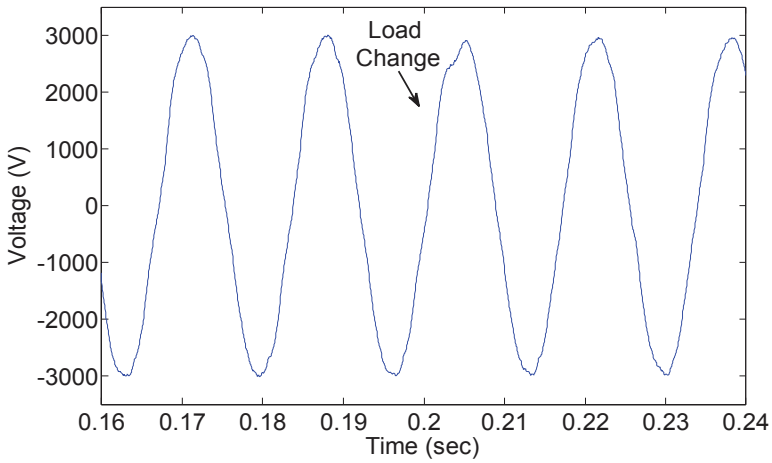

Fig. 5.21 Voltage across capacitor C_1

Table 5.4 compares the voltage frequency deviation and voltage amplitude deviation before and after the load is changed, for the conventional voltage droop method and the proposed flux droop method, respectively. It can be seen that there is about 7 V amplitude deviation of the voltage in order to compensate 0.1 MVAR reactive power unbalance, for both the $V - Q$ droop characteristic and $|\psi_V| - Q$ droop characteristic. However, if there is 0.1 MW active power unbalance from the load, the frequency features 0.4478 Hz deviation for voltage droop while only 0.0891 Hz for flux droop, i.e. the frequency quality is much better using the flux droop method with simpler control structure.

TABLE 5.4 Voltage Deviations for ΔP = 0.1 MW and ΔQ = 0.1 MVar

Methods	Frequency Deviations (Hz)	Amplitude Deviations (V)
Voltage Droop	0.4478	7.4507
Flux Droop	0.0891	7.3680

5.4 Coordinated Control of a Microgrid with PVs and Gas Microturbine

There are several aspects need to be concerned in microgrid control, such as load sharing, power quality, seamless transfer, system stability, and protection during faults, as mentioned in Chapter 1. It is noted that all these aspects mentioned above are seldom isolated in a microgrid system. For instance, in load sharing, the design of droop controller has to consider the system stability. Power quality is always an issue during the transition from the grid-connected to islanded mode when a grid fault occurs. This section focuses on a microgrid with PVs and gas microturbine from a renewable energy integration facility (REIF) laboratory at CSIRO. Essential issues such as proper load sharing, power quality, and protection during faults are concerned. Firstly, the microgrid structure is presented. The inverter performance of each DG will be studied and demonstrated. A coordinated control strategy of PVs and microturbine will then be proposed, and finally a series of cases based on the experimental test will be provided and discussed.

5.4.1 Microgrid configuration and problems identification

Fig. 5.22 shows the laboratory microgrid topology under study which includes a gas microturbine (MT), a solar PV array, a programmable load bank (LB), and an electric motor, all connected to a common AC bus with nominal line-line voltage of 415 V and nominal frequency of 50 Hz. The control of the DGs and loads, and the data acquisition are fulfilled through a SCADA system. In order to design a proper controller for this microgrid, it is necessary to study the characteristic of each component of the microgrid.

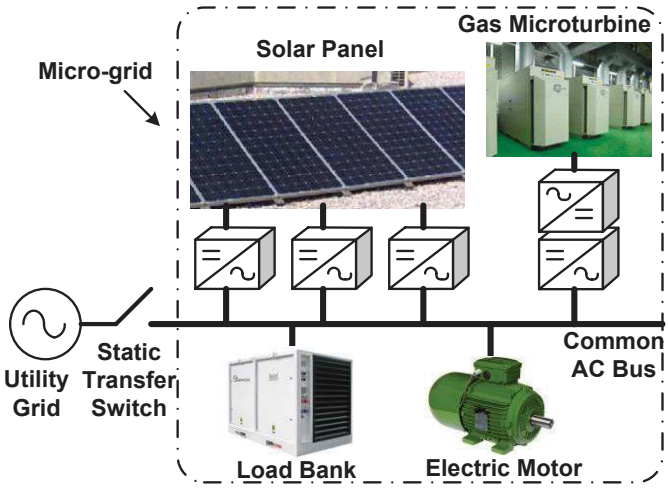

Fig. 5.22 Microgrid under study

A. PV

The series of PV panels are connected in the form of a single string, and each string is connected to a SMA Sunny Boy single phase inverter. These inverters are then distributed evenly across the three phase AC common bus with a total rated output power of about 20 kW. The PVs are controlled to output the maximum power with constant unit power factor. The performance of a PV array can be affected by many factors such as temperature, sun light strength, and shading, etc. Fig 5.23 shows the total power output performance of the PV array from 6:00 am to 8:00 pm in a sunny day (21-10-2011) and a cloudy day (23-10-2011). It can be seen that, in a sunny day, the PV output power increased smoothly in the morning, reached the peak value of about 19 kW at around 2 pm, decreased gradually in the afternoon, and hit the bottom of 0 kW at around 7 pm. However, the output power features an obvious fluctuating characteristic in a cloudy day.

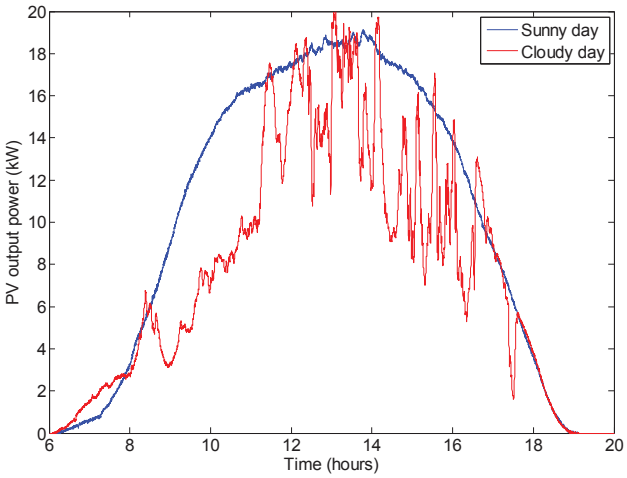

Fig. 5.23 Total PV output power measured in two different days.

It is noted that there are three characteristics of this kind of PV inverters. Firstly, it is always operated in the MPPT mode for solar panels without reactive power regulation, as mentioned previously. However, it is desired that DGs are not only controlled to generate active power, but also generate reactive power to participate in power quality improvement and system stabilization. Secondly, it requires a voltage signal to synchronize to, which it is not a problem in grid-connected operation. Nevertheless, this voltage must be produced by other power source in islanded mode. Fig. 5.24(a) shows the response of three phase PV output currents to the loss of external grid. It can be seen that the inverter stopped supplying current at about 30 ms after grid disconnection at zero second, i.e. this type of inverters loses the ability of supplying power if there is no external voltage signal that the inverters can synchronize to. The third feature of this type of inverter is that it is quite sensitive to the voltage variation. Fig. 5.24(b) shows one of the inverters responses to the frequency variation. The grid frequency increases gradually from 50 Hz at 0 second up to 50.5 Hz at 0.2 second, as depicted by the solid line. It is clearly to find that the power supplied by this photovoltaic inverter drops abruptly when the system frequency reached 50.3 Hz at 0.12 second, and reached the bottom of zero Watts in 50 ms, as depicted in the dashed line. The inverter response to the frequency decreasing was also investigated. It stopped supplying power when the frequency dropped down to 49.8 Hz, which is not shown here.

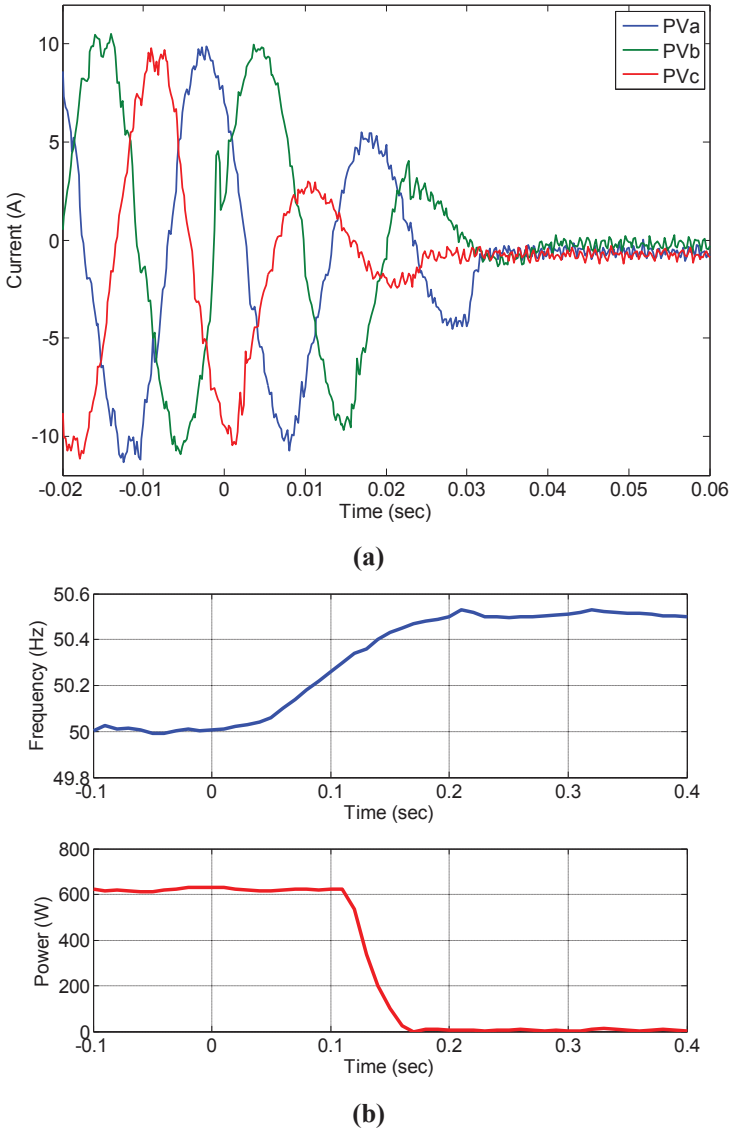

Fig. 5.24 PV characteristics. (a) dynamic response to the loss of external grid voltage, (b) dynamic response to the voltage variation.

The features of the PV system mentioned above are highly concerned in microgrid control. How to manage the PV system and how to coordinate the PV system with other DGs are the main issues need to be solved in the microgrid control.

B. Gas MT

Another type of DG source in the laboratory is the 30 kW gas MT. It drives a synchronous generator, which supplies electricity to the microgrid through a back-to-back converter. The high frequency AC power generated by the synchronous generator is first rectified to DC, and then converted to AC. Fig. 5.25 shows a microturbine

system in microgrids. This paper focuses on the grid-side inverter, which can be controlled to produce a voltage with specified magnitude and frequency based on a droop method.

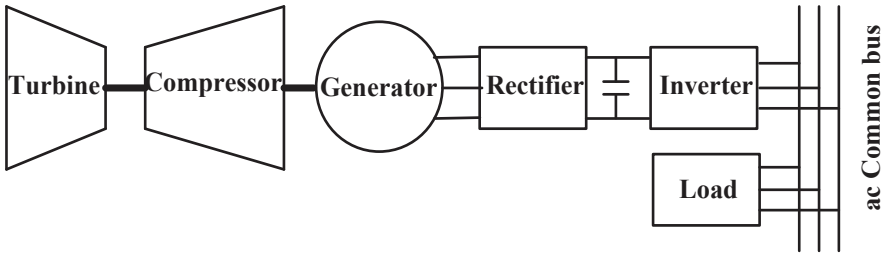

Fig. 5.25 A simplified diagram of a microturbine generation system in a microgrid.

Although will not be studied in this paper, it is worth mentioning that the MT consists of several control units besides the power conversion system, such as speed and acceleration control system, fuel control system, and temperature control system [5.36], [5.37].

C. Load bank and electric motor

The load bank (LB) comprises of a 63 kW resistive load, a 63 kVAR inductive load, and a 63 kVAR of capacitive load, which are arranged in a binary fashion. For instance, the resistors are arranged in powers of 2, i.e. to draw 1kW, 2kW, 4kW, 8kW, 16kW, and 32kW of power, such that any amount of power consumption can be achieved by a combination of these six resistors, following the standard binary code. The protection is another crucial issue in microgrid, which becomes more important with the increase in penetration of a large amount of renewable and other distributed generation because they may affect the conventional protection mechanism. Therefore, an electric motor was also used in this study with the purpose of introducing an apparent fault.

5.4.2 Coordinated control strategy

The microgrid can operate in grid-connected or islanded mode. In grid-connected operation, the DGs together with the utility grid supply power to the local loads. If the power generation is greater than the load consumption, the excess will be injected into the grid. On the other hand, if the power generation is smaller than the load demand,

more power will be imported from the grid. In islanded operation, the DGs should be able to provide a stable voltage at PCC and pick up the loads automatically. In addition, the microgrid should be re-connected to the utility grid seamlessly when the grid is available. Specifically, in this microgrid under study, the PV and microturbine should be controlled properly to be engaged in energy management. Besides, the PCC voltage should be stable enough to guarantee the normal operation of the PV system.

A. Grid-connected operation:

In this case, the grid voltage is available for the PV inverters to synchronize to. Therefore, the PVs are connected to the common AC bus and supply as much power as possible to the local load, and the excess will be fed back to the utility grid.

B. Islanded operation:

In this case, all the DGs and load is isolated from the grid to form an energy island. Within this microgrid, the power generated must match the demand. However, the utility grid voltage is unavailable for the solar inverters to synchronize to. In addition, the power generated by the PV is only active power, which cannot meet the requirement of reactive power consumption of the loads. Therefore, the MT is also utilized in islanded operation. Although the inverters of PV are operated with MPPT at unit power factor, the grid-side inverter of the MT can be controlled to provide a stable PCC voltage and supply power to the local load together with PVs.

C. Fault protection:

Fault protection is an important feature of the conventional electricity grid. However, the future smart grid will incorporate a significant amount of renewable and DGs, which may affect operation of protection. A short circuit fault can potentially involve very large amounts of energy, and thus can be destructive and dangerous to the electronic components in the circuit. In this work, the microgrid response to the short circuit fault will also be investigated, in both grid-connected and islanded modes.

5.4.3 Cases study

Fig. 5.26 shows the laboratory microgrid to be studied, with the control room at the centre, PV panels on the roof, PV inverters on the left, and gas microturbine, load bank

and motor behind the control room. The structure of this microgrid is illustrated in Fig. 5.21, which incorporates 20 kW solar PV, 30 kW gas microturbine, a programmable load bank, an electric motor, and the monitor and control system, as described previously.

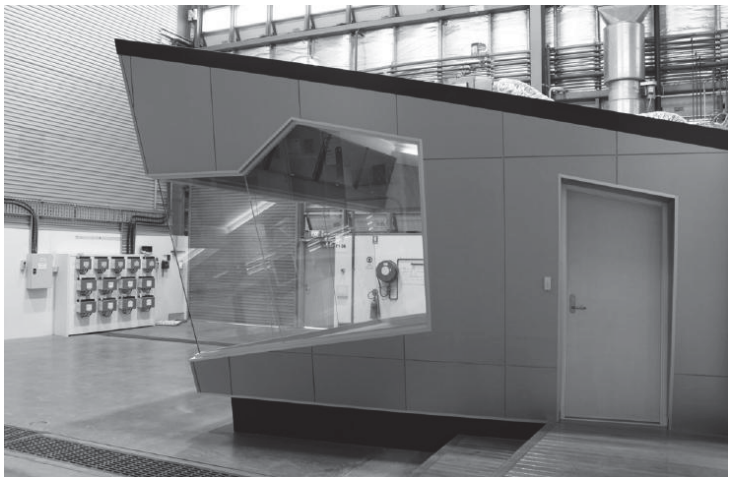

Fig. 5.26 The renewable energy integration facility (REIF)

A. Grid-connected mode

In this case, PV and LB are connected to the AC common bus and the microgrid is then connected to the utility grid. The total active power output of PV at this time of the current experiment is about 4.5 kW. The LB is set to zero at the beginning, and then raised up to 3 kW (less than the PV output power) and 10 kW (greater than the PV output power) at 2.2 s and 5.3 s, respectively. Under such circumstances, the power flow between the microgrid and the utility grid, and the power flow between the PV and load demand, would be interesting to see. Besides, the voltage response at the AC common bus in terms of amplitude and frequency will be investigated.

Fig. 5.27 shows the active power sharing between a PV-based microgrid and utility grid. It can be seen that the PV produced stable power of about 4.5 kW throughout this test. At no-load operation at the beginning, the power flow from the utility is -4.5 kW, which indicates that all the power generated from the PV was fed to the utility grid. When the load bank was set to 3 kW at 2.2 s, the power flow from utility becomes -1.5 kW. This is to be expected, as PV provided all the load demand, resulting in only 1.5 kW (4.5 kW – 3 kW = 1.5 kW) exported to utility. When 10 kW was loaded at 5.3 s, it can be observed that extra 5.5 kW (10 kW – 4.5 kW = 5.5 kW) power was imported

from the utility because now the load demand is greater than the power generation from DG.

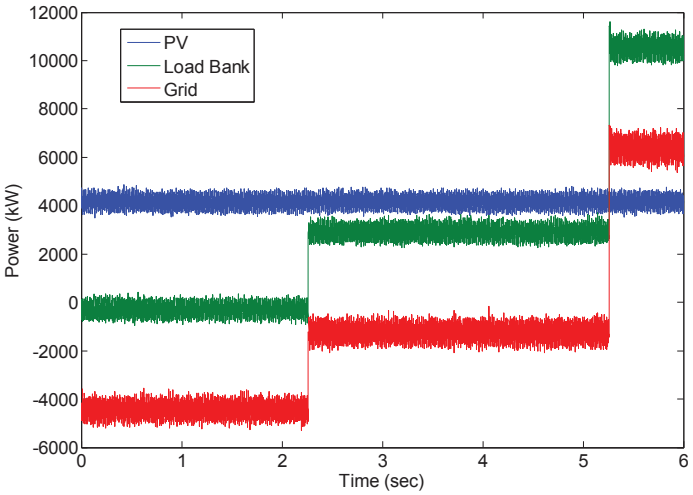

Fig. 5.27 Power flow in grid-connected mode

On the other hand, the amplitude and frequency are quite stable, presenting a voltage variation of only 0.6 V and frequency variation of 0.02 Hz frequency variation, as expected because of the connection to the utility grid, as shown in Fig. 5.28.

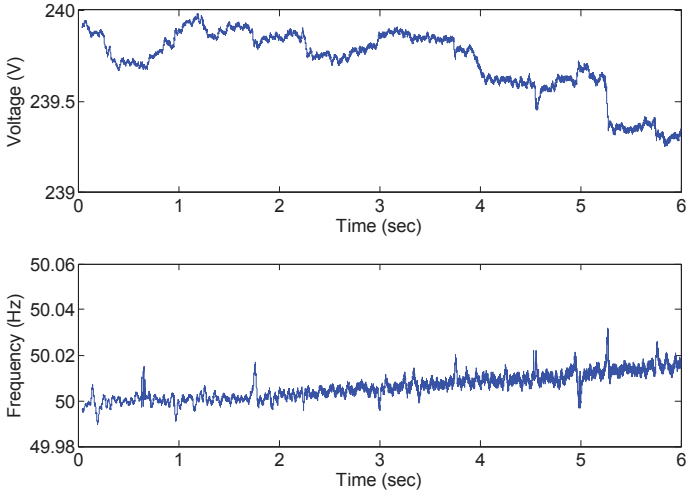

Fig. 5.28 Voltage and frequency response in grid-connected mode

B. Islanded mode

In this scenario, the microgrid was isolated from the utility grid, and the PV and MT together supplied power to the load bank. The MT regulated its output voltage

instantaneously so that the change in the power demand can be picked up quickly. In fact, the microturbine should reacts to provide the difference in active power between that demanded by the load and the PV output, and then provide all the reactive power. The total active PV output power at this time of the current experiment was about 2.8 kW. The load profile was set in such a pattern that there was constant 5 kW resistive load throughout this test while 5 kVAR inductive load was added and removed at 1.9 s and 3.5 s, respectively.

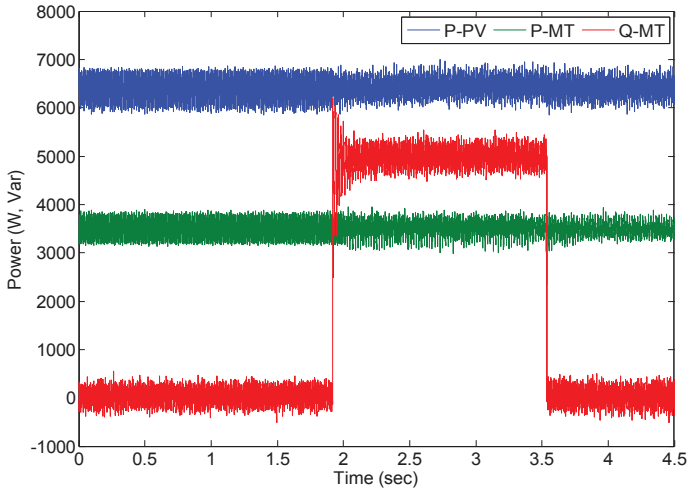

Fig. 5.29 Active and reactive power sharing in islanded mode

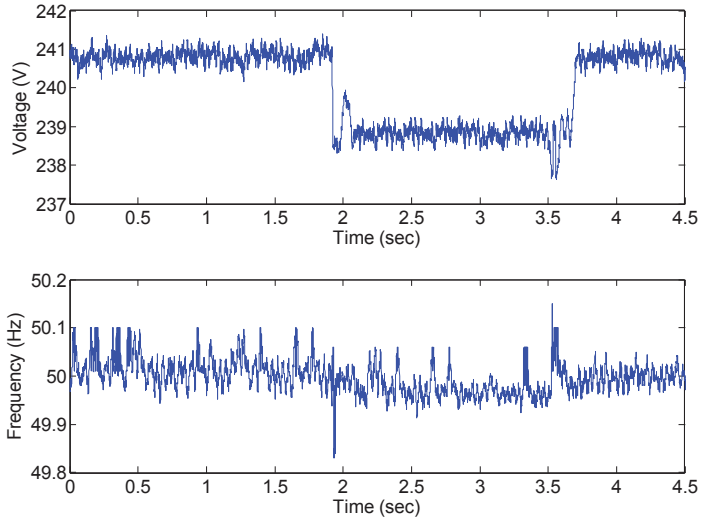

Fig. 5.30 Voltage and frequency response islanded mode

Fig. 5.29 shows the power sharing between PV and MT in islanded mode. It can be seen that the MT originally supplied active power together with PV to the load bank. At t =1.9 s, the MT raised its reactive power from 0 to 5 kVAR to meet the new power

requirement. However, the PV stopped supplying power once the load was changed. Note that the load bank was controlled in a binary manner, a very large load would be induced during the transition of load change, as illustrated in Section 5.4.2. Therefore, obvious power surge can be observed at 1.9 s, leads to the abrupt drop of voltage and frequency, as depicted in Fig. 5.30. In fact, it is exactly the frequency drop (49.35 Hz) causing the PV to shut down, which has been demonstrated in Section 5.4.1. Instantaneously the MT also increased its active power output for the constant 5 kW resistive load once the PV shutting down was detected. The performance of MT output current during the load change is shown in Fig. 5.31. At t = 3.5 s, the inductive load was removed, the MT continued provided 5 kW active power while reactive power dropped back to zero.

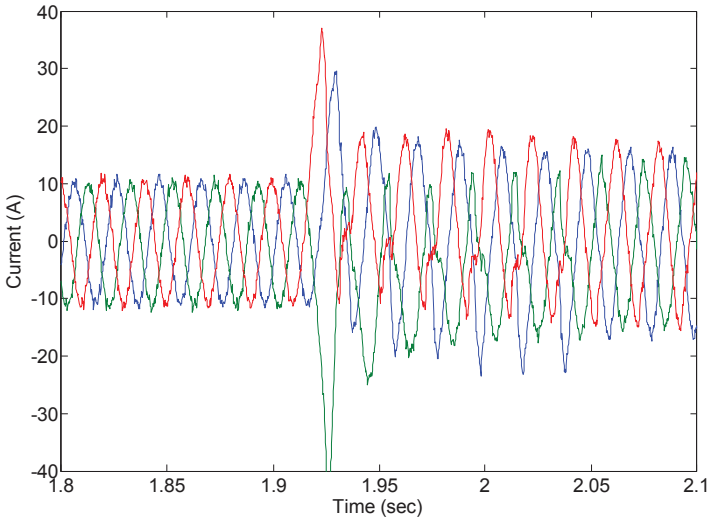

Fig. 5.31 Microturbine output current

C. Protection during faults

In order to investigate the response of the microgrid system with large penetration of DGs under short circuit fault and propose protection methods, an apparent fault is introduced by starting an electric motor directly. The main aim of this test is to know whether the penetration of DGs will lead to an increased fault current and whether the protection mechanism of the conventional power system is adequate to deal with this new situation without redesign or adjustment.

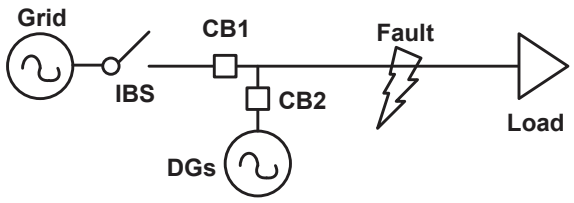

Fig. 5.32 Simplified diagram of test system under faults

(1) Test 1: Fault occurring in grid-connected mode

In this scenario, the PVs, the MT and the load bank are connected to the AC common bus and the IBS is switched on, as shown in Fig. 5.32, where CB1 and CB2 are the circuit breakers. The MT produced 30 kW power and PV generated 6 kW at the time of this test with 20 kW resistive load bank.

The microgrid response to the short circuit fault is shown in Fig. 5.33. It can be seen the *rms* current measured at CB1 (solid curve) was about 22 A per phase before the fault, then rises up to 160 A during fault, as shown in Fig. 5.33(a). The load current presents a similar dynamic behavior only the fault current rises up to around 100 A. It is noted that the circuit breaker can be set to a single threshold, and therefore, the conventional protection mechanism of threshold based circuit breakers will provide adequate protection and does not require modification. It is worth mentioning that the current flow has reversed direction at t = 0 s. Before the fault, the current flowed from the microgrid to the utility grid because the total power generation was greater than the load demand. When fault occurred, the current flowed the other way, from the utility grid to the microgrid. On the other hand, a small PCC voltage dip is also observed, as presented in Fig. 5.33(b), which shows that small dip in voltage would not allow a reliable indication of a fault condition. Similar results were obtained from using 10 kW load bank and 30 kW load bank. Therefore, based on the behavior of current and voltage, the fixed threshold detection of current method is suitable for a protection system in this case.

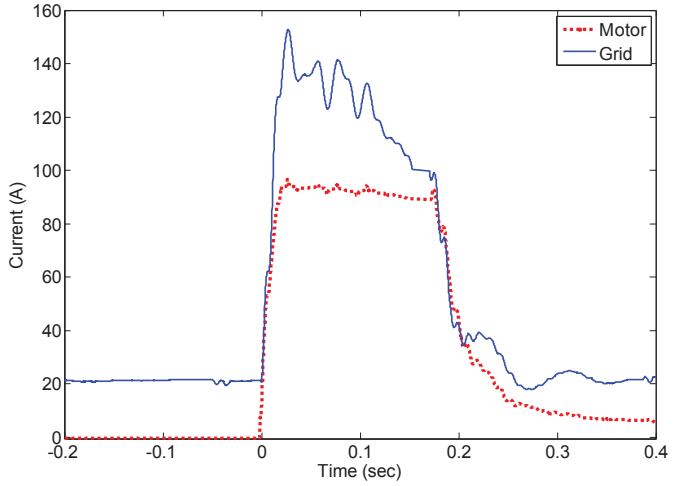

(a)

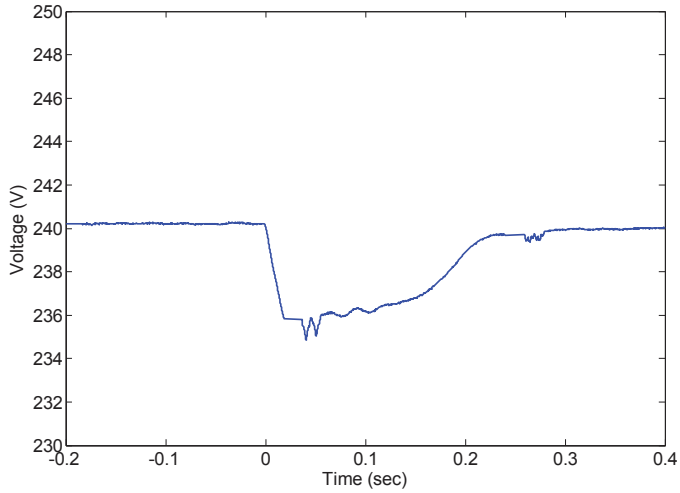

(b)

Fig. 5.33 Response of current and voltage during a fault in grid-connected mode (a) Currents, (b) PCC Voltage.

(2) Test 2: Fault occurring in islanded mode

The difference between this case from the previous one is that the IBS is switched off and the load bank was set at 10 kW, and the MT controlled the PCC voltage. To the limitation on the amount of power that can be supplied by the DGs, the fault current (the total current seen by DGs at CB2) only reaches 50 A per phase, as shown in Fig. 5.34(a). In fact, the PV did not contribute any current because it shut down completely due to the severed voltage drop, as demonstrated in Section II. In other words, the entire fault current is supplied by the MT. On the other hand, Fig. 5.34(b) depicts that the

voltage dropped down to 100 V during the fault, which is very different to the previous case. Therefore, both the current and voltage should be utilized as a reliable indication of a fault condition in islanded mode.

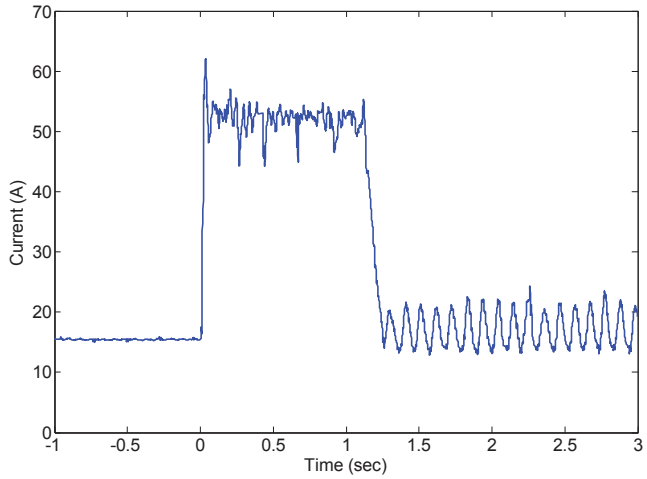

(a)

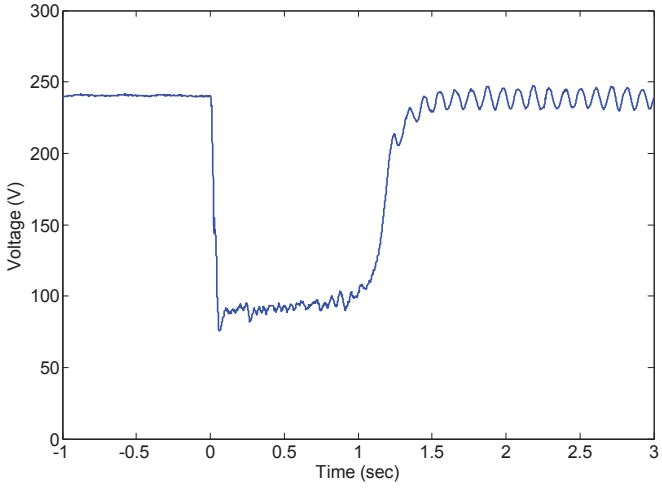

(b)

Fig. 5.34 Voltage and current response to grid fault in islanded mode (a) current at CB2, (c) PCC Voltage.

In this section, the intermittent nature of the renewable energy source and the behavior of inverters of PV and microturbine are firstly studied in order to define the roles and the required control system. An energy management strategy was then presented for a microgrid with PV operating with MPPs at unit power factor and a microturbine operating with droop control for load sharing. A series of case studies were carried out to validate the control strategy. In the grid-connected mode, the PV and the utility grid supply power to the load. In the islanded mode, the microturbine

dispatch active and reactive power while the PV simply attempts to push as much as active power as possible into the local AC bus. In addition, grid faults in various scenarios were investigated and the corresponding microgrid protection schemes proposed.

5.5 Model Predictive Control of Microgrids

Nowadays most of the previous works in microgrids control mainly focus on a two-parallel-DG based system, and droop control method is generally used to control the inverters for autonomous power sharing between DGs, as introduced in Section 5.3. In Section 5.4, a more complicated microgrid system including PV array, microturbine and programmable load bank is studied, and a coordinated control strategy is proposed to ensure proper operation in both grid-connected and islanded mode.

However, it is commonly necessary to combine different kind of DG sources and loads together with the storage technologies in order to ensure both long-term and short-term energy storage, thus smooth the gap between power generation and power consumption within the microgrid. Due to the complexity of such a power system including several kinds of energy sources, energy storage systems, and loads, the appropriate control of these DGs to achieve optimal power flow and maintain high power quality becomes a big challenge.

From the perspective of the energy sources, the power converters should be controlled to capture the maximum real power and inject the excess into the utility. From the utility/grid perspective, the power electronics interface should be also able to provide reactive power according to the requirement to improve power quality and enhance grid stability. In this sense, advanced techniques of microgrids including DGs, load and energy storage system (ESS) for power flow optimization are desired.

5.5.1 Microgrid modeling

Microgrids consisting of different types of DGs and storage system represent an area of growing interest due to the possibility to integrate clean and reliable power into household and industries. In such a small power system, the proper decision regarding operation is closely related to the system efficiency. The multiple sources and loads in a microgrid make the efficient operation a rather complicated task, such as the microgrid

configuration shown in Fig. 5.4 previously, which will be the research objective in this section. For easy illustration, it is shown here again as new Fig. 5.35.

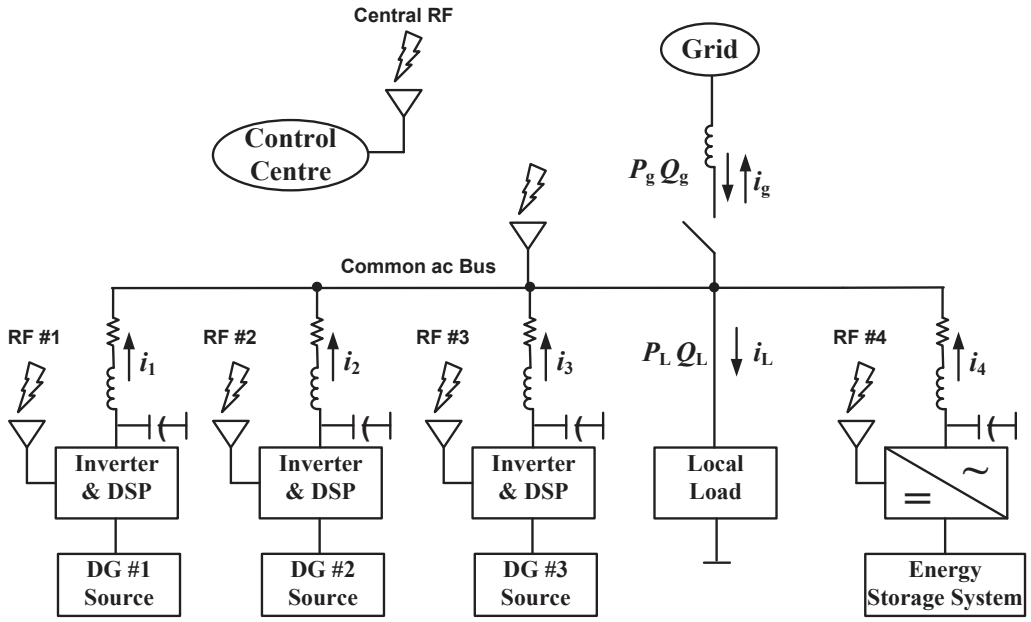

Fig. 5.35 Smart microgrid topology.

This microgrid includes the following components:

A. PV system

The PV system is illustrated in Fig. 5.36.

(a)

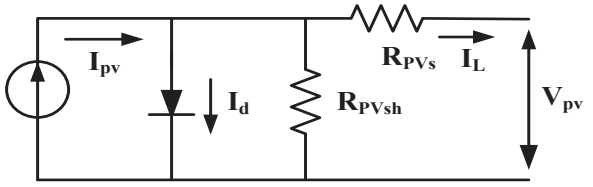

(b)

Fig. 5.36 PV system, (a) PV array, (b) Equivalent circuit of the PV cell

The current source I_{pv} represents the photocurrent, I_d the current shunted through the diode, and R_{PVs} and R_{PVsh} are the intrinsic series and shunt resistances of the cell ($R_{sh} >> R_s$). The PV cells are assembled in larger units known as PV modules, which are further grouped in a parallel-series configuration to form a PV array. The corresponding mathematical equation that describes the current-voltage characteristics of a PV array can be expressed as [5.38], [5.39]

$$I = N_p I_{pv} - N_p I_{rs}\left[\exp\left(\frac{q}{k\beta A}\frac{V_{dc}}{N_s}\right)-1\right] \tag{5.40}$$

where V_{dc} is the PV array output voltage, I and I_{rs} are the PV array output current and reverse saturation current of a *p-n* junction, respectively, q (=1.602×10^{-19} C) is the unit electric charge, k (=1.38×10^{-23} J/K) the Boltzman's constant, β the p-n junction temperature (in Kelvin), A the ideality factor, and N_s and N_p are the number of cells connected in series and the number of modules connected in parallel, respectively. It is noted that the photocurrent I_{pv} is proportional to the solar irradiation level S and to the cell temperature, as

$$I_{pv} = [I_{scr} + k_\beta(\beta - \beta_r)]\frac{S}{100} \tag{5.41}$$

where β_r is the cell reference temperature, I_{scr} the short-circuit current of one PV cell at the reference temperature and irradiation level, and K_β the temperature coefficient. From (5.41), the power delivered by the PV array can be written as

$$P_{pv} = N_p I_{pv} V_{dc} - N_p I_{rs} V_{dc}\left[\exp\left(\frac{q}{k\beta A}\frac{V_{dc}}{N_s}\right)-1\right] \tag{5.42}$$

The performance of a PV array can be affected by many factors such as temperature, sun light strength, and shading, etc. Fig 5.37 shows the total power output performance of a PV array at CSIRO from 6:00 am to 8:00 pm in a sunny day (21-10-2011) and a cloudy day (23-10-2011). It can be seen that, in a sunny day, the PV output power increased smoothly in the morning, reached the peak value of about 19 kW at around 2 pm, decreased gradually in the afternoon, and hit the bottom of 0 kW at around 7 pm. However, the output power features an obvious fluctuated characteristic in a cloudy day.

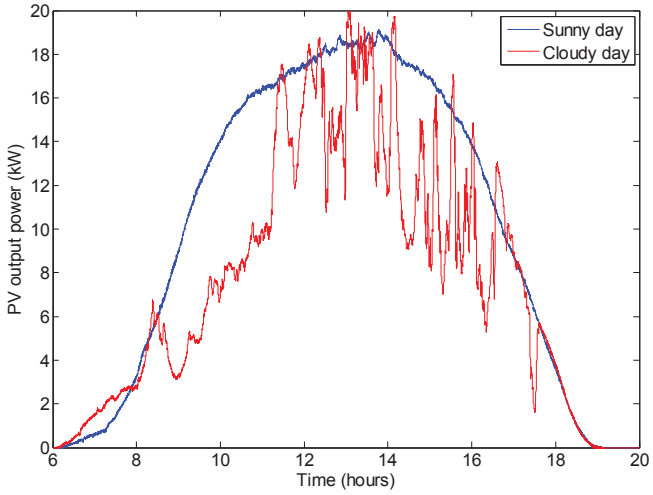

Fig. 5.37 Total PV output power measured in two different days.

B. Wind power system

Doubly fed induction generator (DFIG) based wind power system currently dominate the wind energy market due to their four-quadrant active/reactive power control, variable speed operation, low converter cost, and reduced power loss compared to other solutions, as illustrated in Chapter 2. A laboratory DFIG-based wind power system is shown in Fig. 5.38(a). The wind turbine is emulated by a 20 kW DC motor, which is connected to a 20 kW DFIG via a 1.33:1 gear box for increased torque at lower speed. A dSPACE system is used to control the torque output of a 4 quadrant thyristor DC motor drive according to the shaft speed and a programmable simulated wind speed input, in order to match the expected torque output of the actual wind turbine. On the other hand, the DFIG is controlled by another dSPACE system with MPPT. The equivalent circuit of the DFIG is depicted in Fig. 5.38(b).

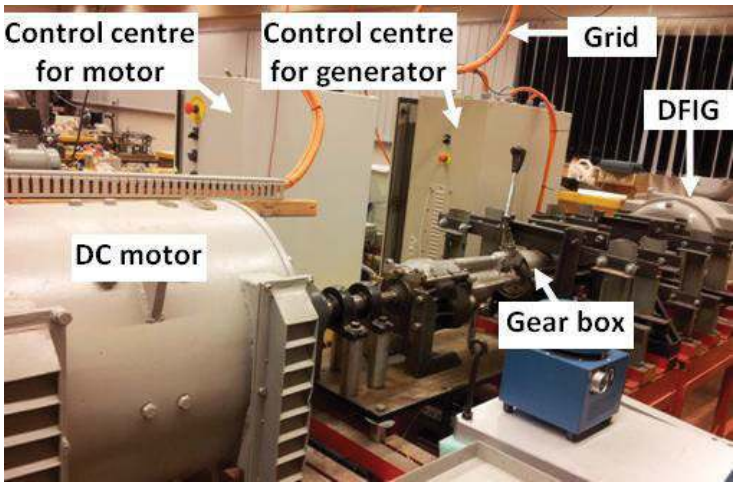

(a)

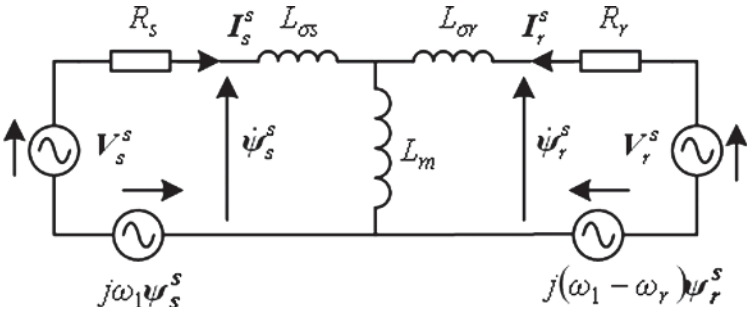

(b)

Fig. 5.38 DFIG based wind power system in the University of Technology, Sydney, (a) experimental platform, (b) equivalent circuit of a DFIG in the synchronous reference frame

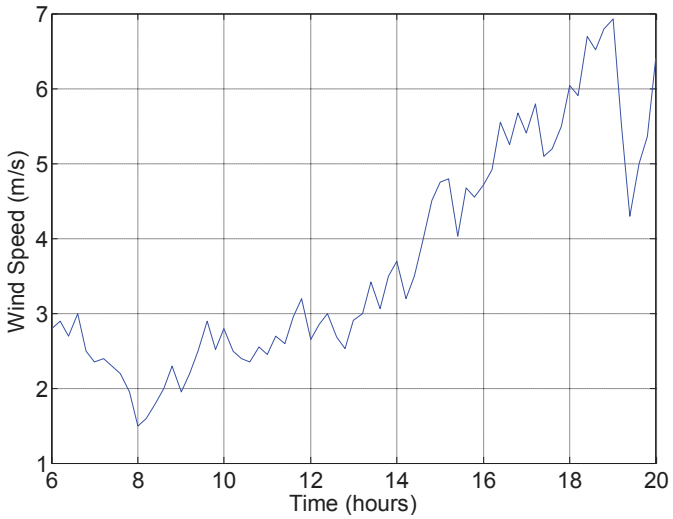

Fig. 5.39 Wind speed.

Fig. 5.39 shows the actual wind speed information measured in a wind farm during a day [5.40]. It can be observed that the wind speed presents a stochastic characteristic during a day, from 2 m/s to 7 m/s with obvious fluctuation. Consequently, using this wind speed information as the input, the power output of the DFIG based wind power system (see Fig. 5.38(a)) can be obtained, as presented in Fig. 5.40. It can be seen that the power output features apparent oscillations with the range between 0 kW and 15 kW, approximately tracks the profile of the wind speed with slightly smoother characteristic and some delay due to the inertia of the generator. It is noted that the DFIG will not produce any power until the wind speed reaches a cut-in value mainly due to the following reason: the small among of power generated in quite low wind speed condition cannot compensate the power required for the normal operation of the wind power system, which will cause economic lost.

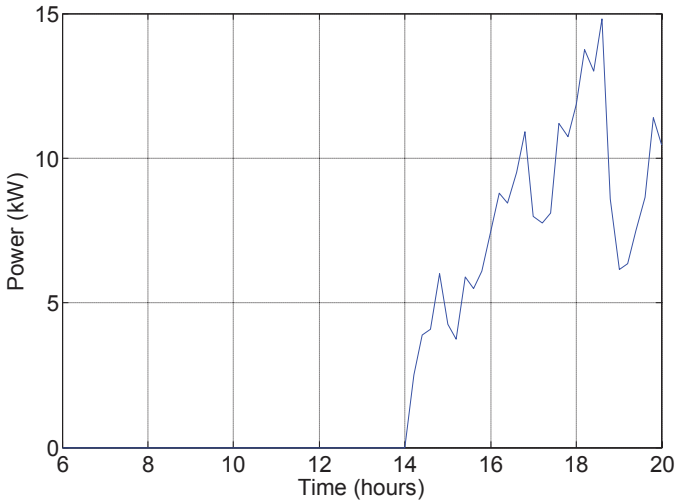

Fig. 5.40 Power output of the wind power system.

C. PEM fuel cell

Fig. 5.41 show a proton exchange membrane fuel cell (PEMFC) stack, it is a self-humidified, air-breathing, 60-cell stack with an overall size of 22.0 cm × 10.5 cm × 7.0 cm. PEMFC is clean and efficient power generation source, which is currently under intense research efforts, being particularly useful in portable applications, and vehicle propulsion.

The advantages of fuel cell are high efficiency, high power density, relatively low corrosion, and fast start-up compared with other distributed generation system. The PEMFCs consume hydrogen and oxygen to produce electricity. The hydrogen is sent to the anode catalytic layer where it is dissociated into electrons and protons. The latter ones flow through an electrolytic membrane, which blocks the electrons, to the catalytic layer of the cathode, producing electric current in this process. Simultaneously, oxygen is delivered to the cathode, arriving to its catalytic layer, where the oxygen, protons, and electrons react, generating water and heat in the surface of the catalytic particles.

To use the PEMFC stack as the energy power source, there is one polarization curve given in the operator's manual [5.41] that will be used here. Fig. 5.42 depicts the current-voltage and power characteristics of the PEMFC stack [5.42]. It can deliver a maximum power of 300W and the maximum power slew rate is limited to 20W/S. In order to match the power level of the proposed microgrid system and for the easy illustration, the maximum power of the PEMFC stack is set to 10 kW and the maximum power slew rate is limited to 200W/S, which will be presented in the test in Section 5.5.3.

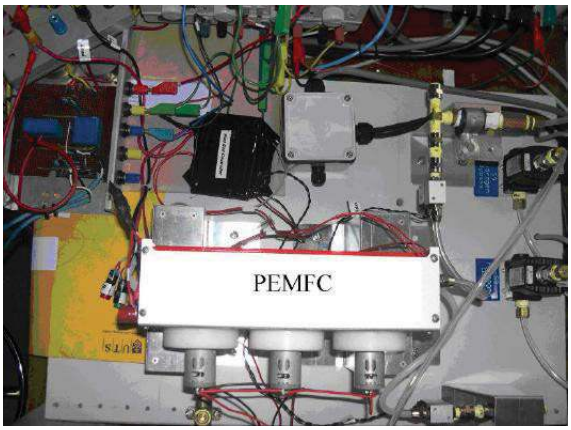

Fig. 5.41 300W PEMFC stack.

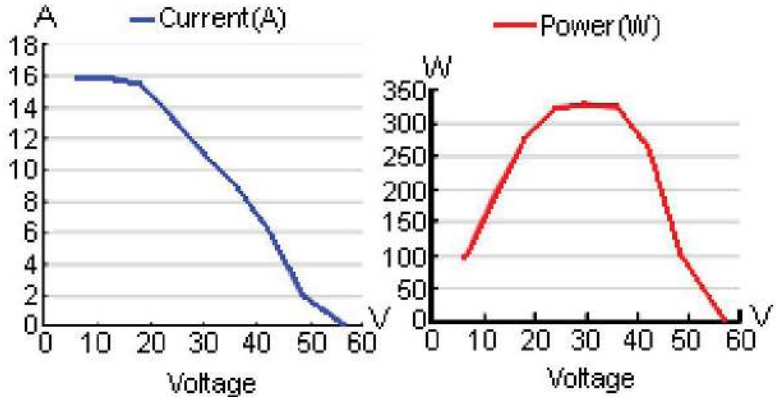

Fig. 5.42 Current-voltage and power characteristics of a 300W PEMFC.

C. Battery bank

The battery bank is used as the energy storage device here to absorb the surplus power from the energy sources when the power generated is greater than the power consumed, and deliver it back in the opposite situation. The batteries are advanced stationary Pb-acid type with a total capacity of C_{120} = 367 Ah. The battery model is shown in Fig. 5.43. Normally the manufacturer prevents intensive use of the batteries and also to protect them from a deep discharging or overcharging. The batteries can support a specified peak current, but smooth operation is strongly recommend by the manufacturer for expanding lifetime of the battery.

(a)

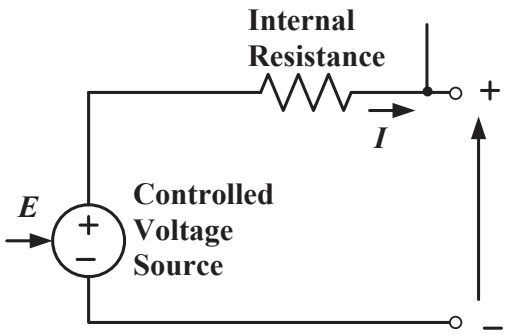

(b)

Fig. 5.43 Battery Bank model, (a) Pb-acid type battery, (b) Equivalent circuit of battery bank.

D. Load

The load profile is taken from the actual electricity power consumption of a building during a day. The rated power of all the electric appliances including lights, personal computer (PCs), air conditioner, and a printer is 30 kW. Fig. 5.44 shows the load profile during a day. It can be observed that the load profile features an obvious fluctuation with peak power consumption at around 7am, 12pm, and 19pm, respectively.

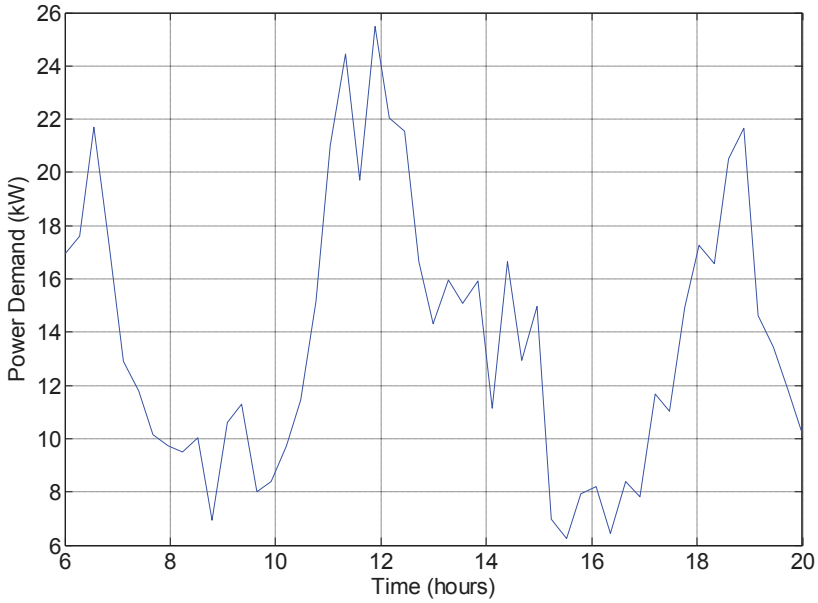

Fig. 5.44 Load profile of an office during a day [5.44].

In order to meet the power demand with such a stochastic profile in a microgrid system, it seems that it is impractical to connect the renewable power generation units directly to the loads because the power output of the energy sources themselves are oscillated. Therefore, the utilization of battery bank become essential since it can absorb the power fluctuation thus mitigating the power mismatch.

It is noted that there is some scenario when some large power rating electric appliances are connected to the common AC bus suddenly, leading to a huge power mismatch. In order to deal with this problem, some DG source with fast start-up ability is required. That is why PEMFC is also employed, as mentioned previously.

E. Control centre and communication

The control centre is a high-performance computer, which takes charge of the operation of the entire microgrid, including the real-time system performance measurement, data processing, and the delivery of the control demands.

For the communication between the DG units and the control centre, the wireless transmission is utilized in this microgrid system, and the XBee OEM RF modules are used to receive and transmit data [5.45]. One XBee module connected to the PC through USB as the master. Other XBee modules connected to the DGs as slavers, where for each module, the voltage or current analog sampling signals are connected to the ADC

pins of the module while the module is also connected to the microcontroller (e.g., DSP). Slave XBee modules correct the voltage/current information of DG, send it to the master XBee module then deliver to the PC to process. The PC then sends the commands to the master XBee, which will transmit the commands to each slave module. Finally, the slave module will send this command to DSP to control the power converters.

In the communication, firstly, a control panel is built up using MATLAB to exchange data with the master module through serial communication (though serial communication is operated with UART, the USB connection is already the serial communication). Then the AT commands are sent from the software to control the master module. In order to get communication between the PC and the XBee module, it is necessary to know the protocol of the XBee module. Secondly, the communication between XBee modules should not be point to point anymore, it should be like mesh networking, where each module has its own address. Thirdly, the slave module communicates with the DSP using SPI communication.

5.5.2 Problem description

As described in Section 5.5.1, the power demand varies in every single minute. Unfortunately, the DG units within the microgrid cannot meet this demand because the power generation also varies with fluctuation. If no ancillary devices are used and no proper control strategies are implemented, the microgrid system would become unstable in terms of oscillated common AC bus voltage, large circulated currents between DG units, distorted load currents, and etc., due to the power unbalance, which will damage the power electronics and cause negative influences on the electric appliances.

Given the noncontrollable and intermitted nature of the renewable energy sources, and hence that of their corresponding power production together with the fluctuated load demand, an appropriate solution is the use of an ESS which allows accumulating the surplus energy in those periods in which the production is higher than the power commitment and delivering it back in the opposite situation.

In addition, it is necessary to protect the battery bank from deep discharging and overcharging, and to coordinated control the fuel cell to provide the additional power when some high-power rating electric appliances are suddenly connected to the

common AC bus while the renewable energy sources and the battery bank cannot handle such a power mismatch in a short time.

Basically the constraints need to be taken into account in such a microgrid system can be described as the following:

- In a microgrid system, the main aim is to supply high-quality power to the loads, regardless of fluctuated load profile and power generation. Therefore, the first objective of the MPC strategy is to establish a stable PCC voltage for the loads, in terms of frequency and amplitude. In other words, power demand from the load should be satisfied with high voltage quality regardless of the intermitted nature of the renewable energy.

- Due to the intermitted nature of the renewable energy sources and the fluctuated load profile, the power generation and consumption are changed every minute, or even every second. Consequently, it is commonly necessary to use energy storage system (ESS) to smooth the gap between power generation and power consumption within the microgrid. For instance, if the power generated by DGs is greater than the load demand, the power will be stored in the ESS and the excess will be injected to the utility grid. On the other hand, if the load demand is greater than the power generated by the DGs, the ESS together with the utility will compensate the unbalance. In a word, the power flow within the microgrid should be optimized.

- Since most of the power outages and disturbances take place in the distribtution network, ancillary services for distributed generation systems become a challenging issue to smartly integrate renewable energy sources into the grid. Besides, grid codes from the Transmission System Operators describe the behavior of the energy source, regulating voltage limits and reactive power injection to remain connected and support the grid under fault. Therefore, the microgrid is not only ocntrolled to supply power to the local loads, but also to ride through and support the grid voltage under grid faults. A common method to achive the grid support is to inject reactive power into the utility grid when grid faults occur. In this microgrid under studied, the reactive power can be generated by the DFIG based wind power system, as illustrated in Chapter 2.

- Protect the battery bank from deep discharging and overcharging. The manufacturer highly recommends to prevent intensive use of the batteries and also to protect them from a deep discharging or overcharging, with the purposing of expanding the lifetime of these expensive equipment.

- Use the grid connection and the fuel cell only when the renewable sources are unavailable or the load demand is greater than the power generated by the renewable sources and the battery bank.

To summarize, the main control objectives of the microgrid system can be illustrated in Fig. 5.45, including stable PCC voltage, power flow optimization, battery protection from deep discharging and over charging, and utility grid support.

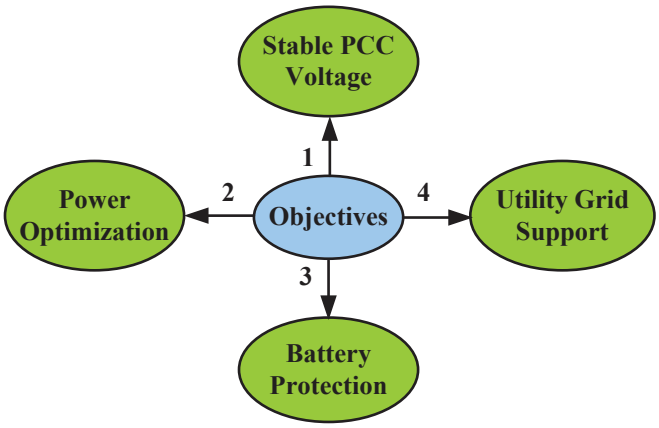

Fig. 5.45 Control objectives of microgrids.

5.5.3 Proposed concept of model predictive control for microgrids

Most of the previous works in microgrids control mainly focus on a two-parallel-DG based system, and droop control method is generally used to control the inverters for autonomous power sharing between DGs. However, it is commonly necessary to combine different kind of DG sources, loads and storage technologies in order to ensure both long-term and short-term energy storage, and thus smooth the gap between power generation and power consumption within the microgrid. Therefore, advanced techniques of microgrids including DGs, load and ESS for power flow optimization are desired.

Some works in the whole microgrid control are based on heuristic control algorithms, such as “hysteresis band control” [5.47]. Fuzzy control also gives some hope, due to contribute with more simple formulation control rules. The results of the fuzzy controllers are satisfactory for keeping the batteries around a defined SOC, although forcing the electrolyzer and the fuel cell (the necessary elements to storage and use hydrogen) to excessive intermittent operation [5.48],[5.49]. Since this has a very negative impact on their lifetimes, these constraints should be considered in the future control strategies.

Model Predictive Control is a good candidate to solve this problem, since it integrates optimal control, control of processes with dead time, multivariable processes and it can use the future references when available. The basic principle of MPC approach has been depicted in Chapter 3 previously. Generally the design of the MPC controller can be divided into three steps, namely, system predictive model, cost function and parameters selection. Firstly, the system model can be expressed as a discrete-time state-space model, the output of which is determined by the input, the current state of the model, and the discrete interval. In this way, the future behavior of the system can be predicted until a certain horizon of time. Secondly, the control problem can be defined as the determination of an appropriate control action that will force a generic system variable $\boldsymbol{x}(t)$ as close as possible to a desired reference value $\boldsymbol{x}^*$. A cost function over a finite horizon of length N is then utilized to evaluate each switching state, the one minimizing the error between $\boldsymbol{x}(t)$ and $\boldsymbol{x}^*$ will be selected for the next sampling period. Besides, MPC has the inherit ability to handle efficiently constraints and uncertainties in multivariable dynamic systems. MPC computes at each discrete time instance the control action by solving a finite-horizon open-loop optimal control problem. By using a strategy with finite control horizon allows the consideration of constraints and nonlinear processes [5.50].

Thus, MPC has been widely adopted in industry, although there are few works regarding MPC implementation in MGs. In [5.51], MPC is used for energy scheduling on a hydrogen-based MG without batteries, while MPC is applied for renewable energy power management with battery storage in a water desalination plant in [5.52]. Another example is the work of [5.53], where MPC is performed for a plug-in renewable energy source with battery storage. The electrical power transferred to the network and stored are the control variables that are considered. Also, [5.54] presented the application of hybrid modeling control for a Photovoltaic-fuel cell power plant.

However, the literatures using MPC for microgrids only focus on one specified energy source, a more complicated system with several renewable energy sources is still under further investigated. Besides, the MPC control strategies proposed so far did not take into account the grid connection from the point of view of the utility grid, and the potential grid supporting capacity of the microgrid is not yet exploited. Here, a new MPC strategy is developed on the top level of the microgrid system, which optimizes the power flow within the microgrid, and provides grid support during grid faults.

A. Formulation of the MPC controller

The problem described in Section 5.5.2 can be approached by means of an MPC strategy. The main idea is to minimize a given objective function J defined within a future horizon N, while the problem constraints are satisfied.

Define the power generated as P_{gen}, considering the power demand P_{demand}, the constraints referred to the net power available in the common AC bus can be expressed as

$$P_{net} = P_{gen} - P_{demand} \tag{5.43}$$

Since the total powers are generated by the PV array, wind turbine, and the fuel cell, therefore, P_{net} can be further calculated as

$$P_{net} = P_{PV} + P_{wind} + P_{FC} - P_{demand} \tag{5.44}$$

where P_{PV}, P_{wind}, and P_{FC} represent the power generated by the PV, wind turbine, and the fuel cell, respectively. P_{net}, known as the net power, is the available power in the common AC bus, which should be balanced through ESS and the utility grid for energy saving considerations.

The essential of the MPC controller is to set P_{net} to zero. As a matter of fact, in the normal operation of the microgrid system, the ($P_{PV} + P_{wind} - P_{demand}$) adds a perturbation on this variable that the controller must balance using the rest of the control variables in order to track the reference output. Therefore, the supervisor control target is to determine the optimal operating power references for the fuel cell output power P_{FC}^{*} and the power purchase or sold to the grid as auxiliary power reservoir P_g^{*} to compensate the unbalance.

According to the characteristics of each DG unit as described in Section 5.5.1, since the rated power of the wind turbine and the PV array are both 20 kW, the maximum net power is 40 kW, corresponding to rated power generated and no load. In contrast, the minimum net power is -30 kW, corresponding to zero generation and full demand. Therefore, the constraints aforementioned can be written for the control problem formulation as:

$$P_{FC,\min} = 500W \le P_{FC} \le 10kW = P_{FC,\max} \tag{5.45}$$

$$P_{g,\min} = -20kW \le P_g \le 20kW = P_{g,\max} \tag{5.46}$$

$$P_{net,\min} = -30kW \le P_{net} \le 40kW = P_{net,\max} \tag{5.47}$$

Considering the dynamics of the batter bank charging and discharging and the PEMFC power generation, the constraints regarding the power slew rate with the purpose of protecting the equipment from over-currents can be formulated as

$$\Delta P_{FC,\min} = -200W/s \le \Delta P_{FC} \le 200W/s = \Delta P_{FC,\max} \tag{5.48}$$

$$\Delta P_{g,\min} = -1kW \le \Delta P_g \le 1kW = \Delta P_{g,\max} \tag{5.49}$$

$$\Delta P_{net,\min} = -3kW/s \le \Delta P_{net} \le 4kW/s = \Delta P_{net,\max} \tag{5.50}$$

Another constraint needs to be taken into consideration is the protection of the battery from deep charging and over discharging, which can be implemented by setting the state of charge (SOC) as

$$SOC_{\min} = 35\% \le SOC \le 90\% = SOC_{\max} \tag{5.51}$$

$$\Delta SOC_{\min} = -4.16\times10^{-3} SOC/s \le \Delta SOC \le 4.16\times10^{-3} SOC/s = \Delta SOC_{\max} \tag{5.52}$$

B. Cost function

The cost function of the microgrid is defined as

$$\begin{aligned} Min.\ J = & \sum_{k=0}^{N} \alpha_1 P_{FC\_k}^2 + \alpha_2 P_{g\_k}^2 + \alpha_3 P_{net\_k}^2 + \beta_1 \Delta P_{FC\_k}^2 + \beta_2 \Delta P_{g\_k}^2 + \beta_3 \Delta P_{net\_k}^2 \\ & + \gamma_1 (SOC_k - SOC_{ref})^2 \\ & + \lambda_1 Q_k^2 \end{aligned} \tag{5.22}$$

In this cost function, N is the control horizon, the first three norms are in charge of the power flow optimization within the microgird. Hence, the penalization of the P_{net} variable drives the actual value of P_{net} to zero, i.e. the gap between the power generated and the power consumed can be smoothed, the power balance can then be satisfied. The following three norms are in charge of the increments of the power flow. Each term has a weighting factor, which represents the priority of the control objective.

Notice that the last term of the cost function is related to the reactive power compensation during grid faults (the balanced voltage sag is considered here). The selection of its weighting factor λ_1 is quite interesting, instead of setting a fixed value, λ_1 is determined by the extend of the voltage dip, which can be expressed as

$$\lambda_1 = \frac{V_{normal} - V}{G} \tag{5.45}$$

where V_{normal} is the normal RMS value of the grid voltage while V is the actual RMS value of the grid voltage, and G is the transfer factor. In this way, the microgrid can be controlled to participate in the voltage support. The severer of the voltage sag, the larger of the weighting factor λ_1, thus more reactive power can be generated.

Another aspect needs to point out is that the power fed to the utility grid should be also determined according to the electricity market. For instance, the surplus power generated can be fed to the utility grid rather than stored in the battery bank during those periods when the electricity market price is higher, provided the SOC is relatively high. Though the electricity market price is not considered in this MPC strategy, it would be an interesting topic in the future work.

5.5.4 Results and discussions

In order to check the feasibility of the proposed MPC strategies for smart microgrids, the performance of the microgrid system (see Fig. 5.35) was simulated over a day from 6 am to 8 pm using MATLAB. The profile of the power generated by the renewable energy sources and the power consumed by the loads are taken from Section 5.5.1. For the solar PV system, the power generation in a sunny day is used. The system sampling period is 1 second. The horizon N of the MPC controller is set to 10.

The powers generated by the wind turbine and the PV array, and the power consumed by the load during a day are plotted out in Fig. 5.46. It can be observed that the PV output power increased smoothly in the morning, reached the peak value of about 19 kW at around 2 pm, decreased gradually in the afternoon, and hit the bottom of 0 kW at around 7 pm. For the wind power system, the generator did not produce any power until 2pm because the wind speed is quite low in the first half of the day. The output power presents a fluctuated feature, reaching the peak value at around 6pm. On the other hand, the load profile features an obvious fluctuation with peak power consumed at around 7am, 12pm, and 19pm, respectively.

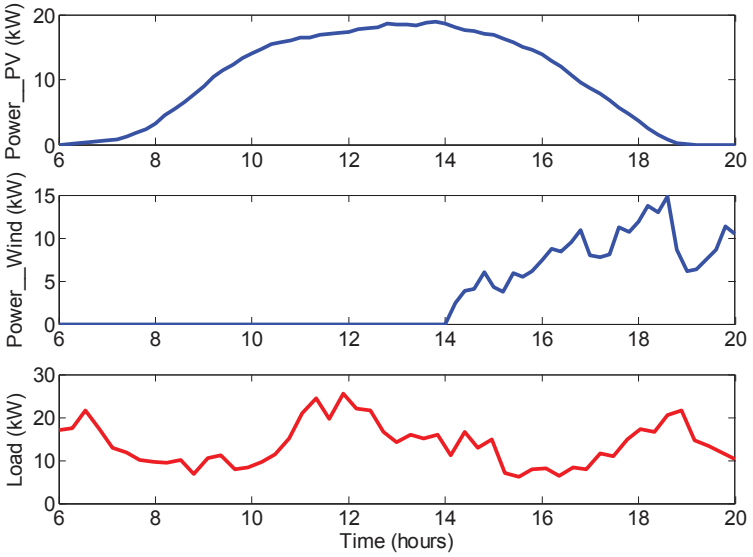

Fig. 5.46 Powers generated and consumed during a day.

The power gap, i.e. $P_{PV} + P_{Wind} - P_{\text{demand}}$, is shown in Fig. 5.47. It can be seen that the mismatched power varies frequently between negative values and positive values due to the intermittent nature of the renewable energy and the fluctuated load profile.

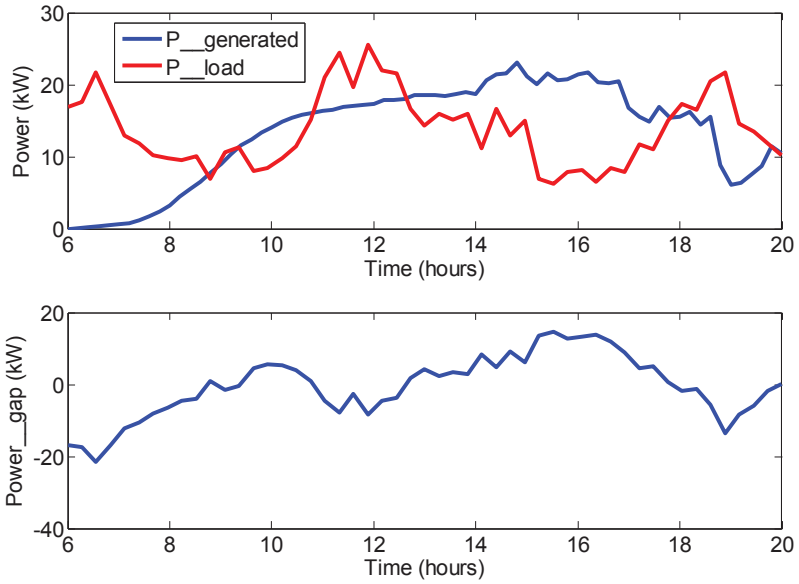

Fig. 5.47 The gap between the power generated and consumed during a day.

Fig. 5.48 shows the SOC of the battery bank. The SOC is calculated by estimating the voltage and current from battery string terminal voltage/current measurements

[5.55]. It can be seen that the battery bank was charging and discharging according to the power unbalance. From 6 am to 9 am, the load demand is greater than the power generation. In order to compensate this unbalance, the energy stored in the battery is flowing toward the load, as a result, the SOC drops gradually until the bottom limit (SOC_{min} is set to 35% in the MPC controller). Besides, it can be seen that the PEMFC is also operated to supply power to the load during this period, as shown in Fig. 5.49. From 2 pm to 6 pm, the power generation is greater than the load demand, and the surplus power is charging the ESS with the SOC raised smoothly until it hit the upper limit (90%). An interesting phenomenon around this moment is that the excess power is fed back to the utility as the ESS cannot store anymore power, as shown in Fig. 5.49. The SOC started to decrease after around 6 pm when the gap power becomes negative again.

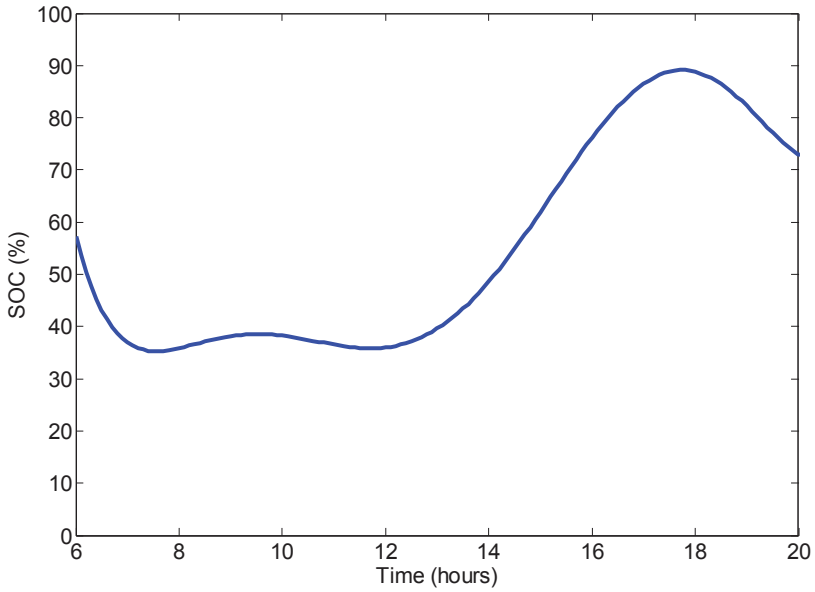

Fig. 5.48 SOC of the battery bank.

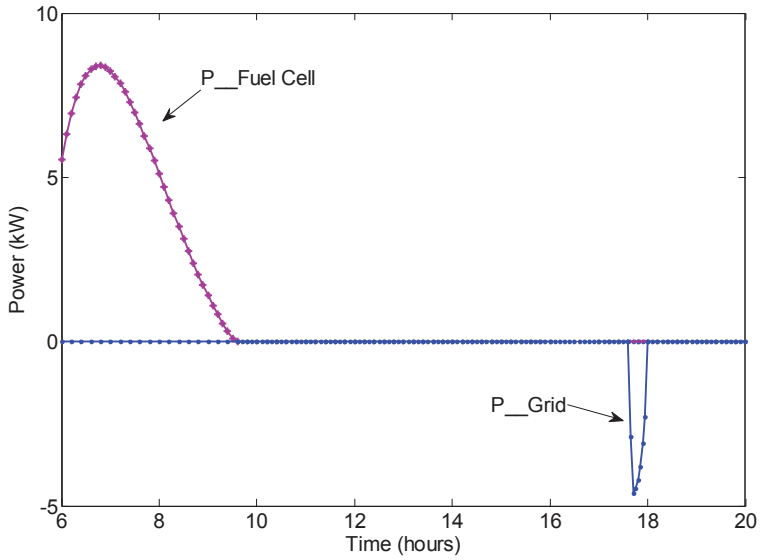

Fig. 5.49 The power generated by the fuel cell and the power exchanged between the micro and utility grid.

The proposed MPC controller can endow voltage ride-though capability during grid voltage sags. In order to validate this ability, the proposed MPC strategy has been also tested in the presence of a voltage sag of 0.15 p.u. which occurs for 2 seconds. In this case, it can be seen that the microgrid provides about 8 kVAr needed to compensate the sag, as shown in Fig. 5.50.

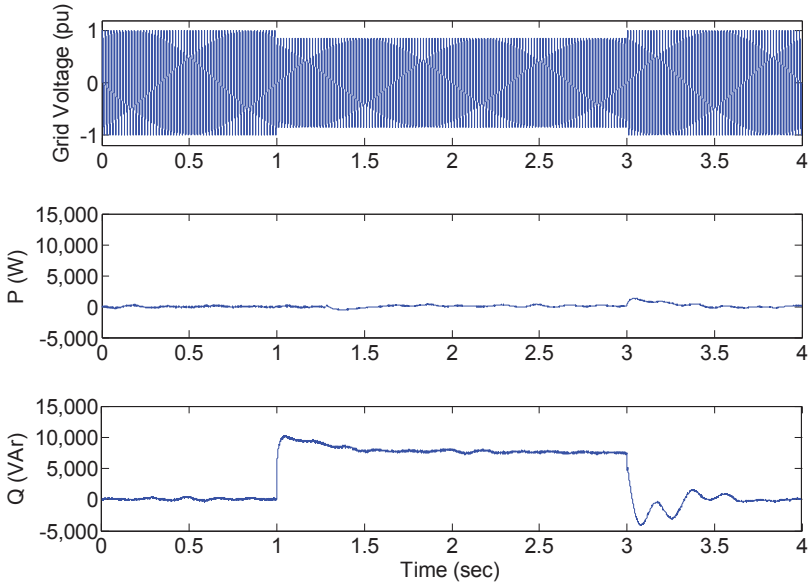

Fig. 5.50 Performance of the reactive power compensation under grid voltage sag of 0.1 pu.

5.6 Summary of the Chapter

This chapter introduces the smart microgrid system and its control strategies. As a systematic organization of DG units, the microgrid has more capacity and control flexibilities to fulfill system reliability and power quality requirements, in addition to all the inherited advantages of a single DG system.

Firstly, the two parallel-connected-DGs based microgrid is studied. The conventional voltage droop control method is introduced, where an artificial droop characteristics is introduced, the active and reactive power supplied by the DGs can be controlled by adjusting the output voltage frequency and amplitude, respectively, according to a pre-defined manner. Therefore, the DGs can meet the new load requirements automatically without rely on intercommunication systems, which is similar to the power system theory where a generator connected to the utility drops its frequency when the power required increases.

However, the conventional complex multi-feedback loops are unavoidable. Besides, the proper power sharing is achieved at the expense of voltage deviation. Based on this background, a new control strategy for parallel connected inverters in microgrid applications by drooping the inverter flux instead of the inverter output voltage. It can achieve active and reactive power sharing with much lower frequency deviation and better transient performance than the conventional droop method. This flux droop control approaches includes a direct flux control (DFC) algorithm, which avoids the use of PI controllers and PWM modulators.

In addition, a microgrid which consists of a 20 kW solar system, 30 kW gas microturbine (MT), and a programmable load bank is focused. The PV inverter is operated at maximum power points (MPPs) with unit power factor while the gas microturbine is controlled by a droop algorithm to dispatch active and reactive power. A coordinated control strategy is then proposed to control the microgrid, both in grid-connected and islanded mode. The experimental results from a renewable energy integration facility (REIF) laboratory show the feasibility of the control strategy by cases study such as grid-connected operation, islanded operation, re-synchronization. Besides, the response of this microgrid under grid faults is investigated and the protection mechanism is studied.

Finally, a model predictive control concept is proposed for a microgrid system, where the power generated by distributed energy sources, power consumed by the load,

power stored by the energy storage system and the power injected to the utility grid are determined according to an optimized cost function, so as to smooth the gap between the generation and consumption. Furthermore, the an additional constraint is added to the cost function so as to inject the reactive power into the utility grid during grid voltage sags, endowing the microgrid with the voltage ride-though capability.

References

[5.1] H. Farhangi, "The Path of The Smart Grid," *IEEE Magazine Power and Energy*, Vol. 8, No. 2, pp. 18-28, 2010.

[5.2] J. Wang, A. Q. Huang, W. Sung, Y. Liu, and B. J. Baliga, "Smart grid technologies," *IEEE Magazine Ind. Electron.,* pp. 16-23, June, 2009. .

[5.3] E. J. Coster, J. M. A. Myrzik, B. Kruimer and W. L. Kling, "Integration issues of distributed generation in distribution grid," *Proceedings of the IEEE.,* vol. 99, no. 1, pp. 28-39, 2011.

[5.4] K. Moslehi and R. Kumar, "A reliability perspective of the smart grid," *IEEE Trans. Smart Grid.,* vol. 1, no. 1, pp. 57-64, 2010.

[5.5] J. Hu, J. Zhu, and G. Platt, "Smart Grid — The Next Generation Electricity Grid with Power Flow Optimization and High Power Quality," in *Proc. IEEE ICEMS Conf.,* pp. 1–6, 2011.

[5.6] A. P. Martins, A. S. Carvalho, and A. S. Araújo, "Design and implementation of a current redundant operation system," in *Proc*. *IEEE IECON*, 1995, pp. 584-589.

[5.7] X. Sun, Y.-S. Lee, and D. Xu, "Modeling, analysis, and implementation of parallel multi-inverter system with instantaneous average-current-sharing scheme," *IEEE Trans. Power Electron*., vol. 18, no. 3, pp. 844-56, 2003.

[5.8] T. F. Wu, Y.-K. Chen, and Y.-H. Huang, "3C strategy for inverters in parallel operation achieving an equal current distribution," *IEEE Trans. Ind. Electron*., vol. 47, no. 2, pp. 273-281, 2000.

[5.9] M. C. Chandorkar, D. M. Divan, and R. Adapa, "Control of parallel connected inverters in standalone ac supply systems," *IEEE Trans. Ind. Appl*., vol. 29, no. 1, pp. 136-143, Jan./Feb. 1993.

[5.10] J. M. Guerrero, J. Matas, L. G. de Vicuña, J. Matas, M. Castilla, and J. Miret, "A wireless controller to enhance dynamic performance of parallel inverters in distributed generation systems," *IEEE Trans. Power. Electron*., vol. 19, no. 5, pp. 1205-1213, Sep. 2004.

[5.11] Y. Li, D. M. Vilathgamuwa, and P. C. Loh, "Design, analysis, and real-time testing of a controller for multibus microgrid system," *IEEE Trans. Power. Electron.,* vol. 19, no. 5, pp. 1195-1204, Sep. 2004.

[5.12] K. D. Brabandere, B. Bolsens, J. V. Keybus, A. Woyte, J. Driesen, and R. Belmans, "A voltage and frequency droop control method for parallel inverters," *IEEE Trans. Power. Electron.,* vol. 22, no. 4, pp. 1107-1115, Jul. 2007.

[5.13] Y. Li and C. N. Kao, "An accurate power control strategy for power-electronics-interfaced distributed generation units operating in a low-voltage multibus microgrid," *IEEE Trans. Power. Electron.,* vol. 24, no. 12, pp. 2977-2988, Dec. 2009.

[5.14] C. Cho, J-H. Jeon, J-Y. Kim, S. Kwon, K. Park, and S. Kim, "Active synchronizing control of a microgrid," *IEEE Trans. Power. Electron.,* vol. 26, no. 12, pp. 3707-3719, December 2011.

[5.15] J. Hu, J. Zhu, and G. Platt, "A droop control strategy of parallel-inverter-based microgrid," in *Proc. IEEE ASEMD Conf.,* pp. 188–191, 2011.

[5.16] A. R. Bergen, Power Systems Analysis. Englewood Cliffs, NJ: PrenticeHall, 1986.

[5.17] M. Abdel-Rahim and J. E. Quaicoe, "Analysis and design of a multiple feedback loop control strategy for single-phase voltage-source UPS inverters,"*IEEE Trans. Power Electron*, vol. 11, no. 4, pp. 532-541, 1996.

[5.18] S. R. H. Amrei, S. M. Alizadeh, A. Yaghoubi, and A. Bemani, "Analysis and design of multiple feedback control loops for both inverters and recitifier of single-phase UPS under non-linear load,"*Interational Journal of Computer Science Issues*, vol. 9, no. 2, pp. 500-512, 2012.

[5.19] M. C. Chandorkar, "New techniques for inverter flux control," *IEEE Trans. Ind. Appl.,* vol. 37, no. 3, pp. 880-887, 2001.

[5.20] M. Cirrincione, M. Pucci, and G. Vitale, "Direct power control of three-phase VSIs for the minimization of common-mode emissions in distributed generation systems," *Journal of Electric Power Systems Research,* vol. 81, no. 4, pp. 830-839, 2011.

[5.21] L. Bhargavi, S. Reddy, and S. K. Sahu, "State space vector based advanced direct power control of matrix converter as UPFC," *International Journal of Research in Engineering and Technology.,* vol. 1, no. 3, pp. 483-495, 2012.

[5.22] M. Abdel-Rahim and J. E. Quaicoe, "Analysis and design of a multiple feedback loop control strategy for single-phase voltage-source UPS inverters," *IEEE Trans. Power Electron.,* vol. 11, no. 4, pp. 532-541, 1996.

[5.23] P. C. Loh, M. J. Newman, D. N. Zmood, and D. G. Holmes, "A comparative analysis of multiloop voltage regulation strategies for single and three-phase UPS systems," *IEEE Trans. Ind. Electron.,* vol. 18, no. 5, pp. 1176-1185, Sep. 2003.

[5.24] P. C. Loh and D. G. Holmes, “Analysis of multiloop strategies for LC/CL/LCL-filtered voltage-source and current-source inverters,” *IEEE Trans. Ind. Appl*., vol. 41, no. 2, pp 644-654, Mar./Apr. 2005.

[5.25] J. M. Guerrero, J. Matas, L. G. de Vicuna, M. Castilla, and J. Miret, “Wireless-control strategy for parallel operation of distributed-generation inverters,” *IEEE Trans. Ind. Electron.,* vol. 53, no. 5, pp. 1461-1470, 2006.

[5.26] A. M. Salamah, S. J. Finney, and B. W. Williams, “Autonomous controller for improved dynamic performance of AC grid, parallel-connected, single-phase inverters,” *IET Gener. Trnasm. Distrib.,* vol. 2, no. 2, pp. 209-218, 2008.

[5.27] J. C. Vásquez, J. M. Guerrero, A. Luna, P. Rodríguez, and R. Teodorescu, “Adaptive droop control applied to voltage-source inverter operating in grid-connected and islanded modes” *IEEE Trans. Ind. Electron.,* vol. 56, no. 10, pp. 4088-4096, 2009.

[5.28] R. Majumder, B. Chaudhuri, A. Ghosh, R. Majumder, G. Ledwich, and F. Zare, “Improvement of stability and load sharing in an autonomous microgrid using supplementary droop control loop,” *IEEE Trans. Power System.,* vol. 25, no. 2, pp. 796-808, 2010.

[5.29] M. Hua, H. Hu, Y. Xing, and J. M. Guerrero, “Multilayer control for inverters in parallel operation without intercommunications,” *IEEE Trans. Power. Electron.,* vol. 27, no. 8, pp. 3651-3663, August 2012.

[5.30] M. Savaghebi, A. Jalilian, J. C. Vasquez, and J. M. Guerrero, “Secondary control scheme for voltage unbalance compensation in an islanded droop-controlled microgrid,” *IEEE Trans. Smart Grid.,* vol. 3, no. 2, pp. 797-807, 2012.

[5.31] M. C. Chandorkar, “New techniques for inverter flux control,” *IEEE Trans. Ind. Appl.,* vol. 37, no. 3, pp. 880-887, 2001.

[5.32] G. S. Buja and M. P. Kazmierkowski, "Direct torque control of PWM inverter-fed AC motors ─ A Survey," *IEEE Trans. Ind. Electron.,* vol. 1, no. 4, pp. 744-757, 2004.

[5.33] P. Cortés, M. P. Kazmierkowsik, R. M. Kennel, D. E. Qeuvedo, and J. Rodríguez, “Predictive control in power electronics and drives,” *IEEE Trans. Ind. Electron.,* vol. 55, no. 12, pp. 4312-4321, 2008..

[5.34] S. Kouro, P. Cortés, R. Vargas, U. Ammann, and J. Rodríguez, “Model predictive control – a simple and powerful method to control power converters,” *IEEE Trans. Ind. Electron.,* vol. 56, no. 6, pp. 1826-1838, 2009.

[5.35] M. P. Kazmierkowski, R. Krishnan, and F. Blaabjerg, *Control in Power Electronics*. New York: Academic, 2002.

[5.36] A. K. Saha, S. Chowdhury, and P. A. Crossley, "Modeling and performance analysis of a microturbine as a distributed energy resource," *IEEE Trans. Energy. Convers.,* vol. 24, no. 2, pp. 529-538, 2009.

[5.37] S. Grillo, S. Massucco, A. Morini, A. Pitto and F. Silvestro, "Microturbine control modeling to investigate the effects of distributed generation in electric energy networks," *IEEE Trans. Systems.,* vol. 4, no. 3, pp. 303-312, 2010.

[5.38] K. H. Hussein, I. Muta, T. Hoshino, and M. Osakada, "Maximum photovoltaic power tracking: An algorithm for rapidly changing atmospheric conditions," *Proc. Inst. Elect. Eng., Gen., Transm., Distrib.,* vol. 142, no. 1, pp. 59–64, 1995.

[5.39] A. Yazdani and P. P. Dash, "A control methodology and characterization of dynamics for a photovoltaic (PV) system interfaced with a distribution network," *IEEE Trans. Power. Delivery.,* vol. 24, no. 3, pp. 1538–1551, 2009.

[5.40] S. Hao, Y. Zhang, X. Li, and Y. Yuan, "Equivalent wind speed model in wind farm dynamic analysis," in Proc. *IEEE Electric Utility Deregulation and Restructuring and Power Technologies Conf.,* 2011, pp. 1751–1755.

[5.41] Horizon Technology, "300W fuel cell stack operating instruments," www.horizonfuelcell.com.

[5.42] Y. Zhan, J. Zhu, Y. Guo, and H. Wang, "A PEMFC/Battery hybrid UPS system for backup and emergency power applications," in *Proc. IEEE Power Electronics and Drive Systems Conf.*, 2007, pp. 1513-1517.

[5.43] L. Valverde, C. Bordons, and F. Rosa, "Power management using model predictive control in a hydrogen-based microgrid," in *Proc. IEEE IECON2012.*, 2012, pp. 5653-5660.

[5.44] Australian Energy Market Operator (AEMO), https://www.aemo.com.au.

[5.45] XBee/XBee-PRO ZB OEM RF Modules, Digi International Inc, 2008.

[5.46] E. Perez, H. Beltran, N. Aparicio, and P. Rodriguez, "Predictive power control for PV plants with energy storage," *IEEE Trans. Sustains. Energy,* in press.

[5.47] Ø. Ulleberg., "The Importance of Control Strategies in PV-hydrogen Systems", *Solar Energy,* no 76, pp. 323-329, 2001.

[5.48] A. Bilodeau, K. Agbossou, "Control analysis of renewable energy system with hydrogen storage for residential applications", *Journal of Power Sources,* no 162, pp. 757–764, 2006.

[5.49] E.M. Stewart et al., "Modeling, analysis and control system development for the Italian hydrogen house", *International Journal of Hydrogen Energy,* pp. 1638-1646, 2009.

[5.50] E. F. Camacho and C. Bordons, *Model Predictive Control*, London: Springer-Verlag, 2004.

[5.51] P. L. Zervas, H. Sarimveis, J. A. Palyvos, and N. C. G. Markatos, "Model-based optimal control of a hybrid power generation system consisting of photovoltaic arrays and fuel cells," *Journal of Power Sources,* no. 181, pp. 327-338, 2008.

[5.52] W. Qi, J. Liu, and P. D. Christofides, "Supervisory predictive control for long-term scheduling of an integrated wind/solar energy generation and water desalination system," *IEEE Trans. Control Systems Technology.,* vol. 20, no. 2, pp. 504-512, 2012.

[5.53] M. Khalid, "A model predictive control approach to the problem of wind power smoothing with controlled battery storate," *Renewable Energy,* pp. 1520-1526, 2010.

[5.54] A. Del Real, A. Arce, C. Bordons, "Hybrid model predictive control of a two-generator power plant integrating photovoltaic panels and fuel cell," *46 IEEE Conference on Decision and Control,* New Orleans, 2007.

[5.55] L. Wang, M. P. Polis, G. G. Yin, W. Chen, Y. Fu, and C. C. Mi, "Battery cell identification and SOC estimation using string terminal voltage measurements," *IEEE Trans. Vehicular Technology.,* vol. 61, no. 7, pp. 2925-2935, 2012.

CHAPTER 6

CONCLUSIONS AND FUTURE WORK

6.1 Conclusions

In this thesis, advanced control strategies for smart microgrids have been studied and developed. The general conclusions of this thesis can be summarized as:

1. Review of the state of art of renewable energy technology and microgrid control, comprehensive study of control strategies of power converters.

2. Development of a new predictive control strategy for the doubly fed induction generator based wind power system, which considers fast grid synchronization, smooth grid connection and flexible power regulation.

3. Development of a new model predictive control strategy for PV systems, which can achieve islanded operation, seamless transfer, and grid-connected operation.

4. Development of an improved multi-objective model-predictive control approach for power converters to reduce switching frequency in microgrid applications.

5. Development of a new droop control technique for microgrids with less frequency deviations and simple control structure, compared to conventional voltage droop control method.

6. Proposal of a new model predictive control concept for microgrids including DG sources, load, and energy storage system, aiming to smooth the power flow and grid support during faults.

6.2 Future Work

Advanced control techniques for microgrids and smart grids are critically desired since the existing electricity network is undergoing a major transformation and the penetration of renewable energy sources connected to the grid are rapidly increased, and

they will be the ongoing research topic in the following decades. Based on the progress obtained in this thesis, the continued work of this research area can be described as

- Based on the work of Chapter 3, develop a flexible control strategy of grid-connected inverters to address utility voltage distortion such as voltage unbalance and voltage sag.

- Validate the new droop control strategies developed in Chapter 5 with experimental results, demonstrating the effectiveness of power quality improvement using the proposed flux droop.

- Further develop the model predictive control strategy of microgrids proposed in Chapter 5 and carry out the experimental test, including the control objectives in the cost function such as PCC voltage, optimized power flow and economic penalties reduction, taking into account the renewable energy characteristics, energy storage dynamic and the electricity market scheduling.

APPENDIX A:

PUBLICATIONS BASED ON THE THESIS WORK

Journal Papers

[1] J. Hu, J. Zhu, G. Platt, and J. M. Guerrero, "A novel virtual-flux-based droop control strategy for the parallel operation of inverters in microgrids," *IEEE Trans. Smart Grid,* under second review.

[2] J. Hu, J. Zhu, G. Platt, and D. G. Dorrell, "Model predictive control of inverters for both islanded and grid-connected operations in renewable power generations," *IET Renew. Power Gener.,* in press.

[3] J. Hu, J. Zhu, G. Platt, and D. G. Dorrell, "Multi-objective model-predictive control for high power converters," *IEEE Trans. Energy Convers.,* vol. 28, no. 3, pp. 652-663, Sep. 2013.

[4] J. Hu, J. Zhu, Y. Zhang, G. Platt, Q. Ma and D. G. Dorrell, "Predictive direct virtual torque and power control of doubly fed induction generators for fast and smooth grid synchronization and flexible power regulation," *IEEE Trans. Power Electron.,* vol. 28, no. 7, pp. 3182–3194, July 2013.

[5] J. Hu, J. Zhu, and G. Platt, "Smart grid – the next generation electricity grid with power flow optimization and high power quality," *Journal of International Conference on Electrical Machines and Systems.,* vol. 1, no. 4, pp. 29–37, Dec. 2012.

Conference Papers

[1] J. Hu, J. Zhu, Y. Qu, and J. M. Guerrero, "A new virtual-flux-based droop control strategy for parallel connected inverters in microgrids," in *Proc. of IEEE Energy Conversion Congress and Exposition (ECCE) 2013 Asia DownUnder,* pp. 585-590, 2013.

[2] J. Hu, J. Zhu, G. Platt and D. G. Dorrell, "Model-predictive direct power control of AC/DC converters with one step delay compensation," in *Proc. IEEE IECON Conf.,* pp. 4874–4879, 2012.

[3] J. Hu, J. Zhu, and G. Platt, "Smart Grid — The Next Generation Electricity Grid with Power Flow Optimization and High Power Quality," in *Proc. IEEE ICEMS Conf.,* pp. 1–6, 2011.

[4] J. Hu, J. Zhu, and G. Platt, "A droop control strategy of parallel-inverter-based microgrid," in *Proc. IEEE ASEMD Conf.,* pp. 188–191, 2011.

[5] J. Hu, J. Zhu, Y. Zhang, G. Platt, Q. Ma, and D. G. Dorrell, "Predictive direct control of doubly fed induction generator for grid synchronization in wind power generation," in *Proc. IEEE ECCE Conf.,* pp. 2381–2388, 2011.

[6] J. Hu, J. Zhu, Y. Zhang, and Y. Guo, "Predictive direct power control of doubly fed induction generator with power ripples reduction and one step delay compensation for wind power generation," in *Proc. IEEE ICEMS Conf.,* pp. 1–6, 2011.

[7] J. Hu, J. Zhu, and D. G. Dorrell, "A Comparative Study of Direct Power Control of AC/DC Converters for Renewable Energy Generation," in *Proc. IEEE IECON Conf.,* pp. 3453–3458, 2011.

[8] J. Hu, J. Zhu, Y. Zhang, Q. Ma, and Y. Guo, "Simple and Robust Predictive Direct Control of DFIG with Low Constant Switching Frequency and Reduced Torque and Flux Ripples," in *Proc. IEEE Int. Electric Machines and Drives Conf.* 2011*,* pp. 781–786.

[9] J. Hu, J. Zhu, D. G. Dorrell, Q. Ma, Y. Zhang, and W. Xu, "Control strategies of variable-speed wind system under new grid code requirement – A survey," in *Proc. IEEE IECON Conf.,* pp. 3061–3066, 2010.

[10] J. Hu, J. Zhu, D. G. Dorrell, Y. Wang, Y. Zhang, W. Xu, and Y. Li, "A novel control strategy for doubly fed induction generator and permanent magnet synchronous generator during voltage dips," in *Proc. IEEE AUPEC Conf.,* pp. 1–6, 2010.